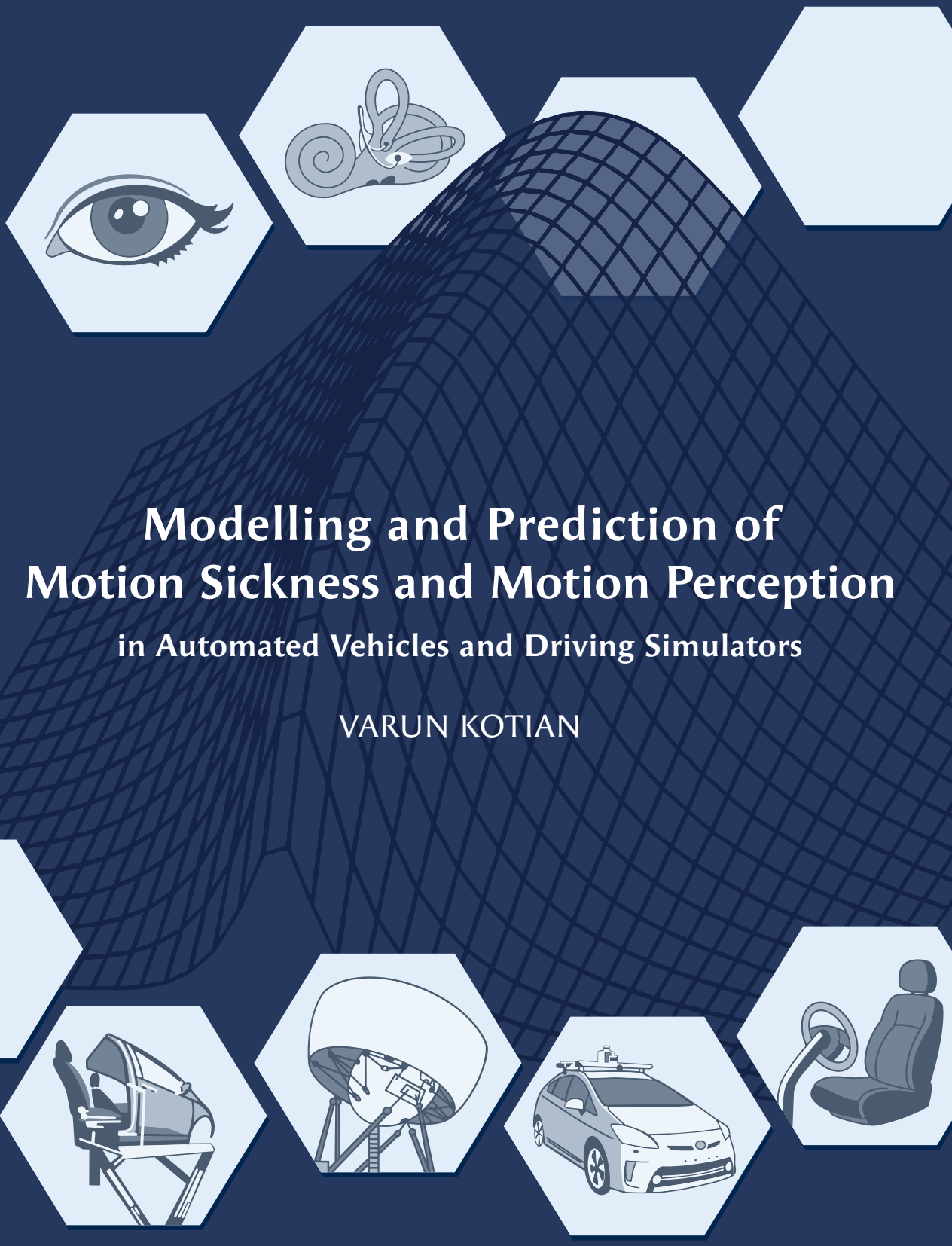

Modelling and Prediction of Motion Sickness and Motion Perception

in Automated Vehicles and Driving Simulators

VARUN KOTIAN

Motion Perception and Sickness Modelling and Prediction for Automated Driving and Simulators

Motion Perception and Sickness Modelling and Prediction for Automated Driving and Simulators

DISSERTATION

for the purpose of obtaining the degree of doctor
at Delft University of Technology,
by the authority of the Rector Magnificus Prof. dr. ir. H. Bijl,
chair of the Board for Doctorates,
to be defended publicly on
Thursday, 12 March 2026 at 12:30 pm

by

Varun KOTIAN

This dissertation has been approved by the promotors.

Composition of the doctoral committee:

Rector Magnificus	Chairperson
Prof. dr. ir. R. Happee	Delft University of Technology, promotor
Dr. ir. D. M. Pool	Delft University of Technology, copromotor
Independent members:	
Prof. dr. ir. M. Mulder	Delft University of Technology
Prof. dr. J.E. Bos	Vrije Universiteit Amsterdam, the Netherlands
Prof. dr. T. Wada	Nara Institute of Science and Technology, Japan
Prof. dr. J.F. Golding	University of Westminster, UK
Dr. T.K. Clark	University of Colorado, USA
Prof. dr. J. Alonso-Mora	Delft University of Technology, reserve member

Dr. B. Shyrokau from Delft University of Technology has contributed greatly to this dissertation.

The work in this thesis was made possible by the TIPP project funded by Toyota Motor Europe.

Keywords: Comfort, Discomfort, Motion sickness, Motion perception, Modelling, Driving simulators, Automated vehicles, Vision, Personalisation

Printed by: Gildeprint

Cover: Rucha Khot

Style: TU Delft House Style, with modifications by Moritz Beller and Varun Kotian
`https://github.com/Inventitech/phd-thesis-template`

The author set this thesis in LaTeX using the Libertinus and Inconsolata fonts.

ISBN 978-94-6518-261-2

An electronic version of this dissertation is available at
`http://repository.tudelft.nl/`.

Knowledge and awareness are vague, and perhaps better called illusions.
Everyone lives within their own subjective interpretation.

Itachi Uchiha

Contents

Summary

Motion sickness is becoming a more significant concern with the rise of automated vehicles and the increasingly extended application of driving simulators. In traditional cars, drivers and front-seat passengers can usually anticipate the vehicle's motion, which helps prevent sickness. In automated vehicles, however, people often take on a passive role –reading, looking at screens, or simply not paying attention to the road – while the vehicle automatically moves through traffic. This induces conflicts between what the eyes see, what the body feels, and what the brain expects, increasing the risk of motion sickness. A similar problem occurs in simulators, where visual cues and physical motion are generally not fully in natural agreement. Building on this, sensory-conflict models have been developed that fuse vestibular and visual cues and whose predicted integrated conflicts correlate with reported motion sickness. Yet most of these models were tuned to match group-average sickness responses in simple laboratory experiments, ignoring vision's role and individual variability. Validation of these models is limited for the typically more complex motion stimuli that characterise passive automated driving and modern simulators, where vision can dominate and motion differs significantly. Moreover, validation often relies on Motion Sickness Incidence (MSI) – the predicted fraction of people who vomit over a given exposure – which captures only the most severe outcome, but misses the lower-level symptoms (nausea, dizziness, oculomotor discomfort) that are best avoided as well. For automated driving acceptance and simulator usability, models must thus predict these sub-vomiting severities and their time course, incorporating visual scene properties, and person-specific susceptibility.

To tackle these challenges, this research first collects and uses data from both real-world driving and simulator experiments, focusing on how sickness develops in each individual instead of considering only aggregated group averages. All datasets involve passive driving, with multiple motion and/or vision conditions tested within the same participants, enabling controlled comparisons of inside versus outside cabin view, real versus simulator driving, or different motion-cueing algorithms versus no simulator motion. From this collected data, it was quantified that while stronger motion generally causes more severe sickness, the way motion sickness develops and progresses can vary greatly from person to person, making group-average models systematically biased for many users. This thesis demonstrates that personalised models which adapt only a few parameters per person can yield significantly more accurate predictions of motion sickness over time.

Another key part of the thesis investigates how vision affects both people's perception of motion and their development of motion sickness. Through careful testing and comparison, the research reveals that existing models struggle to accurately predict both how people perceive movement and how sick they might get, especially when it comes to situations involving visual cues. Some models predict perception better and others predict

sickness better, but none do both well with their current designs and proposed parameter settings. After careful testing, SVC-VR – the Subjective Vertical Conflict model with a visual rotational-rate input – was selected as the best compromise for sickness prediction. Still, how vision and motion together cause sickness requires further study.

Next, the thesis makes an important step forward by developing a new model framework that combines general group trends with minimal selective adjustments for individual differences, making it possible to predict how motion sickness accumulates in each person over time and in a variety of conditions. Instead of treating everyone the same, this framework estimates two key accumulation parameters — representing motion sensitivity (gain) and how quickly sickness develops (time constant) — for each individual. Building upon these personal parameters, a stochastic population model capturing the distribution of these parameters is presented. This allows the model to simulate not just one person's experience, but the entire range of possible responses in a population. By sampling from these distributions, it becomes possible to predict how a group with different susceptibilities will respond to new motion conditions, reducing the need for large-scale human testing. The approach demonstrates strong predictive power even on data from scenarios not used for model parameterisation, supporting its use in practical vehicle and simulator applications.

While SVC-VR showed promise for sickness prediction, a physiologically valid sensory-conflict model should ideally predict not only the resulting sickness but also the underlying spatial orientation perception that drives the conflict. To evaluate this unified predictive capability, visual–vestibular integration was tested in a pitch-perception study with 32 participants experiencing ramp-like pitch motion at 0.5–5 deg/s under Only Vision, External/Internal Vision, and No Vision conditions. The perceived pitch amplitude was underestimated by about 20% with an average 0.75 s delay, and vision had no significant effect when mechanical motion was present. With its original published parameters, the SVC-VR gave unrealistic pitch perception estimates and even predicted an opposite direction perception in the Only Vision condition. After retuning the SVC-VR model and adding vestibular perception thresholds, its capacity for matching the experiment data improved markedly. These findings reveal the limits of current parameter settings and highlight the need for careful parameter tuning to support vision-aware personalisation and joint perception–sickness modelling.

Building on these advances, the thesis applies the modelling approach to develop a new motion cueing algorithm for driving simulators. This algorithm actively minimises motion sickness by adjusting how mechanical motion is presented to users in the simulator, taking into account both the predicted conflict between different sensory signals and individual response patterns over time. The result is an algorithm that reduces motion sickness by over 50% compared to traditional methods, without sacrificing the (subjectively reported) sense of realism that is essential for effective simulation. Importantly, this method shows that real-time motion sickness mitigation is achievable and that such solutions can be used to make automated vehicles and simulators more comfortable for a broad and diverse range of users.

In conclusion, this work demonstrates that motion sickness can be predicted and mitigated at the level of the individual by modelling how conflicts accumulate over time and how visual conditions shape both perception and sickness. The core contribution is a person-specific predictive framework that captures large inter-individual differences with two individual parameters and significantly outperforms group-average models. Building on this, a model-predictive control motion cueing algorithm was developed that reduces sickness in simulators without sacrificing realism, illustrating how the models can drive practical mitigation. Together, these advances provide a foundation for automated vehicles and simulators that adapt in real time to each passenger, improving comfort and supporting broader acceptance.

1

Introduction

You have control over action alone, never over its results.
Therefore, begin your work without attachment.

Bhagavad Gita, 2.47

1

1.1 Background

As transportation technologies evolve, especially with the projected rapid rise of automated vehicles, a new challenge has been introduced for passenger comfort and safety. In traditional vehicles, occupants can often anticipate motion either as front-seated passengers or as drivers, but in future automated vehicles, users are expected to become passive passengers who engage in activities such as reading or using electronic devices (Bertolini and Straumann, 2016; Griffin and Newman, 2004; Kuiper et al., 2018; Salter et al., 2019). In these scenarios of eyes-off-the-road driving, the motion experienced is fully controlled by automated motion planning algorithms, leaving passengers unable to anticipate or prepare for unexpected movements. This passive role can increase conflicts between visual, vestibular, and expected motion cues, substantially raising the risk of motion sickness (Diels and Bos, 2016). If left unchecked, this problem could become a significant obstacle to the widespread acceptance and success of automated vehicle technology (Diels et al., 2022). Driving simulators also share the same issue of motion sickness. In driving simulators, realistic (unscaled) visual motion is presented with scaled-down, or even without any, physical motion. This causes a mismatch between expected and perceived motion, eliciting motion sickness (Bos et al., 2020). Even though these two examples – cars and driving simulators – are different and referred to as car and simulator sickness (Golding, 2016), respectively, the inherent mechanism that causes motion sickness in both, i.e., *sensory-expectancy conflict*, is the same (Reason, 1978b). Therefore, an urgent need is present to better understand and manage motion sickness in these environments, so that automated vehicles can be designed to optimise passenger comfort. However, addressing this challenge is not feasible without robust predictive models of motion sickness.

Motion sickness is a syndrome that arises when there is a mismatch between sensory signals sensed by the body (such as from the eyes and the vestibular system) and what the brain expects to sense (Oman, 1982; Reason, 1978a). These mismatches, commonly called '*sensory conflicts*', can be caused by exposure to a wide range of self-motion and orientation cues. The symptoms of motion sickness typically include sweating, headache, dizziness, and stomach discomfort, which can increase in severity to nausea, retching, and even vomiting (Bertolini and Straumann, 2016). Some of these symptoms have been observed across various species (Bäuerle et al., 2004; Hickman et al., 2008; Wang and Chinn, 1956; Wassersug et al., 1993), indicating the fundamental nature of the mechanisms involved. Despite these numerous studies, the exact origin and processes of motion sickness continue to be actively researched.

Motion sickness is a broad term and encompasses many subtypes, as seen in figure 1.1. These subtypes are generally classified into three categories according to the conflicting sensory modalities (Reason, 1978b): (1) the presence of physical motion in the absence of corresponding visual input; (2) the presence of visual stimuli suggestive of motion without actual physical movement; (3) the simultaneous presence of both motion and visual cues that are either uncorrelated or contradictory; and (4) artificial imagery is presented that creates a self-motion percept differing from the real world, a specific challenge in driving simulators (Bos et al., 2021). This thesis, will focus on modelling car and driving simulator sickness, where the vertical motion is of a smaller magnitude compared to other directions

of motion. The aim is to make a model that is accurate for use in real cars and driving simulators. Furthermore, it is anticipated that the proposed model may demonstrate adequate generalizability to other forms of motion sickness, such as air, sea and cyber sickness.

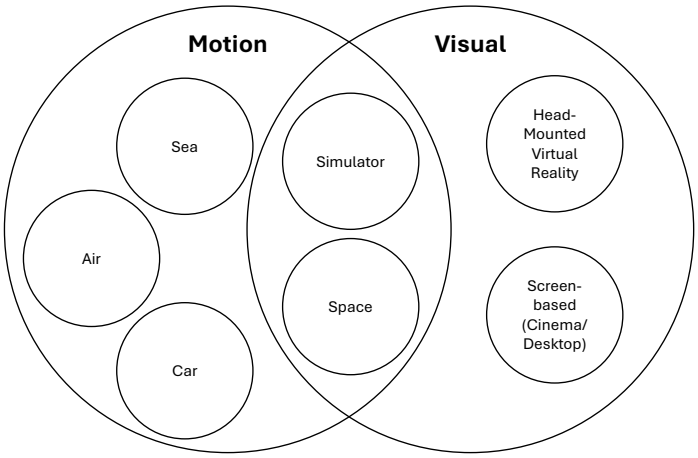

Figure 1.1: Types of motion sickness. This thesis focuses on car sickness and driving simulator sickness.

Two main theories are often used to explain the development of motion sickness: the *Neural Mismatch Theory* (Oman, 1982; Reason, 1978a) and the *Postural Instability Theory* (Riccio and Stoffregen, 1991). The latter posits that postural instability is a necessary and sufficient condition for sickness. However, as noted by Bos (2011), this strict causality is debated, as instability may not be the cause of sickness, but rather a parallel symptom or a precursor that occurs as the body struggles to maintain balance in a provocative environment. Consequently, this thesis extends on the well-known neural mismatch theory, which has the most developed mathematical models (Bos and Bles, 1998; Khalid et al., 2011a; Wada, 2021) and argues that motion sickness is mainly caused by a conflict between the actual sensory signals and the signals expected by an internal model in the brain. This is shown in a high-level representation in figure 1.2. This internal model is thought to work like a neural store or observer, estimating the body's state by combining imperfect sensory signals (Angelaki et al., 2004; Laurens et al., 2013; Merfeld et al., 1999; Oman and Cullen, 2014). The estimation error or conflict, which is the difference between the sensed and expected cues, is believed to cause motion sickness after sufficient magnitude and duration of exposure.

Understanding how this conflict leads to motion sickness has practical importance. Improved knowledge allows sickness to be predicted and controlled in vehicles and simulators (Wada and Yoshida, 2016; Wijlens et al., 2022) by explicit adjustment of vestibular or even visual inputs. This can also enable participant pre-screening (Bos et al., 2010; Irmak et al., 2020). However, traditional models often predict sickness at the group level, using measures such as Motion Sickness Incidence (MSI), defined as the proportion of people who will vomit (Bos and Bles, 1998; Lawther and Griffin, 1988; O'Hanlon and McCauley,

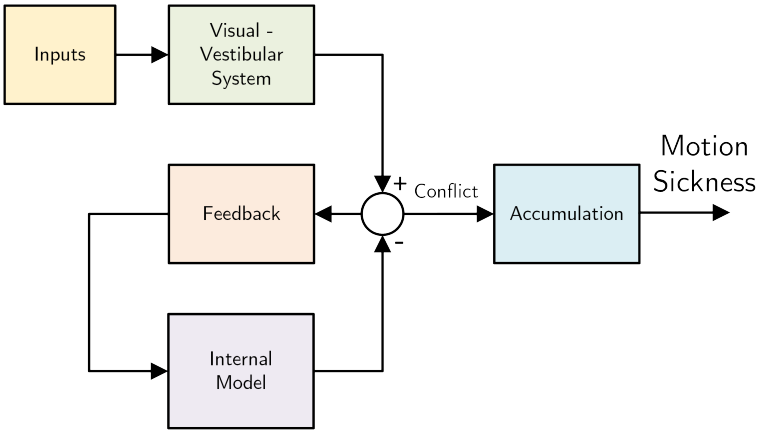

Figure 1.2: High-level representation of motion sickness models based on neural mismatch theory.

1974). While group-level relationships, such as the effect of acceleration magnitude, have been described (Irmak et al., 2020), these models do not capture the full progression of symptoms, such as the lower levels of sickness which do not relate to vomiting or the hypersensitivity effects seen on repeated exposure (Golding et al., 1997; Oman, 1990).

Models that predict motion sickness trajectories in time, such as the Oman model, have been developed previously (Oman, 1990). Furthermore, personalisation of model parameters has been shown to significantly improve predictions of motion sickness scores at the individual level (Irmak et al., 2020). Despite these advancements, validation of these models has predominantly focused on responses to purely one-dimensional vestibular stimuli. In contrast, real-world environments commonly involve mixed acceleration and different sensory conditions, which require more advanced models that take into account both visual and vestibular information. Furthermore, current models are limited in their ability to account for variations in motion sickness associated with differences in individual susceptibility. Although these models can be fitted to an individual's motion sickness trajectory, they fail to generalise to other individuals because they do not establish a relationship between motion sickness susceptibility and the model parameters. Consequently, a clear research gap remains that makes generalisation across populations difficult and limits the predictive usefulness of current individualised modelling frameworks.

The effect of vision is also limited or even absent in most current sickness prediction models. This is at odds with the fact that visual cues play a particularly noteworthy role in motion sickness development. Motion sickness is made worse in many situations where visual and vestibular information do not agree, such as when strongly moving visual stimuli are presented without matching physical motion (as in simulators and virtual reality) (Bos and Bles, 1998; Nooij et al., 2017; Wada et al., 2020). The incidence and severity of sickness are increased in automated vehicles and during simulator use, where all users act as passengers and often prefer to engage in other activities (Bertolini and Straumann, 2016; Bos et al., 2020; Griffin and Newman, 2004; Kuiper et al., 2018; Salter et al., 2019). In this context, vision can take three forms: external vision, when the outside view is available and

broadly congruent with the motion; internal vision, when only the vehicle interior is seen and is often incongruent with the motion; and no vision, when the eyes are closed. Existing models lack the capability to capture visual inputs, and those that include vision, lack empirical validation. Consequently, a research gap exists concerning the quantification and validation of the effects of vision on motion sickness development.

Most of the motion sickness models have been solely validated on datasets with purely vertical motion stimuli, such as McCauley et al. (1976). The performance of these models in driving scenarios, which include more horizontal-plane accelerations, is therefore subject to evaluation. Thus, there is a need to collect, test and validate the existing models on driving datasets, either naturalistic or from driving simulator studies. This may result in the modification or updating of the parameters of the models.

1.2 Objectives

To develop a motion sickness model for predicting motion sickness in automated vehicles and driving simulators, this doctoral thesis aims to achieve the following objectives:

Objective 1: Collect, measure and predict motion sickness in person-specific metrics.

Objective 2: Evaluate how vision influences perception and motion sickness in humans and computational models

Objective 3: Develop a personalisable mathematical model capable of predicting variance in motion sickness, for application in motion cueing algorithms that regulate sickness in driving simulators.

By achieving these objectives, it will be shown that accurate and personalised prediction of motion sickness is possible, and could be used to optimise comfort, safety, and testing efficiency in future automated mobility and simulation environments.

For ease of navigation, this thesis is divided into seven chapters. Chapters 2 and 4 correspond to Objective 1, while Chapters 3 and 5 correspond to Objective 2. Chapters 4 and 6 correspond to Objective 3. Finally, chapter 7 discusses the findings and gives recommendations for future research. The overview of the dissertation is given in figure 1.3.

This thesis utilises datasets that were either independently collected by the author, or obtained from datasets and publications from external researchers specialising in comparable domains. In chapters 2, 5 and 6, the dataset was independently collected by the author and his research group. In chapters 3 and 4, the used data were sourced from previously published datasets and publications, which are detailed in tables 3.3 and 4.1. Overall, this thesis uses four datasets obtained from real vehicle driving and four datasets obtained from tests on a driving simulator. All datasets involve passive driving, with multiple motion and vision conditions tested within the same participants, enabling controlled comparisons of internal versus external vision, real versus simulator driving, and different motion cueing algorithms versus no simulator motion.

1

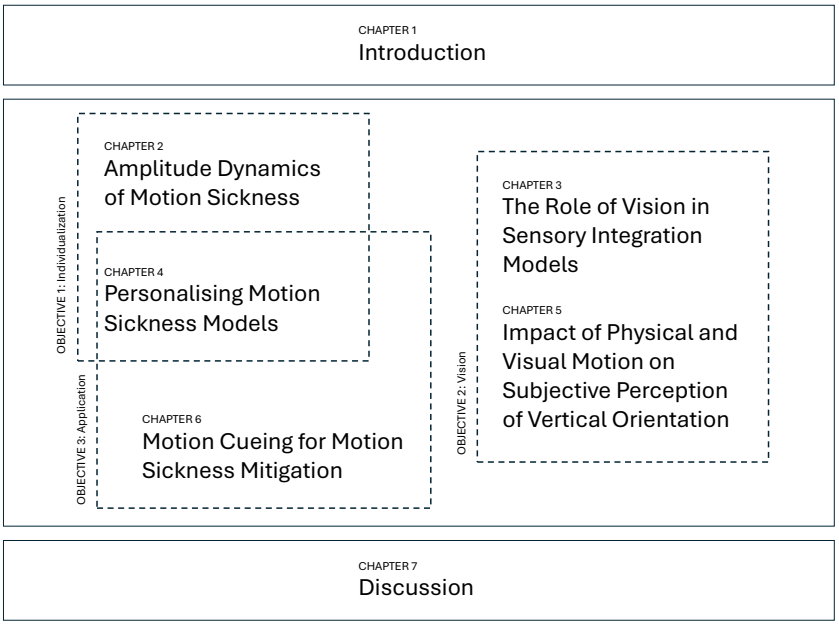

Figure 1.3: Structure of this thesis

In chapter 2, ”Amplitude Dynamics of Motion Sickness,” the relationship between stimulus amplitude and motion sickness development is studied. The effect of a sinusoidal stimulus with different magnitudes in different sessions was tested on participants with their eyes closed. A linear relationship between the amplitude of motions and motion sickness severity was found. Oman’s accumulation model was adopted to describe the build-up and recovery of sickness over time, including post-exposure effects and hypersensitivity. A first step toward personalisation was made by identifying which parameters could be fixed at the group level (e.g., an output scaling with exponent 0.4 to accommodate amplitude changes) and which should be estimated per person (e.g., accumulation gain and time constants). This enabled accurate predictions of an individual’s motion sickness evolution.

Chapter 3, ”The Role of Vision in Sensory Integration Models for Predicting Motion Perception and Sickness,” investigates how the integration of visual information affects the prediction of human motion perception and motion sickness. Here, published models of motion perception and motion sickness were validated on previously collected datasets. Both naturalistic driving data and laboratory motion paradigm data were used for evaluation. Understanding subjective motion perception is also crucial for identifying if the mechanisms linking physical motion stimuli to motion sickness responses are present in the models. No model could accurately capture both motion perception and motion sickness. Thus, a unified model that jointly captures perception and sickness remains to be developed. The SVC model represents an encouraging step in this direction, as it integrates sensory processing

with good motion sickness predictions and motivates future work towards more comprehensive models. As a practical compromise for sickness prediction with visuals, SVC-VR — Subjective Vertical Conflict model with visual rotational rate input — was selected for use in subsequent chapters, while a unified model that jointly captures perception and sickness remains to be developed.

In chapter 4, "Personalising Motion Sickness Models: Estimation and Distribution of Individual-Specific Parameters," the focus is placed on methods for estimating and modelling individual differences in motion sickness susceptibility. A model framework was developed that combines a group-averaged conflict-generation model (SVC-VR, as selected in Section chapter 3) with an accumulation model (building upon Oman's model from chapter 2) that accounts for individual differences in motion sickness susceptibility across various conditions. Three available datasets containing sickness in naturalistic drives and driving simulators were used. Furthermore, a stochastic model for the distribution of model parameters was developed, enabling population sampling to simulate variance in motion sickness responses. The model framework demonstrated good performance even in unseen (for the model) datasets with an average RMSE of 0.47 MISC. This model reduces the need for large-scale experiments, potentially accelerating research and development.

Chapter 5, "Impact of Physical and Visual Motion on Subjective Perception of Vertical Orientation," examines how both physical and visual stimuli influence the subjective perceptions of spatial orientation that are known to contribute to motion sickness. The effect of various pitch velocities and vision conditions on human perception was studied in a simulator experiment. It was found that, on average, humans underestimate pitch by 20%. The effect of variation of vision was found to be not significant. Models of motion perception, specifically the SVC model, poorly captured the experimental observations of orientation perception, with the published parameters. However, with adapted parameters, the SVC model provided a good fit. The study revealed the complexity of sensory integration in motion perception and demonstrated the limitations of the current models.

In chapter 6, "Reducing Discomfort in Driving Simulators: Motion Cueing for Motion Sickness Mitigation," an advanced motion cueing algorithm is developed and evaluated to minimise motion sickness in simulators, while maintaining realistic motion perception. Human-in-the-loop experiments were carried out to compare the proposed motion cueing algorithm with the state-of-the-art. The proposed motion cueing algorithm was able to reduce motion sickness by 50% from MISC of 3 to 1.5 without any significant reduction in subjective perception of realism. This is a significant advance in achieving control of motion sickness while having specific force recreation in driving simulators. This achievement paves the way for more immersive and tolerable long-duration driving simulator experiences.

Finally, chapter 7 presents the overall conclusions, summarising the key findings and contributions of this work, and outlining recommendations for future research and application.

This set of chapters significantly advances the understanding and predictive capability of motion sickness models in vehicles and driving simulators. Through the development of personalised metrics and models, it contributes to overcoming limitations of group-average approaches, enabling more accurate, individualised predictions. The work also thoroughly explores the role of visual inputs in sensory integration, revealing limitations of current

models and offering improvements to better capture human perception. Most importantly, the creation and validation of a mathematical model framework that integrates these insights allows for a direct practical application in motion cueing algorithms, demonstrating a substantial reduction in motion sickness during simulator use without compromising realism. Collectively, these contributions provide a foundation for optimising comfort and safety in future automated mobility environments and enhancing the realism and tolerance of driving simulators, thereby pushing the field toward more personalised and effective solutions for motion sickness mitigation.

2

Amplitude and Temporal Dynamics of Motion Sickness

Life is really simple, but we insist on making it complicated

Confucius

This chapter is based on *Irmak, T., Kotian, V., Happee, R., de Winkel, K. N., & Pool, D. M. (2022). Amplitude and Temporal Dynamics of Motion Sickness. Frontiers in Systems Neuroscience, 16.*

The appendices for this chapter can be found at Appendix A.

Abstract

The relationship between the amplitude of motion and the accumulation of motion sickness in time is unclear. Here, we investigated this relationship at the individual and group level. 17 participants were exposed to four oscillatory motion stimuli, in four separate sessions, separated by at least one week to prevent habituation. Motion amplitude was varied between sessions at either 1, 1.5, 2 or 2.5 m/s^2. Time evolution was evaluated within sessions applying: an initial motion phase for up to 60 minutes, a 10-minute rest, a second motion phase up to 30 minutes to quantify hypersensitivity and lastly, a 5-minute rest. At both the individual and the group level, motion sickness severity (MISC) increased linearly with respect to acceleration amplitude. To analyse the evolution of sickness over time, we evaluated three variations of the Oman model of nausea. We found that the slow (502 s) and fast (66.2 s) time constants of motion sickness were independent of motion amplitude, but varied considerably between individuals (slow STD=838 s; fast STD=79.4 s). We also found that the Oman model with output scaling following a power law with an exponent of 0.4 described our data much better as compared to the exponent of 2 proposed by Oman. Lastly, we showed that the sickness forecasting accuracy of the Oman model depended significantly on whether the participants had divergent or convergent sickness dynamics. These findings have methodological implications for pre-experiment participant screening, as well as online tuning of automated vehicle algorithms based on sickness susceptibility.

2.1 Introduction

Motion sickness is a syndrome that arises as a consequence of a wide range of self-motion and orientation cues. It is characterised by symptoms of sweating, headache, dizziness, stomach awareness, where these symptoms usually grow in severity until nausea, retching and ultimately vomiting occurs (Bertolini and Straumann, 2016). The fact that adverse motions may, in a wide range of species (Bäuerle et al., 2004; Hickman et al., 2008; Wang and Chinn, 1956; Wassersug et al., 1993), cause a diverse set of symptoms is peculiar.

Therefore, the aetiology of motion sickness remains an active area of scientific inquiry. There are two main theories of motion sickness, these are the ”Sensory Conflict” (Oman, 1982; Reason, 1978a) theory and the ”Postural Instability” theory (Riccio and Stoffregen, 1991). The most developed mathematical models and tools exist for the sensory conflict theory (Bos and Bles, 1998; Khalid et al., 2011a; Wada, 2021). Therefore, this paper will study motion sickness through the concepts of state estimation and sensory conflict, and will not cover postural instability theory nor attempt to evaluate postural precursors to motion sickness.

The sensory conflict theory (Reason, 1978a) argues that motion sickness is mainly due to a conflict between the sensed sensory signals and the sensory signals expected by the brain. These expectations originate from an internal model, which takes the form of a neural store. The conflict leads to adaptation of the internal model. In the formulation of Oman (1982) this conceptual model is likened to a Luenberger Observer (LO). The LO has an internal model of the system (body) and sensor dynamics. Due to the imperfect and noisy nature of the sensory signals, one cannot use the sensor measurements directly. Instead, the true states of the system must be observed (estimated) by integrating sensory information using an internal model of the system itself. Indeed, there is strong neuronal evidence for the use of internal models for state estimation (Angelaki et al., 2004; Laurens et al., 2013; Merfeld et al., 1999; Oman and Cullen, 2014). To quantify estimation accuracy, the central state estimates are passed through an internal model of sensory dynamics and compared with the actual sensory signals. The resulting error is the estimation error, or the sensory-expectancy conflict. It is hypothesized that the magnitude of the conflict and the duration of exposure then leads to the subsequent symptoms of motion sickness.

There are practical implications that come with a firm understanding of the relationship between the magnitude of sensory conflict and motion sickness accumulation. Firstly, such knowledge allows us to better generalise motion sickness predictions to mixed acceleration environments that are ubiquitous to vehicular transport (Feng et al., 2017). Such predictions may then be used as an objective function to minimise sickening vehicle motions. Secondly, a functional model will allow for the development of control algorithms that can automatically adjust the amplitude of sickening simulator motions such that participants track a desired sickness trajectory. Currently, in experimental studies, researchers must fix their stimulus beforehand and hope that participants do become sick, but do not terminate the experiment prematurely. Active control will allow for setting the desired level and variance of motion sickness, which will increase the statistical quality of data collected. Lastly, a predictive model of sickness accumulation will allow for tuning of automated ve-

hicle algorithms to the susceptibility level of the individual passenger, whilst also allowing prescreening of participants for a desired level of susceptibility. To allow for these novel methods and technologies, the mathematical process that links sensory conflict to the time evolution of motion sickness must be elucidated.

For simple motions, such as single degree-of-freedom vertical or horizontal accelerations, the conflict vector is assumed to be proportional to the acceleration stimulus itself. There is literature on the relationship between the acceleration magnitude (a proxy for the magnitude of the conflict) and group-level responses to sickness. Lawther and Griffin (1988), for instance, show a linear relationship between the amplitude of vertical accelerations on ships and motion sickness incidence (MSI), which is the percentage of people who vomited during the exposure. Likewise, using the more sensitive metric of mean subjective illness score, they also observed a strongly linear relationship between acceleration amplitude and sickness. However, their tested acceleration amplitudes were only in the range of 0-0.7 m/s^2, which covers a small linearisable part of the complete, possibly nonlinear sickness amplitude dynamics. Indeed, looking at the data of O'Hanlon and McCauley (1974), in the range of 0.25-3.9 m/s^2 there seems to be a sigmoidal relationship between acceleration amplitude and MSI. The subjective vertical model developed by Bos and Bles (1998) captures this sigmoidal relationship by first rectifying the conflict vector, and then input scaling it with a non-linear Hill-function. The resulting scaled conflict is then integrated with a second-order system, to match the MSI observations of O'Hanlon and McCauley (1974).

The approach of combining sensory conflict and accumulation model is unique because it clearly discriminates between conflict *generation*, which is a by-product of spatial orientation and state estimation, and conflict *integration*, which leads to motion sickness. There are two shortcomings in this approach. Firstly, at the practical level, the motion sickness prediction is made using motion sickness incidence (MSI), defined as the percentage of people that have vomited. This misses the finer increments in symptom development that precede vomiting, which are more relevant for most practical applications of motion sickness modelling. Secondly, the approach conflates the internal dynamics that lead to sickness at an individual-level with the averaged group-level dynamics. For a physiologically valid model of motion sickness, the final sickness predictions should map to individual ratings, not group-averaged ones.

An individual-level model of the temporal dynamics of motion sickness was developed by Oman (1990). This model is also uniquely able to describe the phenomenon of 'hypersensitivity', which is an essential part of sickness development over time. Hypersensitivity is characterised by the fact that after exposure to sickening motions, any further exposure to sickening motions leads to a more rapid rise in sickness than in the initial exposure (Golding et al., 1997). Modelling hypersensitivity is particularly relevant for automated driving, as sickening motions are usually separated by long durations of rest (i.e., at the traffic lights). In our previous work, the Oman model was validated in the context of motion sickness generated by slalom manoeuvres performed by a car at 0.2 Hz with a lateral acceleration of 4 m/s^2, for up to 30 minutes (Irmak et al., 2020). Here, it was seen that the model provided a good fit to subjective sickness scores as measured on the MIsery rating SCale (MISC) (Bos et al., 2010). Moreover, using the Oman model, parameters governing the tra-

jectory of motion sickness could be used to predict individual responses in re-exposure to the same paradigm. This indicated a high degree of intra-individual repeatability in sickness dynamics. In this previous experiment, we only used an acceleration of a single magnitude. However, in traffic, humans generally encounter mixed acceleration stimuli. The original form of Oman (1990)'s model predicts the end level of sickness to be a quartic of the input acceleration amplitude. This is because of the model's 'slow' path acting as a gain on its 'fast' path and the output power scaling, p_o shown in Figure 2.2, being set to 2. It is, however, not clear whether this proposed amplitude relationship is correct. Nor is it clear whether the Oman model can generalise to fit sickness for different acceleration inputs, or whether its parameters must be refitted on a case-by-case basis.

In the present study, we assessed the relationship between conflict magnitude, using acceleration stimulus amplitude as a proxy, and the temporal dynamics of motion sickness symptoms at the individual-level. We did this by exposing 17 participants to sinusoidal fore-aft motions of four different acceleration amplitudes. The experiment was performed in the SIMONA Research Simulator at the Aerospace Engineering faculty of TU Delft (Berkouwer et al., 2005; Stroosma et al., 2003). In the subsequent analyses, we first confirm previous literature findings for the relationship between acceleration amplitude and group-level responses. Uniquely, we show that motion sickness at an individual-level for different stimulus amplitudes can be modelled adequately with individually varying Oman model time constants that are independent of motion amplitude, but the same group-level averaged power law scaling at the output for all individuals. Moreover, we show that the Oman model in its current form can forecast the future evolution of motion sickness, but the accuracy of the forecasting is dependent on the qualitative form of individuals' sickness dynamics. This has important consequences for prescreening of participants for motion sickness experiments, and tuning of automated driving algorithms to individual passengers.

2.2 Methods

2.2.1 Ethics Statement

All participants provided written informed consent prior to participation. The experimental protocol was approved by the Human Research Ethics Committee of TU Delft under application number 1425.

2.2.2 Participants

In total, 17 participants completed this study (mean age: 25.3 years, STD: 2.6 years; 2 female, 15 male). The 17 participants had a mean motion sickness susceptibility questionnaire short form (MSSQ-Short, Golding (2006a)) score of 16.2 (STD = 10.1) indicating that they had above average susceptibility, corresponding to the 65^{th} percentile.

2.2.3 Apparatus

The experiment was performed in the SIMONA Research Simulator at TU Delft (Figure 2.1). The simulator has a six degree-of-freedom hydraulic hexapod motion system, which can provide a maximum displacement of 1.12 m, a maximum velocity of 0.9 m/s and a maximum acceleration of 13 m/s^2 (Berkouwer et al., 2005; Stroosma et al., 2003). The participants were placed inside a closed cabin, within which they were seated and secured using a five point harness. To prevent unwanted head movements, their head was supported with a neck restraint. To remove any visual cues, they wore blackened goggles and the cabin lights were turned off (see Figure 2.1). Continuous communication with the experimenter was possible via an intercom system.

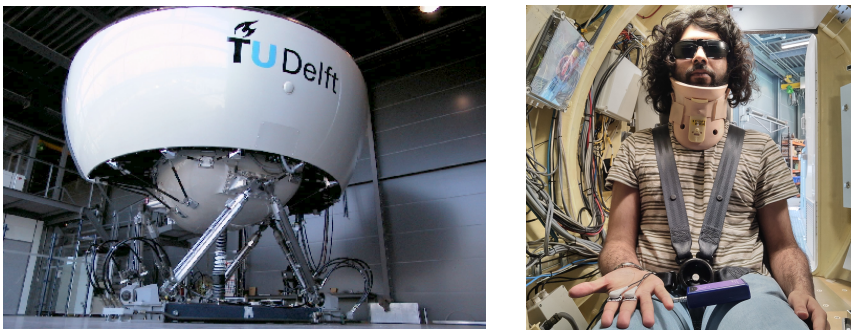

(a) (b)

Figure 2.1: Experimental setup. (a) is the SIMONA Research Simulator used in the experiment to elicit motion sickness via fore-aft sinusoidal motions of differing amplitudes. (b) shows the second author as a participant in the experiment, wearing a 5-point safety harness, a neck restraint, and blackened glasses

2.2.4 Task

Each condition was tested on participants with a rest of at least 1 week (mean: 30.6 days, STD: 20.6 days) in between any two test conditions. In these sessions, participants were subjected to sinusoidal fore-aft motions at a frequency of 0.3 Hz. The amplitude of the accelerations used were; 1, 1.5, 2 and 2.5 m/s^2. The choice of the highest acceleration was constrained by the maximum possible simulator velocity of 1 m/s. The choice of the frequency was based on the highest frequency observed for which the population incidence of sickness does not decrease (Golding and Markey, 1996; Golding et al., 1997; Irmak et al., 2020).

In each session, participants underwent two motion exposures. The first exposure lasted for 60 minutes, or until the participant reached a MISC of 6. They were then permitted 10 minutes rest, after which the second exposure lasted for 30 minutes, or until they reached a MISC of 6. After which, they first rested for 5 minutes in the simulator, and then for as long as they desired to in the staging room. At the beginning and end of each motion, the motions were faded in and out with a linearly increasing and decreasing amplitude from

zero to the level specified over a 10-second period.

Each session only tested one amplitude of the range of acceleration stimuli. Due to time limitations and a desire to sample as broad a range of amplitudes as possible, conditions were not repeated. This is justified by good trial-to-trial repeatability found previously in the measured motion sickness responses (Irmak et al., 2020; Miller and Graybiel, 1969). The order in which each amplitude was experienced was balanced between participants using a Latin square. This prevented confounding effects of habituation between the different amplitudes.

2.2.5 Quantifying Sickness

Participants were instructed to report their sickness on the 11-point MISC scale (Bos et al., 2010; Reuten et al., 2021). The MISC scale is anchored to specific motion sickness symptoms: 0 is no symptoms, 1 is uneasiness, 2, 3, 4, 5 represent increasing severity of non-nausea symptoms from vague to severe, 6 is mild nausea, 7 is moderate nausea, 8 is severe nausea with 9 and 10 being retching and vomiting, respectively. The MISC is useful because the ratings are directly linked to symptoms, which is not the case with other scales such as the Fast Motion Sickness Scale (FMS) (Keshavarz and Hecht, 2011) and the Magnitude Estimate scale (Bock and Oman, 1982). Having a non-anchored scale would make the ultimate aim of minimising of sickness predictions with respect to vehicle motions infeasible. It has been reported by Reuten et al. (2021) that there is a clear non-monotonic relationship between a MISC level of 5 and 6 in terms of the feelings of unpleasantness that are often used to characterise the sickness response. However, recently De Winkel et al. (2022) have demonstrated that this observed break from monotonicity was semantic in nature. The discomfort associated with each level of the MISC, as it was used to express motion sickness during exposure to a sickening stimulus, was found to increase monotonously and the MISC could be characterised by a power law of exponent 1.206 (De Winkel et al., 2022). All together, these considerations were deemed sufficient to warrant using the MISC directly for our modelling work.

Every 30 s, a 1 kHz beep was played over the simulator intercom to prompt the participant to verbally state their MISC level. In addition to this prompted response, participants were told that they could voluntarily give a MISC report whenever they thought it changed substantially since the last response was requested. Responses were recorded on audio and transcribed after the experiment session by the experimenter. The audio recordings were voice activated and recorded only for the duration the participant was speaking. Each MISC rating given by the participant was time stamped to the start of the audio sample.

Drop-out Rate & MISC Rate

To quantify the dynamics of sickness with respect to acceleration amplitude, the severity of sickness must be specified. To this end, we used the MISC rate and the drop-out rate. The MISC rate is defined as the MISC rating at the end of motion exposure, divided by the time in minutes to this end. Whereas, the drop-out rate is simply defined as the percentage of participants that have prematurely terminated a motion exposure.

2.2.6 Sickness Model

The sickness accumulation model in this study is the Oman (1990) model shown in Figure 2.2. Here, the input to the model is the magnitude of the rectified sensory-expectancy conflict. In advanced sensory integration models, the sensory conflict is a product of the state estimation/motion perception process (Clark et al., 2019; Wada, 2021). In this experiment, the motions encountered were simple fore-aft accelerations and the sensory conflict was therefore assumed to be proportional to the acceleration stimulus itself.

The output of the model is a generic sickness level, which may be quantified with a sickness rating scale such as the MISC. In the model, there is a 'fast' path and a 'slow' path. The fast path is given by a repeated root second-order system with a time constant β_1. The slow path is given by a repeated root second-order system with a time constant β_2. The slow path controls the gain on the fast path. The existence of the two paths, enables Oman (1990)'s model to describe the phenomenon of hypersensitivity.

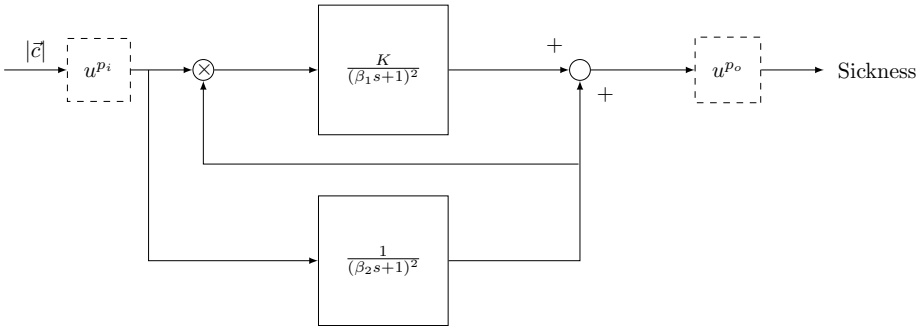

Figure 2.2: Oman's model of motion sickness development in time. The rectified conflict signal $|c|$ is fed in to the model. There is a fast (upper) path and a slow (lower) path. The slow path multiplies with the conflict as the gain of the fast path. Both systems are second order with repeated poles. The fast and slow path are then summed. The model has either an input power scaling or an output power scaling given by u^{p_i} and u^{p_o}, respectively

The original form of the Oman model has an output scaling (u^{p_o}), where the sum of the fast and slow paths are raised to the power of 2 ($p_o = 2$), a choice which has, to the best of our knowledge, not been validated. An alternative is an input scaling, which represents a direct sensitivity relationship between sensory-expectancy conflict and motion sickness at the input level, as proposed in Bos and Bles (1998). In this study, both input and output scaling were explored, but as output scaling provided a better fit to the data, this is the model form reported in the results. Nevertheless, we discuss the effect of input and output scaling in the discussion section.

All poles of the Oman model are negative, meaning it has a stable response that eventually converges to a steady-state level of sickness $MISC_{ss}$. For a step input of amplitude A, the effect of output scaling on the model output, is given by the equation

$$\text{MISC}_{ss} = (KA^2 + A)^{p_o} \tag{2.1}$$

where K is the gain of the fast path and p_o is the output power scaling of the conflict

amplitude.

Error Metric

The formulation of the Oman model considered in this study has four parameters. These are the fast and slow path time constants β_1, β_2, the gain K and the output power scaling exponent p_o.

The error metric used for the optimisation was the mean absolute error (MAE), which is given by the equation:

$$\text{MAE} = \frac{\Sigma_{t=1}^{n} |F_t - A_t|}{n} \tag{2.2}$$

For each iteration of the optimisation an error is calculated using the predicted MISC ratings F_t and the measured A_t ratings. The MAE is not scaled, this means it fits the higher MISC ratings more faithfully than the lower scores. Moreover, it is easy to interpret, as the MAE directly quantifies the average absolute deviation from the observation.

Optimisation Procedure

Three variations of Oman's model were fitted to the individual participants' data:

1. **Session Fit, Unit Power:** As a baseline for how well the model could feasibly fit the sickness profile, but also to assess how the model parameters may vary between conditions, each session was fitted separately. This means that the time constants β_1, β_2 and the gain K were fitted for each individual session, and thus stimulus amplitude. The power was assumed to be unity, i.e., $p_o = 1$, and fixed for all fittings. The optimisation was performed using the MATLAB fmincon function. Due to the presence of local minima, this was done using 10 multi-starts.

2. **Joint Fit, Individual-level Power:** The first model does not have a generalisable amplitude relationship from which one can make predictions across acceleration levels. For this reason, the sickness to amplitude relationship is assumed to be an idiosyncratic property of the individual, and so another model was fitted where the power law term was allowed to vary between participants. The fits were done jointly for all conditions for a given individual, meaning that both the time constants (β_1 and β_2), the gain (K) and the power law (p_o) terms did not vary within an individual between the different conditions, but did vary between individuals. The optimisation was performed using fmincon with 10 multi-starts.

3. **Joint Fit, Group-level Power:** To assess whether an individual power law was needed to adequately capture the sickness observations, or whether a group-level power law metric is sufficient, the model was fitted with a power law p_o term that was fixed between participants. The fits were done jointly for all conditions for a given individual, meaning that both the time constants (β_1 and β_2) and the gain (K) did not vary within an individual between the conditions. The optimisation was done using fmincon with 10 multi-starts.

2.2.7 Statistical Analysis

AICc

Models with more free parameters generally give better fits to experimental data. To assess the significance of such additional model parameters, we used the corrected Akaike Information Criterion (AICc). This is a measure of model fit that is based on the likelihood of the data given the model, whilst including a penalty term for the number of parameters. It is a corrected form of the AIC where the parameter penalty scales quadratically, but approaches the AIC when the number of observations, n is many times larger than k^2. Fabozzi et al. (2014) explains how to interpret the absolute value of differences in the AICc between the models, in terms of strength of evidence. According to these rules of thumb, absolute differences in the indices >2, >6, and >10 provide positive, strong, and decisive evidence, respectively, in favour of the model with a lower AICc value.

Friedman Test

As our metrics do not satisfy the assumptions required for parametric testing, the Friedman test was used for statistical comparisons between different amplitude conditions. The Friedman test is a non-parametric test analogous to the parametric repeated-measures ANOVA. The significance level is reported in much the same way as in an ANOVA, where a p-value that is less or equal to 0.05 is taken as indication of a statistically significant result.

Logrank test

Logrank test is a hypothesis test used to compare the survival distribution of two samples. In this study, it was used to compute a pairwise comparison between the termination curves of different motion conditions.

2.3 Results

2.3.1 Group-level Observations

The experiment proved to be very sickening. Figure 2.3 shows the group-level results for all 17 participants over the first 60-minute motion exposure. The dropout rate for all four conditions is shown in Figure 2.3(a) and was high, whereby the three highest amplitudes – 2.5, 2.0, and 1.5 m/s^2 – had similar dropout rates after 60 minutes of approximately 94%. The lowest amplitude setting had an appreciably lower dropout rate of 64.7%. Using a logrank test between the amplitudes 1 and 1.5 m/s^2, 1.5 and 2 m/s^2, and 2 and 2.5 m/s^2, a significant increase in drop-outs were found between the survival curves of 1 and 1.5 m/s^2 (Bonferroni corrected $p = 0.0047$), 1.5 and 2 m/s^2 ($p = 0.0107$), but not between 2 and 2.5 m/s^2 ($p = 0.473$). The hazard ratios were 1.64, 1.56 and 1.25, respectively, indicating a monotonic increase in the probability of dropout with increasing acceleration amplitude.

In this experiment, the most discriminative measure of how sickening a certain stimulus

was given by the MISC rate. Figure 2.3(b) shows a monotonically increasing MISC rate on average across the group of participants (for the individual MISC rates of all participants, see figure A.1). This monotonicity is further supported by the fact that a linear model provides a significantly better fit to the MISC rate data than a constant (intercept-only) model (AICc = -1.92 vs AICc = 29.4).

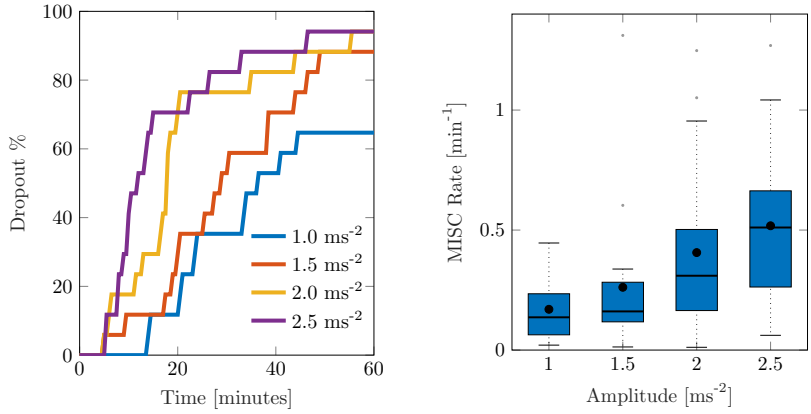

(a) (b)

Figure 2.3: Main group-averaged results for the first motion exposure. (a) indicates the early termination rate where participants reached a MISC level of 6 prior to the 60-minute mark in first motion exposure. (b) shows the median MISC Rate (as the solid black line inside blue shaded box) the mean MISC Rate (black circle) and the 25th and 75th percentiles (bounds of the box)

Figure 2.4 shows a more detailed breakdown of time to reach each a certain MISC rating, where the left-most lightest coloured bar graph for each condition is for a MISC of 1 and the right-most darkest colour is 6, for all tested amplitude conditions. Both data for the first (shade of blue) and the second motion exposure (shade of red) are presented. Figure 2.4 again shows that with increasing amplitude, there is a decrease in the time it took to reach a certain MISC level. Furthermore, the presence of motion sickness hypersensitivity is observed during the second motion exposure, shown in the yellow to orange coloured bars, where time to a certain MISC rating is reduced by 61% on average compared to the first exposure.

2.3.2 Oman Model

As motivated in Section 2.2.6, three model variations were evaluated: the Session Fit Unit Power, Joint Fit Group-level power and Joint Fit Individual-level Power. The results for these cases are presented separately in this section.

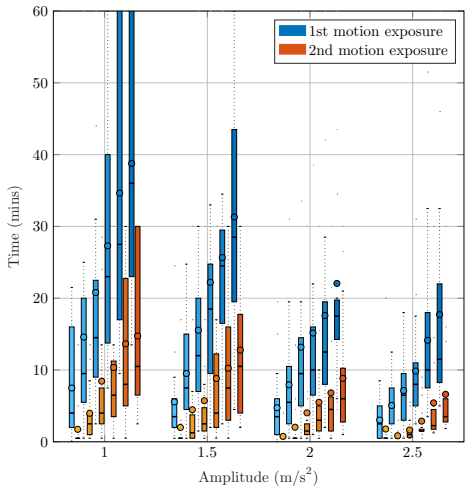

Figure 2.4: Time to reach a certain MISC level as a function of amplitude during the first and the second motion exposures, given by the blue and orange-shaded bars, respectively. Colour saturation indicates sickness severity: the lightest shade (leftmost) corresponds to MISC 1, progressing incrementally to the darkest shade (rightmost), which represents MISC 6.

Session Fit, Unit Power

For the Session Fit, Unit Power case, the Oman model is fitted to all amplitude conditions individually for each participant, as also done in Irmak et al. (2020). Figure 2.5 shows Box plots of the fitting errors (MAE), the gains, and the long and short time constants for each amplitude condition.

A Friedman test shows significant differences in the MAE, with an average of 0.54, ($\chi^2 = 9.15$, $df = 3$, $p = 0.027$) across motion amplitude conditions, meaning there is a significant difference between model fitting accuracy across the different amplitude conditions. A post-hoc test, however, shows no significant difference between any set of individual amplitude conditions. On average, E_{joint} is 0.94 (STD = 0.29).

Figure 2.5 shows a significant downward trend in the gain of the model with increasing amplitude ($\chi^2 = 12.8$, $df = 3$, $p = 0.005$). There were no significant differences in either the fast nor the slow path time constants across the amplitude conditions ($\chi^2 = 4.05$, $df = 3$, $p = 0.26$ and $\chi^2 = 1.43$, $df = 3$, $p = 0.7$, respectively). On average, β_1 and β_2 had median values of 73.6 s and 510.4 s, respectively. The implication of this is that the fast and slow path time constants are seen to be acceleration amplitude invariant and can thus be considered a constant property of each individual.

Joint Fit, Individual-level Power

The Session Fit shows that the gains change as a function of input amplitude, whereas the time constants may be fixed. To get a single set of parameters (rather than amplitude dependent gains) that will predict across all amplitudes, the model requires an *output power-*

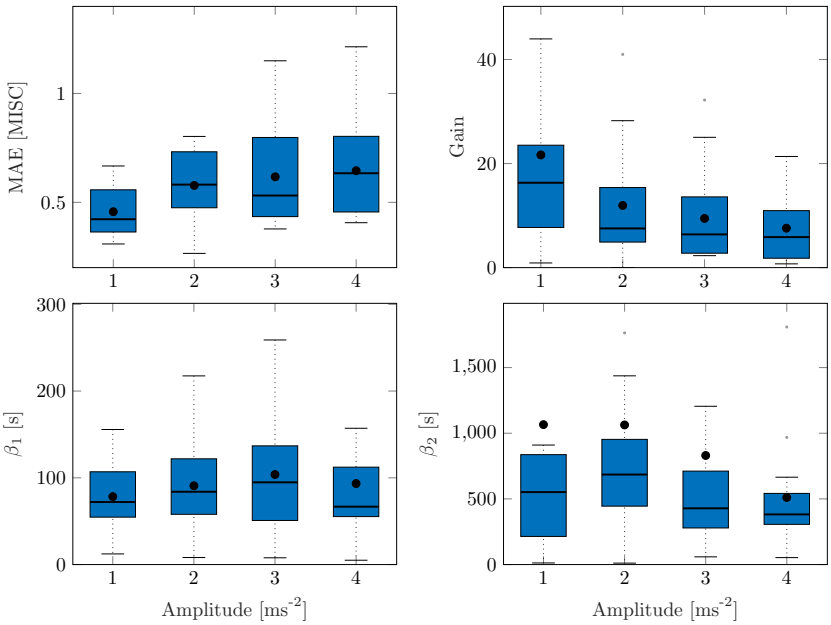

Figure 2.5: Box plots showing the mean absolute error, the gain and the two time constants of the Session Fit, Unit Power model variation. The Box plot is in standard form, with the centre black line indicating the median, the dots indicating the means, and the sides of the box indicating the quartiles. Some outliers are above the maximum y-value limits chosen for the respective subplot.

law scaling. In the Joint Fit, Individual-level Power model variation, the dynamics of sickness with respect to input amplitude are given by allowing this output power scaling p_o, to freely vary between individuals. This means that the amplitude sensitivity, just like both the gains and the time constants, is modelled as an idiosyncratic property unique to the individual.

For this model variation, the joint error E_{joint} was 1.01 (STD = 0.23), this is only marginally above the 0.94 of the Session Fit model variation (which is clear from the time domain plots shown in Figure 2.7), indicating that the model simplification from 12 to 4 parameters was successful.

Joint Fit, Group-level Power

In the previous model form, an individual power term was used. This power term can be fixed such that only three individual parameters are required to describe the motion sickness response, rather than four.

Figure 2.6 shows the variation in the joint error term E_{joint} as a function of the output power scaling, which was fixed for the whole population. It can be seen that the error term is minimised to 1.028 (STD = 0.23) when the output power scaling p_o is 0.4. The medians

of the other Oman model parameters for output power scaling were 66.2 s and 502.4 s for the fast and the slow path time constants (β_1 and β_2), respectively, and 70.8 for the gain (K). Using the output scaling of 2 proposed by Oman (1982) led to an error of 2.54, higher than the minimum we find using an output scaling of 0.4.

Contrary to previous findings by Irmak et al. (2020), there was no correlation between the fast and slow time constants (r = 0.074). This may be explained by the fact that we tested multiple amplitudes rather than one in the current study, fitting all concurrently with an associated output-scaling term. This may have reduced any potential correlation between the two time constants. A second factor may be that the previous finding was a spurious correlation, which this study was not able to replicate. This is plausible because the two time constants in fact represent different classes of responses, hormonal and neural (Oman, 1982). These are likely to be independent and uncorrelated processes.

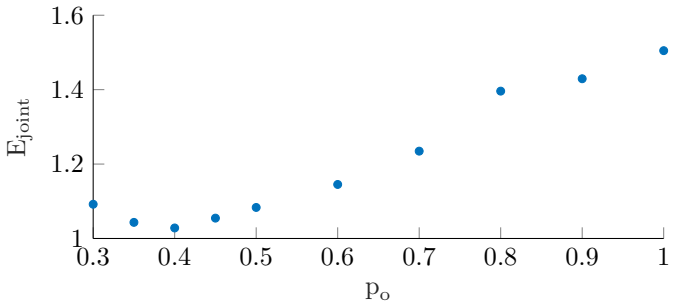

Figure 2.6: The error term E_{joint} with respect to the output power scaling, which is taken to be constant between participants. The lowest E_{joint} occurs when power is equal to 0.4.

By setting $p_o = 0.4$ in equation 2.1, the relationship between the conflict magnitude and the predicted sickness output of the model is given by:

$$\text{MISC}_{ss} = (KA^2 + A)^{0.4} \tag{2.3}$$

K is the Oman model gain and is usually large with a median value of 70.8. This means that the steady state sickness value predicted by the model has an approximately linear relationship to input motion amplitude $\text{MISC}_{ss} \approx K^{0.4} A^{0.8}$

Fitting Comparison

The three variations of the model evaluated each have a joint error E_{joint} for each participant. These model errors (shown in Table 2.1) can be compared using the Friedman Test across models to evaluate whether their fit quality differs significantly. Doing so, the three tested models were found to differ significantly from each other ($\chi^2 = 6.14$, $df = 3$, $p = 0.046$) but this difference was marginal and indeed pairwise testing revealed no significant differences.

Figure 2.7 shows a representative sample of fittings for the three model variations for participants 11, 12, 13 and 14 (for the data of all participants, see figure S2). It is clear that there is little difference between the three model variations. It can therefore be concluded that individuals have time constants that are invariant of the motion amplitude, and that an output scaling power of 0.4 allows the model to fit across multiple amplitude conditions just as well as fitting to a single session. This means that the 3 parameter model with the output power fixed across participants, but the gain and the time constants allowed to vary at the individual level offers a good compromise between fitting performance and model complexity.

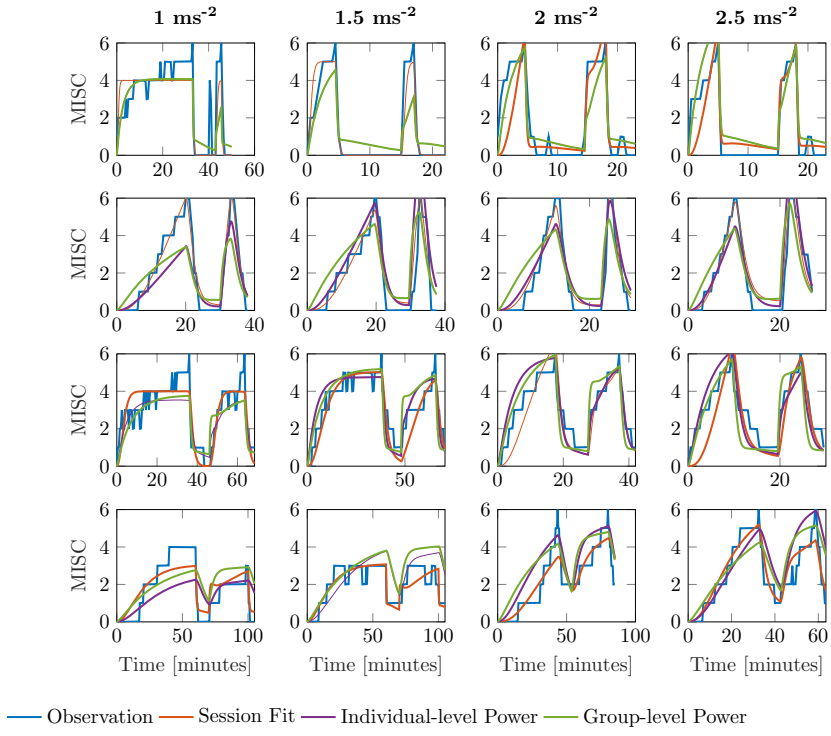

Figure 2.7: Representative sample of fittings for the three model variations for participants 11, 12, 13 and 14. The columns show responses for each amplitude condition, increasing in magnitude from left to right. The rows show results for each participant

Model Variation	Average E_{joint}	STD	# Parameters
Session Fitting, No Power	0.94	0.29	12
Joint Fitting, Individual-level Power	1.01	0.23	4
Joint Fitting, Group-level Power	1.03	0.23	3

Table 2.1: Summary of fitting results, with the error averaged over participants E_{joint}, the standard deviation over participants in the MAE, and the number of parameters for each model variation

2.3.3 Amplitude Cross Validation

Evaluation of model variations so far was with respect to how well they could fit the data. However, for a predictive model, it is also important to identify the capacity for generalising to conditions not explicitly fitted to. We therefore performed cross-validation of the model between the different amplitude conditions. To do this, we looked at the mean MAE when we fitted to one, two and three conditions whilst predicting three, two and one condition. There were 4 combinations for the 1 fitting case, 6 combinations for the 2 fitting case and 4 combinations for the 3 fitting case, leading to 14 cross-validation data sets.

Figure 2.8 shows a Box plot of the mean absolute prediction errors for the procedure described above. Both models with an individual-level and a group-level power term variations show decreasing prediction errors with the number of conditions fitted. The group-level power model with $p_o = 0.4$ has overall a lower prediction error than the individual-level power model (Friedman test, $\chi^2 = 12.3$, $p < 0.001$, $df = 1$), particularly for when fitting to data from only 1 amplitude condition.

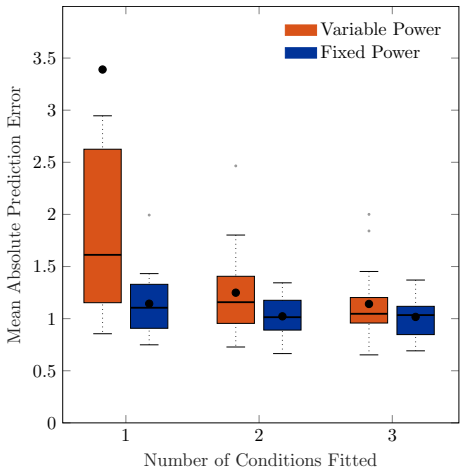

Figure 2.8: Box plot showing the mean absolute prediction errors for when 1, 2 and 3 cases are fitted to predict 3, 2 and 1 other conditions, respectively. The orange Box plots show prediction errors for the individual-level power law, and the blue Box plots show the prediction errors for the power law fixed to 0.4.

Importantly, the group-level power on average has a fitting MAE of 0.90, which is close to the average prediction error of 1.15 after fitting only one condition. This indicates a high degree of regularity in the amplitude response that can be predicted by a power law of 0.4, and one that cannot be captured by the individual-level power model without larger amounts of data.

2.3.4 Sickness Forecasting

One of the properties of an effective predictive model is its ability to forecast future development of the modeled system's states. In this section, we evaluate this forecasting ability

of the Oman model.

Figure 2.9 shows the first motion phase responses of participants 11-14, where the rows represent the different participants and the columns the different amplitude conditions (for the data of all participants, see figure S3). In our experiment, participants 10, 11, 14 and 17 vomited or retched (MISC 10 and 9, respectively) very shortly after (<30 s) reaching a MISC level of 6. Because this occurred very shortly after reaching 6, in Sections 2.3.2 and 2.3.3, a MISC of 6 was taken as the end point of the experiment data used for fitting. In Figure 2.9 the full MISC trajectories are shown (blue lines), which for participants 11, 12,and 14 show a region of stable growth until a MISC of 6, then a blow-up to vomiting, as similarly reported in the results of Graybiel (1969).

This phenomenon cannot be captured by the Oman model, which, as noted before in section 2.2.6, converges in a stable manner to a final sickness level that may be higher than 10. Predicting such high levels of sickness may not be a concern for most practical applications, for which the aim generally is to keep sickness at the lower MISC levels. Figure 2.9 shows Oman model predictions (in orange) when the model is fitted to all data up to a MISC value of 3 (blue shaded ranges) and sickness is then forecasted until the end of the experiment. It can be seen that this extrapolation from lower MISC levels in to the future for some participants suffers from premature convergence (e.g., participant 11 in Figure 2.9), where the model captures an initial seeming convergence of the MISC data to a final rating. This effect is explained by the small amount of data provided (only up to and including MISC 3) and the inherently convergent nature of the Oman model.

Overall, it is the diverging sickness trajectories that show the largest forecasting errors, e.g., participants 12 and 14 in Figure 2.9. This can be shown statistically, by fitting a model of the form

$$\text{MISC} = at^b \tag{2.4}$$

as proposed in Irmak et al. (2020), where t is time since the start of exposure and a, b are model coefficients. The responses that can be described by $b \geq 1$ have a diverging sickness response with respect to time, whereas those with $b < 1$ have a converging response. The fitted model had an average coefficient b of 1.085 (25–75th percentiles: 1.043–1.448). This means that the MISC is approximately linear with respect to time. When fitting the Oman model using a long fitting window, it can describe both converging and diverging responses equally well. This is despite its natural tendency to converge. This is because for divergent cases, the model estimates a very large steady-state value, meaning that the initial rising part of the response is able to approximate the divergent cases quite well. However, when forecasting from lower MISC levels, using a shorter observation window, it is seen that forecasting performance for divergent cases is significantly worse than forecasting for convergent cases. This can be seen by comparing a constant (intercept-only) and a linear mixed-effect model, relating the power term to the mean absolute error in the forecast region (AICc = 149.0 and 136.9, respectively). With a difference between AICc values > 10 Fabozzi et al. (2014), it can be seen that the linear model is significantly better, meaning that the forecast error increases with increasing divergence of the sickness response.

The cause of the suboptimal forecasting is partly due to the model form, which is always stable, but also due to the limited data used for fitting and extrapolating from.

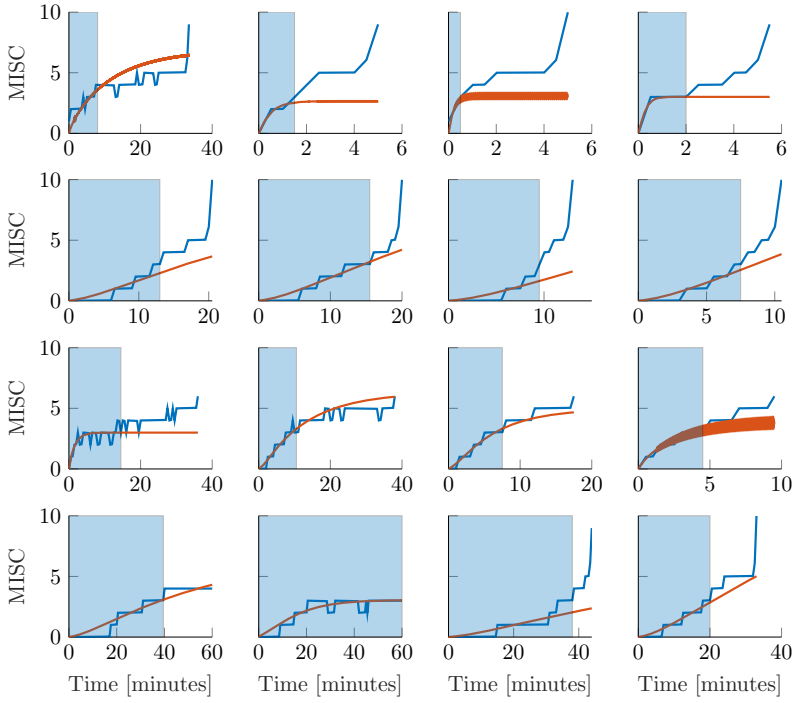

Figure 2.9: Representative sample of extrapolations from MISC 3 to the end of the first motion phase, for the Oman model. The columns show responses for each amplitude condition, increasing in magnitude from left to right. The rows show results for participants 11, 12, 13 and 14. The blue shaded area gives the observations the model uses to make forecasts.

At the individual level, 15 out of 17 participants had MISC responses that were in at least 3 out of 4 conditions either consistently divergent or consistently convergent. The remaining 2 participants showed convergent MISC responses in half of the conditions and divergent responses in the other half. This means that, on average, individuals show a propensity towards one type of motion sickness trajectory. This supports the existence of idiosyncratic differences in the qualitative form of sickness dynamics. We did not find a difference in the power term between the motion conditions ($\chi^2 = 1.2$, $df = 3$, $p = 0.75$). This indicates that the divergent/convergent dynamics is not modulated by differences in the motion amplitude in the range explored in this study.

In our study, the MSSQ was correlated marginally significantly with overall sickness susceptibility ($\rho = 0.50$ $p = 0.05$). The overall sickness susceptibility was quantified by averaging the MISC rates during the first motion exposure of an individual for all amplitude conditions. This finding indicates the usability of the MSSQ for predicting sickness susceptibility

and hence as a tool for participant selection. However, a better selection could be made by first perturbing the participants at 2.5 m/s^2 until they reached a MISC of 3 which would on average take 8 minutes. The Oman model may then be used to estimate participants' susceptibility directly. Doing this on the data from the experiment, there is a very strong correlation between the Oman model estimation of susceptibility and the overall sickness susceptibility as computed from the average MISC rate for a participant ($\rho = 0.72$ $p = 0.002$). This level of predictability with respect to actual sickness susceptibility is directly useful in candidate participant screening. A better predictive model would have higher susceptibility discrimination, at even lower MISC levels, requiring less simulator time. Indeed, the correlation between the Oman model forecasting and overall susceptibility is not significant $\rho = 0.15$ ($p = 0.58$) when data to only MISC of 2 is considered.

2.4 Discussion

This study investigated the amplitude and temporal dynamics of motion sickness at both the group and the individual levels. Participants underwent fore-aft sickening motions at four different acceleration amplitudes. Motion sickness development over time was reported using the MISC scale. First, using the dropout percentage and the MISC rate, the group-level response to varying amplitudes was evaluated. Also, three variations of the Oman model of nausea were used to characterize the dynamics of motion sickness at the individual-level. This was done by both fitting observed sickness at different amplitudes, but also by assessing the cross-amplitude validity of the model. Lastly, we investigated how well the Oman model can forecast future sickness based on a shortened measurement of initial sickness development.

2.4.1 Group-level Observations

For the group-level response to increasing acceleration amplitudes, *we found a significant increase in sickness severity with increasing acceleration amplitude*, and hence sensory conflict magnitude, on the development of motion sickness. As seen in Figure 2.3, not only was this effect monotonous with respect to the acceleration amplitude, it could also be accurately characterised by a linear relationship, which was shown by comparing a constant mixed-effect model of MISC rate with a linear mixed-effect model (AICc = -1.92 vs. AICc = 29.4).

Previous studies by Alexander et al. (1947); Griffin and Mills (2002a); O'Hanlon and McCauley (1974) also reported a monotonic increase in sickness with respect to acceleration amplitude. In the study of Griffin and Mills (2002a) only low-amplitude motions in the range of 0.4-1.56 m/s^2 were used, and only the last two conditions were significantly higher in sickness severity from the baseline case of no motion. Therefore, a functional relationship between motion amplitude and sickness could not be formulated. The studies by O'Hanlon and McCauley (1974) and Alexander et al. (1947) assessed vomiting incidence at the end of their experiments (MSI) and found a log-normal relationship between MSI and acceleration amplitude. However, it would be incorrect to say sickness itself exhibits log-

normal behaviour for the range of accelerations used in these studies. Indeed, in our study, we report both the dropout rate and the rate of sickness development. For the dropout rate, which is a similar metric to the MSI, dropout percentages for 2.5 and 2 m/s^2 are not significantly different, whereas MISC rate indicates a linear, rather than a log-normal, relationship between sickness and acceleration amplitude. The data of Lawther and Griffin (1988) suggest that this linear relationship may continue down to the range of 0.1-0.7 m/s^2, i.e., to lower amplitudes than tested in our experiment. At the lowest acceleration magnitudes, i.e., below 0.1 m/s^2, experienced sickness did not differ from the stationary case. This apparent 'sickness threshold' is equivalent to reported translational acceleration perception thresholds (Gianna et al., 1996; Heerspink et al., 2005). As remarked previously, acceleration is often used as a proxy for sensory conflict for experiments lacking visual stimuli, and in our current experiment set up the two are assumed to be proportional to each other. Very sickening stimuli, such as the cross-coupled coriolis, which can elicit vomiting in minutes as opposed to > 10 minutes as in this study, likely produce much higher sensory conflicts, which may be translated to an equivalent acceleration, indicating that the monotonic amplitude relationship likely holds at even higher accelerations than 2.5 m/s^2. Approximately 95% of all vehicle accelerations are within the maximum acceleration used in this study (Feng et al., 2017). Therefore, we can conclude that linearity in the sickness response can be an adequate modelling assumption at the group-level for automated vehicles.

With respect to the metrics used to quantify group-level responses, we chose the drop-out rate and MISC rate. The drop-out rate provides an easy to interpret measure of sickness, whilst also allowing us to perform survival analysis. For our experiment, the MISC rate is less directly dependent on our selected termination criteria. It is defined as the MISC rating at the end of motion exposure, divided by the time in minutes to this final value. In the current study, we fitted the model at^b to all MISC responses; the resulting average value for b is 1.085 (25–75th percentiles: 1.043–1.448). This means that the MISC is approximately linear with respect to time, increasing monotonously with respect to time, with no long-duration decreases. Therefore, computing the average gradient of the MISC curve, i.e., our MISC rate, is an appropriate parametrisation of the response.

In cases such as naturalistic driving where such monotony is not observed, a model-based approach may be more appropriate. The kind of model used for this purpose is a formal accumulation model, such as the Oman model. This is because in such a scenario, the sickness response will be complex and time-varying, depending on the accelerations encountered. Using traditional ways of parametrising the sickness response will make both within- and between-participant comparison difficult, requiring, in the least, many sessions to average across a representative sample of acceleration exposures. With a model-based approach, the parameters of the fitted model will be invariant with respect to the motions encountered and easier to compare.

2.4.2 Individual-level Modelling

In this study, we showed that motion sickness development over time could be accurately modelled at the individual level, for the different tested amplitude conditions separately,

with a modified version of Oman's sickness model. We found that the time constants of sickness development were approximately motion amplitude independent, with median time constants of 66.2 s and 502.4 s for the model's 'fast' and 'slow' time constants, respectively. One concern of automotive engineers in utilising the findings of motion sickness studies could be the fact that usually the motions encountered in these studies are aggressive, with the intent of quickly making participants motion sick, whereas motions that lead to motion sickness in vehicles tend to be more gradual and accumulate over the span of up to an hour. In this study, we tested both aggressive motions (2.5 m/s^2) and gentle motions (1 m/s^2). The fact that no difference in the time constants was found implies that the temporal dynamics of motion sickness are amplitude-independent, with only varying scaling factors affecting the final level of sickness. This suggests that the findings of sickness studies, all else equal, can be directly applied to automotive control and design.

In this study, we report only on nonlinear output scaling in Oman's model. However, we also investigated the use of both input and output scaling, see Figure 2.2. The original Oman model has the conflict vector as an input, which is processed by the two paths, whose outputs are then summed. This summed output is the *latent* sickness. The output power scaling transforms this latent sickness in to a subjective magnitude estimate, via an exponential term corresponding to Steven's power law (Stevens, 1946), which maps stimulus intensity to perceived intensity. As employed by Bos and Bles (1998), the reasoning for input scaling is different. Here, the conflict signal itself is assumed to be remapped with a nonlinear scaling (sigmoid), where small sensory conflicts remap to zero and large conflicts are saturated. We approximate this through an input power law. We found that the output power law provided a much better fit to our data, with a mean joint error (E_{joint}) of 1.03 compared to 1.4 for the input scaling. As Figure 2.6 shows that with output scaling for all powers up to 0.8 the joint fitting error is below the optimum result for input scaling, we conclude that output scaling on the modelled latent sickness metric is superior for our experiment data.

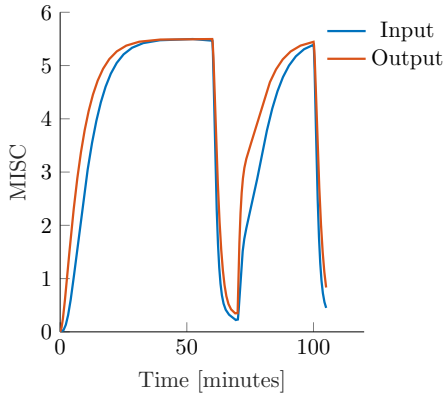

Figure 2.10: Example showing the effect of input (blue line) and output (orange line) power scaling on the predictions of the Oman model for constant amplitude input

While both with input and with output scaling Oman's model can model convergence to

an identical final steady-state sickness level (with adapted gain and power law exponent), see Figure 2.10, this will always result in differences in the temporal dynamics. In these example model responses, the input and output power scaling, as well as the short and long time constants, are all the same, while the model gain is adjusted such that both modelled responses converge to the same steady-state sickness. Regardless, it can be seen that for constant amplitude stimuli, the output scaling responds faster to the input, particularly in the hypersensitivity phase. This is because the output of the slow and fast paths accumulate more slowly when the input signal strength is reduced by an input scaling, than when it is not. The reason why this steeper increase may better represent our data is that the MISC is on an ordinal scale. Participants are likely to spend less time at the lower ends of the MISC scale, which represent smaller increments on a scale of subjective discomfort (De Winkel et al., 2022), than the higher end of the MISC scale. This is particularly relevant for the hypersensitivity phase.

As shown in Figure 2.6, an output scaling of 0.4 provided the best fit to our dataset. The power of 0.4 approximately linearises the conflict to sickness relationship, where for large values of K, equation 2.3 reduces to $\text{MISC}_{ss} \approx K^{0.4} A^{0.8}$. Likewise, for the input scaling this optimal power was found to be similar, i.e., 0.5. This value fully linearises the conflict to sickness relationship. This means that irrespective of the scale used to measure sickness the Oman model, or any other model of sickness accumulation, should have a power-law relationship that enforces linearity, whereby only the gain of the system is expected to change depending on the rating scale used. Finding the system gain for the different rating scales would greatly contribute to comparing and generalising the findings of different motion sickness experiments.

For the first time, this study evaluated forecasting/predicting sickness at the level of the individual, based on a short duration of initial sickness data (MISC<3). The development of sickness over time in the first motion exposure could be predicted accurately, with a MAE of 0.93. In our previous work (Irmak et al., 2020), we identified two groups of participants by fitting a power law to measured MISC as a function of time (see equation 2.4). The participants for whom the exponent $b \geq 1$ were classified as *divergent* and those with $b < 1$ were classified as *convergent*. In that study, the Oman model was able to fit both groups equally well, which cast doubt on whether these two groups were indeed qualitatively different. However, in the present study we found that the Oman model had significantly higher accuracy when *predicting* convergent, as compared to divergent cases, thus supporting the notion that MISC trajectories are indeed qualitatively different between individuals.

One notable property of the Oman model that affects forecasting of future motion sickness is that it is always stably convergent. That is, there is a steady-state sickness value $MISC_{ss}$ that it will converge to as time tends to infinity. This means that if the participant has converging dynamics, and sickness is observed until a MISC of 3, the model will predict a convergence to approximately a MISC of 3. However, it is known from the data that this is not the case, and that participants likely continue to become more sick, especially if they have reached moderate sickness relatively quickly. A striking example of this issue is shown in Figure 2.9 for the first participant. Here, the observations indicate convergent dynamics, even though the participant reaches a MISC of 4 in under 4 minutes. This participant will inevitably vomit in finite time. The model, however, cannot account for this.

Moreover, some participants (such as the first participant of Figure 2.9) show convergent sickness behaviour at first, followed by a sudden increase towards vomiting. There can be multiple reasons for this. One explanation is that the participants use the MISC scale as a subjective discomfort scale, and that for these participants, a MISC of 6, which was the termination criterion in this study, was seen as the point after which they could not continue because they would otherwise vomit. Alternatively, it can also be that these participants experienced an unstable ”avalanche” of symptoms. Such an effect has been reported in literature (Bock and Oman, 1982; Graybiel, 1969). To account for both the stable and unstable behaviour seen in motion sickness responses, the next step should be to model the dynamics of sickness as a *bistable* system. In this, participants may have two equilibrium points. One that is at a level of sickness below 10, depending on motion amplitude, and the other at a MISC level of 10. Modeling this requires higher degree non-linear differential equations than included in Oman's model.

Sickness forecasting as demonstrated in this paper is not only a theoretical exercise, but has methodological implications for both motion sickness studies and applications such as the individualisation of automated driving algorithms. In this study, we showed that using the Oman model and a short duration perturbation at the highest amplitude, one can reliably predict the overall motion sickness susceptibility of an individual. Such a paradigm can be used as a screening method for ensuring participants of similar sickness susceptibilities are enrolled in to motion sickness studies. This would for instance increase the power of studies comparing different mitigation methods. Moreover, such a method provides a basis for individualised and online sickness-mitigating adaptive tuning of automated driving algorithms.

Well-known models of motion sickness development contain two components, being 1) Conflict models predicting conflicts resulting from sensory integration, and 2) Accumulation models predicting motion sickness development in time. One example of a motion sickness model is the subjective vertical conflict (SVC) model (Bos and Bles, 1998; Wada, 2021). The conflict generation part of the model is based on the difference between the sensed vertical and the subjective vertical, which is thought to drive motion sickness. It is a specific implementation of the idea of sensory-expectancy conflict put forth in Oman (1982). Conflict models are needed to capture sensitivity towards complex motion stimuli, including multiple motion directions and frequencies. The conflict derived in the SVC is then accumulated using a simple second order filter. This accumulation model is less sophisticated than the Oman model used in this study, which is able to describe hypersensitivity.

Our study focuses on motion sickness accumulation in time for a single degree-of-freedom motion stimulus, i.e., a 0.3 Hz sinusoidal fore-aft seat motion. For such a simple stimulus, conflict models degrade to a simple gain, where the exact gain (proportion of fore-aft acceleration that is attributed to the subjective vertical) is dependent on the stimulus frequency and the subjective vertical time constant.

In our approach, this gain is (implicitly) identified in our fitting of Oman's model. Therefore, if, the actual sensory conflict would be only 50% of the input motion, then the gain of our fitted model would simply be 50% larger. Thus, our method of using acceleration as the

input to Oman's model is, for our specific stimulus, equivalent to the conflict between the sensed and the expected vertical that can be derived from the SVC model.

One important application of this work is that now that the relationship between conflict and the subsequent sickness is known, the system that maps motion inputs to sensory-conflict can be identified by using closed-loop system identification techniques (Qian et al., 2017; Rojas et al., 2007).

2.4.3 Limitations

As discussed previously, particularly at the lower amplitudes, there might be an amplitude threshold below which people do not experience motion sickness. In this study, the range of the amplitudes studied was between 1 and 2.5 m/s^2. In future studies, it is essential to also include lower amplitudes to also gain an improved quantitative understanding of motion sickness severity and temporal dynamics for low-amplitude stimuli. In addition to increasing the range of accelerations for which our motion sickness models are effective, experiments that include a high number of different motion amplitudes measured within the same experimental session, as representative of real vehicular transportation, would further help to strengthen motion sickness model validation.

In the present study, the model successfully described hypersensitivity after a 10-minute break. In a previous study, Irmak et al. (2020) the break duration was until the participant reached a MISC of 2, which only very rarely exceeded 10 minutes. This means that the model can describe hypersensitivity observed after break durations up to 10 minutes. One limitation is therefore the lack of data to verify whether the same modelling accuracy is retained for longer rest durations. Being able to model these longer rest durations may not be relevant for short distance journeys, however, it may be useful for predicting motion sickness during multi-stage long distance travel.

Lastly, it is likely that the amplitude and temporal dynamics found in this study do not depend on the direction of motion. Therefore, pure vertical and lateral motions will likely have similar time constants, gains and output power. This is given by the fact that the severity of sickness in different directions is similar to each other (Donohew and Griffin, 2004). However, if a coupling exists between different degrees-of-freedom, such that the resultant stimulus has a complex frequency spectrum, this may cause currently unknown interactions in the conflict signal due to differing frequency sensitivities (Irmak et al., 2021). Similarly, with reduced motion predictability (Kuiper et al., 2020) compared to our current sinusoidal acceleration stimuli, a greater sickness response is expected. In these cases, particularly the gains of the accumulation model may need to be calibrated.

2.5 Conclusion

This study investigated the individual amplitude sensitivity in motion sickness caused by sensory conflicts induced by fore-aft accelerations. At the group-level, we found that sickness severity increases linearly with acceleration amplitude between 1-2.5 m/s^2 and argue

that it does so for all relevant acceleration amplitudes in vehicular transport. From fitting a modified version of Oman's model of sickness progression, we found that, at the individual-level, sickness on average increased linearly with acceleration amplitude, even though some participants exhibit higher or lower order amplitude sensitivities. Importantly, we note that the time constants governing motion sickness development vary between individuals, but are independent of the acceleration amplitude. Furthermore, our data shows that a group-level fixed output scaling with an exponent of 0.4 enables Oman's model to inherently account for stimulus amplitude variations, as considered in our tested amplitude conditions. Lastly, we showed that the Oman model can be used to forecast the temporal evolution of sickness beyond a brief observed initial exposure. In this we found that forecasting works better for convergent, rather than divergent responses, this is largely due to the inherently convergent dynamics of the model. Overall, these findings enable improved modelling of motion sickness accumulation in mixed acceleration environments, such as traffic, and better participant prescreening for motion sickness experiments, as well as tuning of automated driving algorithms for individual passengers.

3

The Role of Vision in Sensory Integration Models for Predicting Motion Perception and Sickness

Everything we hear is an opinion, not a fact.
Everything we see is a perspective, not the truth.

Marcus Aurelius

This chapter is based on *Kotian, V., Irmak, T., Pool, D., & Happee, R. (2024). The role of vision in sensory integration models for predicting motion perception and sickness. Experimental Brain Research, 242(3), 685–725.*

The appendices for this chapter can be found at Appendix B.

Abstract

Users of automated vehicles will engage in other activities and take their eyes off the road, making them prone to motion sickness. To resolve this, the current paper validates models predicting sickness in response to motion and visual conditions. We validate published models of vestibular and visual sensory integration that have been used for predicting motion sickness through sensory conflict. We use naturalistic driving data and laboratory motion (and vection) paradigms, such as sinusoidal translation and rotation at different frequencies, Earth-Vertical Axis Rotation, Off-Vertical Axis Rotation, Centrifugation, Somatogravic Illusion, and Pseudo-Coriolis, to evaluate different models for both motion perception and motion sickness. We investigate the effects of visual motion perception in terms of rotational velocity (visual flow) and verticality. According to our findings, the SVC_I model, a 6DOF model based on the Subjective Vertical Conflict (SVC) theory, with visual rotational velocity input is effective at estimating motion sickness. However, it does not correctly replicate motion perception in paradigms such as roll-tilt perception during centrifuge, pitch perception during somatogravic illusion, and pitch perception during pseudo-Coriolis motions. On the other hand, the Multi-Sensory Observer Model (MSOM) accurately models motion perception in all considered paradigms, but does not effectively capture the frequency sensitivity of motion sickness, and the effects of vision on sickness. For both models (SVC_I and MSOM) the visual perception of rotational velocity strongly affects sickness and perception. Visual verticality perception does not (yet) contribute to sickness prediction, and contributes to perception prediction only for the somatogravic illusion. In conclusion, the SVC_I model with visual rotation velocity feedback is the current preferred option to design vehicle control algorithms for motion sickness reduction, while the MSOM best predicts perception. A unified model that jointly captures perception and motion sickness remains to be developed.

3.1 Introduction

A wide range of studies indicate that motion sickness is caused by mismatches between *perceived* sensory signals – i.e., from the eyes, otoliths, semicircular canals, etc. – and *expected* sensory signals from the central nervous system (e.g., Reason (1978b)). These mismatches are particularly triggered during passive motion – i.e., when the motion is due to external forces that cannot, or only imperfectly, be anticipated – with strongly moving visual surroundings, for example as experienced on ships and by passengers in horse-drawn carriages (Huppert et al., 2017). With the current trend towards fully automated vehicles, motion sickness is expected to become much more widespread (Bertolini and Straumann, 2016; Griffin and Newman, 2004; Kuiper et al., 2018; Salter et al., 2019), as all vehicle users will be passengers that passively experience the vehicle's motion, while preferably engaged in other activities. Minimizing the incidence of motion sickness in automated vehicles requires improved knowledge of motion sickness and how it relates to human motion perception mechanisms, as well as accurate models with which its development over time can be predicted, to design comfortable vehicle motion control strategies.

In motion sickness models, the '*sensory conflicts*' that are assumed to cause sickness (Reason, 1978b) are generally defined as the difference between the sensed and expected sensory signals. Hence, these models are often referred to as '*sensory conflict models*', due to their ability to quantitatively predict the conflicts that, when accumulated over time, lead to the worsening of motion sickness symptoms (Bos and Bles, 1998; Irmak et al., 2022, 2020; Kufver and Förstberg, 1999; Oman, 1990). For example, Bos and Bles (1998) conceptualized the Subjective Vertical Conflict (SVC) model, which is based on the assumption that motion sickness is caused by conflict in the sensed vertical (i.e., orientation with respect to gravity). The SVC model has been extended by Kamiji et al. (2007) to account for all six degrees of freedom (DOF) in the 6DOF-SVC model, which matched some available motion sickness data sets at reasonable accuracy. However, the 6DOF-SVC model in Kamiji et al. (2007), only accounts for vestibular sensation and how this impacts the subjective vertical, and motion sickness.

It is well-known that the visual system has a crucial impact on both our perceived motion, as well as motion sickness. For example, illusory perceived subjective orientations that occur with only vestibular stimulation no longer occur when a visual reference (e.g., horizon line or straight walls) is perceived. Furthermore, the sickening drive data from Irmak et al. (2020) show that participants become at least 1.83 times as sick when not being able to see the vehicle's movement (internal view) as compared to when looking outside the vehicle (external view). Motion sickness is also observed in studies using virtual reality or using fixed-base driving simulators. Since there is no physical motion in these cases, this is commonly called Visually Induced Motion Sickness (VIMS). To account for such effects, a number of perception models include visual perception contributions of angular rotation velocity, verticality, or both such as the Multi-Sensory Observer Model (MSOM) by Newman (2009), the extension of the 6DOF-SVC model with vision by Liu et al. (2022); Wada (2021); Wada et al. (2015, 2020), the spatial orientation and motion sickness model by Bos et al. (2008), and the sensory weighting model by Zupan et al. (2002). At this moment, some of the sensory conflict models that include visual perception have been validated for

specific motion perception paradigms (e.g., MSOM by Newman (2009)) or for motion sickness prediction in real-world naturalistic driving (e.g., (Yunus et al., 2022)). However, so far no single model has been shown to describe both the perceptual effects of vision, and its effects on motion sickness development, which is required for physiologically valid and interpretable predictions of motion sickness (Irmak et al., 2023).

Hence, the goal of this paper is to verify the accuracy of available sensory conflict models that include visual motion perception, for predicting human perception responses in well-known motion perception paradigms, as well as motion sickness data from laboratory experiments (Correia Grácio et al., 2013; Merfeld et al., 2001; Vingerhoets et al., 2006; Waespe and Henn, 1977) and real-world driving experiments (Irmak et al., 2020). In this paper, we focus on comparing only the most recent versions of the motion sickness and motion perception models that include visual rotational velocity and visual orientation perception, namely the Subjective Vertical Conflict (SVC) model (Inoue et al., 2023; Liu et al., 2022; Wada et al., 2020), and the Multi-Sensory Observer Model (MSOM) (Clark et al., 2019; Newman, 2009), as the most promising candidates. Similar to Irmak et al. (2023), we present a two-part analysis, where we first focus on these models' match to well-known frequency and amplitude sensitivity characteristics of motion sickness (Golding and Markey, 1996; Griffin and Mills, 2002b; Howarth and Griffin, 2003; Irmak et al., 2021, 2022; McCauley et al., 1976). Furthermore, the extent to which the models can replicate the effect of vision conditions in the real-world sickening drive study of Irmak et al. (2020) is analyzed. In the second part, we assess the model's ability to replicate well-known fundamental motion perception tests, i.e., Earth vertical Axis Rotation (EVAR) (Vingerhoets et al., 2006; Waespe and Henn, 1977), Off-vertical Axis Rotation (OVAR) (Vingerhoets et al., 2006), centrifuge (Merfeld et al., 2001), somatogravic illusion (Correia Grácio et al., 2013) and pseudo-Coriolis (Newman, 2009).

Apart from the aforementioned suggested models, alternative theories about the origin of motion sickness are also present. According to the work of Riccio and Stoffregen (1991), another proposition is that motion sickness arises due to '*postural instability*'. This implies that animals feel sick when they are in situations where maintaining proper postural stability becomes difficult. Consequently, this theory suggests that postural instability acts as a direct precursor to the symptoms of sickness. However, as the majority of existing mathematical models for motion sickness are grounded in the sensory conflict theory, this paper will not delve into the postural instability theory.

Thus, this paper directly extends the work of Irmak et al. (2023), who focused on vestibular-only perception and sickness modeling, to also include the essential visual component. Based on this quantitative performance comparison of available sensory conflict models, we formulate recommendations on the most critical and promising model structures for predicting motion perception and motion sickness, as well as provide crucial suggestions for much-needed experiments for further model validation.

3.2 Method

3.2.1 Sensory Integration Models

In this paper, we evaluate several versions of the subjective vertical conflict (SVC) model (figure 3.1) with parameters in table 3.1, and the MultiSensory Observer Model (MSOM) (figure 3.2) with parameters in table 3.2. Both models consider two vestibular inputs: the specific force sensed by the otoliths and the angular velocity sensed by the semicircular organs. Both models also include two visual inputs: a visual cue of rotational velocity (*visual rotational velocity* or VR; ω_{vis} in the figures 3.1 and 3.2) and a visual cue of verticality (*visual vertical* or VV; υ_{vis} in the figures 3.1 and 3.2). The reasoning behind *visual rotational velocity* is that the human eye can perceive rotational velocities through rotational (optic) flow (Ehrenstein, 2003). *Visual vertical* is included because human eyes tend to find earth vertical or horizontal objects such as trees, buildings, and horizons to orient themselves with respect to the earth (Cano Porras et al., 2020). The two approaches look promising. Human vision, as discussed in Berthoz and Droulez (1982), also is able to perceive linear (translational) motion (linear velocity and linear position). These have been modeled in the MSOM (Newman, 2009) as well. However, in the model, these do not contribute to either verticality, acceleration, or angular velocity estimates. They are solely used for improving linear velocity and linear position estimates and do not affect sickness predictions. Hence, these visual linear motion pathways are not considered in the analysis in this paper.

SVC Model

Bos et al. (2008) developed the Subjective Vertical Conflict (SVC) model, which estimates the conflict between the sensed signals from the sensory systems and the expected sensory signals derived from the central estimates computed by the central nervous system. The model has three parts: the 'Visual-Vestibular System', the 'Internal Model' of the visual-vestibular system, and the 'Feedback' of errors between sensed signals and internal model predictions, see figure 3.1. The main concept of this model is that the dominant conflict causing motion sickness is the mismatch between the estimation of verticality (orientation with respect to gravity) and the sensed verticality. The otolith dynamics are assumed to be unity (OTO $= 1$), while the semicircular organs are modeled as a high-pass filter (SCC $= \tau_{scc}\, s^2/(\tau_{scc}\, s+1)^2$). These same sensory models (SCC and OTO) are also used in the internal model. The LP block calculates the subjective vertical (direction of gravity) using specific force and angular velocity through a low-pass filter with a time constant τ (Bos and Bles, 1998; Mayne, 1974), see the black lines and blocks in figure 3.1b.

Kamiji et al. (2007) extended the SVC model by Bos and Bles (1998) to include all six degrees-of-freedom (DOFs). The working principle is identical to the original SVC model and the parameters of each pair of three DOFs (linear and rotational) are identical. So for example, vertical, longitudinal, and lateral motions will all give the same conflict. Kamiji et al. (2007) also added loops that aid in state estimation during active motion (dashed pathways in the bottom left of figure 3.1a). These loops model active knowledge about the sensory consequences of the anticipated motion of the body, as was also mentioned by Oman (1990). This helps to improve estimation in the internal model by including the

effect of the efference copy for the active movement, the predictable motion in passive cases, and unmodeled sensory signals such as proprioception. We tested the simulations with and without these (K_ω, K_a) parameters where we found only a 10% difference in the conflict magnitude while carrying out motion sickness frequency sensitivity analysis. However, the frequency dynamics are fully consistent between both cases. Also, the results for the motion perception tests are similar across all motion paradigms. Hence, as also done in previous work (Irmak et al., 2023), this loop was disregarded in the current paper as the conditions studied involve purely passive motion only, without any prior information to predict the motion stimuli. All model parameters are taken from Wada et al. (2020), Liu et al. (2022), and Inoue et al. (2023), which were set by tuning them to match the vertical motion sickness data by O'Hanlon and McCauley (1974).

SVC$_I$ model The SVC model by Kamiji et al. (2007) was further extended by Wada et al. (2020) and Liu et al. (2022) who added loops for simulating vision, see figure 3.1. The pathways in blue show the *visual rotational velocity* loop and the pathways in red show the *visual vertical* loop. The models with a *visual rotational velocity* loop will be referred to with a 'VR' at the end of their abbreviated names and the models with a *visual vertical* loop will be referred to with a 'VV'. The sensory dynamics for both these visual inputs (VIS$_g$ and VIS$_\omega$) are unity matrices, as it is generally assumed that the eyes approximate a perfect sensor (Liu et al., 2022; Wada et al., 2020). The SVC$_I$ model includes integration (I) for the acceleration conflict feedback term (see the dotted box in figure 3.1d) and is hence referred to in this paper as the SVC$_I$ model.

SVC$_{NI}$ model The SVC$_I$ model was found to not reproduce fundamental motion perception paradigms like roll-tilt perception during centrifuge (Inoue et al., 2023). However, Inoue et al. (2023) found that the removal of integration for the acceleration conflict in the feedback loop (see the dotted box in figure 3.1d) greatly improved model performance for roll-tilt perception during centrifuge, though only for the case without vision. The model by Inoue et al. (2023) (no integration, NI) is referred to in this paper as the SVC$_{NI}$ model.

Multi-Sensory Observer Model (MSOM)

Merfeld et al. (1993) proposed a one-dimensional observer model to predict the angular vestibular-ocular reflex to yaw rotation about the earth's vertical axis. Furthermore, they extended this model to a 6-DoF model by including the otolith organs to account for acceleration storage and gravity storage central estimates analogous to angular velocity storage in the one-dimensional model. Here, the sensory dynamics of the semicircular canals (SCC) were modeled as a first-order high-pass filter with a time constant (τ_{scc}) of 5.7 s while the otolith dynamics (OTO) is unity. The G block calculates the subjective vertical (direction of gravity) using the angular velocity. The internal models of the central nervous system were assumed to be identical to these sensory dynamics. Using this approach of an observer feedback model, and adding additional processing layers, Zupan et al. (2002) proposed a 3D model consisting of three processing layers: frequency completion, conversion of sensory estimates to central estimates, and multi-cue weighted averaging of the central

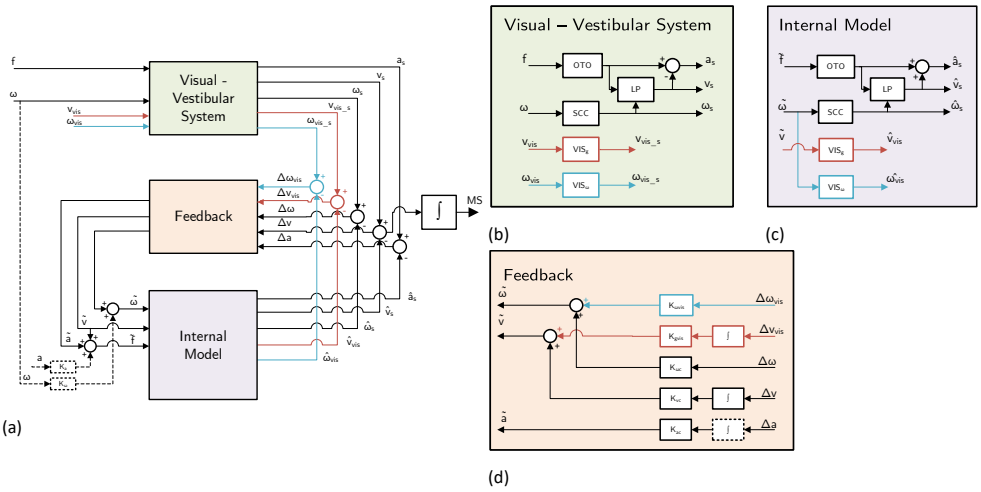

Figure 3.1: Subjective Vertical Conflict (SVC) Model: (a) high-level diagram and (b)-(d) details of different subsystems. Vestibular loops (black) are as in Kamiji et al. (2007); 'VR' (*visual rotational velocity*) loops (blue), as in Wada et al. (2020); 'VV' (*visual vertical* (direction of gravity or orientation)) loops (red), as in Liu et al. (2022). The SVC_I model integrates the acceleration conflict (dotted box in (d)). This integrator (I) is replaced by a unity gain (no integration, NI) in the SVC_{NI} model in Inoue et al. (2023).

Table 3.1: SVC_I and SVC_{NI} model parameters; Parameters for the SVC_{NI} model in parenthesis

	Parameter Symbol	Value	Explanation
Anticipation Gains	K_a K_ω	0 0	Fully passive motion assumed
Vestibular Feedback Gains	K_{ac} K_{vc} $K_{\omega c}$	1 (0.5) 5 10	as in Wada et al. (2020) (as in Inoue et al. (2023))
Visual Feedback Gains	K_{gvis} $K_{\omega vis}$	5 10	VV gain as in Liu et al. (2022) VR gain as in Wada et al. (2020)
Perception Time Constants	τ τ_{scc}	5 (2) 7	as in Liu et al. (2022) (as in Inoue et al. (2023))

estimates. The internal models were made such as to complement the sensor dynamics and complete the frequencies to which perception remains sensitive. Additionally, using central estimates and calculating weighted averages helps in improving the central estimates. Newman (2009), using the vestibular core of this observer model, added additional estimates (position and velocity) to form the Multi-Sensory Observer Model (MSOM). This

model, like the SVC model, has 3 parts – the models for the visual-vestibular system (green), the internal model of the visual-vestibular system (purple), and the feedback (orange) as can be seen in figure 3.2. The model's parameters are listed in table 3.2.

The MSOM was developed as a motion perception model (Clark et al., 2019; Merfeld et al., 1993; Newman, 2009) and at the time of writing, did not define a conflict term for calculating motion sickness. Despite this, Irmak et al. (2023) used the MSOM model to predict motion sickness, for which he evaluated various conflict terms and concluded that only the otolith conflict, Δf_{oto}, was correlated to motion sickness. However, the otolith conflict was found to be unable to capture the well-known frequency sensitivity for sickness with vertical acceleration stimuli as in McCauley et al. (1976). This is further discussed in section 3.4.1. Still, in this paper we consider the integrated otolith conflict as the MSOM's proxy for motion sickness.

The MSOM includes an explicit two-way coupling between the semicircular canals and the otoliths that helps to capture the somatogravic effect, which is closely linked to motion sickness induced by horizontal accelerations in absence of vision (Irmak et al., 2021; Wood, 2002; Wood et al., 2007). The MSOM, like the SVC models, has two pathways for simulating vision. The pathways in blue show the *visual rotational velocity* loop ('VR') and the pathways in red show the *visual vertical* loop ('VV').

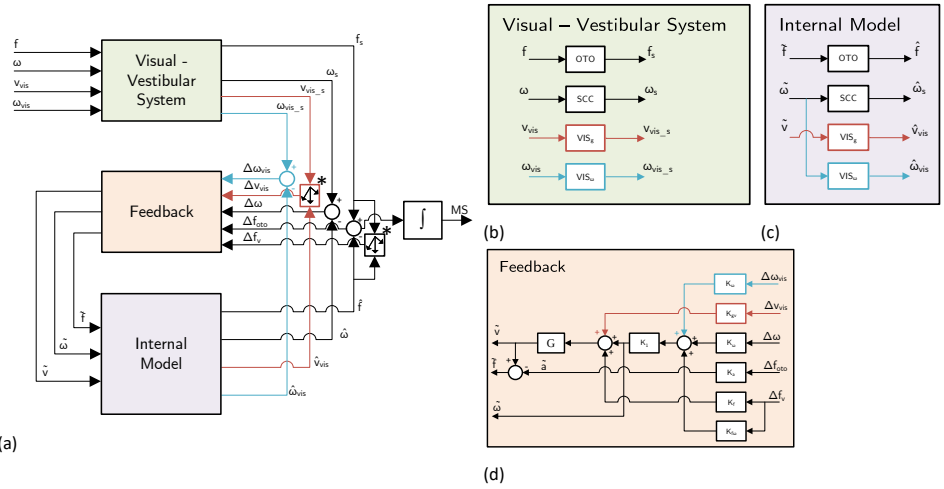

Figure 3.2: Multi-Sensory Observer Model (MSOM) as in Newman (2009): (a) high-level diagram and (b)-(d) details of different subsystems. Vestibular loops (black); 'VR' (*visual rotational velocity*) loops (blue); 'VV' (*visual vertical* (direction of gravity or orientation)) loops (red);
∗ calculates the rotation required to align the actual and expected sensory estimates (see Newman (2009) for more details).

Table 3.2: Parameters for the MSOM model

	Parameter Symbol	Value	Explanation
Vestibular Feedback Gains	K_a	-4	as in Newman (2009)
	K_f	4	
	$K_{f\omega}$	8	
	K_ω	8	
	K_1	$K_\omega/(K_\omega+1)$	
Visual Feedback Gains	K_{x_v}	0.1	as in Newman (2009)
	$K_{\dot{x}_v}$	0.75	
	K_{g_v}	10	
	K_{ω_v}	10	
Perception Time Constants	τ_{scc}	5.7	as in Merfeld et al. (1993)

3.2.2 Tests for validation

The models (either VR, VV, or both) are validated using the model parameter values that were reported in their respective publications. While it is possible to enhance the modeling accuracy through a parameter optimization step, such retuning of model parameters is considered to be beyond the scope of the current paper. A brief exploration in Appendix B.1 shows that the applied vision loop gain parameters are adequate for sickness prediction. To not further complicate the comparison of the relative effectiveness of the VV and VR loops in the SVC and MSOM models in this paper, the specific published forms of the models and their parameters were used. This means that these results are most applicable to SVC models and MSOM models when using the specific parameter sets we employed. Furthermore, given the lack of available comprehensive experiment data that cover the different vision cases studied in this paper, we present a qualitative assessment of the relative effects of modeled vision, rather than a quantitative one. By adhering to these defined parameters, we have achieved meaningful insights and valuable findings in this context.

Table 3.3 specifies the experimental motion paradigms used for validation in predicting sickness and perception, with reference to published data. Each of these validation paradigms was simulated for four different vision cases. These vision cases, and how they are implemented for the two possible vision inputs (*visual vertical* v_{vis} and *visual rotation rotational velocity* ω_{vis}) were implemented as follows:

- '*External vision*' is when the subject has the eyes open and has an outside view of a moving vehicle or motion simulator providing world-referenced visual information. v_{vis} is the same as the direction of the true vertical. ω_{vis} is the same as the true head

angular velocity.

- '*Internal vision*' is when eyes are open, but the subject's vision is limited to the stationary interior of the vehicle. Assuming that the head rotates with the vehicle v_{vis} is set as constant pointing down ($v_{vis} = [0, 0, -9.81]$) and ω_{vis} is set to zero.
- In the '*Only vision*' case there is no physical motion, but only visual inputs (also referred to as VIMS for motion sickness and vection for motion perception in literature). v_{vis} is the same as the direction of true vertical. ω_{vis} is the same as the true head angular velocity.
- In the '*No vision*' case, the eyes are closed and only an inertial motion input is given. The vision loops are disabled.

The visual inputs are determined by making an assumption that the vision is a perfect sensor. The definitions given are true for simple motion paradigms. However, in complex motion paradigms such as real driving, these may not hold true due to the interaction of the view, inside and outside of the vehicle. Nonetheless, we assume the visual input to be only the outside view, thus simplifying the calculation of the visual inputs.

The expected result for the models' motion sickness predictions is that 'internal vision' will give higher conflicts than both 'external vision' and 'no vision' (Griffin and Newman, 2004; Wada and Yoshida, 2016), as will be further discussed in sections 3.4.1 and 3.4.2. The comparison of these vision cases with the case of 'only vision' (VIMS) for the same motion paradigm and on the same participants is not known in the literature yet. Nonetheless, the simulation results for the 'only vision' case are shown to demonstrate the capability of the model in 'only vision' cases, as for example occur in fixed-base (driving) simulators.

The performance of the models for different vision conditions will be evaluated by measuring the linear integration (accumulation) of *conflict* over time. This is used as an indicator of motion sickness levels or motion sickness incidence. This approach eliminates the use of nonlinear integrators (Kamiji et al., 2007; Kotian et al., 2023), which are usually placed at the end of the model to convert conflict into a true motion sickness metric (i.e., MISC or MSI). In this paper, we use a simple linear integrated conflict to directly compare the results of various models in varying vision conditions. Using a simple linear integrated conflict makes it easier to compare the results of various models as well as the experimental data to computational results by normalizing them. Hence, we use *conflict* to compare the models and their performance in various vision conditions.

Motion Sickness Frequency Sensitivity Mapping of the frequency response of a model gives a quantitative measure of the sickness magnitude as a function of frequency and motion amplitude. In our case, this is shown with 3D plots of the accumulated conflict across a range of stimulus frequencies and amplitudes.

For the motion sickness frequency sensitivity analysis for linear DOFs, the simulated input was a fore-aft motion with frequencies from 0.06 to 0.63 Hz and amplitudes from 0.1 g to 0.7 g, where g is the acceleration due to gravity (9.81 m/s^2). The simulations were done for

60 min to predict the MSI at the end of this exposure. The simulation time, frequencies, and accelerations were chosen to be identical to that of the validation data given by McCauley et al. (1976) and simulation data presented by Kamiji et al. (2007). This is done to enable a comparison of the frequency and amplitude dynamics of conflict generation with the Motion Sickness Incidence (MSI) in the experimental dataset. As we are comparing accumulated conflict output from the models, the scale differs greatly from the 0-100% scale of MSI.

For frequency sensitivity analysis for rotational DOFs, the simulated input was a sinusoidal pitch motion with frequencies of 0.01 to 1 Hz and of varying amplitudes from 2 to 22°, which corresponds to horizontal specific forces of 0.34 to 3.68 m/s^2, respectively. The simulations were done for 30min to compare the accumulated conflict at the end of this exposure. The simulation time and frequencies were chosen to match the available experimental data of Howarth and Griffin (2003).

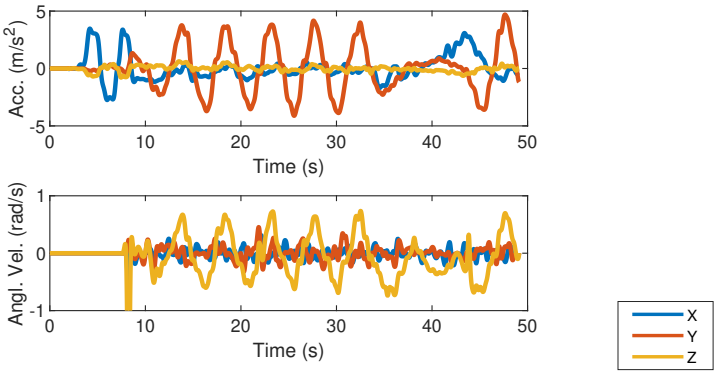

Figure 3.3: Head motion signals in slalom driving (10-35 s) followed by braking and turning (40-50 s) from Irmak et al. (2020).

Real-World Sickening Drive A real-world slalom driving experiment was conducted by Irmak et al. (2020), where a passenger was driven through a route with slaloms of an amplitude of 0.4 g and a frequency of 0.2 Hz followed by braking and turning (figure 3.3). Measured 3D head motion was always used as the vestibular input to the models, as well as the visual input when an external view is available (in 'external' and 'only' vision scenarios). For 'internal vision', the visual inputs are set to constant specific values: 'visual vertical' pointing downward and 'visual rotational velocity' set to zero. Lastly, in the case of 'no vision', the visual loops of the models are fully disabled.

Motion Perception Paradigm Tests Five fundamental motion perception paradigms were simulated to verify the fidelity of the models (table 3.3, lower half). In all these paradigms, participants are subjected to passive motion without vision. They are requested to indicate the perceived velocity and/or perceived verticality through a handheld device. Thereby, such experiments demonstrate perceived motion resulting from the sensory integration of otolith and semicircular canal information.

Table 3.3: Experimental motion paradigms used for validation.
All experiments involved seated subjects with the head upright.

Motion Paradigm	Details	Reference
Sickness Experiments		
Frequency Sensitivity for vertical accelerations	Frequency sensitivity (0.03 to 0.7 Hz) with varying amplitudes (0.027 to 0.55 g) for the vertical direction; internal vision; active neck stabilization	McCauley et al. (1976)
Frequency sensitivity for lateral accelerations	Frequency sensitivity in lateral accelerations (0.2 to 1 Hz) of 3.6 m/s^2; internal vision; active neck stabilization	Golding and Markey (1996)
Frequency sensitivity for fore-aft accelerations	Frequency sensitivity in fore-aft accelerations (0.15 to 0.5 Hz) of 2 m/s^2; internal vision; active neck stabilization	Irmak et al. (2021)
Amplitude sensitivity for fore-aft and lateral accelerations	Amplitude sensitivity for longitudinal and lateral accelerations (0 to 1.78 m/s^2) at a fixed frequency of 0.315 Hz; internal vision; active trunk and head stabilization	Griffin and Mills (2002a)
Amplitude sensitivity for fore-aft accelerations	Amplitude sensitivity (1 to 2.5 m/s^2) in fore-aft accelerations at a fixed frequency of 0.3 Hz; internal vision; active neck stabilization	Irmak et al. (2022)
Frequency sensitivity for pitch oscillations	Frequency sensitivity for pitch oscillations (0.025 to 4 Hz) at a fixed amplitude of 8˚; internal vision; active trunk and head stabilization	Howarth and Griffin (2003)
Frequency sensitivity for pitch oscillations	Frequency sensitivity (0.01 to 1 Hz) with varying amplitudes (2 to 22˚) for pitch oscillations	No experiment data available
Real-World Sickening Drive	Car driving with 0.2 Hz, 0.4 g slalom with braking and turning	Irmak et al. (2020)
Perception Experiments		
Earth Vertical Axis Rotation (EVAR)	Yaw angular velocity perception during EVAR at 30˚/s	Vingerhoets et al. (2006); Waespe and Henn (1977)
Off Vertical Axis Rotation (OVAR)	Yaw angular velocity perception during OVAR with 10˚ head roll	Vingerhoets et al. (2006)
Somatogravic Illusion	Pitch perception during constant acceleration of 4 m/s^2	Correia Grácio et al. (2013)
Centrifuge	Roll-tilt perception during centrifuge at 250˚/s	Merfeld et al. (2001)
Pseudo-Coriolis	Angular velocity, pitch angle, and roll angle perception during a Coriolis stimulation at 138˚/s with 45˚ head tilt	No experimental data available. Using data as mentioned in Newman (2009)

3.3 Results

3.3.1 Motion Sickness Frequency Sensitivity Analysis

Sickness with Head Translation

Figure 3.4 shows the frequency and amplitude sensitivity with sinusoidal translational head acceleration without vision (i.e., vestibular inputs only). For pure translation in the SVC models, identical results are obtained when the direction of acceleration is along the longitudinal (fore-aft), lateral (left-right), or vertical (up-down) axis. On the other hand, the MSOM has an identical response, conflict increasing with frequency, with longitudinal (fore-aft) and lateral (left-right) acceleration, but conflict does not depend on the frequency with vertical (up-down) acceleration.

It can be observed in Figure 3.4 that the peak conflict occurs around 0.16 Hz for the SVC-based models, which is consistent with experimental observations of McCauley et al. (1976) for vertical accelerations, as shown in figure 3.4e. In McCauley et al. (1976)'s experiments, participants had to keep their eyes open, which is analogous to our 'Internal vision' condition. Still, in Fig. 4 we have compared this experiment data to the modeled 'No vision' condition. We have done this for consistency with previous work, e.g. Kamiji et al. (2007), on benchmarking purely vestibular motion sickness models. Furthermore, currently no comprehensive 'Internal vision' dataset comparable to the McCauley et al. (1976) dataset is available. We show this comparison only to verify our implementation of the models.

While similar comprehensive data is not available for horizontal motion, still some data with either frequency or acceleration fixed is available as a reference. For longitudinal (fore-aft) motion, Irmak et al. (2020) have used motion perturbations at a peak acceleration of 2 m/s^2 and frequencies of 0.15, 0.2, 0.3, 0.4, and 0.5 Hz to measure motion sickness measured in terms of the MIsery SCale (MISC). Also, Irmak et al. (2022) have conducted experiments at a fixed frequency of 0.3 Hz and varying amplitudes of 1.0, 1.5, 2.0 and 2.5 m/s^2 to collect MISC ratings. Furthermore, Golding and Markey (1996) and Golding et al. (1997) have perturbed subjects with lateral motion with a peak acceleration of 3.6 m/s^2 and frequencies of 0.2, 0.35, 0.5, 0.7 and 1.0 Hz. A direct comparison of the data from these studies (black lines) with our model simulations (colored lines) is shown in figure 3.5.

It is interesting to note that the group-averaged results (figure 3.5d and figure 3.5a) are close to the integrated conflict from the simulations of the SVC-based models, while at an individual level (figure 3.5b, transparent lines) the differences can still be very large. It is to be noted that the SVC$_I$ and SVC$_{NI}$ model parameters are tuned by Kamiji et al. (2007) using data for vertical accelerations from McCauley et al. (1976), and hence may not hold true for other directions (Kamiji et al., 2007). It should be noted that all figures show the normalized conflict (normalized for each figure, not on the whole) to easily compare different models. Hence, we show the ability of the models to reproduce relative trends between conditions as a function of motion frequency and amplitude, and as a function of visual condition.

Figure 3.6 shows the effect of vision on the frequency and amplitude sensitivity with fore-aft sinusoidal accelerations for the compared models. In the left column (No Vision) the

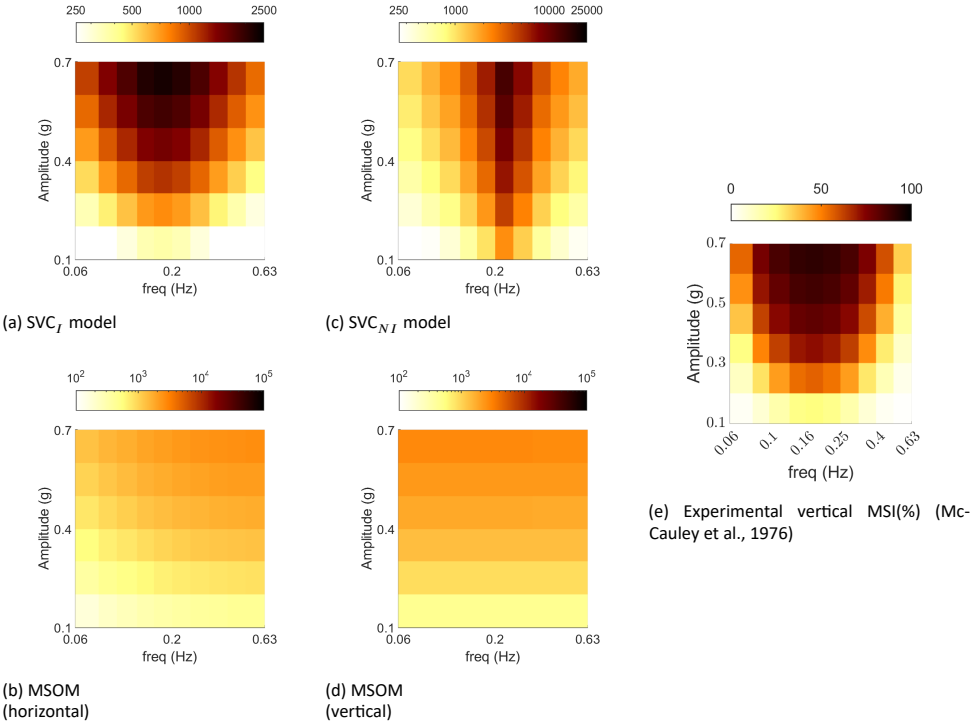

(a) SVC_I model

(c) SVC_{NI} model

(e) Experimental vertical MSI(%) (McCauley et al., 1976)

(b) MSOM (horizontal)

(d) MSOM (vertical)

Figure 3.4: Frequency (horizontal axis) and amplitude (vertical axis) sickness sensitivity in linear acceleration without vision. Comparison of experimentally observed MSI (%) with accumulated conflict (m/s^2) from simulations of SVC_I, SVC_{NI}, and MSOM models. (Conflicts for SVC models are the same in horizontal and vertical motion)

'VR' and 'VV' loops are disabled and hence do not affect the results. Vision loops as implemented with *visual rotational velocity* ('VR') in the SVC_I, SVC_{NI}, and MSOM models do not affect the perception of fore-aft accelerations and hence have no effect on the development of motion sickness when subjected to purely translational accelerations (see 'VR' models in figure 3.6). However, when the *visual vertical* ('VV') loop is active, the responses differ from the 'no vision' case in particular at the lower frequencies. In the absence of rotations, the *visual vertical* remains unchanged (i.e., upright) which is expected to counteract the somatogravic illusion. However, this effect is only observed in the MSOM and not for the SVC models (see section 3.3.3). Nonetheless, the *visual vertical* does cause a shift in the peak frequency of conflict to lower frequencies in the SVC models, with both 'internal' and 'external' vision. However, in the MSOM, which shows a limited effect of stimulus frequency on conflict without vision or with VR, adding the VV loop causes the effects of frequency on conflict to become marginal (figure 3.6). None of the models show any conflict in the 'only vision' case. All models with *visual vertical* input are sensitive to vision during pure translations. The influence of vision in pure translation motion in humans is not substantial, as observed by Butler and Griffin (2006), where no significant change in motion sickness was observed during pure sinusoidal fore-aft motion under various vision

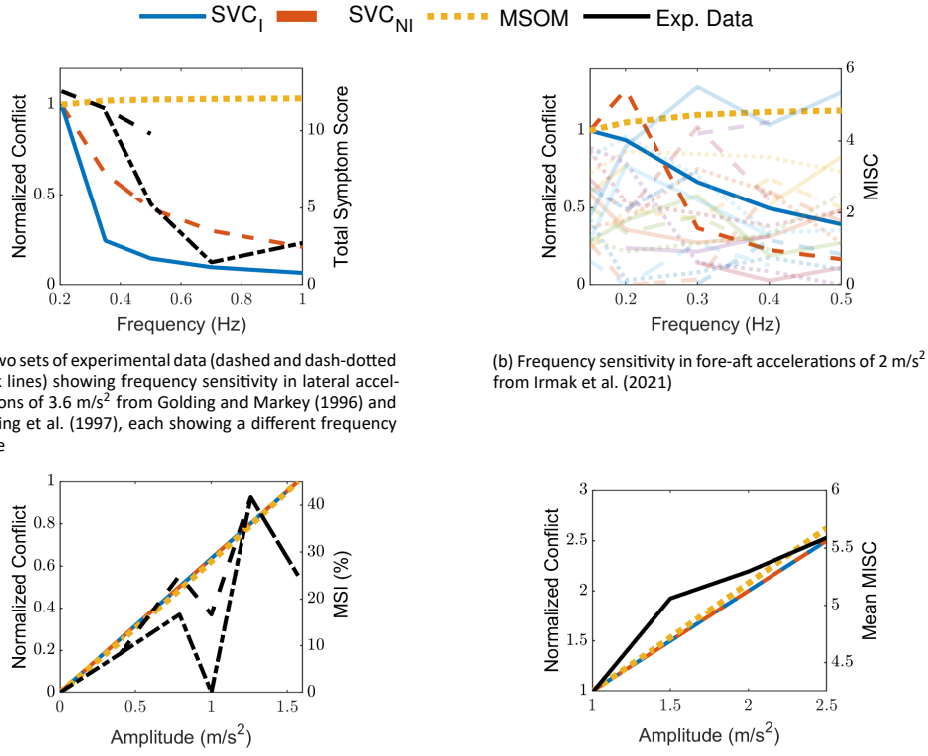

(a) Two sets of experimental data (dashed and dash-dotted black lines) showing frequency sensitivity in lateral accelerations of 3.6 m/s^2 from Golding and Markey (1996) and Golding et al. (1997), each showing a different frequency range

(b) Frequency sensitivity in fore-aft accelerations of 2 m/s^2 from Irmak et al. (2021)

(c) Amplitude sensitivity in longitudinal and lateral accelerations of 0.315 Hz from Griffin and Mills (2002b)

(d) Amplitude sensitivity in fore-aft accelerations of 0.3 Hz from Irmak et al. (2022)

Figure 3.5: Model predictions of frequency and amplitude sensitivity of motion Sickness for linear acceleration without vision. Data from various literature sources plotted for the group in black (in different line styles if there are multiple sets of data) (a,c,d) or individuals in various colors with transparency (b)

circumstances. Therefore, we conclude that the SVC models with *visual rotational velocity* ('VR') more closely replicate motion sickness during pure translation in response to changes in visual conditions.

Sickness with Head Rotation

Pure head pitch or roll rotations can result in equivalent changes in the subjective vertical orientation as those that result from linear horizontal (fore-aft or left-right) accelerations. To compare the effects of rotational inputs in the different models, the predicted frequency sensitivity of motion sickness with varying vision conditions is shown in figure 3.7. The responses to pitch and roll in all models are identical due to identical parameters for these two DOFs. It is to be noted that yaw rotations do not affect the perception of verticality by the vestibular system in these models and hence will have an entirely different response, which is addressed later in this section.

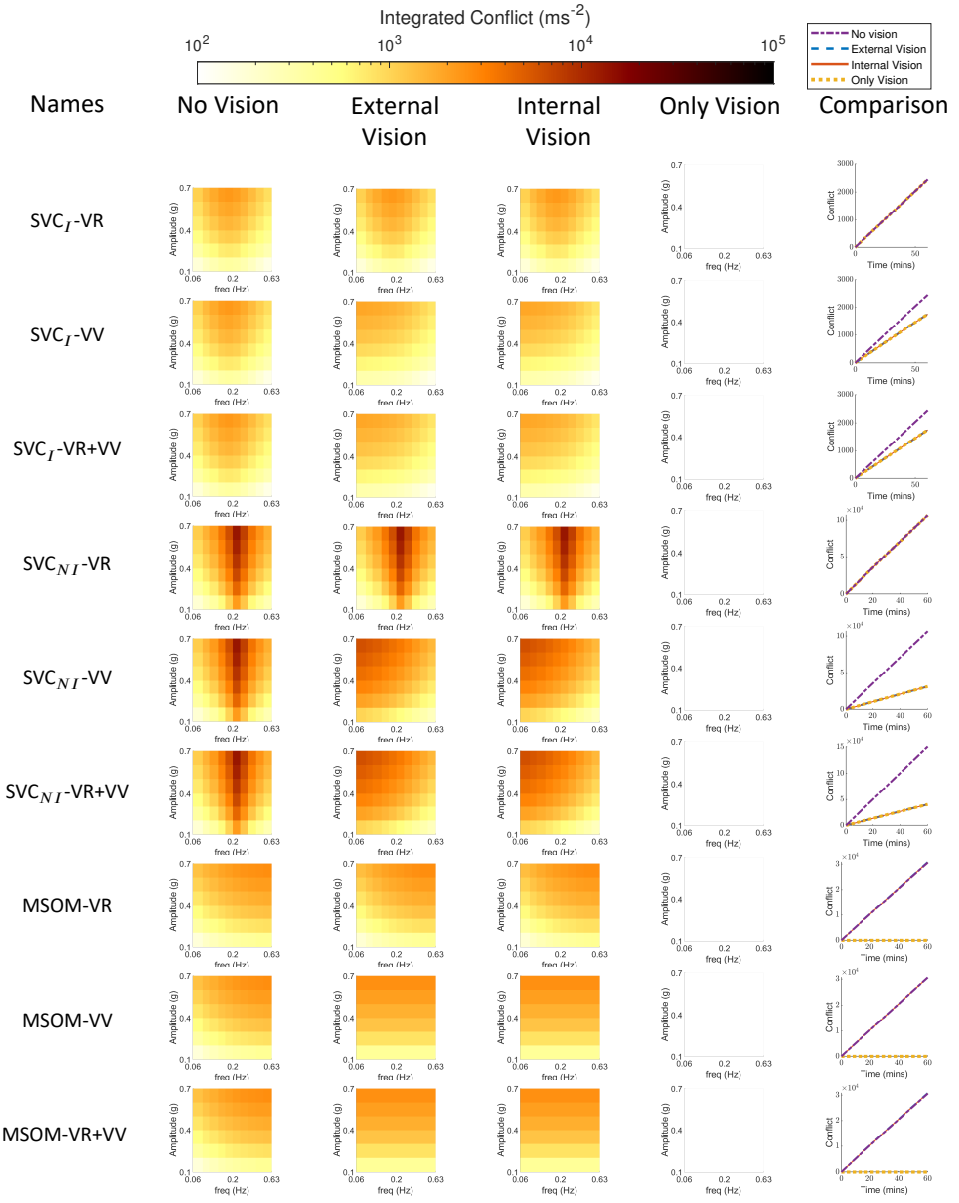

Figure 3.6: Frequency sensitivity of integrated conflict (m/s) with sinusoidal fore-aft motion for different vision conditions: 'no vision' (eyes closed), 'external vision' (eyes open and with outside view), 'internal vision' (eyes open and without outside view), 'only vision' (no motion) and comparison of vision cases at 0.2 Hz and 0.7 g fore-aft motion for SVC_I, SVC_{NI} and MSOM (Plots for the 'no vision' case are the same as in figure 3.4)

The effect of vision on conflicts in rotation shown in figure 3.7 is much stronger compared to the effect of vision in translation shown in figure 3.6. This difference is due to the nature of the vision inputs: they are assumed zero for the translation case, but non-zero and sinusoidal for the rotation case, which amplifies the effect of vision during rotations. It can be observed that the presence of 'external vision' results in a reduction in conflict as compared to the 'no vision' case for six out of nine models, which is in line with experimental results of Wada et al. (2020), Wada and Yoshida (2016) and Griffin and Newman (2004). This is followed by 'only vision', and lastly 'internal vision' in the SVC_I-VR and SVC_{NI}-VR models. The 'internal vision' case shows the largest conflicts across all models. This is due to the contradicting signals between the visual and the vestibular sensors. One thing that is common among all plots of SVC_I and SVC_{NI} models is that the peak conflict frequency is at 0.2 Hz. This peak conflict frequency is the same as the peak motion sickness frequency observed by O'Hanlon and McCauley (1974) in vertical motion in ships. This is achieved by careful tuning of parameters by Inoue et al. (2023); Liu et al. (2022); Wada et al. (2020) and further verified in Appendix B.1 where it was found that the parameters as reported in Inoue et al. (2023); Liu et al. (2022); Wada et al. (2020) are optimal for imitating frequency dynamics of motion sickness. The MSOM, however, has very different frequency dynamics that predict increased sickness with higher stimulus frequencies for the 'no vision' and 'external vision' cases in the MSOM-VV and MSOM-VR+VV. For the 'internal vision' and 'only vision' cases, the same models show a frequency sensitivity that is invariant with frequency. As a clear peak sensitivity frequency is lacking, both these results are in disagreement with available experiment data. This is due to the selection of otolith conflict as the best proxy for motion sickness, by Irmak et al. (2023). This choice may not be suitable for predicting motion sickness in conditions with vision, which Irmak et al. (2023) did not investigate. This has been further discussed in sections 3.4.1 and 3.4.2.

The simulation results in figure 3.7 can, however, only be partially verified, as published data is lacking on motion sickness frequency and amplitude sensitivity in rotational motion paradigms. The most closely related data is from Howarth and Griffin (2003), where motion sickness during roll motion was evaluated at frequencies of 0.025, 0.05, 0.1, 0.2, and 0.4 Hz and a peak amplitude of 8°. The experiment data and the results from the model simulations are shown in figure 3.8. Even though the frequency of 0.2 Hz had the highest number of people reaching an illness rating (IR) of 2 and above, no significant effect of frequency was found by Howarth and Griffin (2003). The peak conflict frequency observed in our simulations in the SVC_I and SVC_{NI} model simulations are 0.2 Hz as well. However, the drop in sickness is much steeper in the models than in the data from Howarth and Griffin (2003). The MSOM, on the other hand, shows a response more like a high-pass filter, which is very different from the SVC models and the experiment data.

In addition to the results in figures 3.7 and 3.8, the conflicts with pitch motion are compared to linear accelerations providing an identical horizontal component of the specific force. These have been shown in figure 3.9. The expected result is a smaller conflict for pitch motion than for linear accelerations (Howarth and Griffin, 2003), even though pitch angles of 5.74 to 44.43° correspond directly to longitudinal specific forces of 0.1 g to 0.7 g. In SVC_I and SVC_{NI} models, the peak conflict frequency has shifted from 0.16 Hz to 0.2 Hz, with no difference in conflict magnitude for the SVC_I model and the SVC_{NI} model. In

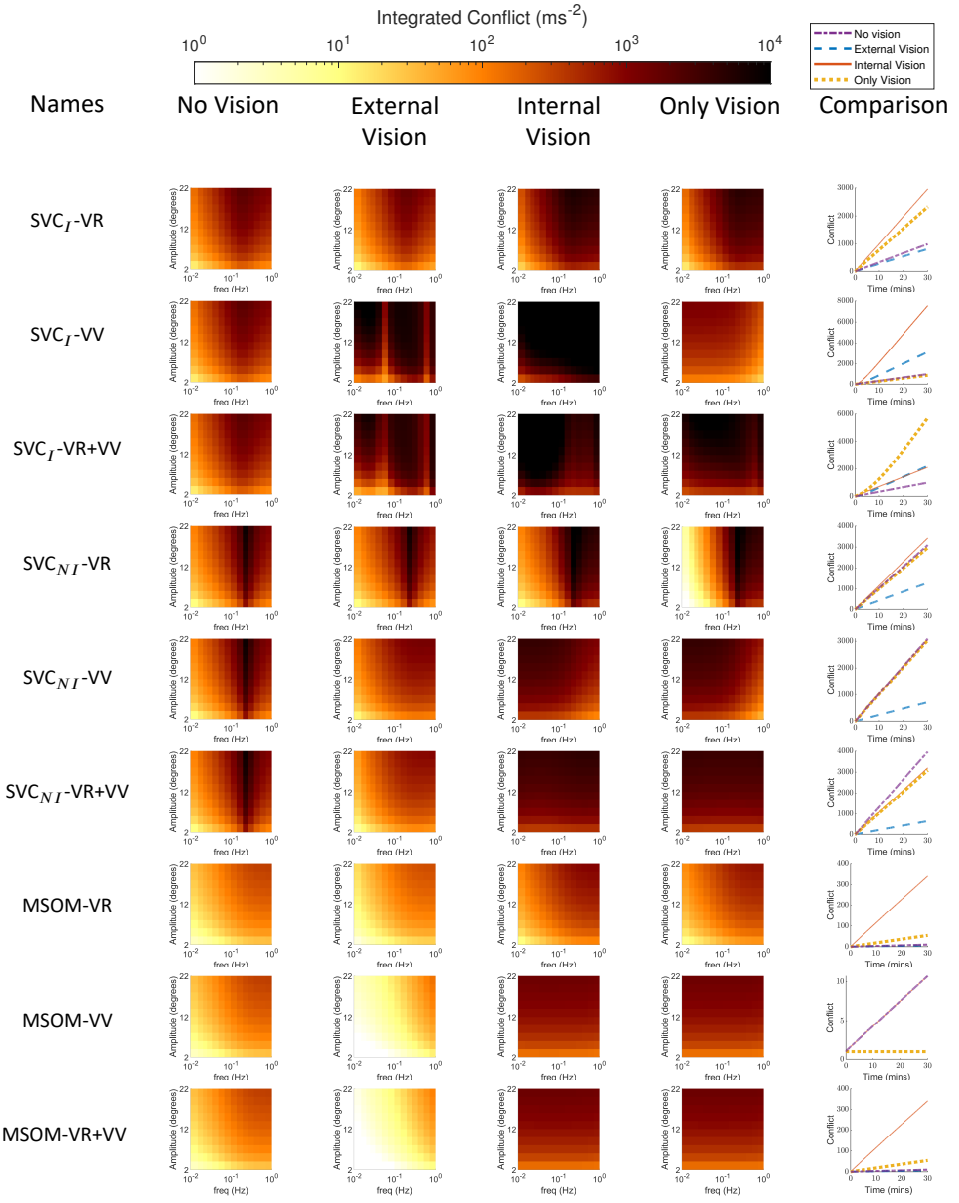

Figure 3.7: Frequency sensitivity of integrated conflict (m/s) with sinusoidal pitch motion for different vision conditions: 'no vision' (eyes closed), 'external vision' (eyes open and with outside view), 'internal vision' (eyes open and without outside view), 'only vision' (no motion) and comparison of vision cases at 0.2 Hz and 20˚ pitch motion for SVC$_I$, SVC$_{NI}$ and MSOM

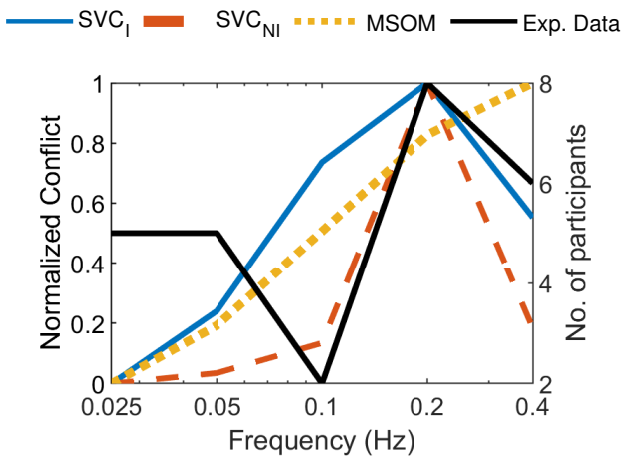

Figure 3.8: Model predictions of the frequency sensitivity for sinusoidal roll motion with an amplitude of 8˚ with eyes closed ('no vision' case) compared with experimental data from Howarth and Griffin (2003) showing the number of participants (out of 20) who reached an illness rating of 2

MSOM, there is an increase (over 2 times) in conflict magnitude for the pitch input at low frequencies. This is because the otolith conflict, used as a proxy for motion sickness, has a low sensitivity to rotations. This makes the MSOM, while using the otolith conflict as a proxy for motion sickness, unsuitable for motion sickness predictions in cases with high rotational velocities, like in vehicles. Experimental data with motion sickness at various frequencies and amplitudes are not available to verify the predicted difference in conflict magnitude.

A very important assumption in the Subjective Vertical model by Bos and Bles (1998) and all SVC-based models tested in this paper, is that motion sickness occurs due to a conflict in the perceived and expected vertical (both direction and magnitude). As pure yaw rotations will not affect the perception of verticality, no conflict and subsequently motion sickness accumulation will be predicted by SVC-based models. The same is true for the MSOM, as the otolith conflict is only affected when the orientation vector is altered, which is not the case during pure yaw rotations. To verify this, all models were simulated for pure yaw motion, and the results showed that no conflict was predicted in any of the vision conditions, as expected, see Appendix B.2. However, this predicted absence of motion sickness during yaw motion is in contradiction with Golding et al. (2009), where 9 out of 12 participants reached a sickness rating of 2 while being earth vertical, and a larger sickness when the visual stimulus was tilted. A potential explanation is that perfect verticality is impossible to achieve experimentally, e.g., due to other motions such as misalignment of the head with the axis of rotation. To explore this, and to investigate the effect of visual feedback, we simulated yaw motion with a constant pitch attitude of 10˚ for all models and vision conditions.

Figure 3.10 shows that a slight pitch attitude indeed results in substantial conflict in the 'no vision' condition, as expected based on Golding et al. (2009). In the model predictions, the

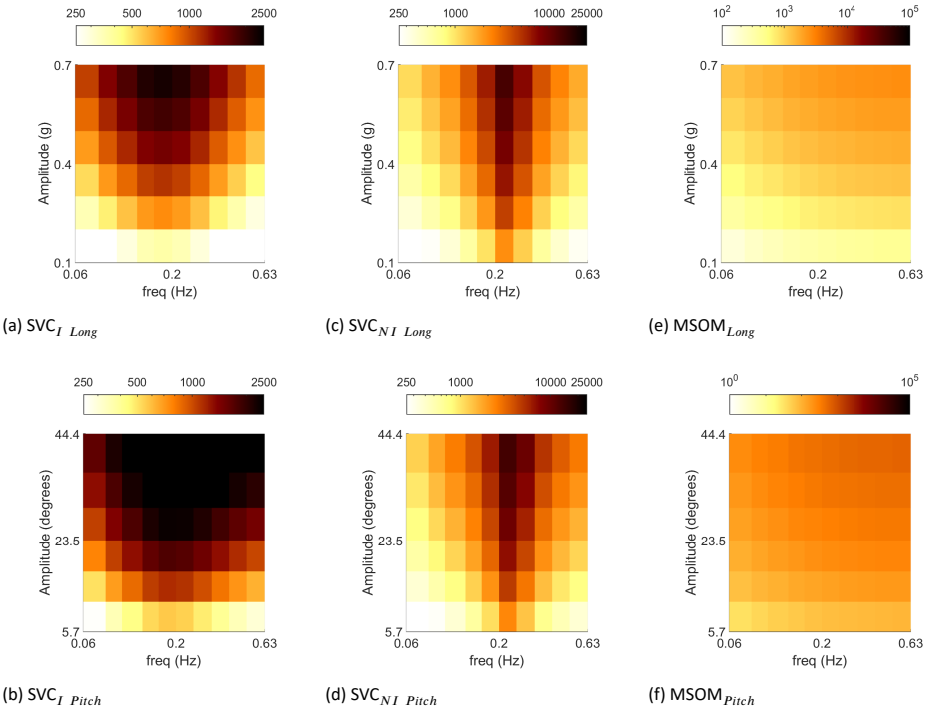

(a) SVC$_{I\ Long}$ (c) SVC$_{NI\ Long}$ (e) MSOM$_{Long}$

(b) SVC$_{I\ Pitch}$ (d) SVC$_{NI\ Pitch}$ (f) MSOM$_{Pitch}$

Figure 3.9: Integrated conflict (m/s) with pitch motion for pitch angles, of 5.74 to 44.43° (bottom row), are compared to linear accelerations, of 0.1 to 0.7 g's (top row, also shown in figure 3.6 with a different scale), providing an identical horizontal component of the specific force

highest conflict is found in 'internal vision' case, as expected due to the substantial disparity between visual and vestibular inputs. Unexpectedly some conditions show a constant conflict being invariant with frequency and amplitude of the applied yaw motion. In these cases the conflict depended only on the applied constant pitch. This applies to 'internal vision' and 'only vision' conditions for models with a 'VV' loop. This result indicating conflict in static pitch with sinusoidal yaw motion is not in agreement with experimental data. This effect occurs due to the constant conflict between the visual and vestibular estimates, a consequence of their constant inputs. For instance, in the case of 'internal vision,' the vestibular inputs maintain a constant value representing the true specific force following a 10° pitch, while the visual input retains a specific force vector pointing downward ([0, 0, -9.81]). In contrast, in the 'only vision' case, these are reversed. Here the visual input is the true specific force following a 10° pitch and vestibular input is a specific force vector pointing downward ([0, 0, -9.81]). For the case of 'only vision', all three models with visual rotational velocity input show negligible conflict. This is because of the constant pitch with the *visual rotational velocity* loop, which only produces yaw angular velocity conflict. This does not influence the otolith and subjective vertical conflict. It is to be noted that the *visual rotational velocity* loop is only concerned with rotation velocities and does not ac-

count for lateral specific forces, induced due to changes in rotation after each cycle. These, however, are captured by the *visual vertical* feedback loop as explained earlier.

Overall, for yaw motion with a constant pitch of 10°, the MSOM predicts smaller conflicts compared to the SVC$_I$ and SVC$_{NI}$ models with the conflict increasing with frequency. This is again due to the lower sensitivity of the MSOM's otolith conflict to rotations. By interpreting the results, it can be deduced that in yaw motion, the SVC$_I$-VR and SVC$_{NI}$-VR models better match the expected relative sickness incidence for different vision conditions than the MSOM.

3.3.2 Motion Sickness Predictions for Real-World Sickening Drive

Slalom experimental data from Irmak et al. (2020), as introduced in section 3.2.2, was used to verify the accuracy of the models' motion sickness predictions for real-world driving scenarios. This data includes measured head accelerations and rotations that are used as input to the models.

Figure 3.11 shows the integrated subjective vertical conflict generated by all the models for the considered 'external vision', 'internal vision', 'only vision', and 'no vision' cases. For the SVC$_I$ models, conflicts in 'internal vision' and 'only vision' are observed to be lower in the SVC$_I$-VV model, followed by the SVC$_I$-VR model, and the highest in SVC$_I$-VR+VV. This suggests that conflict contributions from the different vision loops are cumulative in the combined SVC$_I$-VR+VV model. For the 'external vision' and 'no vision' cases, the conflict is the same for all three versions of the SVC$_I$ model. This is as expected: in the 'no vision' case, the vision loops do not affect the responses, while for 'external vision' the vision matches the vestibular motion inputs, and conflict is always minimized. In all three versions (i.e., VR, VV, and VR+VV) of the SVC$_I$ model, the 'no vision' and 'external vision' case responses show minimal differences, while the responses of the 'internal vision' case always show the largest conflict. This matches the expected effect of vision on motion sickness. Although the SVC$_I$-VV model correctly predicts the expected order of severity for the other vision cases, it shows the least amount of conflict for the 'only vision' scenario, which is contrary to expectations.

The SVC$_{NI}$ model also predicts that the 'external vision' case is less sickening than the 'internal vision' and 'only vision' cases. However, the 'no vision' case shows, unexpectedly, the largest conflicts of all compared cases. This is due to the increase in the magnitude of acceleration conflicts as a result of removing the integration in the acceleration feedback loop. Hence, the SVC$_{NI}$ sacrifices accuracy in replicating conflicts.

For the MSOM model, figure 3.11 shows that in the 'only vision' case, the predicted levels of motion sickness are low. Conversely, the responses for the other vision conditions are essentially the same. This implies that the main contributor to the otolith conflict in the MSOM is the physical motion perceived by the vestibular system and not the contributions from vision.

From the results of all three models in figure 3.11, the SVC$_I$ models seem best for the prediction of the effect of vision on motion sickness, as the order of severity of the different

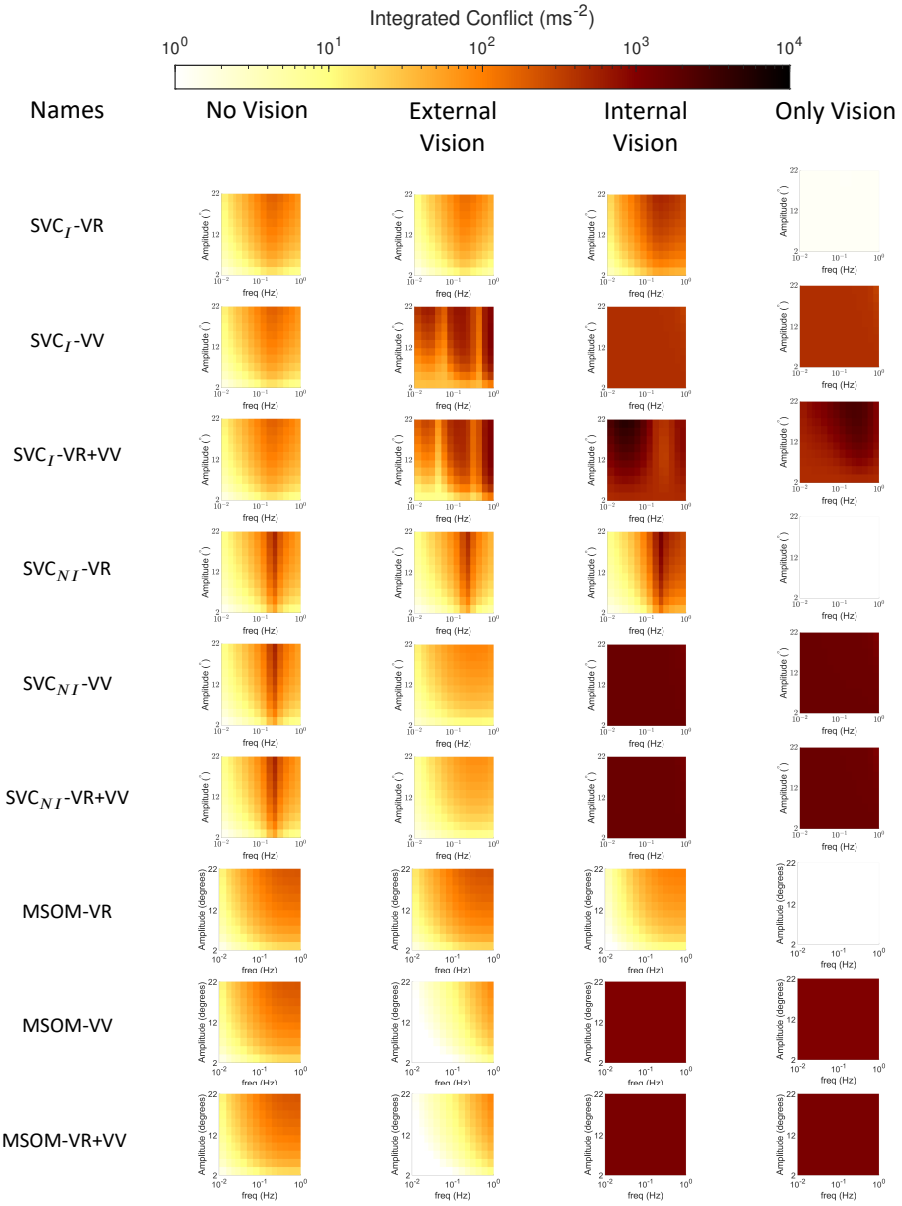

Figure 3.10: Frequency sensitivity of integrated conflict (m/s) with sinusoidal yaw with a constant pitch of 10° for different vision conditions of – 'no vision' (eyes closed), 'external vision' (eyes open and looking out of the car), 'internal vision' (eyes open and on objects inside the car), 'only vision' (no motion) for SVC_I, SVC_{NI} and MSOM

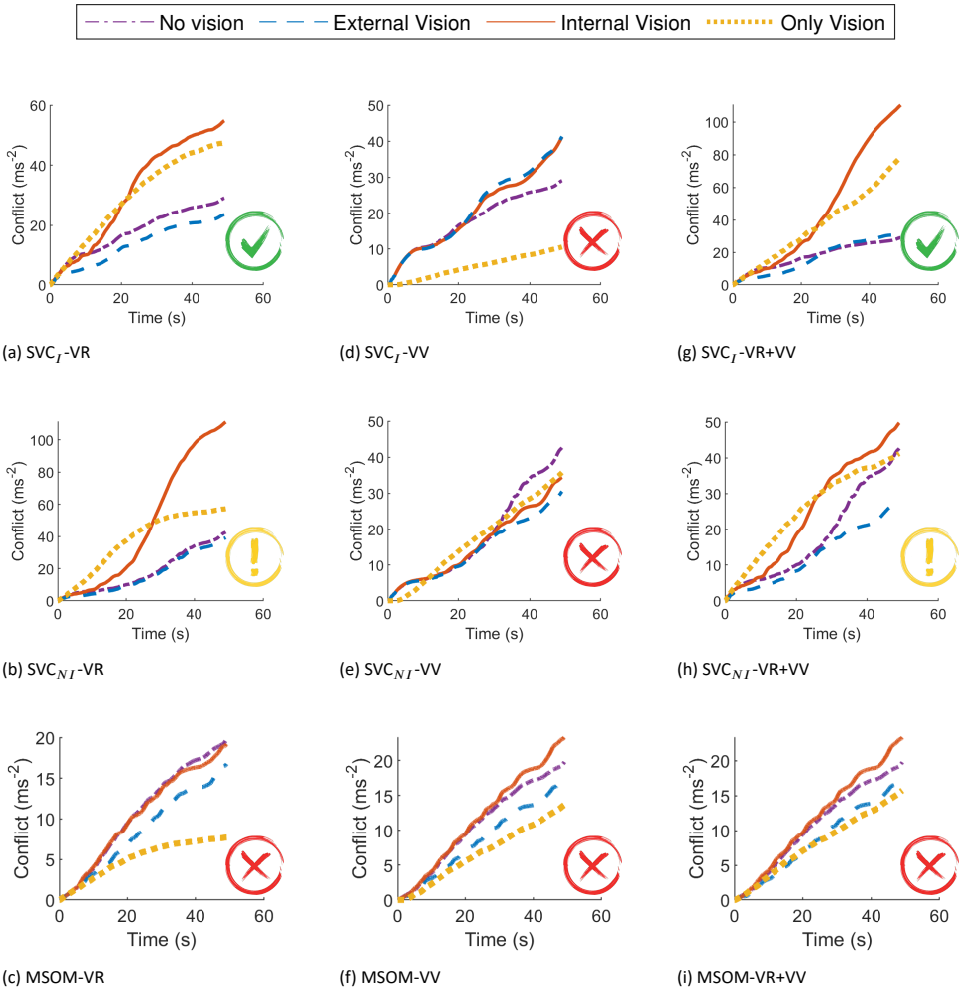

Figure 3.11: Effect of vision on the accumulated conflict (m/s^2) for SVC$_I$, SVC$_{NI}$ and MSOM during slalom drive of 47 s for 'no', 'external', 'internal', and 'only' vision conditions;
Red cross - Incorrect, Yellow Exclamation - Uncertain, Green Tick - Correct order of responses for vision conditions

considered vision conditions matches with expectation. The SVC$_{NI}$ models, however, predict that 'internal vision' is less or about the same sickening as the 'only vision' case, which is contrary to the expected effects. For the MSOM, the otolith conflict term selected by Irmak et al. (2023) as a predictor for motion sickness, is found to be unsuitable for motion sickness simulations with vision, as it does not output the expected order of motion sickness severity of vision conditions in the model's output. These results are consistent with the observations made in section 3.3.1 where the SVC$_I$ model was found to be reliable in replicating sickness results from the literature with a plausible order of severity of vision

conditions.

3.3.3 Motion Perception Paradigm Tests

To further evaluate the realism of the models' simulated perception mechanisms that predict motion sickness, the models' capacity for explaining well-known motion perception responses in fundamental motion perception paradigms, and how the outcomes vary due to the presence of the considered vision loops, was investigated. A summary of the outcomes is shown in table 3.4; the detailed results are discussed per paradigm in the remainder of this section.

Table 3.4: Summary of Motion Perception Test Results;
Red cross - Result in disagreement with literature, Green Tick - Result in agreement with literature, Yellow Exclamation - Some of the results are in agreement with literature

Tests	SVC_I			SVC_{NI}			MSOM		
	VR	VV	VR+VV	VR	VV	VR+VV	VR	VV	VR+VV
EVAR	✓	✗	✓	✓	✗	✓	✓	✗	✓
OVAR	✓	✗	✓	✓	✗	✓	✓	✗	✓
Somatogravic Illusion	✗	✗	✗	✗	!	!	✗	✓	✓
Centrifuge	✗	✗	✗	!	!	!	✓	!	✓
Pseudo Coriolis	✗	✗	✗	✗	✗	!	✓	✗	✓

EVAR (Earth Vertical Axis Rotation) and OVAR (Off-Vertical Axis Rotation) As observed by Waespe and Henn (1977) in monkeys and reproduced here in figure 3.12, it is expected that the perception of rotational velocity in EVAR will converge to a value that approximates the true rotational velocity when vision is active. In the absence of vision, however, the perception of rotation should decay exponentially to zero. Even though similar measured neural responses are not available, the same effects of vision on self-motion perception in EVAR have been observed in humans (e.g., (van der Steen, 1998)). Pure yaw motion, by itself, does not impact the visually perceived orientation relative to gravity. Therefore, in models with *visual vertical* as the sole visual input, the correct prediction of the expected visual effect is not expected. Figure 3.12 shows the models' results for the angular velocity perception, which are similar across all three models because of the similar visual loop implementation. As expected, and consistent with the findings of Waespe and Henn (1977), the models that include a *visual rotational velocity* input ('VR') predict the well-known variation in perceived rotational velocity for the different vision conditions. The models with only *visual vertical* input ('VV') have an identical response for all vision conditions involving

physical motion, i.e., all except 'only vision' for which the models show zero perception of rotational velocity. The models with only *visual vertical* are thus indeed not affected by the vision condition. The model responses are the same as the case with 'no vision' except for the case of 'only vision', which has no response due to the *visual vertical* not registering any yaw rotations. These results show that the models with *visual rotational velocity* ('VR') more realistically model the effect of varying vision conditions in EVAR. This is consistent across all the models including SVC_I, SVC_{NI}, and MSOM.

In OVAR, it is expected, based on the findings of Vingerhoets et al. (2006), that the perception of angular velocity in the dark ('internal vision') will decay exponentially over time. Perception responses for other vision conditions are not available in the literature. The model predictions show that the perception of angular velocity during OVAR is identical to EVAR as in figure 3.12 and are hence not shown.

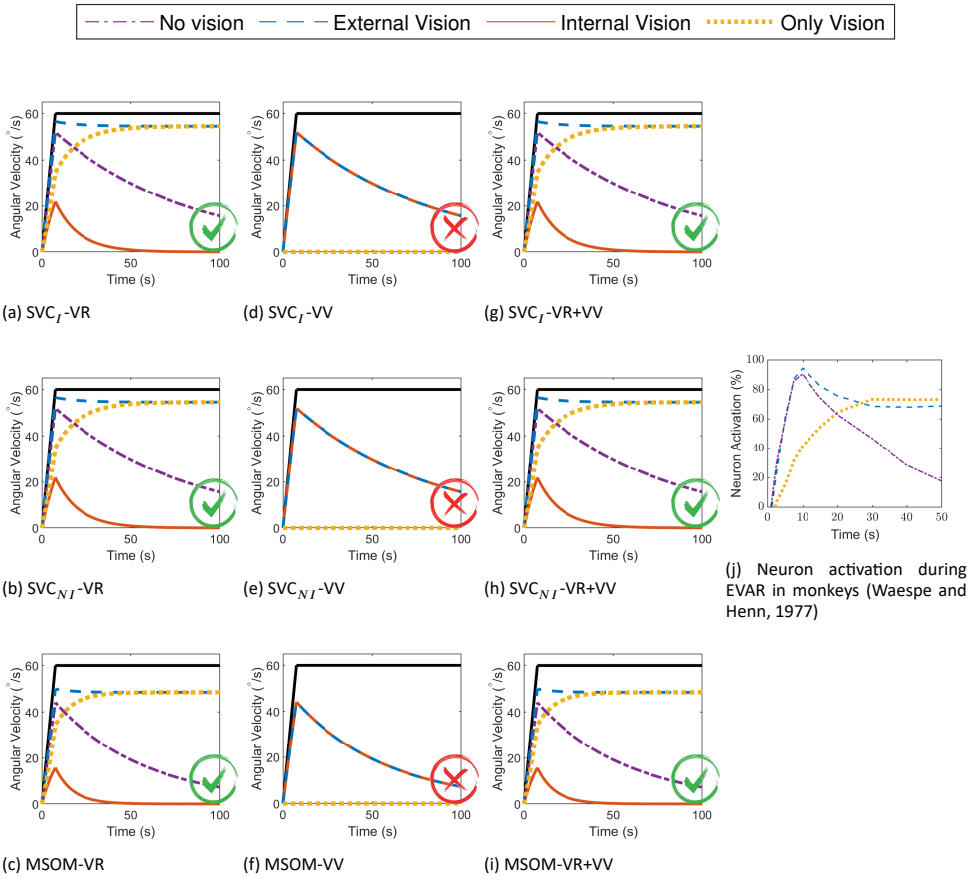

(a) SVC_I-VR (d) SVC_I-VV (g) SVC_I-VR+VV

(b) SVC_{NI}-VR (e) SVC_{NI}-VV (h) SVC_{NI}-VR+VV

(j) Neuron activation during EVAR in monkeys (Waespe and Henn, 1977)

(c) MSOM-VR (f) MSOM-VV (i) MSOM-VR+VV

Figure 3.12: Angular velocity perception during EVAR at 60˚/s;
Red cross - Result in disagreement with literature, Green Tick - Result in agreement with literature.

Somatogravic Illusion The 'somatogravic illusion' is the phenomenon where, in absence of visual cues, low-frequency forward linear accelerations are incorrectly perceived as changes in pitch angle (tilt); lateral accelerations similarly induce a perception of roll. This effect was, for example, observed and quantified in Correia Grácio et al. (2013). Furthermore, Tokumaru et al. (1998) found that the strength of the somatogravic illusion was reduced in the presence of a visible horizon ('external vision'). However, the presence of a vection stimulus ('only vision') did not cause a similar illusory effect. It is expected that this illusion occurs when there is no outside view, i.e. 'internal vision' and 'no vision'. This is an important motion perception test, as somatogravic illusion is known to be closely linked to spatial disorientation (Groen et al., 2022) as well as motion sickness induced by accelerations in the horizontal plane (Irmak et al., 2021; Wood, 2002; Wood et al., 2007).

Figure 3.13 shows the response of the tested models for this paradigm. The lower graphs in each subplot show the input acceleration in bold black, along with perceived linear accelerations in the different vision conditions of 'external vision' (blue), 'internal vision' (red), 'only vision' (yellow), and 'no vision' (purple). The upper graph shows the corresponding perceived pitch angles for the different vision conditions and also the pitch angle corresponding to the gravito-inertial force vector tilt, which is equal to 22.18° for the 4 m/s^2 forward acceleration. Contrary to expectations, figure 3.13 shows that the SVC$_I$ model predicts this illusion to occur for all vision cases, i.e., the responses for all SVC$_{NI}$ models are identical. Furthermore, the SVC$_I$ model also does not show the capability to model this illusion in the presence of vision. Even though adding the *visual vertical* input ('VV') reduces the perception of pitch in the presence of vision, it is still not reduced to zero, which is the expected output. Thus, both visual inputs do not help in the perception of acceleration in SVC-based models. However, the vision input does affect the perception of acceleration in the MSOM with *visual vertical* input. The response of the MSOM-VV is exactly as expected based on existing literature, with the illusion occurring only during the 'no vision' case. This shows, for the first time in our analysis, that the *visual vertical* input positively contributes to predicting human motion perception responses in motion perception models. This is carried forward into the MSOM-VR+VV where the *visual vertical* again helps in capturing this illusion. Thus, the results in figure 3.13 show that only the MSOM with the *visual vertical* input (i.e., MSOM-VV and MSOM-VR+VV) is able to accurately predict the expected variation in the somatogravic illusion due to vision.

Centrifugation When humans are rotated in a centrifuge facing the direction of the local velocity vector in absence of visual cues, they perceive a roll tilt Merfeld et al. (2001). This tilt perception is induced by the constant (lateral) centrifugal force's contribution to the specific force vector perceived with the otoliths, from which humans are unable to differentiate the inertial and gravitational parts. However, in the presence of upright visuals, no roll-tilt is perceived. This well-known suppression of tilt perception is effectively used in moving-base vehicle simulators through tilt-coordination (Berger et al., 2010). Figure 3.14 shows that the different tested models provide a different response for each vision condition. Furthermore, the SVC$_I$ model is found to be unable to predict the expected roll-tilt perception, while the SVC$_{NI}$ (Inoue et al., 2023) does show the expected response for the 'no vision' case. However, in the presence of 'external vision', the responses of the SVC$_{NI}$

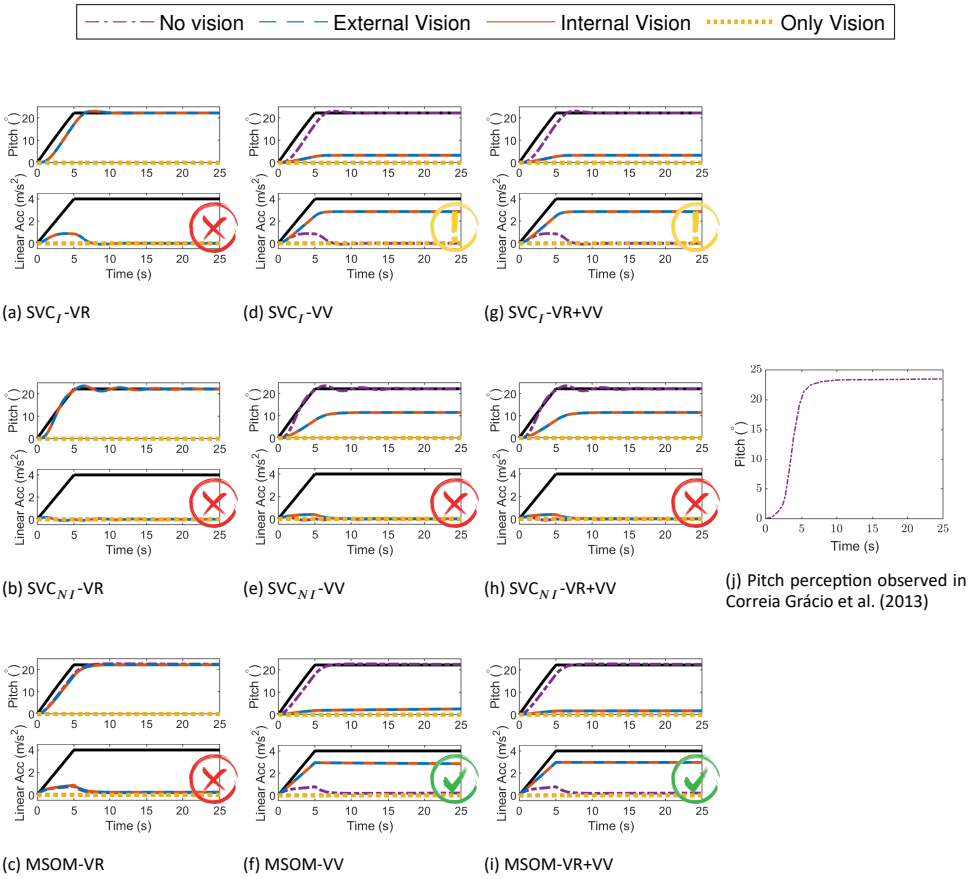

(a) SVC_I-VR (d) SVC_I-VV (g) SVC_I-VR+VV

(b) SVC_{NI}-VR (e) SVC_{NI}-VV (h) SVC_{NI}-VR+VV

(j) Pitch perception observed in Correia Grácio et al. (2013)

(c) MSOM-VR (f) MSOM-VV (i) MSOM-VR+VV

Figure 3.13: Pitch perception during constant acceleration of 4 m/s^2 (somatogravic illusion); For each condition the upper graph shows the perceived pitch and the lower graph the perceived acceleration. Black lines describe the applied acceleration in the lower graph, and the equivalent rotation in the upper graph.
Red cross - Result in disagreement with literature, Green Tick - Result in agreement with literature, Yellow Exclamation - Some of the results are in agreement with literature.

model show a strong perception of roll tilt, which is not the case in real life. The MSOM, on the other hand, is able to simulate all vision cases accurately, showing no roll tilt for the perception for the 'external vision' and 'only vision' cases, but the expected tilt for the 'internal vision' and 'no vision' cases. The only exception is the MSOM with only *visual vertical* (MSOM-VV), which does not predict tilt perception for 'internal vision'. Thus, only the MSOM with *visual rotational velocity* (MSOM-VR and MSOM-VR+VV) is able to accurately capture the effect of roll tilt perception in a centrifuge paradigm.

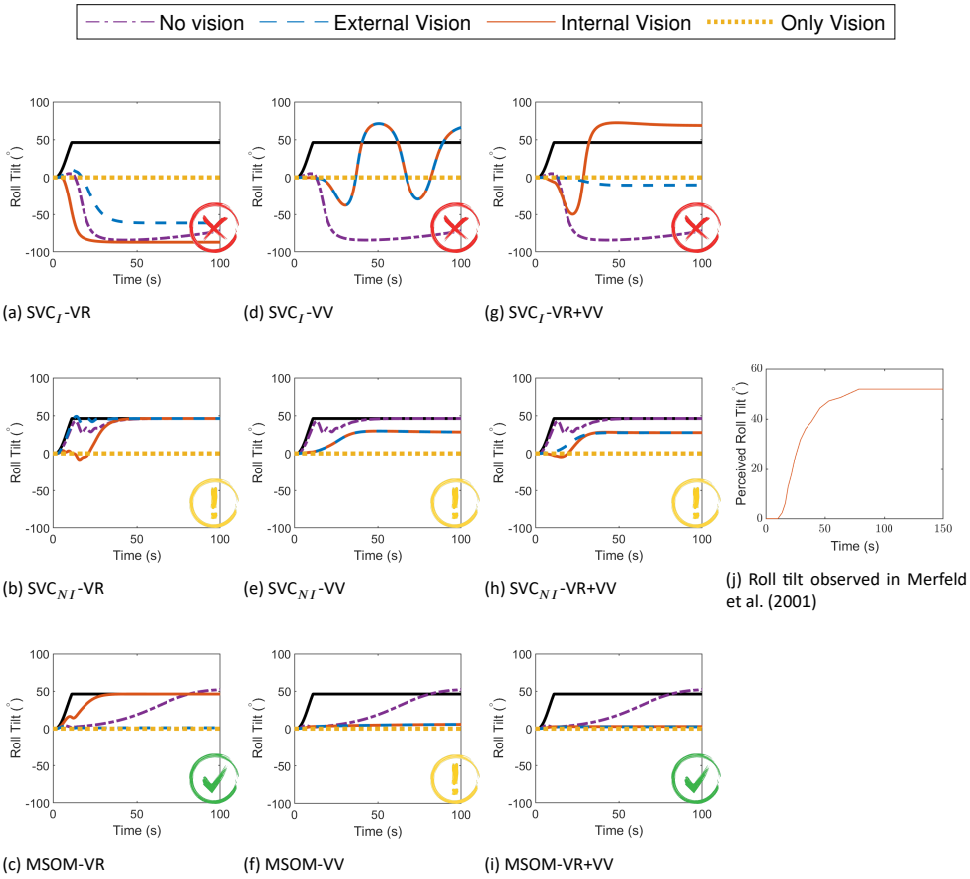

(a) SVC$_I$-VR (d) SVC$_I$-VV (g) SVC$_I$-VR+VV

(b) SVC$_{NI}$-VR (e) SVC$_{NI}$-VV (h) SVC$_{NI}$-VR+VV

(j) Roll tilt observed in Merfeld et al. (2001)

(c) MSOM-VR (f) MSOM-VV (i) MSOM-VR+VV

Figure 3.14: Roll-tilt perception during centrifuge at 250°/s; The black lines describe the applied motion translated to an equivalent tilt angle.
Red cross - Result in disagreement with literature, Green Tick - Result in agreement with literature, Yellow Exclamation - Some of the results are in agreement with literature.

Pseudo-Coriolis The pseudo-Coriolis perception paradigm (Dichgans and Brandt, 2009) is elicited by tilting the head out of the axis of rotation of a circular moving surrounding visual. This tilting of the head elicits a stimulus in the third (unexcited) axis of rotation. The resulting sensation is identical to that which arises during actual rotating motions (i.e., Coriolis). Figure 3.15 shows that only the MSOM model with *visual rotational velocity* (MSOM-VR and MSOM-VR+VV) is able to capture the excitation of the third rotational axis, shown by the pitch angle and pitch velocity perception. The models with *visual vertical* (SVC$_I$-VV, SVC$_{NI}$-VV, and MSOM-VV) are seen to be insensitive to the visual yaw rotation, as this motion is not captured by the model's inputs: the *visual vertical* input is unaffected by yaw rotations and even when there is a head tilt, there may be roll angle perception, but there is no roll or pitch velocity perceived by the model. The SVC$_I$ models with visual rotational

velocity inputs (*visual rotational velocity*) do show pitch responses, but the perceived rotation angles do not return to zero after the end of the stimulus, which is unrealistic. The SVC_{NI} model, on the other hand, does show a response to the stimulus and convergence back to zero, however, the responses are oscillatory with 'VV' active. Figure 3.15 shows that a visual rotational velocity input is required for predicting human motion perception during the pseudo-Coriolis paradigm. However, there is no literature with continuous measurement of the perceived pitch rotation angle or rotational velocity during pseudo-Coriolis to validate these model responses.

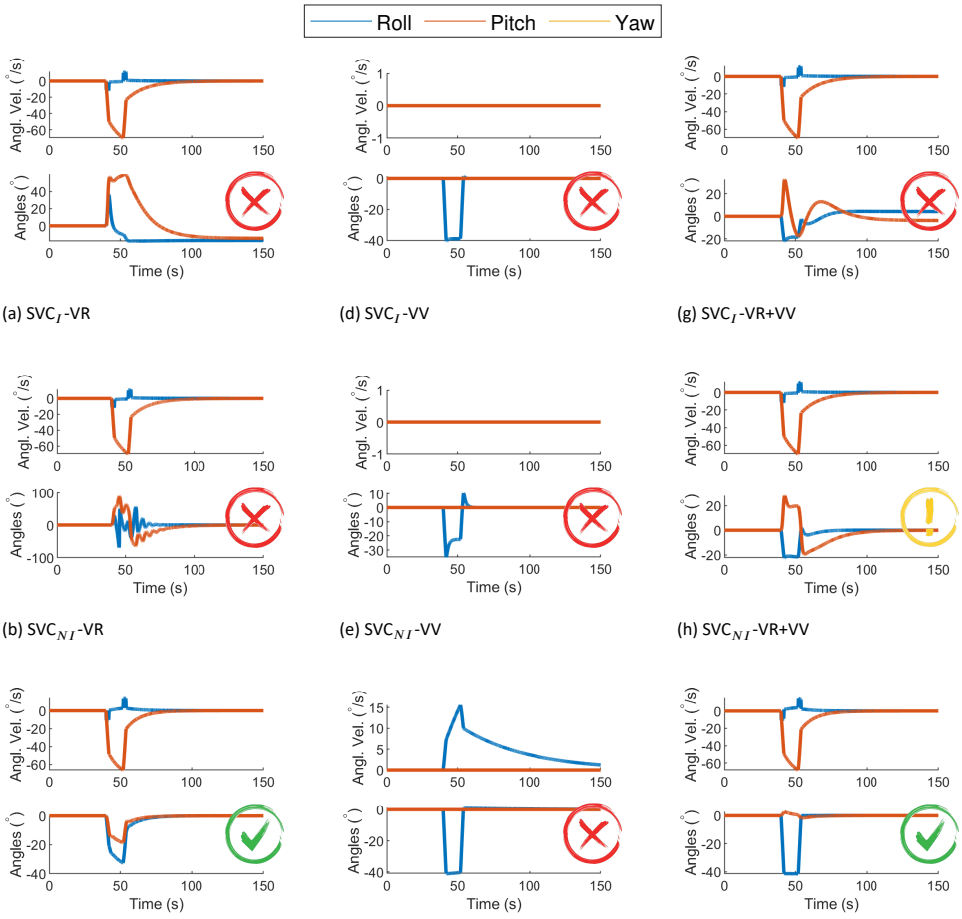

(a) SVC_I-VR (d) SVC_I-VV (g) SVC_I-VR+VV

(b) SVC_{NI}-VR (e) SVC_{NI}-VV (h) SVC_{NI}-VR+VV

(c) MSOM-VR (f) MSOM-VV (i) MSOM-VR+VV

Figure 3.15: Angular velocity, pitch angle, and roll angle perception during Pseudo Coriolis stimulation at yaw rotation of 138°/s with a stimulus of 45° head tilt applied from 42 to 52 seconds;
Red cross - Result in disagreement with literature, Green Tick - Result in agreement with literature, Yellow Exclamation - Some of the results are in agreement with literature.

3.4 Discussion

For the first time, the implementation of the effects of vision in state-of-the-art motion sickness and motion perception models was broadly validated. Vision loops were selectively disabled or enabled to compare the models' responses to various stimuli. These included the well-known frequency sensitivity of motion sickness, sickness in a slalom drive, and perception responses in fundamental motion paradigms. Of the nine tested model variants, none was able to reproduce all experimental sickness and perception results. All models showed (some) realistic effects of vision, but all were unable to reproduce at least one experimental finding. Overall, the SVC best matched the experimental motion sickness data, whereas the MSOM showed the best match for motion perception. In the following, findings will be discussed and recommendations will be formulated on the most critical and promising model structures for simulating motion perception and motion sickness.

In this paper, the models were validated using the parameters reported in their respective publications. While enhancing modeling accuracy through parameter optimization was possible, it falls beyond the paper's scope. For simplicity in comparing the VV and VR loops in the SVC and MSOM models, we utilized the models' original published forms and parameters. Consequently, these results should not be generalized to SVC or MSOM models with different parameters. However, while adhering to these defined parameters, we have achieved meaningful insights and valuable findings in this context.

3.4.1 Motion Sickness Frequency Sensitivity

Comparing the frequency and amplitude sensitivity of motion sickness incidence in the vertical direction, from McCauley et al. (1976), to the conflict predictions from motion sickness and motion perception models (SVC_I, SVC_{NI}, and MSOM), it is observed that the SVC_I and SVC_{NI} accurately capture the frequency and amplitude dynamics. In its current published form (Clark et al., 2019; Newman, 2009) and with the acceleration conflict used as a proxy for motion sickness Irmak et al. (2023), the MSOM cannot capture this frequency dynamics and predicts no frequency dependency of conflict in the vertical direction due to the choice of the otolith conflict as an indicator of motion sickness, which is not affected by purely vertical accelerations.

Visual cues are implemented in two ways: *visual rotational velocity* ('VR') and *visual vertical* ('VV'). The sensitivity of the predicted conflicts to the gains of each visual loop in the three models was also tested, see Appendix B.1. The results show that the gains reported by the respective authors are optimal for sickness simulations. To analyze the effects of vision, frequency sensitivity analysis during pitch and fore-aft motion was carried out. A small effect of vision on the conflicts due to translation was observed (see Figure 3.6). However, a large effect of vision on the conflicts due to rotations was observed (see figure 3.7). It was observed that only the SVC models with *visual rotational velocity* (namely, SVC_I-VR and SVC_{NI}-VR) are able to accurately model the sickness severity of various vision conditions relative to each other (from most severe to least severe - 'internal vision', 'only vision', 'no vision' and 'external vision' (Griffin and Newman, 2004; Irmak et al., 2020; Wada and

Yoshida, 2016)). The MSOM, though models the order of vision severity correctly, produces low levels of conflict during pitch motion as compared to SVC models. The peak conflict frequency in the MSOM during pitch motion, around 1Hz, remains unchanged when vision loops are added. Also, in for-aft motion, the peak conflict frequency is around 1Hz, but this changes in the case of *visual vertical* loop is added. Nonetheless, the peak frequency of 1Hz is very different from what is found in the literature (see figure 3.4e). This may be due to the inherent frequency sensitivity of the conflict term used. Using other conflict terms also does not aid in improving the frequency response of the MSOM (Irmak et al., 2023). This different peak conflict frequency combined with its no sensitivity to vertical accelerations shows that the MSOM is not (yet) suitable for motion sickness simulations.

Unfortunately, to the best of our knowledge, there exists only a single experimental dataset (Howarth and Griffin, 2003) to show the frequency sensitivity of motion sickness with rotations. Hence, it is difficult to conclude with certainty which of the models is accurate. Hence, there is a need to plan and carry out experiments to capture the frequency sensitivity with varying pitch/roll angular velocities. Along with this, motion sickness data at different cases of visual stimuli ('external', 'internal', 'no', and 'only' vision) need to be investigated to better understand the effect of vision and verify the effects of vision on frequency sensitivity of motion sickness as predicted by figures 3.4 to 3.9.

Another important conclusion is that none of the models, the SVC_I, SVC_{NI}, and MSOM, show any conflict in vertical due to pure yaw rotations. While there may be conflict generated between perceived and estimated rotational velocities, this is not used for motion sickness predictions. However, this contradicts the finding of Golding et al. (2009), who showed that while being earth vertical and with optokinetic stimulation, motion sickness is still observed during yaw motion: 9 out of 12 participants reached a sickness rating of 2. There's a possibility that some degree of head tilt occurred, leading to an imperfect alignment with the rotation axis, as mentioned in Bos et al. (2008). However, if this were the case, we would expect a significant increase in motion sickness scores when the tilt is introduced, which is not observed in Golding et al. (2009). Another plausible explanation is the presence of inherent irregularities or asymmetry in the vestibular organs, potentially causing motion sickness during pure yaw motion. Nevertheless, it's reasonable to assume that the human brain habituates to such irregularities, updates an internal model to account for the affected vestibular organs, and compensates for them. It's noteworthy that none of the models considered this adaptation process. Alternatively, it's conceivable that multiple sources of sensory conflict exist, with specific conflicts contributing to motion sickness during yaw motion as in Khalid et al. (2011b). Additionally, it was found that even a small constant pitch of 10˚ during yaw motions can incite substantial levels of motion sickness in all models, as has been also verified by Golding et al. (2009). This was also backed up by the conflict generation in high yaw motions during slalom maneuvers as shown in figure 3.11 and in Appendix B.3.

3.4.2 Motion Sickness in Slalom Drive

Until now these motion sickness and motion perception models were only tested either by using fundamental inputs like a sine wave (Kamiji et al., 2007; Wada et al., 2020) or by real-

world driving data while ignoring the vision loops Wada et al. (2015); Wada and Yoshida (2016); Yunus et al. (2022). In this paper, the ability of the vision loops to differentiate various vision conditions was studied using experimental data by Irmak et al. (2020). It is found that only the SVC$_I$-VR and SVC$_I$-VR+VV models are able to accurately model the varying sickness severity of various vision conditions (from most severe to least severe: 'internal vision', 'only vision', 'no vision', and 'external vision' (Griffin and Newman, 2004; Irmak et al., 2020; Wada and Yoshida, 2016)). The use of only *visual vertical* (SVC$_I$-VV) deteriorates the ability of the SVC$_I$ model by increasing the conflict during the 'external vision' case. Hence, it is necessary for the SVC$_I$ model to have *visual rotational velocity* as an input to capture the effects of vision. The SVC$_{NI}$ models, however, predict an incorrect order of severity of vision conditions. Possibly the parameters need to be further tuned to improve performance in vision conditions as opposed to only in case of 'no vision' as was done in Inoue et al. (2023).

The MSOM does predict sickness in the slalom drive but predicts small any effects of vision. In the MSOM, the otolith conflict term selected by Irmak et al. (2023) is found to be unsuitable for motion sickness prediction with vision, as it does not show the expected sensitivity to vision in the model's output. This choice may not be suitable for predicting motion sickness in conditions with vision, which Irmak et al. (2023) did not investigate. Hence, alternate conflict terms, like a combination with angular velocity conflict, can be considered. This was also recently proposed by Allred and Clark (2024), who used a weighted sum of various conflict terms of MSOM. They found the highest weighting factor for conflict in f_v (GIF in their paper) as compared to conflict in ω and conflict in f_{oto} (a in their paper). However, we expect Δf_{oto} and Δf_v to yield similar results as they derive from the same signals. Allred and Clark (2024) do not explicitly reflect on the consequences for their model's fit when any of these two conflict terms are omitted. Also, they do not make any comparisons with other models, such as the SVC$_I$ model, which our paper shows to have better motion sickness frequency dynamics as compared to the MSOM.

In addition to comparing the effects of vision, the contribution of each degree of freedom to the conflict was investigated (see Appendix B.3). This was done by switching each degree of freedom off and seeing its effect. This revealed important insights. It was observed that the conflict from SVC$_I$ and SVC$_{NI}$ models have a low sensitivity on linear degrees of freedom (translational motion). The MSOM, on the other hand, is highly sensitive to linear degrees of freedom while not so sensitive to rotation degrees of freedom. It was hence concluded that only the SVC$_I$-VR is able to match sickness and how it is affected by vision in this naturalistic driving dataset.

3.4.3 Motion Perception Tests

From the motion perception tests, it is evident that MSOM-VR+VV can predict the effects of vision in all motion paradigms. The *visual rotational velocity* (VR) input is essential for capturing the effects of vision on human motion perception. However, the *visual vertical* (VV) input is only useful during the somatogravic illusion, and only in the MSOM. It is understandable that *visual vertical* will not be of any help during yaw angular velocity perception, as there is no feedback from the *visual vertical* due to no change in verticality. In

SVC-based models, the *visual vertical* is not even able to help in cases of rotation angle or acceleration perception (as in somatogravic illusion (figure 3.13), centrifuge (figure 3.14) and pseudo-Coriolis (figure 3.15)). The *visual vertical* does neither perform well for motion perception tests nor does it aid the *visual rotational velocity* when the combined approach is used in the VR+VV models. This was expected from models based on SVC, as these were not designed for motion perception; rather they were designed with the sole purpose of forecasting motion sickness. In the SVC-based models, there exists feedback from the semicircular canals to the otoliths, but not the other way around. This is the reason that the SVC-based models show only a small perception of pitch during somatogravic illusion in dark ('internal vision'). The MSOM, however, is the best out of all the models, as it accurately predicts all considered perception paradigms. Also, the *visual vertical* loop actually helped in estimating pitch (bringing it down from 22.2˚ to 1.7˚) and acceleration (increasing it from 0 m/s^2 to 2.9 m/s^2) during somatogravic illusion (see figure 3.13). This shows the first evidence of *visual vertical* aiding in the simulations of motion perception in our analysis. This superior performance in motion perception tests as compared to the SVC models was expected, as the MSOM was designed to be a motion perception model and not a motion sickness model like the SVC-based models. This is also supported by Groen et al. (2022), where the MSOM reliably predicted the occurrence of somatogravic illusion in an airplane accident investigation. This advantage in modeling motion perception does not translate into motion sickness simulation, however, for which the MSOM performs poorly.

The SVC$_{NI}$ model was developed with the intention of improving the motion perception quality of the SVC$_I$ (Inoue et al., 2023). However, as seen from the results for the somatogravic illusion and centrifugation paradigms tested in our paper (figures 3.13 and 3.14), the model only showed improvement for the 'no vision' case. When vision loops are introduced, the responses are not accurate. This indicates that there is room to improve the SVC-based models, specifically for the cases with vision. One of the possible solutions is to add feedback from the otoliths to the semicircular canals in the SVC-based models to induce a perception of tilt when accelerated, which the current SVC-based models do not account for.

3.4.4 Individual vs. Group-averaged models

In this paper, the integrated subjective vertical conflict, as predicted by sensory integration models, was used as a proxy for experimental Motion Sickness Incidence (MSI), a key metric for quantifying motion sickness evolution Bos and Bles (1998); McCauley et al. (1976). However, MSI is a group-averaged metric and is not representative of an individual's response. For these models to be used in controlling motion comfort in automated vehicles, MSI is not ideal as it targets the average severity of sickness. MSI could be used to design controllers that output sickness levels for 50% of the users. However, this will ignore users outside the envelope of average susceptibility. Thus, we need models that also predict the lower/higher sickness levels, and capture variations between individuals. Thus, using an individual-specific metric like MIsery Scale (MISC), as proposed by Bos et al. (2010), will help not only solve the aforementioned problem, but also enable an improved understanding of how diverse the model parameters and subsequently the responses to a given stimulus

are. This has already been shown by Irmak et al. (2020), where individual MISC responses were fitted to the Oman (1990) model and confirmed that individual models reduce prediction errors by a factor of 2 as compared to group-based models. This was further improved upon by Kotian et al. (2023) where a combination of SVC$_I$-VR and Oman model greatly increased fitting accuracy in varying vision conditions as well. Hence, we emphasize the importance of using the MISC as a metric in future motion sickness studies. The next step of the modeling will thus be to combine such conflict generation models with visual inputs with a conflict accumulation model to be able to predict an individual's motion sickness level, in terms of a MISC score across varying vision conditions.

3.4.5 Comparison of Models and their Visual loops

Studies from Bos et al. (2008); Krapp and Hengstenberg (1996); Tokumaru et al. (1998) imply that we need to have both *visual vertical* and *visual rotational velocity* for estimation of self-motion. *Visual vertical* provides a visual reference for the direction of verticality and is affected by both rotations and linear accelerations. *Visual rotational velocity* provides visual angular velocity perception and is only induced by rotations. *Visual rotation velocity* was shown to be essential in both sickness prediction and motion perception prediction in SVC-based and MSOM models. *Visual vertical* helps only in the case of the MSOM, where it improves the predicted perception of tilt during the somatogravic illusion paradigm. *Visual vertical* has some effects on sickness prediction with SVC-based models, but given the lack of experimental data, we cannot yet conclude whether *visual vertical* can enhance sickness predictions. However, practically in our simulations of the aforementioned models, we have found no convincing use of *visual vertical* in motion sickness simulations of SVC-based models. This is due to the SVC-based models not having feedback from the otoliths to the semicircular canals, which may help in reducing tilt perception when *visual vertical* is included. Hence, changes need to be made in the SVC-based models to more realistically include the effects of *visual vertical*.

The recent Visual-Vestibular Motion Sickness (VVMS) model by Jalgaonkar et al. (2021); Sousa Schulman et al. (2023) has almost the same structure as the SVC model by Kamiji et al. (2007), but integrates vision directly in the sensory part of the model. The Appendix B.4 shows that sickness results are identical to the SVC$_I$-VR without vision. However, the inclusion of visual input does have an impact on sickness results, although not in the expected order of severity with vision. Thus, in its current form the VVMS is not a better predictor of vision effects in motion sickness than the SVC$_I$-VR model.

Comparing the models, it is evident that SVC models with a *visual rotational velocity* loop should be used for motion sickness predictions. Adding the *visual vertical* loop has very limited, and partially negative, effects making SVC$_I$-VR the recommended model for motion sickness prediction. However, for the tested motion perception paradigms, the MSOM with both vision loops (MSOM-VR+VV) performs best. Thus, there exists no universal model to simulate both motion sickness and motion perception. In our recent paper (Happee et al., 2023), we also evaluated the suitability of MSOM and SVCI-VR and SVCI-VR+VV to explain neck stabilization across a range of passive translational and rotational motion conditions. Here we found both MSOM and SVCI-VR+VV to well explain how vestibular and

visual information is integrated for postural stabilization, where the correspondence with human postural stabilization data was not very sensitive towards model type or parameters, but the SVCI-VR, did not correctly capture postural stabilization. This supports the idea that one unified model of sensory integration could explain motion perception, motion sickness and postural stabilization. To create such a unified model, one possible solution could be to implement better otolith-semicircular canal interactions in SVC models as done in the MSOM. This would help to better capture tilt perception during special motion paradigms such as roll tilt perception during centrifuge and pseudo-Coriolis. Another solution could be to apply a band-pass filter to the conflict term of the MSOM, thereby adjusting the frequency responses. However, to accurately see the effects of such modifications, more experiment data, especially with head rotation and under varying vision conditions, are sorely needed.

3.5 Conclusions

The goal of this paper was to validate the effects of vision as currently modeled in state-of-the-art motion sickness and motion perception models, i.e., the Subjective Vertical Conflict model with Integration of acceleration conflict (SVC_I) (Liu et al., 2022; Wada et al., 2015), the Subjective Vertical Conflict model with No Integration of acceleration conflict (SVC_{NI}) (Inoue et al., 2023), and the Multi-Sensory Observer Model (MSOM) (Newman, 2009). The SVC_I-VR model, which includes visual rotational velocity perception, best predicts experimental data for the effects of different vision conditions on motion sickness development. However, at the perceptual level, the SVC_I-VR model's predictions do not match available experiment data for a number of tested paradigms (i.e., somatogravic illusion, tilt perception in a centrifuge). All motion perception paradigm data are accurately matched by the tested MSOM-VR+VV, which includes both visual rotational velocity and visual orientation perception, however, no correct frequency sensitivity of motion sickness is shown in the MSOM. Thus, the performed model comparison shows that no single model exists that can accurately predict the effects of vision on motion sickness and motion perception. Our next steps include expanding our model comparison effort to include other conflict terms such as in (Allred and Clark, 2024). Here we expect the model by Allred and Clark (2024) to provide results similar to our results for the MSOM when comparing the predicted conflicts. The main improvement comes from the use of the nonlinear function by Oman (1990) which greatly improves the motion sickness frequency dynamics as shown in Kotian et al. (2023). Crucial steps towards realizing a unified model are, based on the analysis in this paper, the implementation of more complete otolith-semicircular canal interactions in SVC-based models such as the SVC_I-VR, adding a band-pass filter to correct the frequency dynamics of the MSOM. Along with this, future experiments will be directed towards addressing the gaps in the existing literature identified in this study.

4

Personalising Motion Sickness Models: Estimation and Distribution of Individual-Specific Parameters

Are all human beings truly equal?

Kiyotaka Ayanokoji

This chapter is based on *Kotian, V., Pool, D. M., & Happee, R. (2025). Personalising Motion Sickness Models: Estimation and Statistical Modeling of Individual-Specific Parameters. Frontiers in Systems Neuroscience, 19, 1531795.* and *Kotian, V., Pool, D. M., & Happee, R. (2023). Modelling individual motion sickness accumulation in vehicles and driving simulators. Proceedings of the Driving Simulation Conference, Antibes, France.*

The appendices for this chapter can be found at Appendix C.

Abstract

As users transition from drivers to passengers in automated vehicles, they often take their eyes off the road to engage in non-driving activities. In driving simulators, visual motion is presented with scaled or without physical motion, leading to a mismatch between expected and perceived motion. Both conditions elicit motion sickness, calling for enhanced vehicle and simulator motion control strategies. Given the large differences in sickness susceptibility between individuals, effective countermeasures must address this at a personal level. This paper combines a group-averaged sensory conflict model with an individualised Accumulation Model (AM) to capture individual differences in motion sickness susceptibility across various conditions. The feasibility of this framework is verified using three datasets involving sickening conditions: 1) vehicle experiments with and without outside vision, 2) corresponding vehicle and driving simulator experiments, and 3) vehicle experiments with various non-driving-related tasks. All datasets involve passive motion, mirroring experience in automated vehicles. The preferred model (AM2) can fit individual motion sickness responses across conditions using only two individualised parameters (gain K_1 and time constant T_1) instead of the original five, ensuring unique parameters for each participant and generalisability across conditions. An average improvement factor of 1.7 in fitting individual motion sickness responses is achieved with the AM2 model compared to the group-averaged AM0 model. This framework demonstrates robustness by accurately modelling distinct motion and vision conditions. A Gaussian mixture model of the parameter distribution across a population is developed, which predicts motion sickness in an unseen dataset with an average RMSE of 0.47. This model reduces the need for large-scale population experiments, accelerating research and development.

4.1 Introduction

Automated vehicles and driving simulators are very different technologies. However, they both share two common facts. The first is that they have become very popular in recent years, a trend that is expected to continue in the future. Secondly, they both share a common issue in *motion sickness*. Users of automated vehicles will move away from being drivers to passengers, preferably engaged in other activities such as reading or using laptops and smartphones. In driving simulators, realistic (unscaled) visual motion is presented with scaled or even without any physical motion. This causes a mismatch between expected and perceived motion, eliciting motion sickness (Bos et al., 2020). Even though these two examples are different and referred to as car and simulator sickness, respectively, the inherent mechanism that causes motion sickness in both, i.e., *sensory-expectancy conflict*, is the same (Reason, 1978b).

The mechanisms behind the development and evolution of motion sickness have been studied extensively, relying heavily on models that predict sensory conflicts based on mathematical models of the vestibular and visual sensory systems (Bos and Bles, 1998; Irmak et al., 2023; Kotian et al., 2024; Liu et al., 2022; Wada et al., 2020). In this paper, these models are referred to as 'conflict generation' models. However, these models generally predict group-averaged sickness development in terms of the Motion Sickness Incidence (MSI), which does not directly reflect some crucial dynamics of motion sickness development, such as recovery and hypersensitivity (Irmak et al., 2023; Oman, 1990). Furthermore, such group-averaged models cannot be reliably used for predicting motion sickness at an individual level.

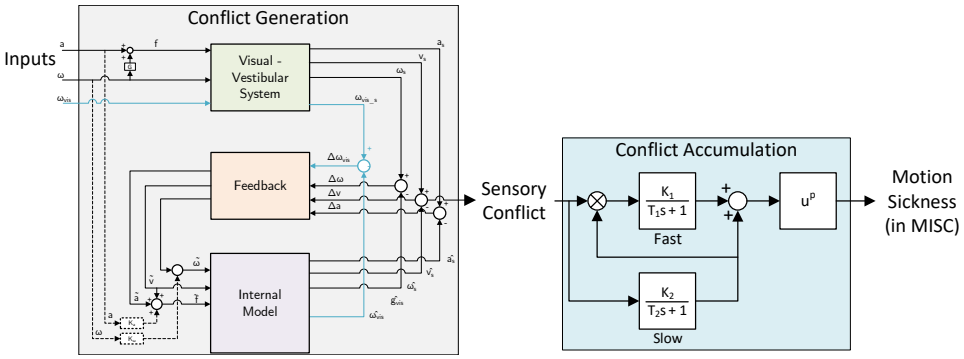

Figure 4.1: Framework for combined 'conflict generation' using the SVC model (Kotian et al., 2024; Wada et al., 2020) and 'conflict accumulation' (Irmak et al., 2022; Oman, 1990) model to predict individual motion sickness, i.e., MIsery SCale (Bos et al., 2010; Reuten et al., 2021)

In this paper, we aim to combine an available group-average 'conflict generation' model – the Subjective Vertical Conflict (SVC) model by Wada et al. (2020) – with an individualised 'conflict accumulation' model (AM) as also used by Irmak et al. (2020) to improve the ability to capture the differences in individual motion sickness susceptibility. This also requires the use of an individual motion sickness metric, such as the MIsery Scale (Bos et al., 2010;

Reuten et al., 2021), instead of a group-averaged metric like Motion Sickness Incidence (MSI). The proposed modelling framework is shown in figure 4.1. The conflict accumulation part is a modified form of the model by Oman (1990). The accumulation model is nonlinear and has conflict in m/s^2 as input, and the output is unitless in MISC (defined in Appendix C.6). This complicates the definition of units for the gains due to the multiplication and the power term. For conflicts generated by motion accelerations in one degree-of-freedom, the personalisation of sickness accumulation parameters has already been shown to improve modelling accuracy by a factor of 2 compared to using group-averaged parameters (Irmak et al., 2020). Our work extends this approach to full 6 degrees-of-freedom motion perceived from visual and vestibular inputs, which requires a 'conflict generation' model to account for realistic sensory conflict predictions, as in figure 4.1. Further details regarding this model structure will be provided in section 4.2.

The goal of the paper is to demonstrate the feasibility of this combined motion sickness model approach – i.e., combining a group-average 'conflict generation' and a personalised 'conflict accumulation' model – for capturing individual differences in motion sickness susceptibility. While evidence exists of individual differences in 'conflict generation' model parameters as well (Irmak et al., 2021), quantifying these would require individual perception experimental data, which was not readily available (an exception is Irmak et al. (2021)). Furthermore, we aim to find a 'minimum effective' implementation of such a personalised motion sickness model by directly comparing different parameterisations of the 'accumulation model'. For this, extending our own preliminary work in Kotian et al. (2023), this paper makes use of four existing datasets, see table 4.1, where MISC was measured under sickening motion stimuli in 1) an experimental vehicle with and without out-of-the-window vision Irmak et al. (2020), 2) vehicle experiments and matched driving simulator experiments (Talsma et al., 2023), 3) vehicle experiments with various non-driving related tasks (NDRTs) (Metzulat et al., 2024), and 4) on road vehicle experiments and sickness recreation experiments on a smaller track (Harmankaya et al., 2024). All datasets involve passive motion, representative of being driven by an automated vehicle, and test two or three different conditions with the same participants. Inoue et al. (2024) also report on a similar approach as used by Kotian et al. (2023), where only the pre- and post-scaling of the 'conflict accumulation' model was varied between different participants. The resulting individualised models were validated using a 1 degree-of-freedom motion stimulus experiment with variation in head movement (Inoue et al., 2024). Our current work performs extended validation with a full 6 degrees-of-freedom motion and with variations in visual and vestibular inputs in real driving scenarios, which requires a 'conflict generation' model to account for realistic sensory conflict predictions. Furthermore, we perform an explicit optimization of the required number of parameters for personalizing the 'conflict accumulation' model, including the model's gains and time constants instead of a simple pre- and post-scaling.

This paper presents a direct comparison of fitting the proposed combined motion sickness model for all individual participants in the first three datasets listed in table 4.1. For every participant, parameters are always estimated *across* the different conditions tested in each dataset to ensure a 'minimum effective' and generalisable result. Additionally, using the individual-specific variations in the parameter values estimated from these datasets, a probabilistic Gaussian mixture model is used to capture the observed statistical variations.

The capacity of this statistical modelling approach for predicting individual variations in motion sickness across a population is verified by predicting the final Sickness Recreation dataset, see table 4.1.

Table 4.1: Experimental datasets used in this study

Datasets	Details	Reference	No. of Participants
Slalom Drive	Slalom with Internal and External vision Motion sickness responses for hypersensitivity	Irmak et al. (2020)	16
Car and Simulator	Naturalistic drive in vehicle and moving base simulator Only External vision	Talsma et al. (2023)	24
NDRT Drive	Naturalistic driving data with varying NDRTs Internal Vision	Metzulat et al. (2024)	20
Sickness Recreation	Naturalistic driving data on road recreated on a smaller track Internal Vision	Harmankaya et al. (2024)	47

By achieving these goals, this paper will show that our proposed modelling framework can be used for personalised motion sickness modelling for automated vehicles. The obtained model predictions can be used to optimise the comfort levels of individual automated vehicle users by adapting its driving style, i.e., by limiting the acceleration and rotations of the car they may be especially sensitive to. Furthermore, the derived statistical model can directly improve and accelerate the design and testing of new driving simulator motion cueing algorithms that aim to minimise simulator sickness, as in (Baumann et al., 2021; Hogerbrug et al., 2020; Jain et al., 2023a).

4.2 Methods

Experimental Datasets

For the analysis in this paper, we make use of four different published datasets, see table 4.1. All datasets include measured sickness responses to passive road vehicle motion, representative of being driven by an automated vehicle. In these datasets, individual motion sickness levels were reported using the MISC scale as a function of time, and all showed major individual differences in sickness susceptibility.

First, the real-world 'Slalom Drive' dataset includes varying vision conditions, i.e., with and without an outside view, where mean MISC levels at the end of motion exposure were 5.3 (severe symptoms) with an outside view and 3.3 (some symptoms) without an outside view (Experiment 1 in (Irmak et al., 2020)), see figure 4.2. The experiment was terminated when a MISC value of 6 was reached. This experiment compared the motion sickness development with and without an outside view from the car. This dataset is ideal for proving that our new model framework can predict individual motion sickness for various vision conditions in real vehicles.

The 'Car and Simulator' dataset (24 participants) contains motion sickness responses from real-world driving and its (matched) simulation on a moving-base driving simulator (Talsma et al., 2023). For this experiment, the mean MISC levels at the end of motion exposure were

around 5.5 (severe symptoms) in the car and 1.5 (slight discomfort or vague symptoms) in the simulator, see figure 4.3. The experiment was terminated when a MISC value of 6 was reached.

The 'NDRT Drive' experiment was performed by 20 participants and focused on a real-world sickening drive around a fixed track with three different non-driving related tasks (NDRTs): visual dynamic, visual static and auditory. The mean MISC levels at the end of each condition were around 4.5 (medium symptoms) for the auditory, 5 (severe symptoms) for the visual static, and 6.5 (some nausea) for the visual dynamic condition, see figure 4.4. This experiment was terminated when a MISC value of 7 was reached. However, several participants still showed a rapid increase to a MISC of 8 before or just after the experiment was actually stopped.

The 'Sickness Recreation' experiment tested a method to efficiently replicate the on-road motion sickness of 47 participants on a smaller track. The mean MISC levels at the end of both drives were around 2 (vague symptoms) figure 4.14.

In this paper, the 'Slalom Drive', 'Car and Simulator' and 'NDRT Drive' datasets are used to demonstrate the capability of the individual modelling framework to generalise across different visual/vestibular input cases, whether these originate from a car or a simulator. Furthermore, the first three datasets are used to study the number of parameters needed to accurately model motion sickness development in different participants, while the 'Sickness Recreation' dataset is used for validation of the statistical model over a new population.

Model Framework: Inputs and Outputs

The structure of the model framework has been introduced in section 4.1. As shown in figure 4.1, inertial vehicle or simulator motion inputs – such as acceleration and angular velocity – as well as vision inputs – such as visual verticality (orientation) and visual rotation (rotational velocity) – are defined as the inputs of the 'conflict generation' model, consistent with the SVC model by Wada et al. (2020) and Liu et al. (2022). For our analysis, we applied the full 6 degrees-of-freedom motion (3 translations and 3 rotations) as model inputs, using the recorded seat motion for the drives in the car for the 'Car and Simulator', 'NDRT Drive' and 'Sickness Recreation' dataset and recorded platform motion for the simulator in the 'Car and Simulator' dataset, and recorded head motion for the 'Slalom Drive' dataset. Example input data for all datasets is shown in Appendix C.1.

The human eye estimates motion through vision by measuring the rotation of visual cues between the current and previous states, a process known as optic flow. We assume the visually perceived rotations to be equivalent to head (or vehicle, as in the case of the Car and Simulator dataset) rotations when observing the external environment. Consistent with Kotian et al. (2024), for internal vision, we select a zero visual input, assuming no visual head motion relative to the vehicle.

The output of the model is chosen to be the score on the MIsery SCale (MISC) by Bos et al. (2010); Reuten et al. (2021), which quantifies the progression of sickness-related symptoms

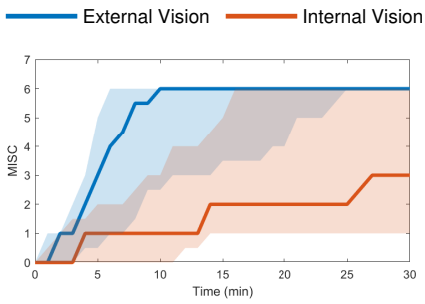

Figure 4.2: Slalom Drive dataset (Irmak et al., 2020) group-averaged MISC levels versus time in the conditions of external (blue) and internal vision (red) with the shaded region showing the 25th to 75th percentiles

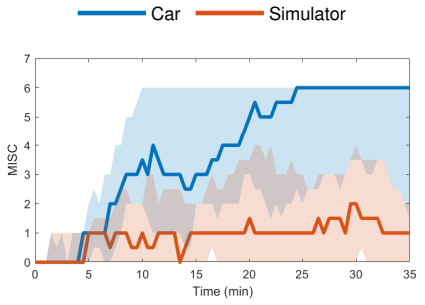

Figure 4.3: Car and Simulator dataset (Talsma et al., 2023) group-averaged MISC levels versus time in the car (blue) and simulator (red) with the shaded region showing the 25th to 75th percentiles

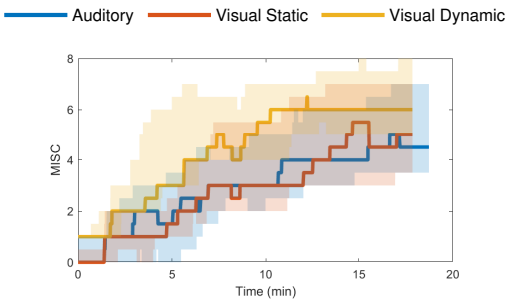

Figure 4.4: NDRT Drive dataset (Metzulat et al., 2024) group-averaged MISC levels versus time in the three different tasks - auditory (blue), visual static (red) and visual dynamic (yellow) with the shaded region showing the 25th to 75th percentiles

and has a positive relation to discomfort (De Winkel et al., 2022; Reuten et al., 2020). The MISC is an 11-point symptom-based scale that measures in discrete symptoms running from 0 to 10, where 0 means no symptoms and 10 stands for emesis (vomiting). In contrast to the discrete MISC scale, the sickness model predicts on a continuous scale. For model fitting, these continuous model predictions are compared with experimentally reported

discrete MISC scores.

Model Framework: Model Structures

As previously discussed, we combine two models in our proposed model framework. The first component of the model is the 'conflict generation' model (see figure 4.1, left), which models the integration of 6 degrees-of-freedom sensory inputs and generates a 1 degrees-of-freedom (scalar) sensory conflict signal. For our application, this model shall be reliable in forecasting conflict signals, especially for 6 degrees-of-freedom (automated) road vehicle motion. Additionally, the model must include explicit visual inputs so that the effects of different vision conditions can be predicted. To select an appropriate model, we refer to our previous study (Kotian et al., 2024), where different 'conflict generation' models and implementations of vision inputs were directly compared.

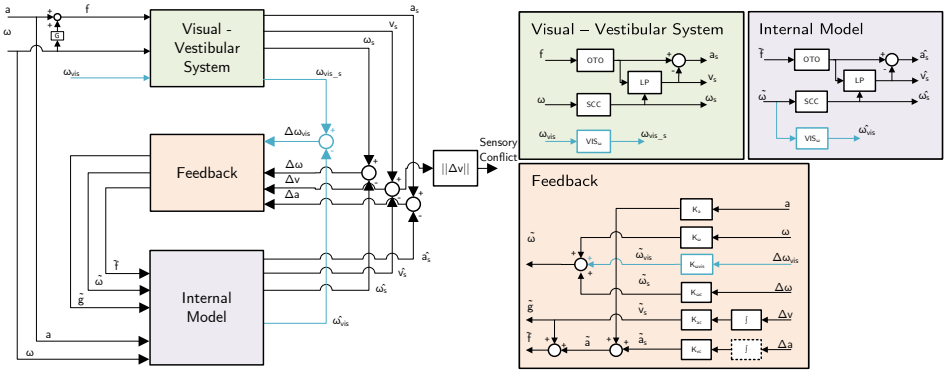

Figure 4.5: The selected 'conflict generation' model, which is the SVC model as in (Kotian et al., 2024) based on the model by Wada et al. (2020)

Based on (Kotian et al., 2024), we select the Subjective Vertical Conflict (SVC) model with only a visual rotational velocity input as proposed in (Wada et al., 2020) for predicting a subjective vertical conflict (a 3-dimensional vector) that drives motion sickness, see figure 4.5. This model has been shown to accurately replicate the frequency and amplitude dynamics of motion sickness as reported in numerous previous studies (Golding and Markey, 1996; Griffin and Mills, 2002b; Howarth and Griffin, 2003; Irmak et al., 2021, 2022; McCauley et al., 1976). Kotian et al. (2024) show that the visual vertical input that has also been proposed by Liu et al. (2022) is not effective for predicting sickness and hence is not used in the current study. The parameters used for the 'conflict generation' model in this paper are directly taken from earlier publications on the SVC model (Liu et al., 2022; Wada et al., 2020) and listed in table 4.2.

The second part of the model is the 'conflict accumulation' model, which accumulates (integrates) the sensory conflict predicted by the first part of the model framework to estimate the build-up of motion sickness over time. The Euclidean norm of the sensory conflict output by the 'conflict generation' model is used as the input to the 'conflict accumulation'

model. Usually, the conflict is integrated using a Hill function combined with a leaky integrator to output a group-level sickness metric such as Motion Sickness Incidence (MSI), which quantifies the percentage of the population that becomes motion sick (Liu et al., 2022; Wada et al., 2020). However, this integration is insufficient to capture the unique dynamics of motion sickness, including hypersensitivity, which is the faster than normal increase of motion sickness after already being subjected to motion sickness before. Thus, we adopt the more advanced model by Oman (1990), which is a five-parameter nonlinear model that integrates the conflict (see the right part in figure 4.1), with fast and slow pathways combined with leakage. The fast path has a low time constant (T_1) and models the direct response to a sickening stimulus. The slow path has a high time constant (T_2) and captures the slower secondary effects of sickening stimuli, such as recovery and hypersensitivity. This is also relevant in simulators where a sudden increase in motion incongruence can make participants hypersensitive. This has been observed by Cleij et al. (2017); Kolff et al. (2022), where it was shown that motion tends to be momentarily bad but not continuously. Both pathways have a gain (K_1 and K_2) to control their contribution. Additionally, there is a power law (p) at the model's output to account for nonlinear scaling effects.

Table 4.2: SVC model parameters

Parameter Class	Parameter Symbol	Value	Explanation
Anticipation Gains	K_a K_ω	0 0	Fully passive motion with no anticipation assumed
Vestibular Feedback Gains	K_{ac} K_{vc} $K_{\omega c}$	1 5 10	as in Wada et al. (2020)
Visual Feedback Gains	K_{gvis} $K_{\omega vis}$	0 10	VV gain set to zero VR gain as in Wada et al. (2020)
Perception Time Constants	τ (s) τ_{scc} (s)	5 7	as in Liu et al. (2022)

Accumulation Model: Parameter Reduction

In addition to studying the accuracy of the Accumulation Model (AM) with all 5 model parameters (T_1, T_2, K_1, K_2, p) fitted individually, we consider reduced parameter variations of the AM model to optimise for a 'minimum effective' number of individually fitted parameters. Such model reduction is important to enhance the generalisability, efficiency, and interpretability of the proposed personalised accumulation model. For example, in many cases, a reduced number of model parameters improves model generalisability due to a reduced risk of over-fitting. Furthermore, a reduced number of tunable parameters simplifies adjusting the model to different individuals' sickness characteristics and may facilitate a more computationally efficient implementation.

As the main basis for model parameter reduction, in this paper, median measured values and empirical relations between different parameters reported in previous studies are used, e.g.:

- $T_1 = 60$ s (Oman, 1990)
- $T_2 = 7T_1$ (Irmak et al., 2020)
- K_1: median value reported for each dataset:
  - $K_1 = 2$ for Slalom Drive dataset
  - $K_1 = 18$ for Car and Simulator dataset
  - $K_1 = 9$ for NDRT Drive dataset
- $K_2 = 5K_1$ (Oman, 1990)
- $p = 0.4$ (Irmak et al., 2022)

The K_1 values were obtained from the median values estimated with the AM5 model (see table 4.3 for details of the AM5 model) on each dataset. It should be noted that the assumed K_1 values are different for each dataset as the motion inputs in each dataset were different. In the 'Slalom Drive', head motion was recorded, but in the 'Car and Simulator' and 'NDRT Drive', only vehicle motion was recorded. Hence, a difference in the magnitude of especially the rotations between datasets exists, which explains the difference in estimated K_1 gains. This is shown in Appendix C.1 where the 'Car and Simulator' dataset clearly has the smallest magnitudes of angular velocities. This could also be partly due to the difference in average motion sickness susceptibility of the participants in each experiment; the 'NDRT Drive' dataset (with $K_1 = 9$) could have less motion sickness susceptible participants than the 'Car and Simulator' dataset (with $K_1 = 18$) due to the lower observed median K_1 values.

We use combinations of these assumptions to obtain reduced implementations of the AM compared to its original definition, i.e., AM5 (Oman, 1990). Table 4.3 summarises the different cases of the accumulation model, indicating which parameters are estimated (marked with a ✓) and which parameters are set based on one of the above assumptions. AM0 is the model with only group-averaged parameters. The *a* and *b* versions of AM1 and AM4 are models with same numbers of parameters (1 for AM1 and 4 for AM4), but with different subsets of parameters being assumed/estimated.

Accumulation Model: Parameter Estimation

To effectively capture individual differences in motion sickness susceptibility with the 'conflict accumulation' model, we choose to model the different conditions tested by the same individual in each experiment together, i.e., using a single set of parameters for each individual. This approach enhances generalisability and enables the model to predict motion sickness across a wider range of conditions. This assumes that people respond exactly the same way to conflicts even in very different settings (e.g., internal vs external vision).

Table 4.3: Reduced parameter versions of the 'conflict accumulation' model (AM). Check marks indicate the free model parameters estimated for each individual.

Model	Number of free parameters	Estimated/fixed parameters				
		K_1	K_2	T_1 (s)	T_2 (s)	p
AM5	5	✓	✓	✓	✓	✓
AM4a	4	✓	$5K_1$	✓	✓	✓
AM4b	4	✓	✓	✓	$7T_1$	✓
AM3	3	✓	$5K_1$	✓	$7T_1$	✓
AM2	2	✓	$5K_1$	✓	$7T_1$	0.4
AM1a	1	2/18/9	$5K_1$	60	✓	0.4
AM1b	1	2/18/9	✓	60	$7T_1$	0.4
AM0	0	2/18/9	$5K_1$	60	$7T_1$	0.4

To fit the model parameters, a constrained optimisation problem is defined and solved in *MATLAB* with the *fmincon* solver using the *sqp* algorithm. Furthermore, *multistart* was used to simultaneously find 16 local minima and then select the overall optimum. This enhances the probability of finding the global minimum of the optimisation problem. The Root-Mean-Square Error (RMSE) between the measured and predicted MISC responses, as a function of the parameter vector $\mathbf{x} = (T_1, T_2, K_1, K_2, p)^T$, is defined as the cost function for model fitting for each individual. When fitting multiple conditions simultaneously, this means that the cost function is the sum of RMSE values for all n_c conditions within each dataset for each individual. The optimisation problem is mathematically defined in equation (4.1), where RMS stands for 'Root Mean Square'.

$$\hat{\mathbf{x}} = \arg\min_{\mathbf{x}} \sum_{i=1}^{n_c} \text{RMS}\left[\text{MISC}_{meas,i} - \text{MISC}_{pred}(\mathbf{x})\right] \tag{4.1}$$

After these models are fitted and their corresponding errors are calculated, we try to select the best model which balances accuracy with loss of generalisability and overfitting. To show this statistically, we used various model selection criteria, such as the Akaike information criterion (AIC) by Akaike (1998) and Bayesian information criterion (BIC) by Schwarz (1978), which take into account the tradeoff between the goodness of fit and the simplicity of the model. In other words, these criteria balance the risk of overfitting and underfitting. A simpler model also means that the simulations will be computationally fast. The model criteria we used are the AIC and BIC, which are defined as,

$$AIC = 2k + n\ln(RSS/n) \tag{4.2}$$

$$BIC = k\ln(n) + n\ln(RSS/n) \tag{4.3}$$

where, k is the number of parameters, n is the sample size and RSS is the Residual Sum of Square. The model with the lowest score is selected as optimal. The number of parameters (k) and the sample size, which is equal to the number of participants (n), are shown in table 4.4. The RSS of each model is calculated by summing the RSS for the fits of each

participant and each condition. In the model fittings, RMSE was used as a cost function. RMSE is proportional to RSS. RMSE is the square root of the average RSS per observation. Thus, the cost function used in the model fitting, RMSE, directly relates to RSS, and the model fitting algorithm would also minimise the model criteria such as the AIC and BIC.

However, in applying the AIC and BIC to our problem, the penalty on the number of parameters in both criteria – defined as $2k$ or $k\ln(n)$ in equations (4.2) and (4.3), respectively – was found to be insufficient. This insufficiency resulted in the selection of the model with the least error by the criteria. To solve this problem, we followed Drop et al. (2018) where a similar situation was observed. Here, they increased the gain on the term of k to increase the penalty. We did the same, and the modified BIC is defined as follows,

$$mBIC = c\ k\ln(n) + n\ln(RSS/n) \tag{4.4}$$

where c is the model complexity (number of parameters) penalty parameter, which is to be tuned to avoid false positives while maintaining sensitivity to small yet important contributions. To do this, we calculated mBIC values with c varying from 1 to 5. We then choose the value of c to not select AM0, which is a group-averaged model, or AM5, which is the model with the most number of parameters estimated. With the chosen value of c, we find the model with the least mBIC value. This model will be the best the tradeoff between the goodness of fit and the simplicity of the model.

Probabilistic Parameter Distribution Model

To facilitate offline prediction of individual variations in motion sickness development with the proposed model, a statistical model that describes the distribution of the parameters across participants is needed. To estimate such a predictive probabilistic model from our considered datasets, first, the estimated parameter sets for the best model (as per the conditions outlined in section 4.2) are clustered into three groups using a k-means clustering algorithm. While attempts were made to use more than three clusters, the results consistently showed three prominent clusters, with any additional clusters being very small and closely resembling the original three. These three clusters effectively classify the parameter sets into three distinct groups of motion sickness susceptibility: high, medium and low. Using these clusters, a three-component Gaussian Mixture Model (GMM) – i.e., a weighted sum of three Gaussian distributions – is used to model the distribution of the parameter set. This model is given by:

$$p(\mathbf{x}) = \sum_{j=1}^{3} \pi_j \mathcal{N}(\mathbf{x}|\boldsymbol{\mu}_j, \Sigma_j) \tag{4.5}$$

Where:

- **x** is the parameter set
- $p(\mathbf{x})$ is the probability density function of the GMM.

- π_j is the weight of the j-th Gaussian component, satisfying $\sum_{j=1}^{3} \pi_j = 1$.
- $\mathcal{N}(\mathbf{x}|\boldsymbol{\mu}_j, \Sigma_j)$ is the Gaussian density function, defined as:

$$\mathcal{N}(\mathbf{x}|\boldsymbol{\mu}_j, \Sigma_j) = \frac{1}{2\pi|\Sigma_j|^{1/2}} \exp\left(-\frac{1}{2}(\mathbf{x}-\boldsymbol{\mu}_j)^\top \Sigma_j^{-1}(\mathbf{x}-\boldsymbol{\mu}_j)\right) \tag{4.6}$$

In this expression, $\boldsymbol{\mu}_j$ is the mean vector of the j-th Gaussian component, and Σ_j is the $k \times k$ covariance matrix where k is the number of parameters in the model. These are fit using *fitgmdist* function in *MATLAB* with the clustering from the k-means algorithm as the starting point.

Finally, using the fitted Gaussian mixture model, we sample 1000 random parameter sets and use them to predict motion sickness (in MISC) on the 'Sickness Recreation' dataset (an unknown dataset to our fitting study). This way, we validate the ability of our model to predict motion sickness in a new scenario.

4.3 Results

This section presents the results of our analysis focused on the proposed new model framework that combines an average 'conflict generation' model with an individualised 'conflict accumulation' model to capture differences in individual motion sickness susceptibility. In section 4.3.1, the model fitting results for various datasets are presented to show the performance of the model with varying numbers of parameters. This outcome is used to demonstrate the effectiveness of our model framework and determine the optimal number of parameters required for the recreation of motion sickness at the individual level. In section 4.3.2, the probabilistic model for the observed variation in accumulation model parameters across individuals is extracted from the data and tested on a new population.

4.3.1 Accumulation Model Performance and Parameter Selection

First, results are presented for the Slalom Drive dataset by Irmak et al. (2020) demonstrating the performance of the model with varying vision conditions. This is followed by results for the Car and Simulator dataset by Talsma et al. (2023) and NDRT Drive by Metzulat et al. (2024), where the adaptability of the model to real-world driving and driving simulators is shown. Fits of the model framework, with different accumulation models (AM), to the actual MISC responses with Motion Sickness Incidence (MSI) predictions overlayed are shown first, followed by a comparison of the models' RMSE values. It is demonstrated that the use of our model framework with individualization improves the accuracy of the simulation of motion sickness compared to the use of MSI. In addition to this, a parameter study is conducted to find the minimum effective implementation of the model.

Model Performance

Figure 4.6 shows the comparison of the most relevant accumulation models with experimental recorded motion sickness responses (MISC) for a representative selection of participants from Irmak et al. (2020)'s experiment for the conditions of internal (left column) and external vision (right column). The obtained model fits for the rest of the participants are shown in Appendix C.2. The experimentally reported MISC is shown in black, and MSI predictions (obtained directly using the model from Wada et al. (2020)) are shown in orange. The predictions of our proposed combined model are shown for only 3 out of the 8 models in table 4.3: AM0 in dotted grey, AM2 in solid green, and AM5 in dashed violet. AM5 is the original version of the accumulation model, with all five parameters being estimated individually. AM0 represents the model with group-averaged parameters. AM2 provides the best compromise fit with only two individual parameters. The AM0 model and MSI predictions both use the same parameter settings for all participants. Any difference in their predictions is thus due to differences in the vehicle motion used as input to these models. In figure 4.6, we show MSI for its full range of 0-100% and MISC across a range of 0-8. These y-axis limits are chosen solely to make both sets of data values readable from the graph and enhance their clarity.

It is evident that our approach of estimating parameters for each individual (in particular for AM2 and AM5 models) offers improved accuracy in predicting MISC responses compared to the use of group-averaged parameters (AM0). The average RMSE reduces from 1.94 (AM0) to 1.13 (AM2) and 0.74 (AM5). This proves that using parameters estimated for each individual (AM2 and AM5) is 40% and 60% more accurate, respectively, than using group-averaged parameters, as in the AM0 model. For example, for P5 and P18 in figure 4.6, it is clear that AM0 greatly underestimates the measured MISC values.

Another important observation is that all accumulation models are able to capture the recovery from motion sickness. This recovery occurs when the sickening stimuli are stopped, and the participant is allowed to rest. This is more evident for P9 and P14 (second and third row in figure 4.6). Consistent with (Irmak et al., 2020), the MSI prediction (in orange) cannot capture this reduction in motion sickness.

Furthermore, we tested the models by fitting them on additional datasets such as the Car and Simulator dataset by Talsma et al. (2023) and the NDRT Drive dataset by Metzulat et al. (2024). The car and simulator dataset had 24 participants, each experiencing motion with external vision in a real-world car and in a simulator. The NDRT Drive experiment had 20 participants, each experiencing three different Non-Driving Related Tasks (NDRT). Figures 4.7 and 4.8 again show the experimental recorded motion sickness responses (MISC) in black, MSI predictions in orange, and fitted model predictions in green, violet, and grey for 4 out of the 24 participants for both cases. It can be seen that even with two parameters, the fits of the AM2 model are very close to the actual MISC responses in both datasets. The MSI prediction values are very low, especially in the Car and Simulator dataset. This is due to the low levels of conflict generated in these experiments (0.12 m/s^2 mean RMS conflict) compared to other datasets, such as the Slalom Drive, which has 1.15 m/s^2 mean RMS conflict. As opposed to the MSI prediction, which is a population-level prediction, the proposed 'conflict accumulation' model is able to account for these combinations of

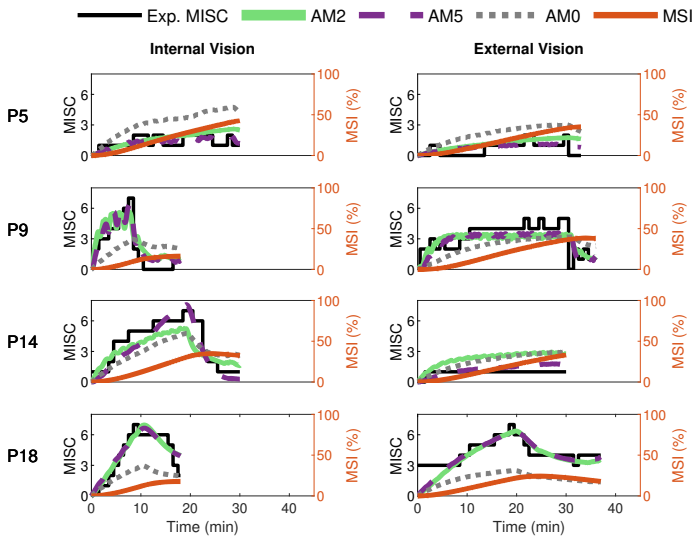

Figure 4.6: Motion sickness responses (MISC) in Slalom Drive experiments by Irmak et al. (2020) in black, fitted AM2 model predictions (MISC) in green, fitted AM5 model predictions (MISC) in dashed violet, fitted AM0 model predictions (MISC) in dotted grey, and MSI predictions from Hill function in orange for 4 participants (participant label shown on the left) for the conditions of internal (left column) and external (right column) vision.

low levels of conflict and high susceptibility of the participants. The fits for the rest of the participants are available in Appendix C.2.

Model Parameter Selection

In the previous section, it was observed that the model with two estimated parameters (AM2) per individual captures the individual responses almost as well as the model for which all five parameters are estimated individually (AM5). To show this quantitatively, we evaluated the need for each of the parameters by comparing all eight models in table 4.3. From figure 4.9a, it is clear that reducing the number of parameters below two leads to a 36% increase in RMSE (from 1.2 to 1.6 in internal vision case and from 1.0 to 1.4 in external vision case when comparing AM2 to AM1a model) in the Slalom drive dataset. Hence, any model with two or more parameters is sufficiently accurate (with RMSE around 1 MISC) to capture individual motion sickness development. We also compared the individual models with a group-averaged version of the accumulation model (AM0), where the parameters are the same for all participants in the dataset. It is observed that AM0 has, on average, 1.7 times higher RMSE as compared to the AM2 model (for example, from 1.22 to 2.25 in the internal and from 1.04 to 1.63 in the external vision case of the slalom drive dataset). Overall, figure 4.9a again shows the improvement obtained with individual model fits compared to using group-averaged parameters.

Furthermore, to demonstrate that the optimal number of accumulation model parameters for our model framework is 2, the previous test was repeated with the Car and Simulator

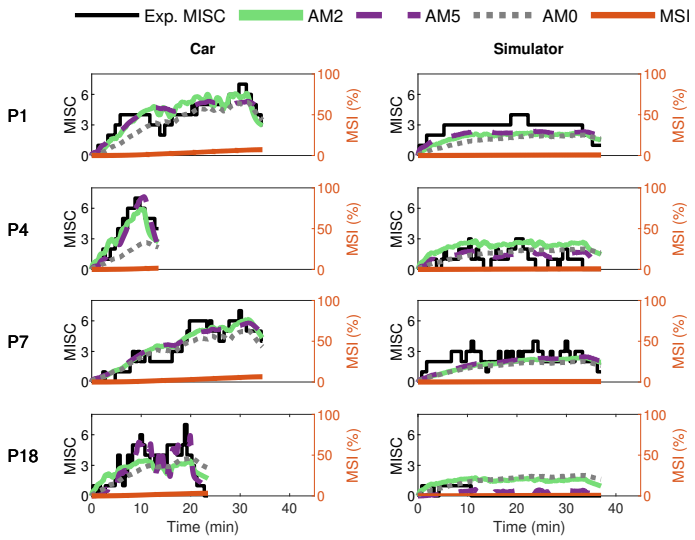

Figure 4.7: Motion sickness responses (MISC) in Car and Simulator experiments by Talsma et al. (2023) in black, fitted AM2 model predictions (MISC) in green, fitted AM5 model predictions (MISC) in dashed violet, fitted AM0 model predictions (MISC) in dotted grey, and MSI predictions from Hill function in orange for 4 participants (participant label shown on the left) for the case in the car (left column) and the simulator (right column).

dataset as shown in Figure 4.9b, where a similar trend is seen with AM2 model offering a good balance between performance and efficiency. When comparing the individual models with a group-averaged version of the accumulation model, it is observed that the group-averaged model, AM0, has 1.64 times more RMSE as compared to the AM2 model (from 1.03 to 1.96 in the internal and from 1.06 to 1.47 in the external vision case). This increase is equivalent to that found for the Slalom Drive dataset (1.7 times increase). This trend was also seen in the NDRT Drive dataset, where the AM2 model offers the best balance between performance and efficiency (see figure 4.9c).

It is clear from the results in figure 4.9 that this model framework is able to capture multiple conditions with 2 individually estimated parameters. Overall, the accuracy is better (by around 60% in RMSE) than using a group-averaged model. This is applicable for various vision conditions, as well as different motions from real cars to simulators.

The variation of the mBIC with c is plotted in figure 4.10. As discussed in section 4.2, the selection of the AM0 and AM5 model must be avoided. AM0 model has zero estimated parameters and acts only as an average model. Choosing AM0 would oversimplify and lose generalisability. Similarly, the AM5 model has five estimated parameters, which may cause overfitting even if it fits the data well. When c values are 1 and 3, The risk of choosing AM5 and AM0 is high when c values are 1 and 3, as these models become more favourable than 50% of other models based on the mBIC metric. With c values above 3, the model AM0 becomes very favourable, which is also undesirable. In our fittings, starting with 100 random initial points yields more than 15 solutions when fitting models with more than two

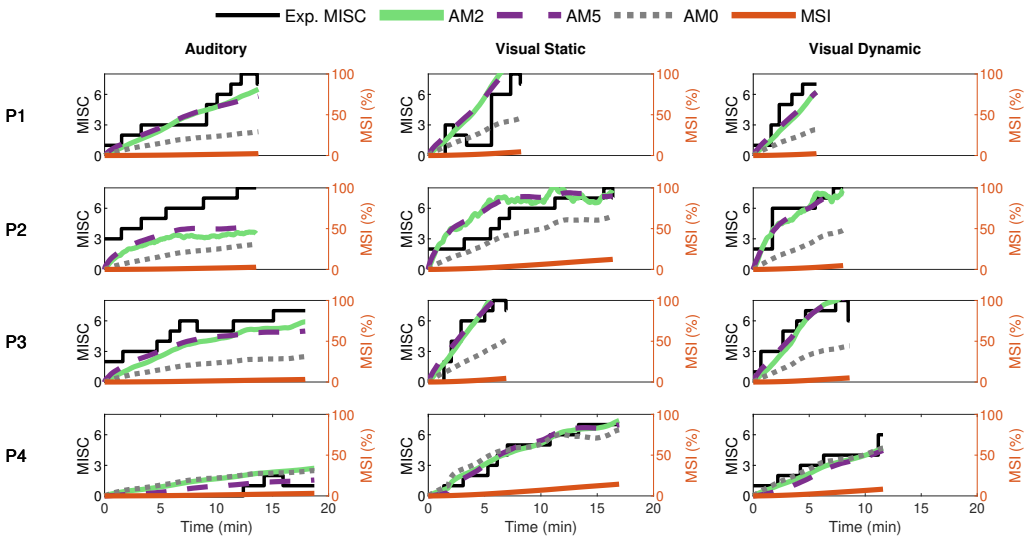

Figure 4.8: Motion sickness responses (MISC) in NDRT Drive experiments by Metzulat et al. (2024) in black, fitted AM2 model predictions (MISC) in green, fitted AM5 model predictions (MISC) in dashed violet, fitted AM0 model predictions (MISC) in dotted grey, and MSI predictions from Hill function in orange for 4 participants (participant label shown on the left) for the case in the auditory (left column), visual static (middle column) and the visual dynamic (right column) task.

parameters (i.e., the AM3, AM4a, AM4b, and AM5 models). In contrast, when using two or fewer parameters (such as the AM2, AM1a, and AM1b models), we achieve 2 unique parameter solutions, one of which is selected 95 out of the 100 fittings. Out of these 3 models (AM2, AM1a, and AM1b), the AM2 model demonstrates the highest accuracy with an RMSE of 1.54 MISC. Therefore, to balance accuracy and model complexity, we select (c = 2) and opt for AM2 as the optimal model.

Table 4.4 shows all models with the number of parameters and metrics of their fits - RMSE and mBIC (with $c = 2$). While it is evident from the table that AM5 achieves the lowest RMSE, the mBIC criterion, which incorporates a penalty for the number of parameters, selects AM2 as the optimal model. This highlights the effectiveness of mBIC in balancing model accuracy with parameter simplicity, ensuring a more robust and generalisable model selection. However, it is important to note that the preferred (c) parameter may vary with different datasets and applications. Some may prioritize simplicity and opt for a higher value of c and choose a single-parameter model instead.

4.3.2 Accumulation Model Parameter Distribution

The parameter sets of 44 participants of the Car and Simulator and NDRT Drive datasets are shown in figure 4.11 for the AM2 model. Vehicle motion is used as input in both of these datasets. The Slalom drive dataset is omitted here for consistency in parameters due to the slalom drive using head motion instead of vehicle motion, as is the case for the other

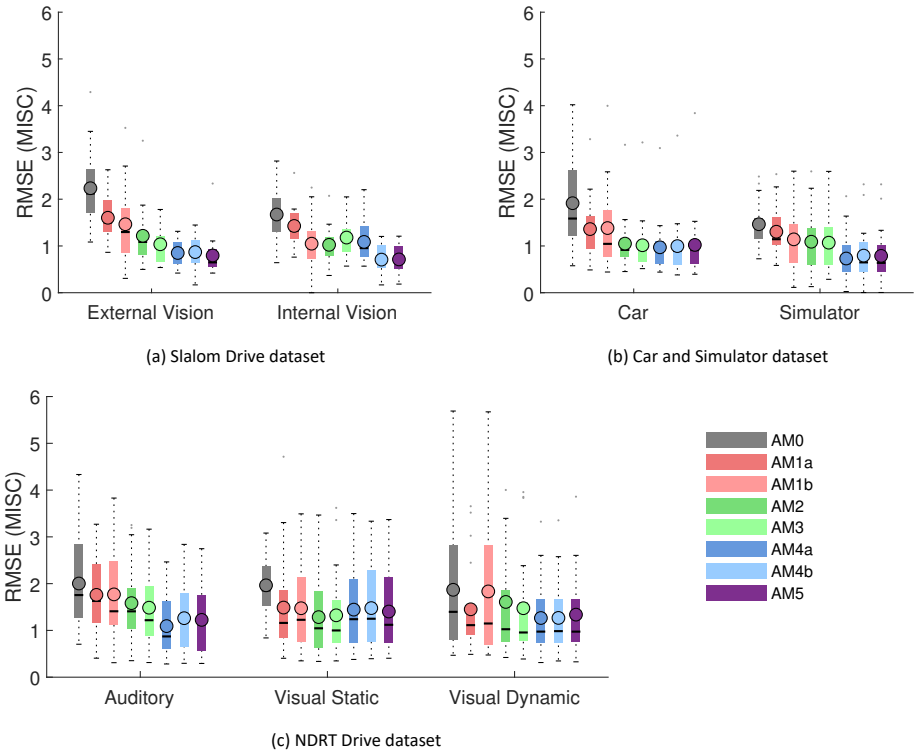

(a) Slalom Drive dataset

(b) Car and Simulator dataset

(c) NDRT Drive dataset

Figure 4.9: Root Mean Squared Error (RMSE) between the predicted MISC from the models and the actual MISC for the Slalom Drive, Car and Simulator and NDRT Drive datasets. Also shown are the mean (circled), median (horizontal solid line), and interquartile range (in a coloured rectangle)

Table 4.4: Model selection criterion. Bold numbers show the smallest value in each metric. The total number of participants is 44 (20 from the 'Car and Simulator dataset' and 24 from the 'NDRT Drive' dataset) for all accumulation models.

Model	Participants (n)	Parameters (k)	RMSE	mBIC ($c = 2$)
AM0	44	0	2.06	101.92
AM1a	44	1	1.72	93.49
AM1b	44	1	1.78	96.66
AM2	44	2	1.54	**91.18**
AM3	44	3	1.32	98.19
AM4a	44	4	1.32	92.8
AM4b	44	4	1.32	92.82
AM5	44	5	**1.3**	99.5

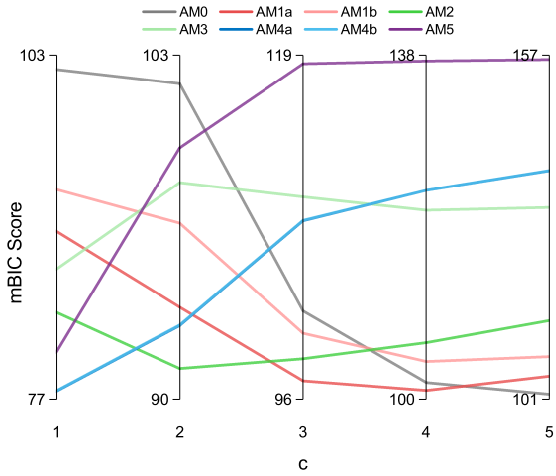

Figure 4.10: Model selection criterion comparison: mBIC scores with varying value of c for various models

two. In the figure, it can be seen that there are three distinct sets of parameters, which are found by using the k-means clustering algorithm:

- High susceptibility are those with high K_1 and low T_1, shown as red dots.
- Low susceptibility have the opposite, low K_1 and high T_1, shown as blue dots.
- Medium susceptibility have low K_1 and low T_1, shown as medium dots.

The mean value of the parameters is 15.2 for K_1 and 52.3 seconds for T_1; see black dot in figure 4.11. The mean value is located in an area that does not correspond to any individual's parameter values. Therefore, using these mean values to represent a group, which is commonly done, is not correct and does not accurately represent any individual in the population. With this knowledge, representative parameters can be sampled to test motion profiles on different motion sickness susceptibilities. Additionally, percentiles can be defined to see which percentile of subjects do or do not get motion sick.

To obtain the probabilistic model, we have fitted a three-component Gaussian mixture model with two dimensions (for the two-parameter AM2 model) on the estimated parameter values obtained for all 44 individuals, see figure 4.12. The figure 4.12a shows the probability density function of the Gaussian mixture model. This clearly illustrates the three clusters of motion sickness susceptibility identified by the model. Additionally, it highlights the variation in density, indicating that there are more parameter sets associated with medium and low susceptibility compared to those linked to high susceptibility. The figure 4.12b, on the other hand, shows the cumulative density function of the Gaussian mixture model. Each colored line represents different percentiles indicating different susceptibility to motion sickness. Any parameter selected along a particular line will yield the same probability of getting motion sickness as any other point on that line. This feature

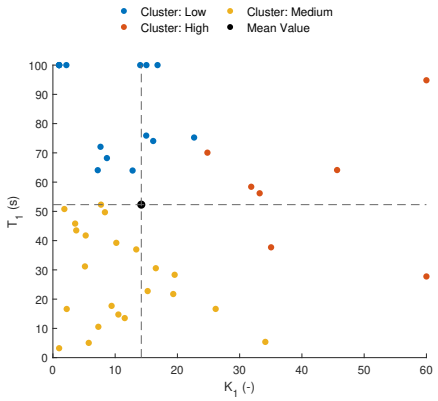

Figure 4.11: Parameter distribution (estimated gain (K_1) and time constant (T_1)) for the AM2 model. Parameter sets are classified into three groups based on the motion sickness susceptibility - high in red, medium in yellow and low in blue. Black dotted lines show the mean values for K_1 and T_1.

is beneficial for evaluating a motion profile at a designated percentile of the population. Additionally, this representation allows researchers and developers to assess the risk of motion sickness in different scenarios by simply selecting a percentile that matches their target audience. By understanding how motion sickness probabilities vary across different parameters, one can better design experiences or products that minimize discomfort for users. Overall, this approach aids in creating tailored solutions to enhance user comfort and experience in motion-related activities. The corresponding parameters for the Gaussian mixture model can be found in Appendix C.3.

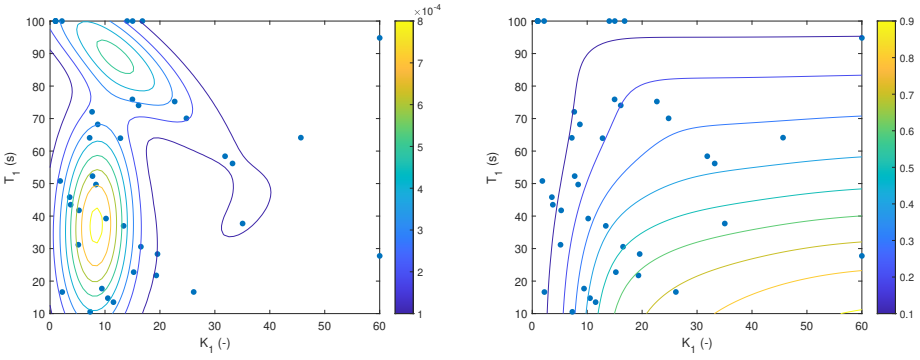

(a) Probability density function (PDF)

(b) Cumulative density function (CDF)

Figure 4.12: Three component Gaussian mixture model's probability distribution of the parameter sets (estimated gain (K_1) and time constant (T_1)) for the AM2 model.

With this probabilistic model, we can sample parameters randomly or based on the probability of getting sick (from 0 to 1). Here, figure 4.13 shows an example of randomly sampled 1000 parameter sets overlayed on the actual parameters estimated from the other

datasets. The sampled parameters have the same distribution as the actual real estimated parameter sets.

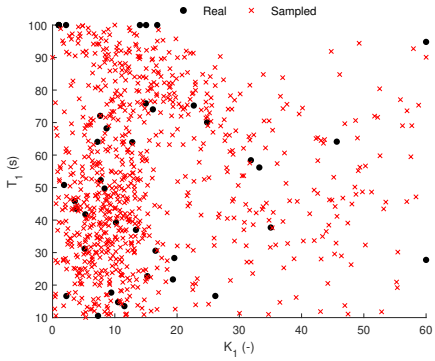

Figure 4.13: Sampled parameter sets (red cross) from the probability density function of the parameter distribution (estimated gain (K_1) and time constant (T_1)) for the AM2 model (black dots).

To show a use case of this probabilistic model, we simulated these 1000 sampled parameter sets on the completely independent Sickness Recreation dataset with 47 participants, see Table 4.1. This dataset is collected with the same participants being driven manually in a semi-urban environment and in automated mode on a test track with the same vehicle. The median MISC with the 25th and 75th percentile is shown below in figure 4.14. This is overlayed with the median and 25th/75th percentiles from the 1000 sampled parameter sets obtained from the probabilistic model. It is observed that the two MISC traces are highly similar, with an average RMSE of 0.47 (RMSE of 0.65 for 'On Road' and 0.29 for 'On Track'). However, the model prediction somewhat underestimates the sickness variance. This can be seen especially at the start, where the experiment data shows some people jumping to MISC of 1 very quickly, which is not seen in the model predictions.

Overall, these results indicate that we can use the probabilistic model to predict the variation in expected motion sickness levels for a new population in untested experiments and scenarios, including those using various motion planning or motion cueing algorithms.

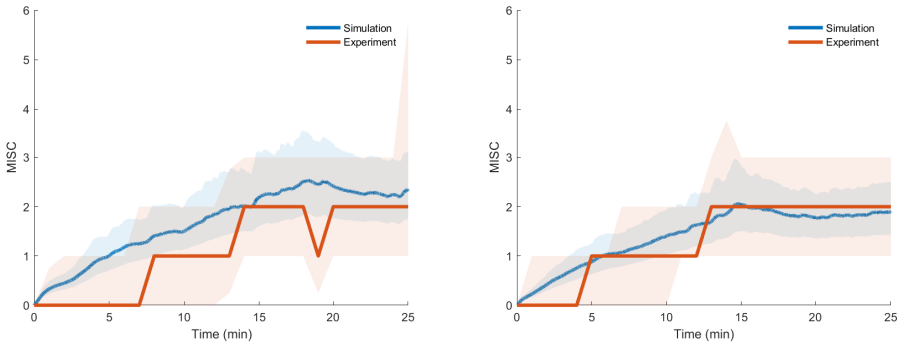

(a) On Road (b) On Track

Figure 4.14: Experimentally reported MISC and predictions of MISC on the 'Sickness recreation' dataset (Harmankaya et al., 2024) from sampled parameter sets from the probabilistic parameter distribution model (estimated gain (K_1) and time constant (T_1)) for the AM2 model with the shaded region showing the 25th to 75th percentiles.

4

4.4 Discussion

Combined Model Framework for Individual Motion Sickness Predictions

This paper introduces and validates a novel combination of models to create a framework to predict an individual's motion sickness level in vehicles and simulators. This model framework combines a group-average 'conflict generation' model with an individual 'conflict accumulation' model to capture individual susceptibility differences. Furthermore, by using a 'conflict generation' model that includes visual inputs, various vision conditions (such as external, internal, and only vision) can be simulated. This is crucial in simulators where motion sickness occurs due to a strong influence of visual cues. We hypothesised that using a 'conflict accumulation' model with individualised parameters will result in greater accuracy compared to a model that uses group-averaged parameters. Hence, in this paper, we assessed the feasibility and accuracy of this new model approach for motion sickness predictions.

It is clear from the obtained results (see figures 4.6 to 4.9 and table 4.4) that 'conflict accumulation' models with individualised parameters enable improved modelling of the motion sickness responses of individuals as compared to using the group-averaged models, as considered for AM0. In addition to this, the 'conflict accumulation' models we use (AM0-5) also capture the recovery phase of the experiment (see figures 4.6 to 4.8) and, theoretically, the hypersensitivity in a following second motion exposure as shown in Irmak et al. (2022, 2020). This recovery phase takes a few minutes and is not captured by often-used MSI predictions that typically implement a leaky integrator with a time constant of 12 min. for conflict accumulation Kamiji et al. (2007); Liu et al. (2022). These results are in line with the work by Irmak et al. (2020) where individualised fits with the same accumulation model

(AM4a) reduced the prediction error by a factor of 2 in a slalom drive with a frequency of 0.2 Hz and lateral accelerations with a peak amplitude of 0.4 g with eyes closed. The limitation of this previous work was that no 'conflict generation' model was considered; instead, the one-dimensional lateral acceleration conflict was simply used directly as the input to the accumulation model. Our work extends this by using a 6 degrees-of-freedom 'conflict generation' model to generate the conflict in realistic driving conditions with varying vision conditions, thereby expanding the coverage to full 6 degrees-of-freedom vehicle motion. Including an explicit 'conflict generation model' allows the model to be used in various conditions as well, be it variation in vision or motion.

This way, a single set of parameters, estimated using data from all required conditions, can characterize an individual across various motion and vision conditions. Estimating the parameters on all available conditions is important as it facilitates a more robust modelling of how different factors contribute to motion sickness. It prevents overfitting, as the model is not solely fitted to specific scenarios but is rather modelled by the collection of individual responses across various contexts. This generalisability is crucial in real-world applications, where individuals may encounter unfamiliar situations that were not part of the initial training dataset.

This approach is not limited to the SVC model, which we used as the 'conflict generation' model. Any other 'conflict generation' model can be used, such as any of the versions of SVC by Kamiji et al. (2007); Liu et al. (2022); Wada et al. (2020) or the Multi-Sensory Observer Model by Clark et al. (2019); Newman (2009).

Accumulation Model Parameter Reduction

We investigated reducing the number of estimated individual model parameters. The 'minimum effective' model (AM2) well-captured sickness in individuals. While models such as AM5, AM4a, and AM4b provide better accuracy than the AM2 model, they require more estimated parameters (5, 4, and 4, respectively). This higher number of individually estimated parameters may cause overfitting and hinder generalisability, leading to non-unique parameters that reduce model's reliability. By using the relations and values mentioned in previous studies, Irmak et al. (2022, 2020); Oman (1990), the number of estimated individual parameters could be limited to 2, ensuring uniqueness and avoiding overfitting on the sparse (in conditions) dataset. Overfitting may degrade a real-world performance where conditions differ from training data. A concise and relevant parameter set enhances the robustness and generalisability of predictions, ensuring application in untested situations. This balance between simplicity and effectiveness positions our model as a powerful tool for predicting motion sickness across diverse situations, improving interventions and user experiences. Additionally, a significant reduction in computation time is achieved for the parameter estimation – by a factor of 4 from 48 to 11 seconds for 40 min of simulation – highlighting the efficiency of the AM2 model. An even larger benefit would be observed in stochastic modelling, where a 5-parameter model would take exponentially more time. However, there is no difference when using these models for online prediction of sickness levels.

Probability Distribution of Individual Parameters

We created a distribution of the parameter sets, which can be used to sample any number of parameter sets (figure 4.13 and simulate the motion profile to predict the distribution of motion sickness levels. This has been demonstrated in figure 4.14 where the simulated sickness predictions closely match the experimentally observed median sickness levels. The difference in the spread of sickness is likely due to the selection of participants with extremely high or low sickness susceptibility, which is sometimes not correctly reported in the self-reported Motion Sickness Susceptibility Questionnaire. Additionally, at the start of the experiments, some of the participants quickly reported a MISC of 1. Our models do not capture this, but instead, due to the inherent nature of the models, there is a continuous increase in MISC over time. If this is instead discretised as is reported by the participants, the sickness predictions match even better, and the spread of MISC is completely inside the experimentally reported MISC (see Appendix C.4). This proves that we can use this probability distribution to predict expected motion sickness levels for untested experiments and scenarios, including those using various motion planning or motion cueing algorithms. Also, this can also be used as a proxy for Motion Sickness Dose Value (MSDV), which is an ISO standard (International Organization For Standardization, 1997) and uses weighted root mean squared acceleration as a measure of motion sickness severity. This has been known to not accurately capture the dynamic nature of motion sickness, especially the quick recovery from sickness, which is not captured by MSDV due to its monotonous nature and lack of any leakage term (International Organization For Standardization, 1997).

Practical Applications

The probabilistic approach enables the model to predict variations in motion sickness outcomes across a population, facilitating advanced vehicle motion planning, such as in Li and Chen (2022), and motion cueing algorithms in driving simulators, such as in Jain et al. (2023a), and flight simulators, such as in Lewkowicz (2019). Using a model-based control method, this model framework can be included in the plant model to forecast motion sickness levels. This way, motion sickness levels can be controlled by considering each individual's susceptibility. Vehicle motion in automated vehicles and platform motion and tilt coordination in simulators can be optimised to minimise their effect in eliciting motion sickness. Using these models, the motion profiles can be tuned to reduce the dropout of participants in simulator experiments due to motion sickness.
Moreover, this model framework can also be used during the process of experiment design. Algorithms can be benchmarked on different thresholds of motion sickness susceptibility. Offline analyses can be run on a large synthetic sample of a population before real-world testing on humans. This will greatly speed up the testing process.

Thus, our next steps involve applying this model both in pre-experiment and real-time during the experiment.

Challenges and Limitations

We now tuned individual parameters of the accumulation model while keeping the (many) parameters of the sensory conflict model constant. This assumes that the conflict generated is the same for all individuals, and the difference in motion sickness development is purely due to the difference in the accumulation of the conflict. This implies that people respond exactly the same way to conflicts, even in very different settings (e.g., internal vs external vision). This assumption is made because the initial stage of conflict generation primarily involves basic sensory mechanisms all humans share. However, the degree to which different individuals accumulate and tolerate this conflict can vary widely. This variation can be influenced by genetic and psychological factors. Previous experiences and conditioning can also influence susceptibility. Additionally, individuals who frequently experience motion sickness may anticipate symptoms more anxiously, exacerbating the response. However, this assumption contradicts the observations by Irmak et al. (2021), where they found a correlation of 0.74 between an individual's sickness susceptibility and their subjective vertical time constant, which is a parameter in the conflict generation model. This correlation suggests that the subjective vertical time constant plays a significant role in how conflicts are generated and perceived, challenging the notion that conflict generation is uniform across individuals. Consequently, it is highlighted that there is a need for a model that incorporates individual differences in both conflict generation and accumulation in order to more accurately reflect the complex interplay of factors influencing responses to motion sickness.

A main limitation of the model during individual fitting is that it does not fit participants who get highly motion sick with internal vision and do not get sick with external vision well (for example, P14 in figure 4.6 and P2 in figure 4.8). This sharp shift in motion sickness dynamics cannot be captured by our model framework. This may be due to the inherent difference in conflict generation, which we assume to be the same in all individuals, or to our assumption that gains in the SVC model are independent of the visual condition. Also, in the 'NDRT Drive' dataset, there are conditions – 'Visual Static' and 'Visual Dynamic' – with internal vision that feature varying levels of visual stimuli. We have chosen to model these identically due to the unavailability of control over the effect of vision on conflict generation, as the vision is either represented as 1 or 0. One solution is to model each condition with a separate set of parameters. Doing this, the RMSE was reduced, on average by 35%, from 1.54 to 1 MISC, compared to fitting all conditions together. However, this comes with a significant reduction in predictive accuracy on other conditions by increasing RMSE by 69% from 1.54 to 2.6 MISC. This means we lose any generalisability in modelling other conditions and overfit the model to that specific condition. A better solution would be to estimate at least one additional parameter, one of which could be the vision gain in the 'conflict generation' model or other perception parameters. People not only differ in motion sickness susceptibility but also in their perception of vision. Each human will have a different contribution of visual and vestibular signals for their state estimation. By adjusting the vision gain in the 'conflict generation' model, the contribution of vision to the estimates can be tuned.

Another limitation is that the model is sensitive to the location of the Inertial Measurement

Unit (IMU), i.e., the input of the model needs to be based on either vehicle motion or head motion for it to predict motion sickness reliably. For the modelling of the distribution of parameters, the inputs are vehicle motion. This is due to the larger number of datasets available with vehicle motion measured as compared to datasets with head motion measured. For example, if we take head motion as input, the estimated gain (K_1) is much smaller than for the datasets which use vehicle motion (see Appendix C.5). Also, the Hill function accumulation model predicted a reasonable MSI magnitude in the Slalom Drive but highly underestimated sickness in the Car and Simulator dataset. Ideally, we would like to always use recorded head motion, which is more representative of the motion experienced by the vestibular system. If this is not available, we could use biomechanical human/seat models or linear transfer functions to convert 6 degrees-of-freedom vehicle motion to 6 degrees-of-freedom head motion (Desai et al., 2023; Happee et al., 2023). This way, even when head motion is not recorded, a head motion based stochastic sickness generation model can be used.

4.5 Conclusion

This study presents a novel framework for predicting motion sickness (in MISC) accumulation in time by integrating a group-average 'conflict generation' model with an individualised' conflict accumulation' model. By utilising acceleration and angular rotational data, the model adjusts parameters specific to each individual's motion sickness response, as measured by the Misery Scale (MISC). By simultaneously fitting for various conditions across different datasets, the model successfully estimates a single set of parameters applicable to each participant, offering a highly personalised approach to understanding motion sickness dynamics. A reduction of estimated parameters not only simplifies the model but also minimises the risk of overfitting, ensuring robust application in real-world scenarios. This framework achieves an average RMSE of 1.54 with just two estimated parameters - a gain (K_1) and a time constant (T_1). The integration of the two models demonstrates significant improvements in predicting motion sickness, achieving better fits by 34% compared to traditional group-averaged models (1.54 RMSE for AM2 vs 2.06 RMSE for AM0).

Moreover, the modelling of the probabilistic distribution of estimated accumulation parameters enables effective sampling of parameter sets, facilitating predictions for untested scenarios and improving the adaptability of motion sickness assessments. Such flexibility reduces reliance on extensive human testing experiments and accelerates testing processes.

Overall, this research paves the way for more refined and personalised applications in both driving simulators and real-world automated vehicle contexts, promising improved user experiences and outcomes.

5

Impact of Physical and Visual Motion on Subjective Perception of Vertical Orientation

Whatever happens, happens

Spike Spiegel

This chapter is based on *Kotian, V., Pool, D. M., Happee, R., Li, S. & Wada, T. (2025). Impact of Physical and Visual Motion on Subjective Perception of Vertical Orientation. Research Square preprint.*

The appendices for this chapter can be found at Appendix D.

Abstract

This paper investigates human pitch motion perception under varying visual and mechanical motion conditions and evaluates whether findings can be captured by the Subjective Vertical Conflict (SVC) model. Thirty-two participants experienced ramp-like pitch rotation stimuli at 0.5, 1, 2.5, and 5 degrees per second, and continuously indicated perceived rotation. Motion was applied, rotating the seat and a dot pattern in a head-mounted display, across four conditions: Only Vision, External Vision (seat rotates, vision locked in space), Internal Vision (seat rotates, vision locked to seat), and No Vision. Results showed that participants underestimated rotation amplitude by around 20% with a response delay of 0.75 seconds, without significant effects of vision across the three conditions involving mechanical pitch motion.

We evaluated the full SVC model with visual verticality (VV) and visual rotation (VR) perception and the SVC-VR model with only visual rotation perception, which was previously shown to best predict motion sickness. With published parameters, both SVC models generated highly unrealistic predictions for pitch perception. The SVC-VR model even predicted an incorrect perceived motion direction in the Only Vision condition. For both SVC models, parameter tuning significantly improved the fit to the subjective perception data while maintaining adequate sickness predictions, and incorporating vestibular perception thresholds further enhanced accuracy. These results demonstrate crucial limitations of current models and published parameters. Future research should validate model adaptations across diverse motion paradigms for motion perception and motion sickness to enhance prediction accuracy in virtual reality, automated vehicles, and simulator environments.

5.1 Introduction

The human perception of motion and spatial orientation relies on a complex interaction of sensory inputs, primarily from the visual and vestibular systems. Visual cues provide critical information regarding self-motion velocity through optic flow, while also serving as a reference for spatial orientation through perception of the visual vertical. Even in the absence of physical motion, visual cues can induce strong illusions of self-motion, known as vection (Brandt et al., 1973). Vection is also linked to Visually Induced Motion Sickness (VIMS) (Nooij et al., 2017). This is particularly relevant for automated vehicles and for virtual reality, where visual information dominates the perception of movement and frequently causes motion sickness. This illusion of self-motion, when people are presented with moving visuals without mechanical motion, can be easily seen in a planetarium with immersive 360˚ projection systems. The moving visuals induce a perception of motion, thereby affecting orientation and balance. This leads to apparent incongruence between visual and vestibular motion cues. Similar incongruences emerging in driving simulators are also associated with motion sickness. However, motion sickness can emerge even when all motion cues are in perfect agreement (e.g., driving with out of the window view) or without vision. This is associated with sensory-expectancy conflicts—the mismatch between currently sensed signals and the expected signals derived from the central nervous system's internal models. Such mismatches are believed to be the dominant cause of motion sickness (Bos and Bles, 1998; Kotian et al., 2024; Wada et al., 2020). The pivotal role of sensory-expectancy conflicts in this process has been long established (Reason, 1978b) and was recently directly validated in humans by Allred et al. (2025), who demonstrated that isolating vestibular conflicts is sufficient to induce motion sickness. Crucially, these vestibular expectations are derived from a multisensory estimate of the body's state. Since visual cues modulate the internal model's estimate of spatial orientation (and thus the expected vestibular signal), investigating how visually induced perception of orientation arises is essential for improving models that predict both motion perception and motion sickness.

Ideally, a single model should be capable of accurately capturing and predicting both motion perception and motion sickness. To evaluate this, we previously validated various models of motion perception and sickness for a wide range of conditions with different combinations of the visual inputs being visual rotation velocity (VR) and visual verticality (VV) (Kotian et al., 2024). In this comparative analysis, it was found that the SVC-VR model (Subjective Vertical Conflict model with visual rotation velocity (VR) input) by Wada et al. (2020) provided the best predictions for motion sickness, specifically in conditions involving visual stimuli. This aligns with the fact that the SVC architecture naturally captures the frequency sensitivity of motion sickness (Irmak et al., 2023), which is a distinct strength of the model. The SVC model is based on the concept that the central nervous system maintains an internal model to estimate the subjective vertical, defined as the direction of gravity relative to the head. This estimate is used to resolve the inherent ambiguity between linear acceleration and tilt. Motion perception and sickness are thus modeled as consequences of the conflict between actual sensed signals and the expected signals derived from this internal estimator. Integrating visual information into this framework is essential. Visual rotation cues, such as optic flow, provide rotational velocity information that is integrated

to update the internal orientation estimate. Furthermore, visual verticality cues, such as the horizon, serve as a primary reference for spatial orientation and strongly influence the internal estimate of gravity. Consequently, visually induced rotation or shifts in the subjective vertical can directly alter the interpretation of vestibular signals, leading to illusory perceptions of body tilt or self-motion. More details on this implementation of the SVC model are provided in section 5.3.2. While alternative architectures exist such as the Multisensory Observer Model (MSOM) (Allred and Clark, 2024; Clark et al., 2019; Newman, 2009) which represents a popular choice and is widely regarded as a leading framework for simulating motion perception. However, while such architectures show promise and are undergoing further development, they currently face challenges in predicting visually induced sickness with the same accuracy as SVC-VR, as demonstrated by Kotian et al. (2025). Furthermore, the SVC architecture naturally captures the frequency sensitivity of motion sickness (Irmak et al., 2023), whereas the MSOM requires additional weighting filters to match human frequency sensitivity data (Allred and Clark, 2024). We acknowledge that the SVC model relies on verticality conflicts and thus does not inherently predict sickness in Earth-parallel (yaw) rotation, where the gravity vector remains constant relative to the head (Nooij et al., 2017). However, just as Allred and Clark (2024) illustrated that sensory integration models can be adapted to include multiple conflict terms (e.g., yaw velocity), the SVC model could theoretically be extended to capture these effects as well. For the current study, however, we focus on the SVC model to determine if its predictive capabilities for pitch perception can be reconciled with its success in predicting motion sickness.

As shown in Kotian et al. (2024) the SVC-VR model accurately matched measured perception responses in several well-known motion perception paradigms. However, testing the SVC-VR model for motion perception, we also found a counterintuitive result. When exposed to visual (pitch or roll) rotation without mechanical motion, the SVC-VR model counterintuitively predicts perceived motion that is of opposite sign compared to the applied input, see figure 5.1, based on (Kotian et al., 2024). As also shown in this figure, the complete SVC model including a visual verticality (VV) input (SVC-VR+VV) does predict the expected direction of perceived motion. No existing literature directly confirms or disputes these predictions. However, the opposite perception of the SVC-VR model contradicts a well-known phenomenon usually experienced in dome cinemas and virtual realities, as discussed before. This counterintuitive finding was not reported or analyzed in (Kotian et al., 2024), but is addressed in the current paper. While many studies examine pitch perception in somatogravic illusions (Correia Grácio et al., 2013), centrifuge experiments (Merfeld et al., 2001), or rotational motion sickness (Joseph and Griffin, 2008; McCauley et al., 1976), the effect of vision in such contexts remains underexplored and poorly understood. Thus, our goal is to investigate how visual cues affect pitch perception and to evaluate how well current motion perception models, like the SVC, can predict the measured variation in human perception responses across different vision conditions.

We address this main goal in multiple stages. First, we conduct a fundamental pitch motion perception experiment where participants are subjected to pitch rotations with various maximum rotational rates and different vision conditions implemented using a head-mounted display (HMD). To measure the perceived pitch rotation, participants continuously report their perceived pitch using a joystick. This allows us to capture both the magni-

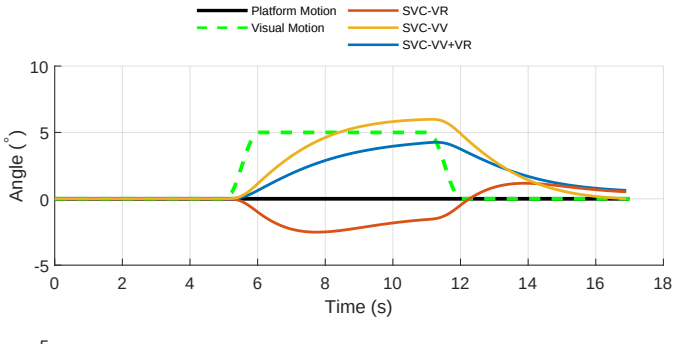

Figure 5.1: Perceived motion predicted by the SVC model in response to a visual pitch motion relative to the head without any mechanical motion; simulation results based on (Kotian et al., 2024). The complete SVC model (SVC-VV+VR) and the SVC-VV model overestimate the actual pitch, but the direction of the perception is as expected: forward rotation of the visual field results in a perception of rearward rotation. However, the SVC-VR model predicts an counterintuitive perception of forward rotation. Here, the complete SVC model includes perception of visual verticality (VV) and visual rotation velocity (VR), where the other SVC variants include only VR or VV perception.

tude and timing of pitch perception variations. Next, we compare the observed responses with predictions made by the SVC model. Finally, we demonstrate that both the SVC-VR and the SVC-VR+VV models can accurately fit the actual human response with adapted parameter values. In Kotian et al. (2024), we demonstrated that the Multi-Sensory Observer Model (MSOM) (Clark et al., 2019; Newman, 2009) best matched perception experiments, whereas the SVC-VR model best matched motion sickness experiments. In Appendix D.5, we show that the MSOM also quite well matches the new perception data presented in this paper.

5.2 Methods

5.2.1 Experimental Design and Participants

Participants were exposed to passive pitch motion on a motion platform where visual motion was presented using a head-mounted display (HMD) (figure 5.5). We selected a ramp-based pitch attitude motion stimulus, as in figure 5.1, to assess static perception of pitch attitude, and varied the maximum rotation rate (ramp steepness) to assess perception dynamics. A within-subjects experiment was conducted with thirty-two participants (N=32), where each participant experienced all 32 experimental conditions. These conditions were defined by combining four vision conditions (section 5.2.3) and four rotational rate settings to cover a broad frequency range (section 5.2.4). Furthermore, both positive and negative pitch stimulus directions (forward/rearward) were tested to assess direction bias. Each of the 32 conditions was tested twice per participant. The order of condition testing was counter-balanced using a Latin square, ensuring that each participant had a unique sequence of experimental conditions.

5.2.2 Participants

Thirty-two healthy students with self-reported normal vestibular function voluntarily participated in the experiment. The group included 8 females and 24 males, with a mean age of 25.9 years (SD = 4.3 years). No formal vestibular function tests were conducted.

5.2.3 Vision conditions

We tested four vision conditions, all using the head-mounted device (HMD), to assess the effects of visual and mechanical pitch motion:

- *Only Vision*: Participants viewed a rotating dot pattern through the HMD (see figure 5.5c) to create a sensation of pitching forward/rearward in the absence of physical motion. A 1-degree mechanical pitch rotation was also applied to prevent participants from detecting the simulator's lack of vibrations in this condition. A 1-degree pitch was chosen so that the maximum angular velocity, in any case, is well below the rotational velocity perception threshold of 3.6 degrees per second (Houck et al., 2005; Reid and Nahon, 1985). This 1-degree platform pitch was directed opposite to the 5-degree visual motion. However, the 1-degree pitch tilt is at the limit of the threshold for specific force perception (Houck et al., 2005; Reid and Nahon, 1985). We acknowledge that vestibular thresholds are frequency-dependent (Lim et al., 2017). Although the angular velocity was sub-threshold, the specific force (tilt) cues were likely near the threshold of detectability. We hypothesize that participants would not perceive the small, 1-degree physical pitch tilt and would perceive pitch in the direction opposite to the visuals. Thus, the counterintuitive SVC-VR model prediction from figure 5.1 would not be observed in the measured perceived rotation.

- *External Vision* (Seat rotates, vision locked in space): To replicate a natural combination of visual and vestibular motion, the visual scene was kept Earth-Stationary (inertially fixed). This was achieved by moving the dot pattern relative to the head with a magnitude equal to the seat rotation, but in the opposite direction (veridical magnitude). Consequently, the visual motion was congruent with the vestibular motion. The hypothesis is that participants would achieve the most accurate perception of self-motion because the visual and physical motions are congruent, as in a natural setting.

- *Internal Vision* (Seat rotates, vision does not rotate relative to the head): Participants viewed a dot pattern where the dots did not move relative to their head within the HMD, while the seat rotates, leading to conflicting visual and vestibular stimuli. This mimics being in a moving vehicle without out-of-the-window view. We hypothesize that there would be a lower perceived pitch rotation due to the fixed visual input, leading to an underestimation of the actual mechanical motion.

- *No Vision*: Participants wore the HMD, but the display was blank, and their eyes were open while the seat physically rotated. The hypothesis is that perception would be

less accurate than in the 'External vision' condition because of the absence of any visual information to support and complement physical motion cues.

5.2.4 Stimuli

Each trial was composed of a randomised sequence of the 32 experimental conditions, with a 20-second rest period in between. To prevent participants from anticipating the stimulus dynamics or direction (predictability confounds), the order of the 32 conditions was randomized and counter-balanced. While the peak amplitude was constant, the variation in rotational rates (and thus motion duration) and directions ensured that the specific motion profile remained unpredictable. Each experimental condition applied a ramp signal, smoothed using a half-sine wave, to reach a pitch orientation of 5 degrees with respect to vertical. A fixed peak amplitude of 5 degrees was chosen to ensure the stimulus remained above perception thresholds while minimizing the contribution of somatosensory cues (e.g., pressure distribution on the seat and backrest), which become dominant indicators of orientation at larger tilt angles. This was followed by a 5-second hold at a pitch of 5 degrees, and another smoothened ramp returning to zero-degree pitch. For the ramp signal, we chose four different ramp durations – 1, 2, 5, and 10 seconds – which correspond to frequencies of 0.5, 0.25, 0.1, and 0.05 Hz for the half-cosine wave and mean rotational rates of 5, 2.5, 1, and 0.5 degree/s (peak rotational rates of 7.85, 3.93, 1.57, and 0.79 degree/s). The frequencies were chosen to cover the relevant range for motion sickness causation, which has a peak sensitivity around 0.16 Hz (McCauley et al., 1976). A zoomed-in version of the 'No Vision' condition with the four different rotation rates is shown in figure 5.2. An example sequence of multiple conditions is shown in figure 5.4.

5.2.5 Measurement

The perceived direction of gravity (perceived rotation angle) by the participant was continuously measured (50 Hz sampling rate) using the custom measurement device shown in figure 5.3. The device utilizes a contactless magnetic rotary position sensor (AS5600) with 12-bit resolution ($\approx 0.088°$). This high precision ensures that the measurement resolution significantly exceeds the human motor variability and perceptual resolution required for the 5 degree range. Participants were instructed to continuously indicate the direction of verticality with this device. In the context of this experiment, the perceived pitch angle is defined as the deviation of the participant's body axis from this reported vertical. It is important to note that this measure reflects the body's orientation relative to the perceived direction of gravity (Subjective Vertical) rather than the true Earth-vertical. We selected this continuous indication task over direct magnitude estimation (e.g., verbal reporting of pitch angle) because it enables the recording of high-frequency temporal dynamics in perception throughout the motion profile, which is difficult to achieve with discrete estimation methods. Thus, this single continuous measure captures the time-varying evolution of perceived pitch orientation, reflecting the integration of both motion cues (dynamic change) and verticality cues (static tilt). An example of a raw measurement of the perceived pitch rotation obtained with this device is shown in figure 5.4. To account for static offsets (e.g., individ-

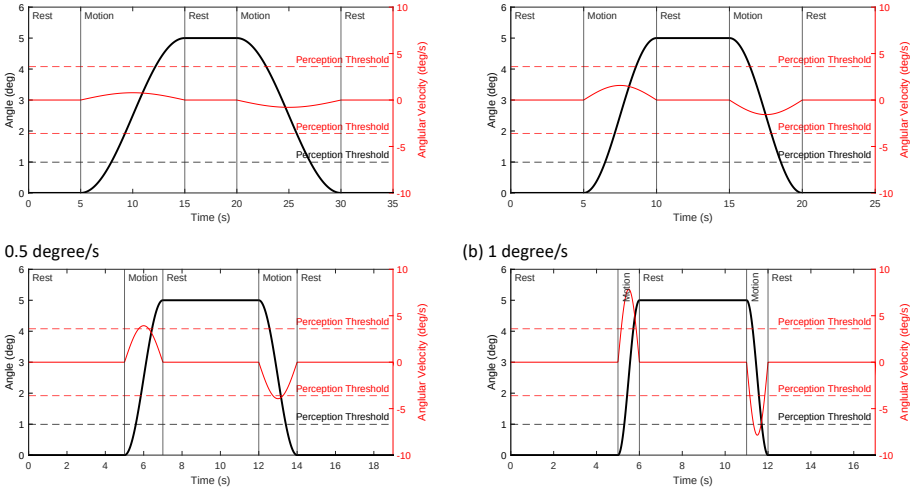

(a) 0.5 degree/s

(b) 1 degree/s

(c) 2.5 degree/s

(d) 5 degree/s

Figure 5.2: Example stimuli for the condition of 'No Vision' for the four tested mean rotational rates, with the different stages of the stimuli separated with vertical lines and described with text. The angular rotation is shown in black, and the angular rotational velocity is shown in red. The black dashed lines indicate the perception threshold for pitch due to the specific force threshold of 0.17 m/s^2, the red dashed lines indicate the pitch velocity threshold of 3.6 degrees per second (Reid and Nahon, 1985).

ual resting position bias), the subjective response data were zeroed during post-processing by subtracting the mean value of the pre-stimulus phase for each individual stimulus.

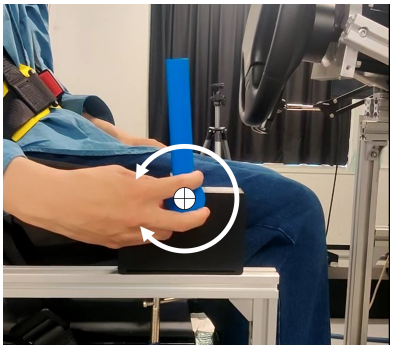

Figure 5.3: Measurement device used by the participants to report the perceived direction of gravity (pitch orientation). The centre of rotation of the device is shown with a white circle, and the direction of rotation is shown with white arrows.

5.2.6 Apparatus

The motion was presented using the '*6DOF Motion Platform*' at the Human Robotics Lab, Nara Institute of Science and Technology. The participant was rotated around the centroid

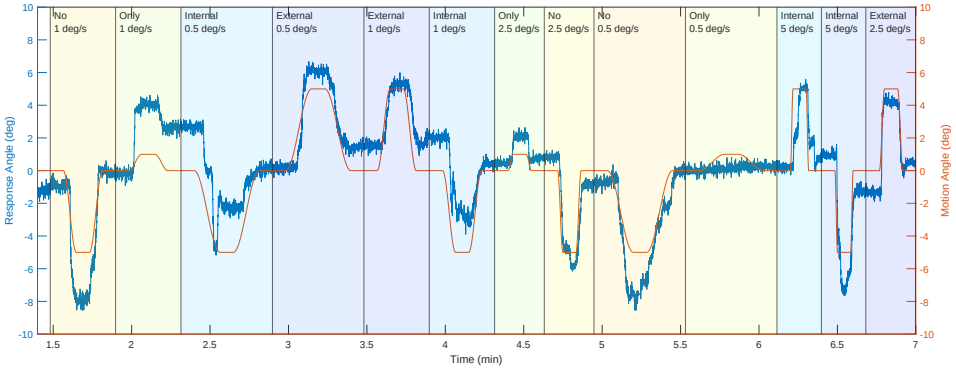

Figure 5.4: Example signals for a sequence of different mean rotational rates and vision conditions mentioned at the start of each stimulus. The applied stimulus is shown in an orange line, and the perceived pitch response of this representative participant is shown in a blue line. Note that the deviations from baseline after motion offset reflect individual perceptual drift and motor variability inherent to the continuous reporting task.

of the lower portion of the seat. Although the eccentric rotation introduces linear translations at the head, calculations estimate the tangential and centrifugal accelerations to be < 0.07 m/s^2, remaining well below the linear perception threshold of 0.17 m/s^2 (Reid and Nahon, 1985). Thus, the primary vestibular stimulus remained the reorientation relative to gravity. The participant was seated in a bucket-style racing seat equipped with a headrest. Seat belts were used to limit the motion of the trunk. To strictly enforce head restraint and prevent compensatory head movements, participants wore a neck brace that limited neck articulation, while the headrest provided posterior support. This setup (see figure 5.5) ensured the head remained almost rigidly coupled to the motion of the platform. The visual stimuli were presented using an HTC Vive Pro 2, head-mounted display (HMD), see figure 5.5b. The visual stimulus consisted of a pattern of white random dots displayed against a black background within the HMD as seen in figure 5.5c. The dots were arranged in a virtual sphere surrounding the participant at a radius of 3 meters. The effective Field of View (FOV) was determined by the HTC Vive Pro 2 HMD (approximately 120° horizontal and 120° vertical), providing sufficient peripheral cues to distinguish rotational pitch flow from translational heave flow.

5.2.7 Analysis of Subjective Responses

To quantify the dynamic characteristics of the participants' pitch perception, four key metrics were calculated: settling time, rise time, lag time, and steady-state amplitude. These metrics are illustrated in figure 5.6 and calculated as follows:

- *Settling time*: the time elapsed from the stimulus onset until the response enters and remains within a $\pm 5\%$ error band of the final steady-state amplitude.
- *Rise time*: the time duration required for the response to transition from the initial rise to the start of the steady-state phase, defined as the interval between reaching

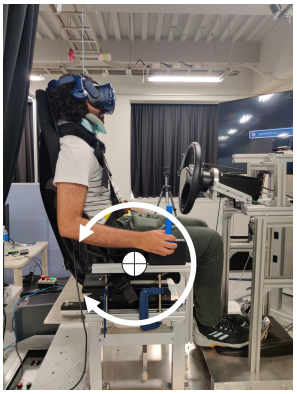

(a) 6DOF Motion Platform. The centre of rotation is shown with a white circle, and the direction of rotation is shown with white arrows.

(b) Head Mounted Display (HMD) and neck brace

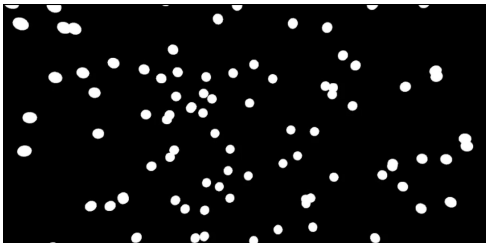

(c) View inside the HMD

Figure 5.5: Apparatus used for the experiment

10% and 90% of the steady-state amplitude.

- *Lag time*: the time duration between the onset of the physical/visual stimulus and the onset of the participant's response. Response onset was defined as the moment the signal rose more than 5% above the initial baseline (zero steady-state) for each condition

- *Steady-state amplitude*: the mean value of the response angle calculated over the final 2 seconds of the constant pitch phase.

Effects of vision condition and rotation rate on these metrics are shown in figure 5.8, and effects of direction and further comparisons are presented in Appendix D.2. A repeated-measures analysis of variance was conducted to determine whether motion direction, vision condition, or the rotational rate had significant effects. This approach was chosen to inherently account for inter-subject variability and individual response biases by isolating the within-subject variance.

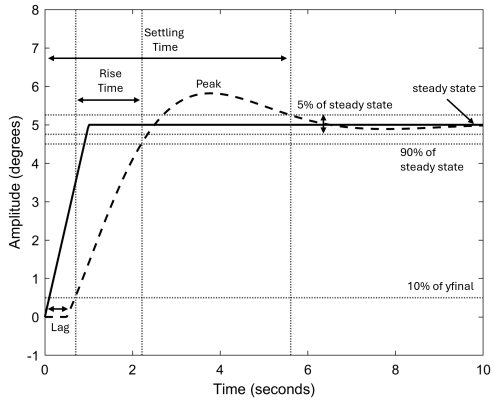

Figure 5.6: Illustration of how the four metrics - settling time, rise time, lag, steady state amplitude - are calculated. The black solid line represents the stimulus (platform tilt), while the dashed line represents an idealised subjective response.

5.2.8 Ethical Approval Declarations

The experiments were carried out in accordance with the relevant guidelines and regulations, and all experimental protocols were approved by the Ethics Review Committee of Nara Institute of Science and Technology (Approval Number: 2024-I-1). Additionally, written informed consent was obtained from all participants before their participation in the experiment.

5.3 Results

5.3.1 Subjective Responses

The median subjective responses of the 32 participants are shown in figure 5.7 for the four tested rotational rates (different subfigures), four vision conditions (colored lines), and two motion directions (top/bottom graphs). The corresponding spread (25th and 75th percentiles) is included in similar graphs in Appendix D.1, but omitted here for brevity. It is clear from figure 5.7 that the participants perceived pitch motion in the same direction as the platform motion stimulus in all vision conditions. On average, they tend to underestimate (on average by 20%) the magnitude of pitch tilt. Additionally, a noticeable delay (on average 0.75 seconds) was observed between the stimuli and the participants' subjective responses. We note that due to inter-subject variability in this onset latency, the aggregate median signal exhibits a smoother transition at motion onset compared to individual trials. Consequently, the model parameters fitted to this data represent the dynamics of a median observer rather than capturing the specific temporal delays of individual participants.

The calculated response metrics defined in section 5.2.7 (Settling Time, Rise Time, Lag Time, Steady-State Amplitude) were analyzed to compare conditions. Effects of vision condition

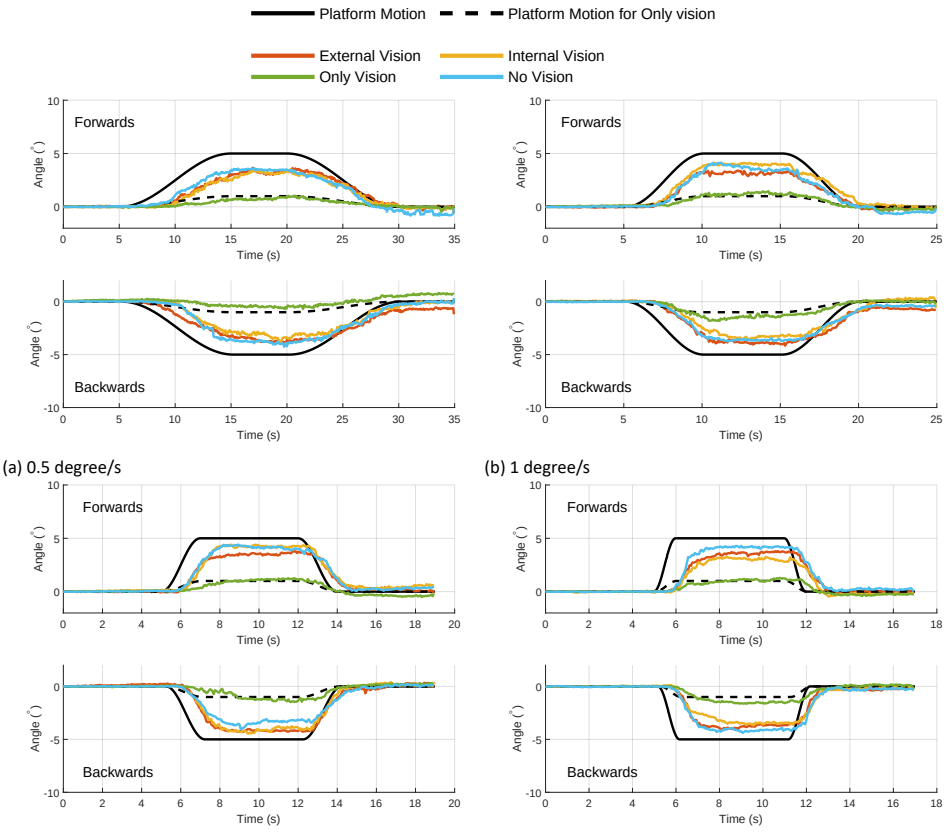

(a) 0.5 degree/s (b) 1 degree/s

(c) 2.5 degree/s (d) 5 degree/s

Figure 5.7: Median response across various mean rotational rates and various vision conditions. For the *Only Vision* case, a 1-degree physical pitch motion (black dashed line) was applied to prevent participants from detecting the simulator's lack of vibrations in this condition.

and rotation rate on these metrics are shown in figure 5.8, and effects of direction and further comparisons are presented in Appendix D.2.

The factor that showed the greatest effect was the rotational rate of the applied stimuli. As expected, a faster stimulus resulted in lower settling times ($p < 0.0001$), lower rise times ($p < 0.0001$) and lower lag times ($p < 0.0001$). The steady-state perception amplitude was not significantly affected by rotation rate ($p = 0.4$).

When comparing across the different vision conditions, there seem to be no significant differences (smallest $p = 0.55$) between all conditions with physical (vestibular) pitch motion ('External', 'Internal', and 'No Vision'). This result contradicts our hypothesis that 'External Vision' would provide the most accurate pitch perception. Specifically, we found no evidence that the addition of congruent visual cues enhanced pitch perception accuracy compared to conditions relying solely on vestibular cues or conflicting visual cues. The

scatter of the steady state amplitude seems invariant with visual condition (and rotation rate). Despite our expectations that congruent visual and vestibular cues in the 'External vision' condition would result in superior perception, and that a missing or stationary (conflicting) visual input would degrade perception in the 'No Vision' and 'Internal Vision' conditions, respectively, participants showed equivalent responses in all three vision conditions. These findings suggest that the visual information – consistent, conflicting or absent – did not influence participants' perception of pitch rotation in this experiment. This indicates a dominant role of vestibular cues but may also relate to limitations in the effectiveness of the selected visual stimuli.

However, there is a significant difference between the 'Only Vision' condition and others in terms of having a lower steady-state amplitude ($p < 0.0001$) and higher lag times ($p < 0.0001$). The steady-state amplitude is lower due to the much lower physical motion in this condition. The mean lag times are higher for 'Only Vision' at 2.73 seconds; however, the median lag times are very similar, in a range of 0.7 seconds, to other vision conditions, which have average lag times of 0.75 seconds.

In figure 5.7, the observed responses of the participants clearly do not show the counterintuitive result in the 'Only Vision' case as shown for the corresponding SVC model prediction in figure 5.1. Our hypothesis for the 'Only vision' condition was that participants would not perceive the small, physical pitch and would perceive pitch in the direction opposite to the visuals. Contrary to this hypothesis, the results show that perception was influenced by the subtle physical motion despite it being below the vestibular thresholds mentioned above.

Between the two directions of the stimuli, no significant differences are observed in rise times ($p = 0.4$) and steady state amplitudes ($p = 0.4$), suggesting that, on average, participants showed an equivalent response regardless of the direction of pitch. However, a significant difference was observed in settling times ($p = 0.031$) and lag times ($p = 0.017$), suggesting a difference in response delay between forward and backward motion. However, this difference is limited to a mean lag time of 1.69 seconds for forward and 2.11 seconds for rearward, and a mean settling time of 13.81 seconds for forward and 13.71 seconds for rearward. Lower lag times during forward movement may be caused by the support provided by the headrest, which pushes the head. Conversely, higher lag times during backward movement may be explained by the lack of head support. On the other hand, the difference in settling times of 0.1 seconds is small, suggesting that settling behavior is largely consistent across directions.

5.3.2 Subjective Vertical Conflict (SVC) model predictions

Modeling Approach

In this subsection, we compare the measured pitch perception responses from the experiment with predictions of different versions of the SVC model, which is a well-known sensory integration model designed to capture motion sickness. Bos and Bles (1998) developed the SVC model, which integrates vestibular motion cues from the otoliths sensing specific force (acceleration plus gravity) and the semicircular canals sensing rotational rate. This

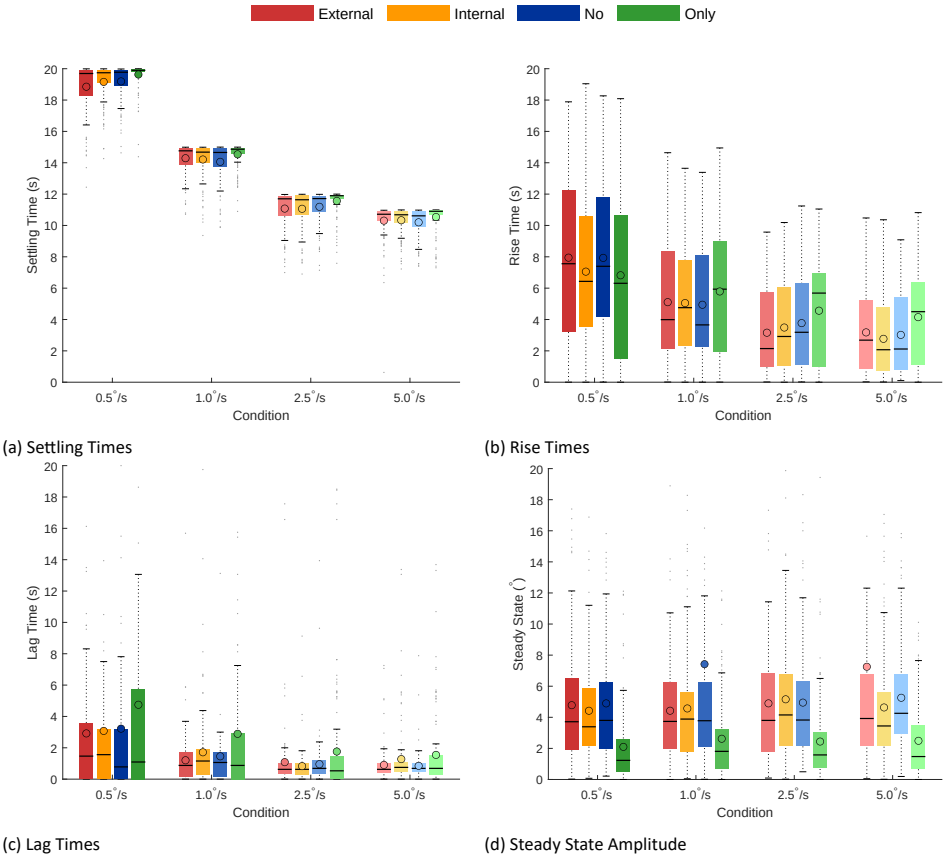

Figure 5.8: Box-plots comparing all 16 conditions of four rotational rates and four vision conditions (while averaging over forward and rearward pitch stimuli). The central black horizontal dash indicates the median, and the circle represents the mean. The box edges indicate the 25th and 75th percentiles (interquartile range), and the whiskers extend to the minimum and maximum values within the lower and upper fences (1.5 times the interquartile range).

model was later extended to six degrees of freedom by Kamiji et al. (2007) and improved by adding visual inputs in Liu et al. (2024); Wada et al. (2020). The model consists of three parts: the 'Visual-Vestibular System', the 'Internal Model' of the visual-vestibular system, and the 'Feedback' of errors (conflicts) between sensed signals and internal model predictions, as shown in figure 3.1. The main concept of this model is that the dominant conflict causing motion sickness is the mismatch between the internal estimate of verticality (orientation with respect to gravity) and the sensed verticality. This mismatch is labeled as Δv in figure 3.1. The otolith dynamics are assumed to be unity (OTO $= 1$), while the semicircular organs are modeled as a high-pass filter (SCC $= \tau_{scc}\, s^2/(\tau_{scc}\, s + 1)^2$). These same sensory models (SCC and OTO) are also included in the internal model. The LP block calculates the subjective vertical (direction and magnitude of gravity) by integrating angular velocity (ω) to rotate the internal gravity estimate, while extracting the constant inertial gravity contri-

bution from the sensed specific force through a low-pass filter with a time constant τ (Bos and Bles, 1998; Mayne, 1974). This interaction is governed by the differential equation $\dot{v} = \frac{1}{\tau}(f - v) - \omega \times v$, where $\times$ denotes the cross product. The model also includes feedforward pathways (dashed lines in figure 3.1) originally proposed by Kamiji et al. (2007) to model signals resulting from the summation of various sources contributing to self-motion perception. These include active knowledge about sensory consequences (efference copy), somatosensory information, and the effects of motion prediction or anticipation (Inoue et al., 2025; Oman, 1990; Wada, 2021) to model active knowledge about the sensory consequences of movement (efference copy) or anticipation (Oman, 1990). In this structure, the signal a represents the anticipated acceleration. However, as the current study investigates purely passive motion without prior motion information, the feedforward gains K_a and K_ω were disregarded ($K_a = 0$ and $K_\omega = 0$), consistent with previous validations (Irmak et al., 2023; Kotian et al., 2024).

In this paper, we adopt the SVC model version from Liu et al. (2024); Wada et al. (2020), based on the findings of Kotian et al. (2024), which is referred to as the SVC$_I$ model. The SVC$_I$ model includes integration (I) for the acceleration conflict feedback term. In the remainder of the current paper, we will refer to the SVC$_I$ model as SVC. The parameters for the SVC model can be found in table 4.2 and were originally published in Wada et al. (2020) and Liu et al. (2024).

This model can accurately replicate the frequency and amplitude dynamics of motion sickness as reported in numerous previous studies (Golding and Markey, 1996; Griffin and Mills, 2002b; Howarth and Griffin, 2003; Irmak et al., 2021, 2022; McCauley et al., 1976). Kotian et al. (2024) shows that the visual vertical input (VV, red pathways in figure 3.1) that has also been proposed for the SVC model is not effective for predicting sickness. Thereby the SVC-VR model disables the pathway for the visual vertical by setting the value of K_{gvis} to 0.

Table 5.1: SVC model parameters as defined in Kotian et al. (2024) and the original sources.

	Parameter Symbol	Value	Explanation
Anticipation Gains	K_a	0	Fully passive motion assumed
	K_ω	0	
Vestibular Feedback Gains	K_{ac}	1	as in Wada et al. (2020)
	K_{vc}	5	
	$K_{\omega c}$	10	
Visual Feedback Gains	K_{gvis}	0	as in (Liu et al., 2024). Set to 0 to disable VV
	$K_{\omega vis}$	10	as in Wada et al. (2020)
Perception Time Constants	$\tau(s)$	5	as in Liu et al. (2022)
	$\tau_{scc}(s)$	7	

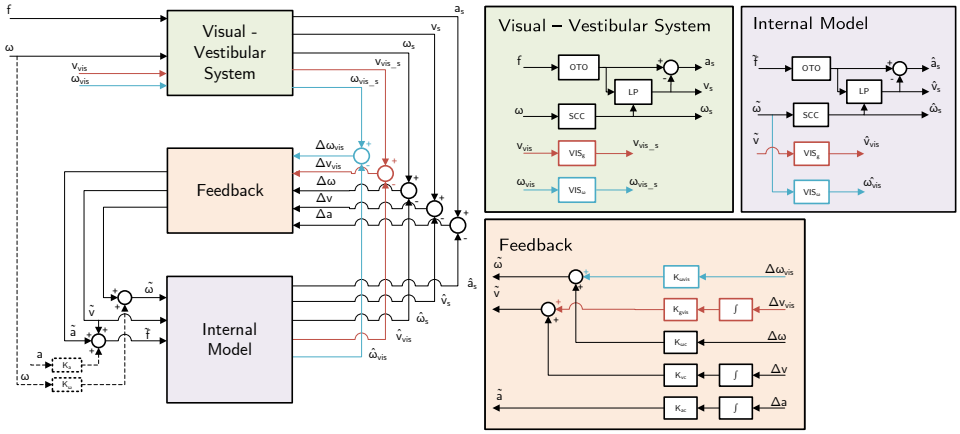

Figure 5.9: The SVC model with both Visual Rotation (VR) and Visual Vertical (VV) inputs from Kotian et al. (2024). Vestibular loops (black) are as in Kamiji et al. (2007); 'VR' (*visual rotational velocity*) loops (blue), as in Wada et al. (2020); 'VV' (*visual vertical* (direction of gravity or orientation)) loops (red), as in Liu et al. (2022). The LP block represents the internal model dynamics governed by the differential equation $\dot{v} = \frac{1}{\tau}(f - v) - \omega \times v$. The output $\tilde{v}$ is the estimated Subjective Vertical vector; perceived pitch is derived from the direction of the vector $\tilde{v}$. The feedback outputs (Δ) represent sensory conflicts used to update the Internal model. τ is the internal model time constant, K terms represent sensory weights, and Δv is the conflict driving motion sickness accumulation.

Modeling Results

Figure 5.10 compares the responses of three different SVC model variants (VR, VV and VR+VV in yellow, orange and blue), with the median subjective responses of the participants (in red), for the condition with a mean rotational rate of 5 degree/s. Figures for lower rotational rates show equivalent results and are included in Appendix D.4. For the 'Only Vision' condition simulations, the 1-degree physical platform motion was included as a vestibular input to the model alongside the visual stimulus. Additionally, to account for the eccentric rotation (where the center of rotation is located at the seat), the model inputs (specific force and angular velocity) were calculated at the head position at the headrest (0.7 meters above the center of rotation). This ensures that the simulations capture the combined angular and linear accelerations experienced by the vestibular system.

In figure 5.10 a strong effect of vision is evident in the SVC model responses, where the magnitude of predicted pitch perception varies greatly depending on the vision condition and the considered active visual loops (VR, VV, or VR+VV). With 'External' and 'Internal' vision, the SVC models strongly overestimate the perceived pitch relative to participants' responses. The counterintuitive finding already shown in figure 5.1 occurs exclusively in the 'Only Vision' condition, where the SVC-VR model predicts a pitch perception opposite in direction to that reported by participants, highlighting limitations of the SVC-VR model in purely visual scenarios. In the 'No Vision' condition, all three models produce the same output because the visual loops are disabled.

With their current published parameter settings, none of the SVC model variants – VR, VV or VR+VV – accurately predict the measured perception of pitch across the vision condi-

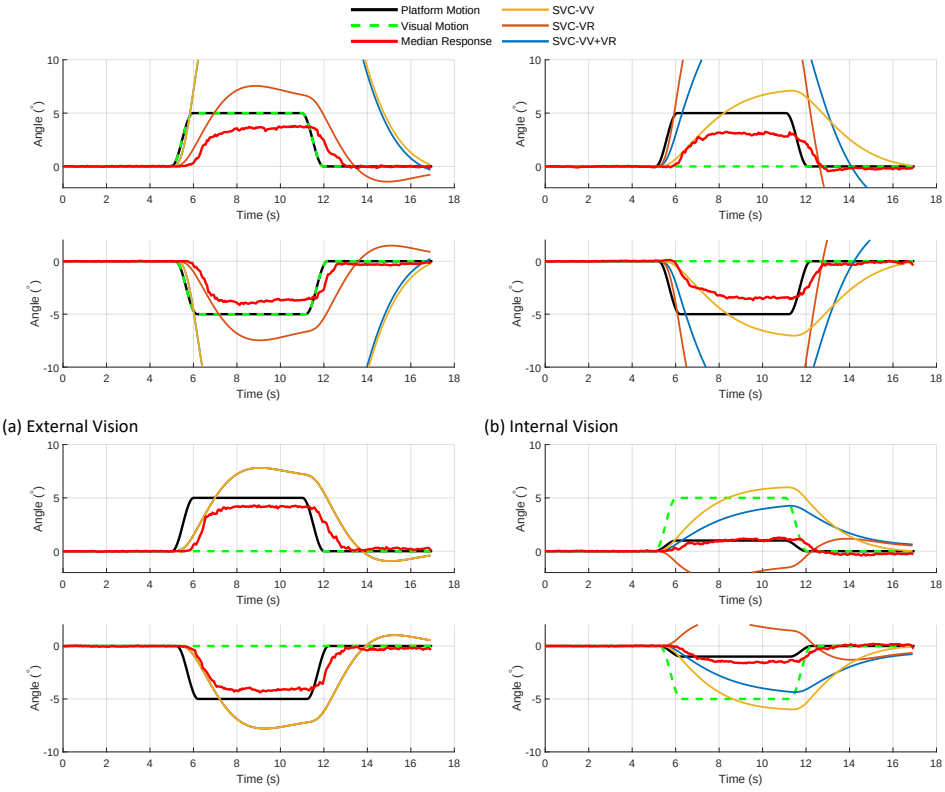

(a) External Vision

(b) Internal Vision

(c) No Vision (the models coincide)

(d) Only Vision

Figure 5.10: Median subjective response for all vision conditions compared with three SVC model variants for stimuli with mean rotational rates of 5 degree/s. Figures for lower rotational rates are shown in Appendix D.4.

tions tested. The models were additionally evaluated with prolonged step durations (see Appendix D.9), revealing that convergence to the true input pitch attitude occurred in only a limited subset of models across the vision conditions. This indicates that the models exhibit inaccuracy (compared to human responses) not only in dynamic conditions, but also in steady-state contexts. This aligns with a recent consideration of convergence towards actual verticality perception by Wada and Bos (2025). This underscores the need to adapt or tune these models and their parameters to improve their accuracy.

5.3.3 Extended and Re-tuned SVC Model Predictions

Re-tuning Approach

To evaluate whether there exists a parameter set that can accurately capture the observed human pitch perception responses, we tuned the SVC-VR model by fitting a single set of parameters to minimise the error between the model's prediction and the median human re-

sponses for all conditions. Results of fitting the full SVC-VR+VV model are in Appendix D.8. The anticipation parameters K_a and K_ω were not fitted and are set to zero as in Kotian et al. (2024), as the experiment data represents fully passive exposures without anticipation. The other seven parameters were considered as 'free' parameters in the fitting process, which was performed in MATLAB using the *fmincon* optimizer.

Additionally, the fitting procedure was conducted under three different conditions, see table 5.2 and table 5.4: Fit 1 allowed broad parameter ranges with large differences between lower and upper bounds to enable maximum flexibility. Fit 2 imposed higher lower bounds of 1 seconds for τ and 5 seconds for τ_{SCC}, reflecting physiologically plausible limits in Bos and Bles (2002); Correia Grácio et al. (2013); De Graaf et al. (1997); Inoue et al. (2023); Irmak et al. (2023); Seidman et al. (1998). Fit 3 applied an additional constraint enforcing the magnitude of K_{vc} being equal to τ in seconds to preserve the peak conflict frequency for purely translational motion at 0.16 Hz. This maintains the highest motion sickness susceptibility at this frequency in line with McCauley et al. (1976), as illustrated in Appendix D.7.

Table 5.2: SVC Fitting Conditions

Fitting Conditions	Description
Original	Original parameter values serving as baseline or benchmark.
Fit 1	Parameter fitting with a large range between lower and upper bounds to allow flexibility.
Fit 2	Parameter fitting with raised lower bounds of 1 second for τ and 5 seconds for τ_{SCC}.
Fit 3	Parameter fitting with additional constraint enforcing the magnitude of K_{vc} is equal to τ in seconds to preserve the system's peak conflict frequency for pure translation of 0.16 Hz. See Appendix D.7 for derivation.

To bring the model responses of the SVC-VR close to the human responses, it was observed that a substantial reduction in $K_{\omega vis}$ (from 10 to 0.01) and K_{ac} (from 1 to 0.1) is preferred by the fitting algorithm. Additionally, the estimated values of the time constants, τ (1 seconds), are at the lower end of their typical physiological range, where τ is reported to range from 1 to 7 seconds in prior studies (Bos and Bles, 2002; Correia Grácio et al., 2013; De Graaf et al., 1997; Inoue et al., 2023; Irmak et al., 2023; Seidman et al., 1998). This suggests a trade-off between minimising model error and maintaining parameter values within physiologically plausible ranges, potentially raising concerns regarding the physiological validity of the refitted model, despite its enhanced fit of the current data. As illustrated in figure D.20, Fit 3, indeed, ensures the peak frequency for motion sickness sensitivity to remain 0.16 Hz.

While reviewing different implementations for otoliths and semicircular canals, we recognised that perception thresholds—or more accurately, 'indifference' thresholds—are so far not incorporated in the SVC model, whereas they are commonly included in motion cueing algorithms for driving and flight simulators such as in Jain et al. (2023a); Telban and Cardullo (2001). To address this, we introduced vestibular acceleration thresholds set to [0.17, 0.17, 0.28] m/s² for longitudinal, lateral and vertical direction, respectively, and vestibular angular velocity thresholds set to [3.0, 3.6, 2.6] deg/s for roll, pitch and yaw rotation rates, respectively, based on values from Houck et al. (2005) and Reid and Nahon (1985). We note

that these values represent 'indifference thresholds' commonly used in motion cueing algorithms for simulators, which are typically higher than absolute detection thresholds found in psychophysical studies (e.g.,Lim et al. (2017); Valko et al. (2012)). We acknowledge that the subjective perception of tilt is an integrated value resulting from combined otolith and semicircular canal stimulation. However, in this modeling approach, we apply thresholds as distinct sensory input deadbands acting independently on the specific force (otolith) and angular velocity (canal) signals prior to central integration. This aligns with standard motion cueing implementations (Telban and Cardullo, 2001) and accounts for the effective signal-to-noise ratio of the individual sensory channels or simulator mechanics rather than the threshold of the final integrated percept. The vestibular thresholds were implemented within the SCC and OTO blocks in the "Vestibular-Visual System" model, but not included in the "Internal Model" (see figure 3.1). We evaluated model variations by applying these thresholds individually and in combination.

Table 5.3: SVC Model Variations

Model Variations	**Description**
Baseline	Baseline model configuration without modifications.
AccelThresh	Inclusion of vestibular acceleration thresholds of $[0.17, 0.17, 0.28]$ m/s^2 to the inputs. From Houck et al. (2005) and Reid and Nahon (1985)
AngVelThresh	Inclusion of vestibular angular velocity thresholds of $[3.0, 3.6, 2.6]$ deg/s to the inputs. From Houck et al. (2005) and Reid and Nahon (1985)
AccelAngVelThresh	Inclusion of vestibular acceleration thresholds of $[0.17, 0.17, 0.28]$ m/s^2 and vestibular angular velocity thresholds of $[3.0, 3.6, 2.6]$ deg/s to the inputs. From Houck et al. (2005) and Reid and Nahon (1985)

Re-tuning Results

The optimised parameters for all model variations and fitting conditions, along with the original values and the average overall RMSE (across all conditions) and per vision condition, are presented in table 5.4. Starting from the SVC-VR-Baseline model, we see that simply adjusting or fitting the parameters already leads to a significant improvement in matching the data, as reflected by a reduction in the average RMSE from 3.84 degrees to much lower values in the fitted versions. Beyond this, exploring other model variations reveals that incorporating acceleration thresholds (SVC-VR-AccelThresh) provides the greatest enhancement, ultimately achieving the lowest average RMSE of 0.62 degrees for Fit 3. In contrast, adding angular velocity thresholds provides limited improvements.

The results of Fit 1, Fit 2 and Fit 3 for the SVC-VR-Baseline are shown in figure 5.11, which indicates that all fitting approaches yield substantially improved accuracy relative to the original baseline parameters. While Fit 1 achieves the lowest average RMSE of 0.70 degrees, Fit 3 exhibits a modest increase in RMSE to 0.86 degrees. Despite this reduction in performance, Fit 3 still performs markedly better than the Baseline with original parameters, which had an RMSE of 3.84 degrees, demonstrating a significant enhancement in

Table 5.4: Parameter values and RMSEs for all model variations compared with the original parameters from Kamiji et al. (2007); Wada et al. (2020)

Model	Variation	Fit type	$K_{\omega vis}$	K_{gvis}	$K_{\omega c}$	K_{ac}	K_{vc}	$\tau(s)$	$\tau_{SCC}(s)$	Average RMSE (deg)	RMSE per vision condition (deg)			
											External	Internal	No	Only
	Parameter Bounds	Fit 1	[0, 15]	[0, 0]	[5, 15]	[0.1, 3]	[0.1, 10]	[0.1, 10]	[0.1, 15]					
		Fit 2	[0, 15]	[0, 0]	[5, 15]	[0.1, 3]	[0.1, 10]	[1, 10]	[5, 15]					
		Fit 3	[0, 15]	[0, 0]	[5, 15]	[0.1, 3]	[0.1, 10]	[1, 10]	[5, 15]					
SVC-VR	Baseline	Original	10.00	0.00	10.00	1.00	5.00	5.00	7.00	3.84	1.47	7.08	2.15	4.65
		Original with no visual input	0.00	0.00	10.00	1.00	5.00	5.00	7.00	1.73	2.21	2.26	2.15	0.33
		Fit 1	7.72	0.00	6.71	0.10	0.99	0.10	1.65	0.70	0.85	0.91	0.79	0.26
		Fit 2	0.58	0.00	13.23	0.29	1.36	1.01	5.36	0.86	1.05	1.13	0.99	0.26
		Fit 3	0.01	0.00	6.99	0.10	1.00	1.00	5.00	0.86	1.06	1.11	1.00	0.25
		Fit 3 with no visual input	0.00	0.00	6.99	0.10	1.00	1.00	5.00	0.86	1.06	1.11	1.00	0.25
	AccelThresh	Original	10.00	0.00	10.00	1.00	5.00	5.00	7.00	3.59	0.98	6.66	1.59	5.15
		Original with no visual input	0.00	0.00	10.00	1.00	5.00	5.00	7.00	1.34	1.63	1.74	1.58	0.40
		Fit 1	0.00	0.00	14.95	0.10	1.20	0.17	12.31	0.47	0.42	0.47	0.35	0.62
		Fit 2	0.07	0.00	13.23	0.85	2.32	1.01	7.13	0.60	0.62	0.66	0.52	0.60
		Fit 3	2.41	0.00	5.00	0.10	1.03	1.03	5.00	0.62	0.61	0.62	0.55	0.69
		Fit 3 with no visual input	0.00	0.00	5.00	0.10	1.03	1.03	5.00	0.62	0.61	0.64	0.55	0.69
	AngVelThresh	Original	10.00	0.00	10.00	1.00	5.00	5.00	7.00	3.35	5.33	1.10	1.00	5.98
		Original with no visual input	0.00	0.00	10.00	1.00	5.00	5.00	7.00	0.85	1.04	1.10	0.99	0.27
		Fit 1	1.64	0.00	14.35	2.44	1.15	0.10	4.00	0.70	0.80	0.92	0.79	0.29
		Fit 2	0.41	0.00	12.87	3.00	4.37	1.08	5.04	0.70	0.67	0.95	0.82	0.37
		Fit 3	0.05	0.00	12.81	1.40	7.93	7.93	8.46	0.83	0.93	1.08	0.99	0.33
		Fit 3 with no visual input	0.00	0.00	12.81	1.40	7.93	7.93	8.46	0.85	1.01	1.08	0.99	0.30
	AccelAngVelThresh	Original	10.00	0.00	10.00	1.00	5.00	5.00	7.00	3.37	5.78	0.65	0.59	6.45
		Original with no visual input	0.00	0.00	10.00	1.00	5.00	5.00	7.00	0.62	0.63	0.65	0.59	0.62
		Fit 1	0.00	0.00	8.95	0.16	1.22	0.17	8.13	0.47	0.42	0.46	0.35	0.62
		Fit 2	0.00	0.00	13.67	3.00	4.92	1.01	8.12	0.47	0.43	0.47	0.36	0.62
		Fit 3	0.00	0.00	13.43	0.39	1.27	1.27	10.00	0.63	0.63	0.66	0.59	0.62
		Fit 3 with no visual input	0.00	0.00	13.43	0.39	1.27	1.27	10.00	0.63	0.63	0.66	0.59	0.62

model accuracy. This suggests that the constraint imposed in Fit 3, which preserves motion sickness frequency sensitivity, results in a slight reduction in fit quality but maintains superior performance compared to the original parameters.

Table 5.4 also shows two types of model fits with no visual input. In all cases, the baseline improves when removing the visual input. Furthermore, the results for SVC-VR-AccelAngVelThresh Fit 3 demonstrate that the model can perform equally well without visual gains. Table 4 supports this: the RMSE for Fit 3 is identical with or without visual inputs, while the Original parameters actually achieve a lower RMSE (better fit) when visual inputs are disregarded.

Appendix D.8 shows equivalent fitted responses with the complete SVC model with both visual rotation velocity (VR) and visual verticality (VV). The SVC-VR+VV model shows a better fit as compared to the SVC-VR model for several variants, but the corresponding RMSE values are equivalent for the best fitting model, AccelAngVelThresh. Interestingly, the additional parameter K_{gvis} of SVC-VR+VV is estimated between 0.21 and 0.62, which is much lower than the original value of 5 reported by Liu et al. (2024).

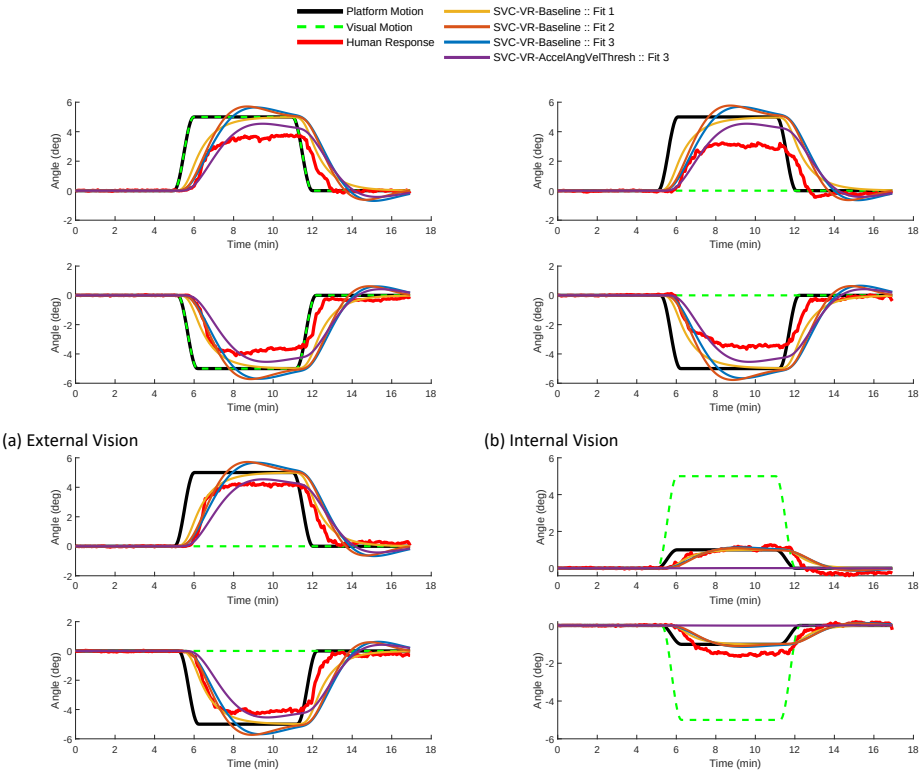

(a) External Vision

(b) Internal Vision

(c) No Vision

(d) Only Vision

Figure 5.11: Results of tuning (Fits 1, 2 and 3) the parameters of the SVC-VR-Baseline model and SVC-VR-AccelAngVelThresh for the stimuli with mean rotational rates of 5 degree/s. Figures for other rotational rates are shown in Appendix D.6.

5.4 Discussion

Experimental results (see figure 5.7) demonstrate that human participants tend to underestimate (on average by 20%) the amplitude of pitch motion across all conditions. Additionally, no significant difference was observed in the three conditions with mechanical platform motion, while varying vision. This finding challenges assumptions that visual cues inherently improve motion perception accuracy and suggests a predominant reliance on vestibular inputs. Notably, in the 'Only Vision' condition, participants' responses still matched the (low magnitude) physical motion, strongly underestimating the visual pitch amplitude. This suggests that the central nervous system prioritizes vestibular information in pitch perception. However, the observed dominance of vestibular inputs likely results from the specific nature of the visual stimulus, which mimics optic flow without a spatial reference. We deliberately utilized a random dot pattern to isolate rotational velocity cues (optic flow), matching the SVC-VR model. However, this design lacked a polarized horizon or ground plane. In the absence of such spatial references, optic flow provides informa-

tion about rotational change, but is ambiguous regarding absolute orientation relative to gravity. In contrast, the vestibular system (specifically the otoliths) provides a direct, albeit weak in this case, reference to the gravity vector. Thus, consistent with optimal integration theory, the central nervous system seemingly prioritized the noisy but absolute vestibular reference over the potentially drifting visual cue. This interpretation is corroborated by our modeling analysis, which indicated a modest role of visual verticality perception in the current experiment (low estimated values for K_{gvis}), reflecting the absence of explicit orientation cues in the provided visual stimulus. We acknowledge that the SVC model computes a subjective vertical, which we utilized as a proxy for pitch perception. While subjective vertical errors are distinct from body tilt perception and subject to specific biases (e.g., systematic overestimation or underestimation of tilt), our model output represents the internal estimate of the gravity vector direction. In the context of our passive pitch task without active line adjustment, we assume this internal vector orientation drives the perceived body orientation relative to Earth.

As shown in figure 5.2, for two out of the four ramp steepness conditions, the presented motion is well below the vestibular angular velocity perception threshold. Using the angular velocity threshold improved the fits, but the improvement was modest. It would have been beneficial to test more ramp steepnesses that exceed this threshold. In contrast, the motion remains consistently well above the vestibular acceleration perception threshold. This is shown in figure 5.2, converted to the equivalent pitch angle that would induce the same acceleration. Having a motion that exceeded the acceleration threshold likely contributed to the noticeably better fits when acceleration thresholds were used, as confirmed by the parameter analysis in table 5.4.

Comparison of experimental results to SVC model variants with their original published parameters (see figure 5.10) reveals a major overestimation of perceived pitch by the models for the 'External' and 'Internal' vision cases. In the 'Only' vision condition, the SVC-VR model even predicts an incorrect sign of the perceived pitch. Hence, the SVC models with their original parameters do not sufficiently capture human responses in pitch perception under varying vision conditions, limiting their reliability for predicting perception and motion sickness in untested scenarios. While adapting the SVC model parameters (as in section 5.3.3) demonstrably improves the fit for our conditions, this doesn't guarantee they will generalise to all vestibular and visual scenarios. Parameter tuning may enhance model accuracy within the tested domain, but the complexity of multi-sensory integration and context-specific factors (e.g., differing visual motion cues, individual sensory reliance, or VR immersion effects) makes a truly 'universal' model challenging. Instead, iterative adaptation and validation across broader scenarios and populations are necessary to achieve coherent improvements. In doing so, we should be careful not to disrupt the motion sickness sensitivity of the model. In this paper, we make an attempt to achieve this with Fit 3, constraining the magnitude of K_{vc} to be equal to τ in seconds. As illustrated in figure D.20, Fit 3, indeed, ensures the peak frequency for motion sickness sensitivity to remain at 0.16 Hz, in line with vertical experimental data by McCauley et al. (1976).

We verified how the fitted SVC parameters affect motion sickness prediction in three vehicle experiments used previously to validate our personalised motion sickness model (Kotian et al., 2025). The SVC-VR parameters for Fit 3 in table 5.4 provided an adequate fit

(the MISC error increased less than 8%). The SVC-VR+VV parameters for Fit 3 in table D.2 provided a 40-60% increase in the MISC error. This once more illustrates that the SVC-VR model better captures motion sickness in passive driving than the SVC-VR+VV model. However, visual verticality perception has been shown to affect motion perception and sickness (Bos et al., 2008; Liu et al., 2024), warranting further efforts to model the role of visual verticality perception.

From table 5.4, it is clear that all fitted models significantly reduce the average RMSE compared to the original parameters, indicating an improved fit to the data. Fit 1 generally achieves the lowest RMSE across model variations, due to it having large parameter flexibility to help better capture the system behaviour. However, this unconstrained flexibility often resulted in parameters reaching the provided bounds, yielding values (e.g., time constants) that deviated from the ranges reported in prior physiological studies (Bos and Bles, 2002; Correia Grácio et al., 2013). In contrast, Fit 2 and Fit 3 impose stricter constraints on time constants or parameter relationships. Although they show slightly higher RMSE values, the difference is marginal (< 0.2 degrees), suggesting diminishing returns in optimizing outside these biologically plausible ranges. Thus, the constrained parameter sets are likely more valid for capturing human perception. Models with additional vestibular thresholds included (AccelThresh, AngVelThresh, AccelAngVelThresh) consistently improve error metrics by 20%, highlighting the benefit of including these thresholds. Overall, flexible parameter fitting combined with known physiological threshold values is found to substantially enhance SVC model performance.

We additionally (results not shown in the paper) investigated the incorporation of a response delay to capture any latencies in the subjective pitch perception data. It was found that introducing a delay of 0.15 seconds (Thorpe et al., 1996) did not enhance the model fit, however, it did significantly affect the estimated SVC parameter values, specifically resulting in the fitted values of (τ) and (τ_{SCC}) tending toward even smaller values of approximately 0.01 seconds. As this is an undesired and counterintuitive effect, the consideration of response delays in subjective perception responses requires attention in future research.

Although AccelThresh, AngVelThresh, and AccelAngVelThresh yielded an improvement in modeling accuracy and more plausible parameter values, the validation of these proposed SVC model extensions remains limited to pitch stimuli of five degrees at various angular velocities. We acknowledge that these relatively small angles may not fully capture the non-linearities or specific biases (e.g., systematic overestimation or underestimation of tilt). Consequently, whether these perception thresholds and model behaviors generalise to larger pitch excursions remains an open question for future research.

Additionally, the role of participant expectations during virtual reality exposure—and how these may shape individual sensory integration strategies—should be systematically explored, as these factors could further limit the generalizability of current findings.

In future work, it is essential to revisit the ‘Only Vision’ condition with purely vision stimuli and replace the 1-degree pitch motion applied in the current experiment with noise or vibration stimuli. Further comparison with a visual stimulus showing an explicit horizon to enable true verticality perception will be interesting. Additionally, exploring vision conditions with larger and faster stimuli can provide further insight into the dynamics of sensory

integration. In the present study, only a limited representation of rotational visual stimuli was provided. Future research should consider measuring motion perception, as in Liu et al. (2024), using more realistic visual scenes, including high-realism images and conditions in which visual verticality cues, such as the ground surface and horizon. The visual input to the SVC model as used in this study does not account for factors such as field of view and contrast, both of which are known to influence visually induced motion sickness (VIMS). In this context, models that can directly process actual image data can be explored. For instance, Liu et al. (2024); Wada et al. (2020) have already proposed an approach using optical flow and visual vertical, respectively, for this purpose. Progress towards predictive and widely applicable models will hinge on expanding both the diversity of motion/visual stimuli and the inclusion of real-world scene realism.

In summary, our findings in figure 5.7 and appendix D.9 and parameter analyses (table 5.4) collectively demonstrate that SVC models with their original published parameters provide highly unrealistic results for human pitch perception under various visual conditions. However, with tuned parameters, a good fit (RMSE $<$ 1 degrees) was obtained for pitch perception. The introduction of perception thresholds within the SVC framework further enhances fidelity to observed human perception and offers improved utility for motion cueing applications as proposed by Telban and Cardullo (2001) and Groen and Bles (2004). This holds for SVC and other sensory integration models such as the multisensory observer model (MSOM), which captures the current data quite well with its published parameters, with scope for further enhancement (see Appendix D.5). Continued validation across complex motion paradigms and inclusion of individual variations will be pivotal for advancing model-based predictions of motion sickness and perception in virtual reality and simulator environments.

5.5 Conclusion

Our study reveals that humans tend to underestimate pitch stimulus amplitude (on average by 20%) across various visual conditions, with no significant effect of vision when comparing the three conditions involving full platform motion. SVC models with their original published parameters provide highly unrealistic pitch perception predictions, with the SVC-VR model even predicting results opposite to experimental results in conditions with only visual motion. Through model tuning, we enhanced the SVC-VR model's ability to capture human responses more accurately and introducing rotational velocity and acceleration perception thresholds further improved this capability. Interestingly, models without any visual input matched the experimental data equally well as models with explicit vision inputs, reinforcing the finding that vision had no measurable effect on participants' pitch perception. These findings highlight the complexity of sensory integration in motion perception and reveal limitations in current models' ability to represent visually driven illusions of self-motion. Future research must validate the proposed model extensions across a broader range of motion paradigms, such as in Inoue et al. (2023); Irmak et al. (2023); Kotian et al. (2024); Newman (2009), and motion sickness conditions, such as in Kotian et al. (2024). Advancing such models is critical for applications in virtual reality, automated ve-

hicles, and simulator environments, where an accurate representation of visually induced motion perception is essential.

6

Reducing Discomfort in Driving Simulators: Motion Cueing for Motion Sickness Mitigation

I shall either find a way or make one.

Hannibal

This chapter was developed concurrently with chapter 5 and therefore does not incorporate findings of chapter 5.

This chapter is based on *Kotian, V., Jain, V., Lazcano A. M. R., Pool, D. M., Happee, R., & Shyrokau, B. (2025). Reducing Discomfort in Driving Simulators: Motion Cueing for Motion Sickness Mitigation. TechRxiv preprint.*

The appendices for this chapter can be found at Appendix E.

Abstract

Driving simulators are increasingly used in research and development. However, simulators often cause motion sickness due to downscaled motion and unscaled veridical visuals. In this paper, a motion cueing algorithm is proposed that reduces motion sickness as predicted by the subjective vertical conflict (SVC) model using model predictive control (MPC). Both sensory conflict and specific force errors are penalised in the cost function, allowing the algorithm to jointly optimise fidelity and comfort.

Human-in-the-loop experiments were conducted to compare four simulator motion settings: two variations of our MPC-based algorithm, one focused on pure specific force tracking and the second compromising specific force tracking and motion sickness minimisation, as well as reference adaptive washout and no motion cases. The experiments were performed on a hexapod driving simulator with participants exposed to passive driving.

Experimental motion sickness results closely matched the sickness model predictions. As predicted by the model, the no motion condition yielded the lowest sickness levels. However, it was rated lowest in terms of fidelity. The compromise solution reduced sickness by over 50% (average MISC level 3 to 1.5) compared to adaptive washout and the algorithm focusing on specific force tracking, without any significant reduction in fidelity rating.

The proposed approach for developing MCA that takes into account both the simulator dynamics and time evolution of motion sickness offers a significant advancement in achieving an optimal control of motion sickness and specific force recreation in driving simulators, supporting broader simulator use.

6.1 Introduction

Since the inception of driving simulator technology, a key challenge has been to bring the driving simulator experience closer to the real vehicle experience. However, the realistic (unscaled) visual motion is still presented with scaled or even without any physical motion. This causes a mismatch between expected and perceived motion, eliciting motion sickness (Bos et al., 2020). Motion sickness is a syndrome that arises as a consequence of a wide range of self-motion and orientation cues. It is characterised by symptoms of sweating, headache, dizziness, stomach awareness, where these symptoms usually grow in severity until nausea, retching and ultimately vomiting occurs (Bertolini and Straumann, 2016). The mechanisms behind the development and evolution of motion sickness have been studied extensively, relying heavily on models that predict sensory conflicts based on well-known mathematical models of vestibular and visual sensory integration (Bos and Bles, 1998; Irmak et al., 2023; Kotian et al., 2024; Liu et al., 2022; Wada et al., 2020).

In driving simulators, motion sickness typically occurs due to the intricate interplay of synthetic parallel visual, vestibular, and proprioceptive cues. A recent meta-analysis on simulator sickness (de Winkel et al., 2022) reviewed 41 studies and reported modest sickness levels across different simulator configurations. It found that improved visual fidelity significantly reduced sickness in motion-base simulators, but not in fixed-base systems. Mechanical motion presence had a minor, non-significant effect on sickness. Active driving reduced sickness compared to passive driving, although these comparisons were across different studies. Notably, active driving rarely induces sickness in real vehicles, highlighting a gap between simulation and reality. In a comparative study (Romano et al., 2016), three motion cueing strategies were assessed against a fixed-base setup. While the motion-cueing strategies improved perceived realism, they were also associated with increased sickness incidence, highlighting a trade-off between immersion and physiological comfort.

In this paper, we aim to develop a motion cueing algorithm (MCA) that can recreate specific forces from a real vehicle drive in a driving simulator, while explicitly minimizing the level of motion sickness. To the best of the authors' knowledge, no prior work has established an MCA explicitly aimed at reproducing or reducing motion sickness in a simulator environment. For this, we need an MCA that can take into account both the simulator dynamics and the time evolution of motion sickness. New approaches to develop MCAs such as Bruschetta et al. (2018); Jain et al. (2023b); Rengifo et al. (2021) based on model predictive control (MPC) are well suited as they solve a constrained optimal control problem and can take advantage of models of simulator dynamics and motion sickness development in their optimization. Traditionally, simple metrics of motion sickness severity are optimised, such as the motion sickness dose value (MSDV) in Bae et al. (2019); Jain et al. (2023a); Lambert et al. (2019); Li and Hu (2021) for vehicle trajectory planning. While effective in optimising the magnitude of horizontal motion in real vehicles, such methods will not capture the effects of the frequency of motion, platform rotation, and conflicting visual and mechanical motion. To capture these effects, we selected the 6-DoF subjective vertical conflict (SVC) model from Wada et al. (2020). Comparing a range of models, this model best matched motion sickness data collected in several laboratory experiments and real-world driving studies (Kotian et al., 2024). In Kotian et al. (2025), we extended this SVC model

with a personalised motion sickness accumulation model. We calibrated the accumulation parameters such that the model predicts sickness rated with the well-established MISC scale. Moreover, a population model was added to predict the sickness variation within a population.

This paper presents a novel MPC-based MCA that mitigates motion sickness, using these motion sickness models to find a balance between motion sickness reduction and specific force recreation. We validate the MCAs in human-in-the-loop experiments, also including a reference adaptive washout MCA and a no motion condition.

The contributions of the work are outlined below:

- Incorporated a six-degree-of-freedom subjective vertical conflict motion sickness model, for the first time, directly into a motion cueing algorithm as part of its cost function.
- Formulated a multi-objective optimisation framework that jointly optimizes for motion sickness reduction and reproduction of reference vehicle motion in the driving simulator.
- Demonstrated that inclusion of the motion sickness model allows for an adjustable trade-off between motion fidelity and predicted motion sickness, enabling the algorithm to prioritise either motion fidelity or participant comfort based on application-specific requirements.
- Conducted a human-in-the-loop experiment confirming that the proposed algorithm effectively mitigates motion sickness, while having minimal impact on perceived motion fidelity.

6.2 Motion Cueing Algorithms

6.2.1 MPC-based MCA

The evaluation framework of the proposed motion cueing algorithm is shown in figure 6.1. The inputs are the reference vehicle specific forces, the reference sensory conflict representing motion sickness, and the yaw acceleration. In this paper, the reference sensory conflict is set to zero, resulting in an MPC that aims to minimise motion sickness.

The upper part of figure 6.1 represents the proposed algorithm combining hexapod dynamics and the sensory conflict generation model in the MPC framework. The considered hexapod dynamics consist of translational (fore-aft and sway) motion, and correspondingly, pitch and roll motion. The equations for the hexapod dynamics are defined in detail in Appendix E.4. Assuming yaw motion is a separate channel, it is controlled via a parallel washout channel to reduce computational complexity. More details regarding the control of yaw motion can be found in Appendix E.6. The vertical motion is neglected in this paper, assuming a perfectly flat road. The reference vehicle specific forces and yaw accelerations are preconditioned by scaling and limitations based on hexapod capability.

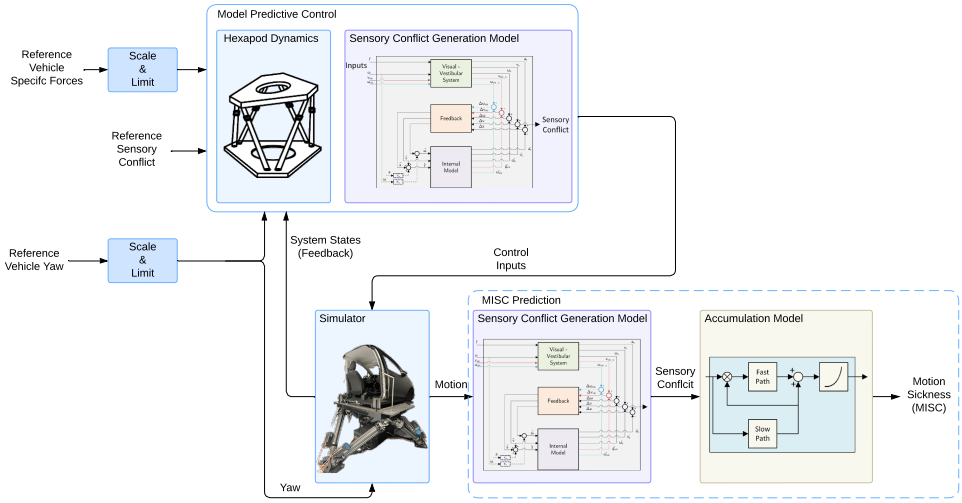

Figure 6.1: Framework to evaluate the MPC-based MCA with the SVC-VR motion sickness model; the two blocks at the bottom right, highlighted by the dashed blue box, are not part of the MCA and are only used to predict the actual resulting motion sickness over the whole experiment duration.

To calculate the sensory conflict, c_v, the subjective vertical conflict model with visual rotational velocity (SVC-VR) is used (Kotian et al., 2023). It is based on the sensory conflict generation model proposed in Wada et al. (2020) with further validation for motion sickness predictions in vehicles (Kotian et al., 2024, 2025). The conflict in this model is a 3-DoF vector; therefore, the vector norm results in a scalar. In this case, the instantaneous conflict is used to predict sensory mismatch, without accumulation dynamics. Hence, the conflict term is effectively scalar and does not directly include the slow integration effects present in accumulation dynamics. Minimising this scalar conflict over the prediction horizon can reduce motion sickness stimuli, but does not replicate the full MISC integration (accumulation dynamics based on Kotian et al. (2025) shown on bottom right, figure 6.1), which is still computed offline for weight selection purposes. More details on the integration of the SVC model in the MPC can be found in Appendix E.3.

The proposed algorithm explicitly optimises the trade-off between motion sickness mitigation and motion perception fidelity. This is achieved by the introduction of the following components in the cost function: J_{MP} is related to the tracking performance, J_{MS} corresponds to the motion sickness through sensory conflict, and state costs J_{pen}. The resulting cost function is defined as:

$$J_c = J_{MP} + J_{MS} + J_{pen}, \tag{6.1}$$

with

$$J_{MP} = (f_{spec} - f_{ref})^\top W_{spec}(f_{spec} - f_{ref}), \tag{6.2}$$

$$J_{MS} = w_c(c_v - c_{vref})^2, \tag{6.3}$$

$$J_{pen} = (X - X_{ref})^\top W_x(X - X_{ref}), \tag{6.4}$$

where $f_{spec} \in \mathbb{R}^2$, $c_v \in \mathbb{R}$, and $X \in \mathbb{R}^{n_x}$ contains all considered states related to the hexapod and the sensory conflict generation model.

The weighting matrices are positive semidefinite and dimensionally compatible with the corresponding cost components:

- $W_{spec} \in \mathbb{R}^{2\times2}$, weighting the two components of the specific force in J_{MP}.
- $w_c \in \mathbb{R}^{1\times1}$, weighting the scalar sensory conflict in J_{MS}.
- $W_x \in \mathbb{R}^{n_x\times n_x}$, a diagonal matrix weighting all states of the hexapod and the sensory conflict generation model in J_{pen}, where $n_x = 34$ (same as the size of X).

The state vector is defined in condensed form as

$$X = \begin{bmatrix} \theta_{hex} & \omega_{hex} & s_{hex} & v_{hex} & f_{tilt} & \delta & a_{hex} & \alpha_{hex} \\ w_s & \hat{w}_s & v_s & \hat{v}_s & \tilde{v}_s & \hat{f}_{spec} & & \end{bmatrix}^T \tag{6.5}$$

where θ_{hex} is the angular position of the hexapod (rad), ω_{hex} is the angular velocity of the hexapod (rad/s), s_{hex} is the position of the hexapod (m), v_{hex} is the velocity of the hexapod (m/s), f_{tilt} is the force due to the tilt component of gravity (m/s^2), δ is a dimensionless slack variable, a_{hex} is the linear acceleration of the hexapod (m/s^2), α_{hex} is the angular acceleration of the hexapod (rad/s^2), w_s and $\hat{w}_s$ are sensed and expected angular velocities in the motion sickness model (rad/s), and v_s, $\hat{v}_s$, $\tilde{v}_s$, and $\hat{f}_{spec}$ are verticality and specific force states in the motion sickness model (m/s^2). The hexapod states $(\theta_{hex}, \omega_{hex}, s_{hex}, v_{hex}, f_{tilt}, \delta, a_{hex}, \alpha_{hex})$ are two-element vectors in $\mathbb{R}^2$, whereas the motion sickness model states $(w_s, \hat{w}_s, v_s, \hat{v}_s, \tilde{v}_s, \hat{f}_{spec})$ are three-element vectors in $\mathbb{R}^3$.

To ensure physically feasible and safe motions, constraints are applied, including workspace limits on positions and orientations, as well as velocity and acceleration limits. Slack variables δ allow for flexible handling of constraint violations. A description of constraints and slack variable implementation can be found in Appendix E.7. Additional workspace management strategies, such as washout and dynamic constraints, are described in Appendix E.5. The weight parameters and the motivation for selecting weight parameters can be found in Appendix E.1.

For this replay scenario, the algorithm is performed offline using the full horizon at each step to compute optimal inputs for the simulator. The prediction horizon has been selected as 3 seconds (60 steps and sampling time of 0.05 s). Shorter horizons reduced performance, while the selected amount of prediction steps and sampling time result in a trade-off between prediction accuracy and computational feasibility, with a real-time factor of approximately 2.1.

6.2.2 Adaptive Washout MCA

In the results below, we compare the MPC-based MCA to a state-of-the-art adaptive washout (AW) MCA introduced in Ariel and Sivan (1984); Parrish et al. (1975); Veltena (2015), with MPC-based direct workspace management as used in Jain et al. (2023b).

This adaptive washout consists of the following components

- Translation channels: 1st order high-pass filter
- Rotation channels: 3rd order high-pass filter
- Tilt coordination: 2nd order low-pass filter

The used parameter settings for the adaptive washout are listed in table 6.1. This configuration is consistent with settings used in our previous work (Jain et al., 2023b).

Table 6.1: Configuration of the adaptive washout algorithm

Parameter	Value
Cut-off frequency (long. and lat.)	$0.5\ Hz$
Max tilt angle (roll and pitch)	$30\ deg$
Maximum tilt rate (roll and pitch)	$3\ deg/s$
Scaling factor (lateral)	0.4
Scaling factor (longitudinal)	0.3

6.2.3 Objective Evaluation of MCAs

This subsection evaluates the performance of the algorithms objectively. Based on the objective evaluation, suitable MCA conditions are selected for the experimental evaluation. Here we already use the driving scenario defined for the experiment, see section 6.3.2.

The MPC-based algorithm under consideration addresses two primary objectives: accurate specific force tracking and minimisation of sensory conflict. To comprehensively explore the trade-off between these competing goals, we vary the ratio between the specific force tracking weight and the sensory conflict weight across the entire range, from pure conflict minimisation to pure force tracking. This is done by varying the sensory conflict weight, w_{con}, between 0 to 1 while maintaining the relation $w_{con} + w_{spec} = 1$.

Figure 6.2 illustrates the resulting performance metrics for different values of w_{con}. The upper two graphs illustrate predicted motion sickness in terms of sensory conflict and MISC, whereas the other four graphs illustrate the corresponding workspace utilisation. In all graphs, the horizontal axis is defined as the specific force tracking error. Hence, the upper graphs represent the typical trade-off of sickness versus fidelity as a Pareto front.

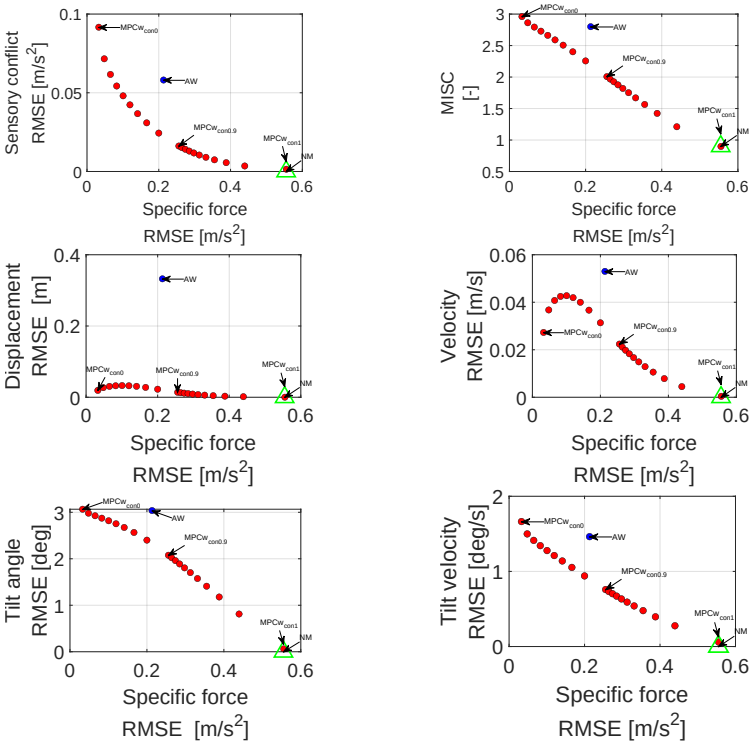

Figure 6.2: Effect of varying the sensory conflict weight, w_{con}, on sickness, specific force tracking and workspace utilisation. The specific force tracking error on the horizontal axis is computed as the square root of the sum of the longitudinal and lateral root-mean-square errors (RMSE) of specific force. MISC development is evaluated over 5 laps; all other metrics are calculated based on the response over a single lap. Adaptive washout (AW) and no motion (NM) are shown as well.

6

Table 6.2: Objective performance of the selected MCAs along with their descriptions.

Algorithm	Specific force RMSE $[m/s^2]$	Shape similarity	Final median predicted MISC	Description
NM	0.536	0	0.9	No motion of platform coincides with $MPCw_{con1}$
$MPCw_{con0.9}$	0.216	0.97	2.0	MPC based MCA with $w_{con} = 0.9$
$MPCw_{con0}$	0.027	0.99	3.0	MPC based MCA with $w_{con} = 0$
AW	0.097	0.89	2.8	Widely accepted motion cueing in industry

The green triangle represents the no motion case, which practically coincides with the conflict weight of unity in our algorithm. Thus, the algorithm indicates the reduction of motion sickness to be the most when the simulator platform does not move at all. The blue dot represents the adaptive washout based MCA as described in section 6.2.2.

For the experimental evaluation, it is important to ensure a clear distinction between the predicted MISC levels of the different algorithm configurations. Therefore, a minimum difference of at least one MISC level is desired. With this minimum MISC difference and other

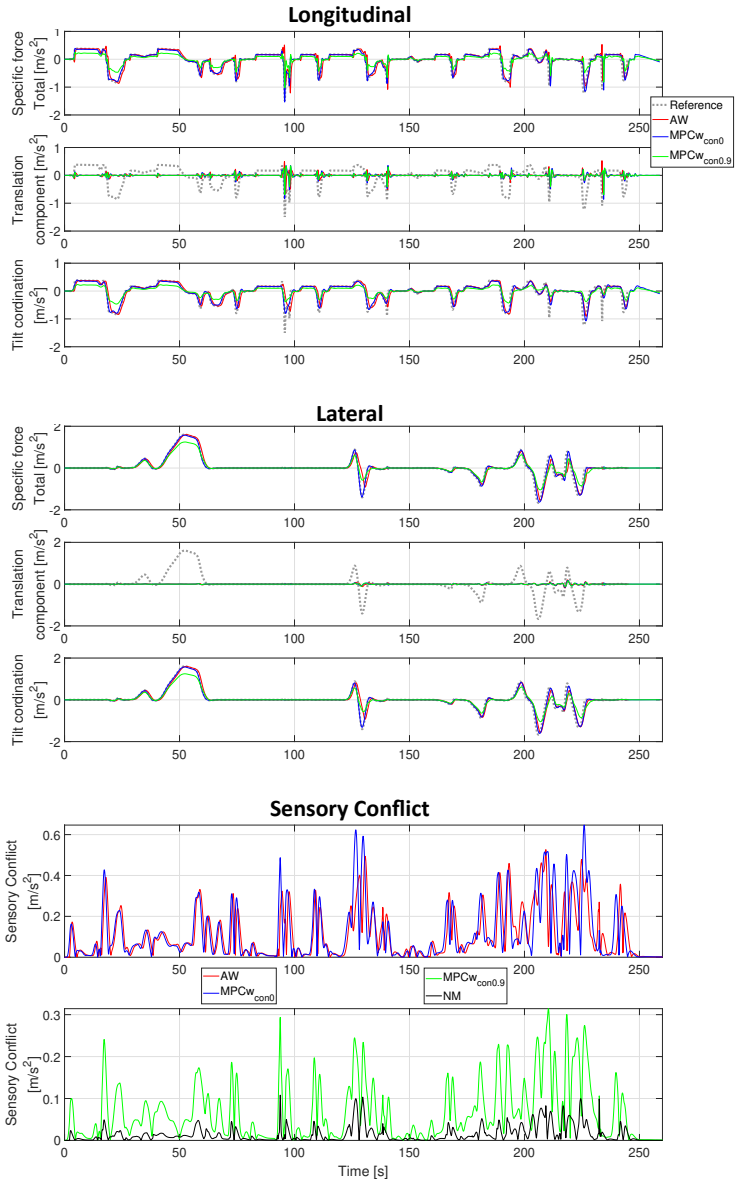

Figure 6.3: Specific force and its components, along with the sensory conflict generated over one lap of the simulation, shown for different algorithm configurations. Longitudinal specific force with its translation and tilt components (upper three graphs), lateral specific force with its translation and tilt components (middle three graphs) and sensory conflict (last two graphs) are shown for the three MCAs with motion. The no motion case is only shown in the graphs of sensory conflict.

metrics in figure 6.2 in consideration, we have chosen two MPC-based MCAs for the experiment along with the adaptive washout and no motion condition. Hence, the four MCA

conditions are:

- *No Motion (NM)*: This is a baseline case, where there is no motion of the simulator, but there still are moving visuals.
- $MPCw_{con0.9}$: This is a MPC-based MCA with a $\omega_{con} = 0.9$. This MCA is expected to be a good compromise, balancing sickness reduction and specific force reproduction.
- $MPCw_{con0}$: This is a MPC-based MCA with a $\omega_{con} = 0$. This MCA is expected to have very good specific force reproduction while causing more motion sickness than $MPCw_{con0.9}$.
- *Adaptive Washout (AW)*: This is a state-of-the-art MCA widely used in industrial applications.

These MCAs and their expected performance are summarised in table 6.2. In the experiment, speed-dependent road-induced vibrations were added as vertical motion in all conditions. For objective comparison of the selected algorithms, *specific force tracking*, *shape similarity*, and the *median predicted MISC* at the end of the experiment are considered.

Specific force tracking is the RMSE between the reference and the obtained total horizontal specific force (resultant of f_x and f_y) from the MCA. It portrays how closely the magnitudes of the reference and generated profiles match/align. For the AW method, the RMSE is 0.097 m/s^2. The $MPCw_{con0}$ configuration achieves lower RMSE values of 0.027 m/s^2, indicating a closer match to the reference. In contrast, the $MPCw_{con0.9}$ configuration results in higher RMSE values of 0.216 m/s^2, reflecting the reduced motion magnitudes.

Shape similarity is the Pearson correlation between the reference and generated profile. This ensures the effectiveness of the algorithm. A manoeuvre with a similar shape to the obtained specific force results in a similar experience. Despite magnitude scaling, a higher shape similarity provides a better recreation of the manoeuvre. The AW method achieved shape similarity scores of 0.89. The $MPCw_{con0}$ configuration yielded higher shape similarity scores of 0.99, indicating near-perfect alignment. The $MPCw_{con0.9}$ configuration also performed well, with scores of 0.97.

The median predicted MISC at the end of the experiment quantifies the induced motion sickness severity of each MCA. The $MPCw_{con0}$ and AW had similar MISC levels of 3.0 and 2.8, respectively. In contrast, NM produced the least MISC of 0.9. The $MPCw_{con0.9}$ had an intermediate MISC of 2.0.

The selected MCA configurations were further analysed based on the rendered specific force profiles. Figure 6.3 presents the specific force profiles produced by each configuration. More detailed graphs with rotation and displacement data are shown in Appendix E.8. The results show that the AW algorithm and the $MPCw_{con0}$ configuration yield very similar profiles, whereas the $MPCw_{con0.9}$ configuration results in noticeably lower specific force magnitudes.

6.3 Human Evaluations

This section describes the simulator experiment and its subjective evaluation. Perceived driving simulator fidelity and motion sickness were evaluated from the perspective of passive users, representative of users of automated vehicles. This work utilises the Delft Advanced Vehicle Simulator (DAVSi), a 6-DoF moving-base driving simulator (Khusro et al., 2020), capable of generating accelerations of up to 1 g in all directions at a frequency of 10 Hz.

6.3.1 Experimental Procedure

All participants provided informed consent before participating in the study. The human research ethics committee of TU Delft, The Netherlands, approved the experimental protocol (application number 4819).

In total, 20 participants from the pool of students and employees of TU Delft participated in the study (mean age: 27.70 years, std: 3.42 years, 6 females, 14 males). The individual motion sickness susceptibility was evaluated using the motion sickness susceptibility questionnaire - short (MSSQ-Short) by Golding (2006b), yielding a mean MSSQ score of 49.6 with a standard deviation of 24.9, which is well above the population mean of 12.9, indicating a high level of motion sickness susceptibility among the participants.

Each participant experienced all four selected motion cueing algorithm configurations, each in a separate simulator session, in a randomised order. To minimise carry-over effects and to mitigate motion sickness influence from previous exposures, the sessions were spaced at least 48 hours apart for each participant.

Before the experiment, the participants underwent a concise briefing session to familiarise themselves with the questionnaire and to understand the objective of the experiment. During the experiment, two-way communication was established between the experimenter and the participant via Bluetooth headphones and microphones.

Measures were taken to ensure that the driving scene remained their sole visual focus, including blocking side window views and part of the windshield to eliminate external cues indicating platform tilt.

During each session, participants reported their motion sickness levels every 30 seconds using the misery scale (MISC) (Reuten et al., 2021), prompted by an auditory beep in the headphones. After completing a session, participants filled out an absolute grading questionnaire (Appendix E.2) assessing different aspects of the driving experience.

To ensure a fair comparison, the sequence of algorithm exposures varied across participants. A latin square design was employed to balance the experimental testing order. Participants were permitted to withdraw from the experiment at any point; however, no individuals chose to exercise this option.

6.3.2 Scenario

The aim of this study is to investigate simulator sickness in relation to motion cueing in driving simulators. To this end, a virtual driving scenario was designed to simulate a naturalistic urban drive that would not typically induce motion sickness in real-world driving, but may do so in a simulator due to sensory mismatch and strong visual motion cues.

Since the ultimate goal is to develop strategies to mitigate simulator sickness, the experiment must first ensure a sufficiently high likelihood of inducing sickness. Given the naturalistic and non-aggressive nature of the driving scenario, participants were exposed to it for an extended period to allow the gradual onset of sickness symptoms. Based on this consideration, the total session duration was set to approximately 30 minutes.

The driving scenario consisted of 240-second laps, followed by a 10-second pause, repeated six times per session. This structure provided consistency across participants while maintaining a manageable session length and data segmentation for analysis. The urban driving scenario included vehicle speeds ranging from 0 to 70 km/h and consisted of a diverse set of manoeuvres: stop-and-go sequences at traffic lights and pedestrian crossings, moderate cornering, a tunnel section, and a double lane-change manoeuvre due to a road diversion caused by an accident. These dynamic events were chosen to replicate realistic driving conditions while introducing sufficient variations in acceleration to challenge the simulator's motion rendering capabilities.

The scenario was created using IPG CarMaker, which provides a realistic virtual environment and high-fidelity vehicle dynamics simulation. CarMaker's vehicle models are experimentally validated, ensuring that the generated accelerations are representative of actual driving conditions. These acceleration signals serve as the reference specific forces for the motion cueing algorithm that drives the simulator platform.

The resulting data shows lateral accelerations within the range of approximately $\pm 4 m/s^2$, longitudinal accelerations up to 1.25 m/s^2, and decelerations reaching $-5 m/s^2$. These dynamic variations are used to evaluate the simulator's motion cueing effectiveness and its relationship with simulator sickness development. The reference provided to all MCAs (MPC based and AW) was scaled down by a factor of 0.3 and 0.4 for the longitudinal and lateral vehicle accelerations, respectively. The choice of the scaling factors is coherent with our paper using MPC in conjunction with a frequency splitting MCA (Jain et al., 2023b), where it was based on participant feedback obtained during pilot studies to enhance realism, and on other studies using similar scaling factors (Bellem et al., 2017; Lamprecht et al., 2022).

6.3.3 Results

Subjective Realism Ratings

Based on participant realism scores collected during the experiment, a subjective evaluation of the motion cueing algorithms was conducted. figure 6.4 presents a summarised boxplot of the ratings for the different motion cueing configurations. The results indicate that the three conditions with platform motion ($MPCw_{con0.9}$, $MPCw_{con0}$, and AW) received

closely clustered ratings across all realism criteria. In contrast, the NM (no motion) configuration consistently received the lowest scores, indicating that participants perceived it as the least realistic. These findings imply that the absence of motion cues in the NM configuration significantly reduced the sense of immersion, making it feel less like a real vehicle drive. Conversely, the other configurations were perceived to deliver comparable levels of realism and immersion, reinforcing the value of motion-based cues in enhancing perceived driving fidelity.

Figure 6.4 highlights statistically significant differences between the configurations, calculated using analysis of variance (ANOVA), using asterisks ('*'). These markers indicate that each motion-based configuration exhibits a statistically significant difference in perceived realism when compared to the NM configuration. However, no significant difference is observed among the motion-based configurations themselves, further supporting the conclusion that they provide a comparable level of immersive experience.

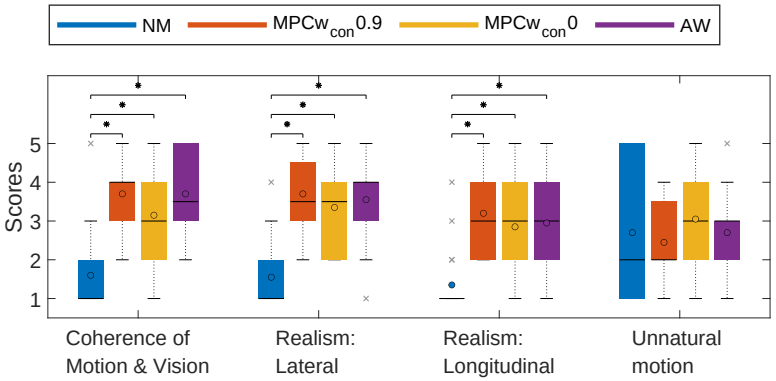

Figure 6.4: Realism scores obtained for the different algorithm configurations during the human-in-the-loop validation experiments. '*' represent significant differences, circles represent the mean, solid lines represent the median, boxes represent 25th and 75th percentiles, with '×' capturing the full range including outliers.

Motion Sickness Ratings

The experimental motion sickness (MISC) as a function of time is presented in figure 6.5, along with the predictions from the model framework. Coloured lines represent experimental (solid) and predicted (dashed) results for the four configurations used in the experiment. The black dotted line shows the predicted motion sickness if the scenario would be driven in a real vehicle with external vision. Dropout rates and variance are predicted using the SVC model in conjunction with our population-based motion sickness model (Kotian et al., 2023, 2025).

The experimental data aligns well with the MISC levels predicted by the model framework. Although experimental values do not exactly match the model predictions, they follow a similar trend across configurations (see figure 6.5). The SVC model generally overestimates MISC levels relative to the observed data, with the exception of the $MPCw_{con0}$ configura-

tion, where the predictions are lower than the measured values at the end of the experiment.

As predicted by the model, in the experiment, the NM configuration results in the lowest levels of motion sickness. Slightly higher levels are seen with the $MPCw_{con0.9}$ configuration, followed by AW, and the highest levels are recorded for $MPCw_{con0}$. This trend confirms that increasing the weight on sensory conflict leads to a reduction in motion sickness, as expected from the offline analysis in figure 6.2. Additionally, only one participant dropped out in the $MPCw_{con0.9}$ condition, compared to six in $MPCw_{con0}$ and four in the AW condition. This confirms that the $MPCw_{con0.9}$ is capable of extending the exposure time in the simulator.

The experimental MISC data were checked for condition effects and order effects using the mean MISC over the last lap. For this analysis, participants who dropped out had their MISC level assumed to be 6 from the point of dropout until the scheduled end of the experiment. The statistical significance, calculated using analysis of variance (ANOVA), is tabulated in Table 6.3, and boxplots are shown in figure 6.6. There was a significant overall effect of conditions on MISC, and there was a significant difference between the pairs (a) NM and $MPCw_{con0}$ (b) NM and AW (c) $MPCw_{con0.9}$ and AW (d) $MPCw_{con0.9}$ and $MPCw_{con0}$, whereas, no significant differences were found between (a) NM and $MPCw_{con0.9}$ and (b) AW and $MPCw_{con0}$. However, there were no significant differences because of order effects, i.e., the order in which the participant was subjected to the algorithms did not have a significant effect on the output of the experiment.

Table 6.3: MCA Condition effects on MISC
(Overall p-value< 0.01)

pairs		p-value
NM	$MPCw_{con0.9}$	0.26
NM	$MPCw_{con0}$	<0.01
NM	AW	<0.01
$MPCw_{con0.9}$	$MPCw_{con0}$	<0.01
$MPCw_{con0.9}$	AW	0.049
$MPCw_{con0}$	AW	0.17

In figure 6.7, we compare the histogram of individual MISC levels at the end of the experiment, as predicted by the model framework and as observed in the experimental data. While there are some deviations in the exact occurrence across MISC levels, the overall trend is reasonably well captured by the motion sickness model. The most notable discrepancy occurs at MISC level zero, where the model underestimates the proportion of participants reporting no motion sickness, failing to predict a MISC of zero for a substantial segment of the population.

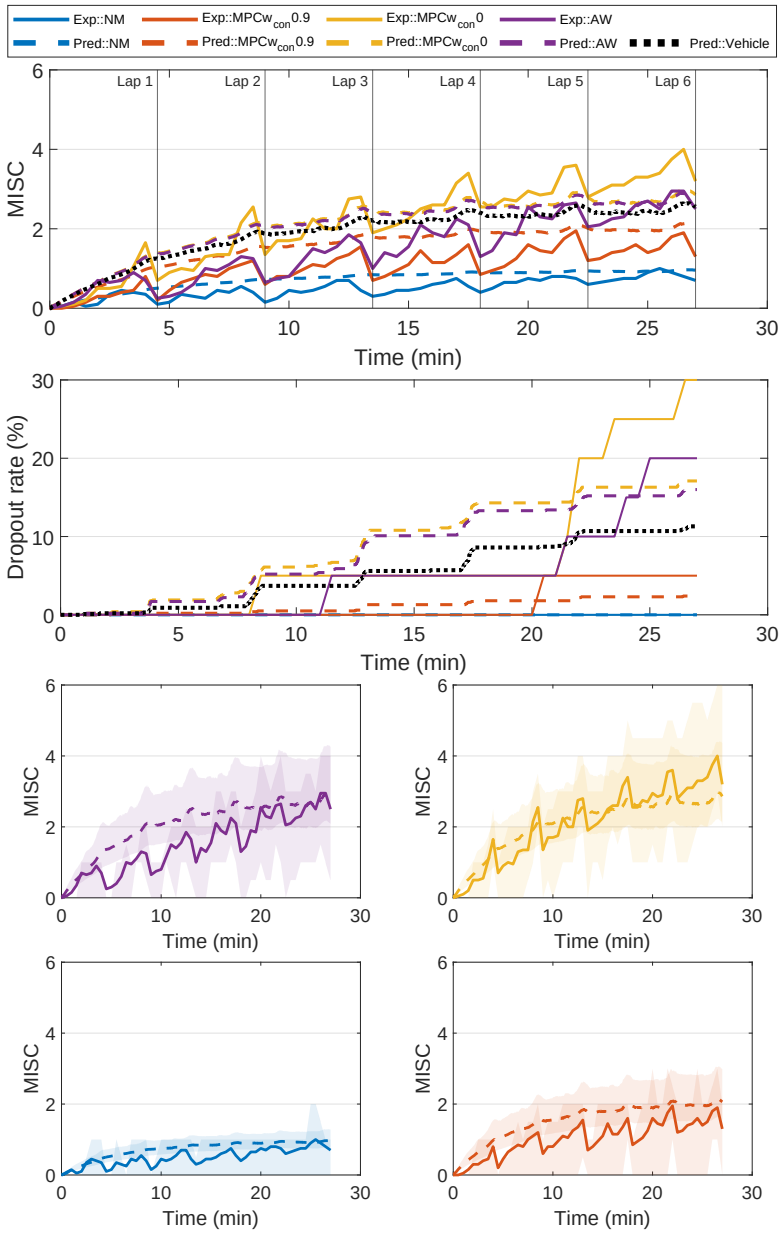

Figure 6.5: Experimental MISC responses along with model predictions for all scenarios considered in the experiment. The solid lines represent the data collected during the experiment, and the dashed lines represent the predictions coming from the SVC model. The black dotted line shows the predicted motion sickness if the scenario would be driven in a real vehicle. Mean response (upper graph), dropout rates (second graph) and variance (four separate graphs) where the shaded region spans from the 25th to the 75th percentile.

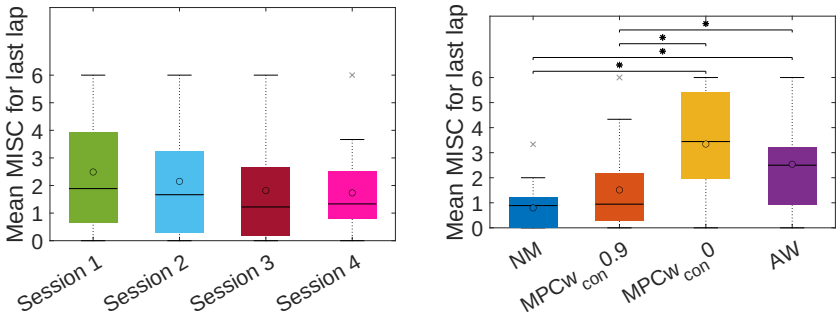

Figure 6.6: Order effect (left) and MCA effect for mean MISC over the last lap in the experiment with '*' representing significant differences ($p<0.05$) between algorithm configurations.

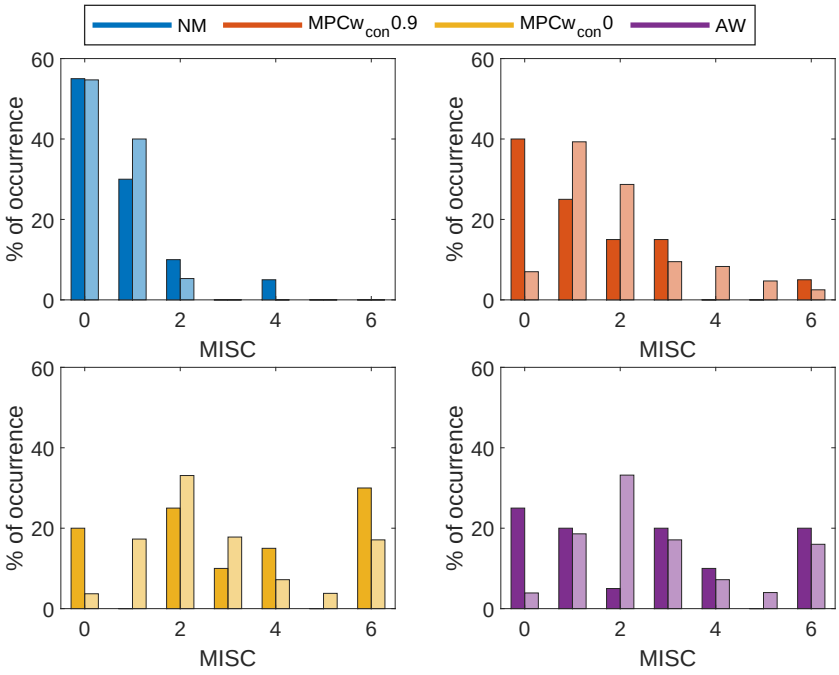

Figure 6.7: Histogram of MISC at the end of the experiment. Experimentally observed MISC in dark colours and predicted MISC in lighter colours.

6.4 Discussion

This work addresses a pivotal gap in the domain of driving simulator motion cueing by directly integrating motion sickness mitigation as an explicit control objective. Historically, the development of MCAs has emphasised fidelity in motion perception, often overlooking the physiological consequences of simulator use, especially motion sickness. While prior works have explored high-fidelity motion rendering through MPC, to the best of the authors' knowledge, no work has incorporated advanced motion sickness models, such as the 6-DoF subjective vertical conflict model (SVC) (Wada et al., 2020), to anticipate and suppress motion sickness.

The algorithm introduced here not only enhances the perceptual accuracy of motion (via specific force tracking), but also integrates a dedicated cost term that helps to minimize human discomfort through sensory conflict. This dual-objective formulation represents a significant methodological advancement.

A notable strength of this work is the experimental validation of this predicted improvement. Through simulation, objective metrics (like RMSE and shape similarity), and human-in-the-loop evaluation, the proposed solution was shown to be robust across both algorithmic performance and perceptual quality. The experimental results confirm that sensory conflict minimisation, even at the expense of reductions in specific force magnitude, can lead to a statistically significant improvement in user comfort without degrading immersion and realism. The successful prediction of MISC levels using a population-based SVC and sickness accumulation model further emphasises the algorithm's predictive validity and practical utility.

6.4.1 MISC Prediction

In a novel contribution to the field, this work presents the first-ever quantitative prediction of absolute motion sickness levels using the SVC model in combination with a sickness accumulation model in driving simulator motion cueing. Here we build on our recent papers where we combine the SVC model with an accumulation model and estimated individual parameters to capture experimental MISC values in vehicle and driving simulator experiments (Kotian et al., 2023, 2025). Prior research has predominantly focused on trends or qualitative sickness development; in contrast, our approach enables the prediction of absolute MISC scores. As sickness varies between individuals, we generalise our model using population-representative parameters. As a result, we provide predicted average MISC responses, accompanied by the standard deviation to capture inter-individual variability. This methodology offers a new standard for objective, model-based evaluation of motion sickness in simulator contexts.

As shown in figure 6.5, the MISC predictions (represented by dashed lines) follow a trend similar to the experimental data (represented by solid lines). Additionally, the predicted MISC levels remain close to the actual values recorded at the end of the experiment.

Interestingly, the adaptive washout and the configuration $MPCw_{con0}$ yield very similar

MISC predictions. However, in the experiment, adaptive washout was more sickening. Likewise, the experimental MISC fluctuates more across time, whereas the predicted MISC increases more gradually, providing scope to enhance the accumulation model and its parameters. MSSQ was reported to be higher in the participants of this experiment, indicating an above-average susceptibility, but the experimental MISC was not higher than the model-predicted MISC. However, MSSQ is an imperfect predictor of susceptibility, see Irmak et al. (2025) for a recent discussion. Certain instances of false cues may have a higher/bigger impact on motion sickness than others, which the model may not be able to discern/quantify (such as prepositioning or coupled translational and rotational motion). However, even with these discrepancies, the trend of prediction of motion sickness severity by the SVC model still matched the measurements. This is particularly evident comparing $MPCw_{con0}$, $MPCw_{con0.9}$ and NM, where the experimental results follow the trend predicted by the SVC model.

A generalised rather than individual-specific motion sickness model was used in the MCA. Nevertheless, the use of generalised parameters still proves valuable for reducing motion sickness. This is because it is more important to lower the sickening stimuli than to precisely predict their impact on MISC levels. In the developed algorithm, sensory conflict is minimised over all time points in the MPC horizon and the slow accumulation process is ignored. One of the reasons for doing this is to make the problem computationally feasible. The offline predictions and the experiment demonstrate that this effectively reduces sickness over the entire experiment duration.

6.4.2 Realism

This work evaluates realism through both subjective and objective measures. The objective metrics include specific force tracking and the shape similarity factor. figure 6.4 indicates that the perceived realism is not significantly impacted by the different motion cueing algorithms. Only no motion had reduced realism perception. Realism remained consistent across the model predictive control (MPC) algorithms and the adaptive washout algorithm, even when the overall motion was substantially reduced, as evidenced by the reduction in specific force RMSE reported in table 6.2. These findings suggest that shape similarity, as calculated by the Pearson correlation coefficient, is a more reliable indicator of perceived realism than the specific force RMSE. This implies that the temporal shape of the motion signal plays a more critical role in realism perception than the magnitude of the experienced forces. Additional data is needed to determine whether realism remains consistent across the entire weight spectrum, particularly in the range $w_{con} = 0$ to 0.9.

It would have been interesting to query the perceived realism continuously, as done in Cleij et al. (2017), to get a better understanding of where exactly in the maneuver the realism breaks down instead of getting a single value over the entire drive. However, in the current study, this could not be done as the participants were already reporting motion sickness levels, and we did not want to increase the mental load of the participants, at the risk of disrupting immersion.

6.4.3 Motion Sickness Manipulation

A key finding is that the algorithm is capable of significantly reducing motion sickness while preserving the perception of motion. Subjective results revealed that a conflict weight of $w_{con} = 0.9$ resulted in an average end MISC level of 2 across participants. In contrast, both the adaptive washout and the MPC configuration with only specific force tracking yielded an average MISC level of 3. This reduction was achieved without any significant reduction of perceived realism. Another important finding is that the MPC-based algorithm, with no restriction on motion sickness ($MPCw_{con0}$), outperforms the adaptive washout algorithm in terms of specific force reproduction.

Although this work specifically targets the reduction of motion sickness, the algorithm can also be configured to recreate motion sickness in real vehicles. For example, the model predictions in figure 6.5 indicate that, in this scenario, replicating real-vehicle motion sickness within a driving simulator would already be nearly achieved with either AW or $MPCw_{con0}$. To minimise motion sickness, the sensory conflict is given a reference of zero. However, by feeding the actual sensory conflict, calculated from real vehicle data, into the MPC as reference, motion sickness can be intentionally reproduced. This could prove valuable for assessing how sick an occupant may feel when exposed to specific automated driving styles, and for conducting human-acceptance or behavioural studies within a simulated environment, especially in cases where real vehicle and simulator responses are directly compared.

The experimental validation confirmed that the no-motion case resulted in the least amount of sickness, as predicted by the SVC model. However, no motion was rated as the least realistic. This aligns with Romano et al. (2016), where the perceived fidelity improved with the addition of motion to the simulator platform, accompanied by an increase in motion sickness. However, this does not align with the meta-analysis of de Winkel et al. (2022), where enhanced visual fidelity reduced motion sickness for moving base, but not for fixed base, indicating that increasing the visual fidelity may be responsible for inducing more sickness. In our experiment, the frontal view was the main focus, thus, the peripheral vision was blocked. This blocking of peripheral vision may have limited the visual influence on participants' sickness levels. In the SVC model used in this study, the visual input is restricted solely to the visual rotational velocity, which is assumed to be perfectly congruent with the actual rotational velocity of the visual stimuli presented on the screen. This simplification may be a limitation, underscoring the need for more comprehensive modelling approaches that more accurately reflect the complexity of visual systems.

6.4.4 Yaw

In this study, yaw motion was controlled via a traditional washout algorithm, which does not consider motion sickness in its design. This decision was made to simplify the MPC computation and limit computational load. A recent study found missing and false yaw cues to affect perceived fidelity and sickness with a similar magnitude as missing and false longitudinal and lateral cues, although the significance of these effects was not reported (Kolff et al., 2025). Future work may explore integrating yaw dynamics into the MPC framework to potentially improve sickness mitigation and deliver more precise rotational cueing.

6.5 Conclusion

The developed motion cueing algorithm demonstrates a strong capability to reduce motion sickness while maintaining a realistic perception of vehicle motion. Experimental results show that increasing the weight for sensory conflict within the model predictive control framework leads to a noticeable reduction in motion sickness experienced by participants. This confirms the effectiveness of penalising sensory conflict as an explicit control objective in an MPC-based motion cueing algorithm.

Subjective evaluations further reinforce the findings, with participants rating motion-based configurations significantly higher in realism compared to the no motion baseline. Even low-amplitude motion significantly enhances perceived motion fidelity compared to no-motion conditions.

In summary, this work marks a significant advancement in motion cueing design by successfully integrating a perceptually-informed motion sickness model directly into the control framework. The algorithm not only proves effective in reducing motion sickness through both simulation and human-subject validation, but also demonstrates that motion fidelity can be preserved while optimising for comfort. This achievement paves the way for more immersive and tolerable long-duration driving simulation experiences, setting a new benchmark for future motion cueing algorithms.

7

Discussion

In the end, it's not the outcome that defines us, but how we faced it.

Erwin Smith

This chapter summarises the main findings of this thesis and their implications, and presents the main recommendations for future work.

7.1 Findings and their Implications

Here, we reflect upon the findings in relation to the three research objectives addressed in this thesis, as defined in chapter 1:

Objective 1: Collect, measure and predict motion sickness in person-specific metrics.

Objective 2: Evaluate how vision influences perception and motion sickness in humans and computational models

Objective 3: Develop a personalisable mathematical model capable of predicting variance in motion sickness, for application in motion cueing algorithms that regulate sickness in driving simulators.

Chapters 2 and 4 pertain to Objective 1, chapters 3 and 5 to Objective 2, and chapters 4 and 6 to Objective 3.

In chapter 2, the relationship between stimulus amplitude and motion sickness development is studied. The effect of a sinusoidal stimulus with different magnitudes in different sessions was tested on participants with their eyes closed. Group-level analysis indicates that sickness severity expressed in MISC increases linearly with acceleration amplitude. Here, Oman's model was adopted as an accumulation model to describe time evolution, including recovery after exposure and hypersensitivity, of motion sickness. Importantly, we note that the time constants governing motion sickness development vary between individuals, but are independent of the acceleration amplitude. A group-level fixed output scaling with an exponent of 0.4 enables Oman's model to accommodate stimulus-amplitude variations under the tested conditions, and the model can forecast the temporal evolution of sickness beyond brief initial exposure. Overall, these findings enable improved modelling of sickness accumulation in mixed-acceleration environments, pre-screening for motion-sickness experiments, and tuning of automated driving algorithms for individual passengers. These results address Objective 1.

In chapter 3, the first broad validation of vision effects within state-of-the-art motion perception and motion sickness models is presented. The Subjective Vertical Conflict (SVC) (Kamiji et al., 2007; Kotian et al., 2024; Wada et al., 2020) and Multi-Sensory Observer Model (MSOM) (Clark et al., 2019; Newman, 2009) models were tested with visual loops selectively enabled or disabled across stimuli covering sickness frequency sensitivity, slalom driving, and fundamental perception paradigms. Of the nine tested model variants, none reproduced all experimental sickness and perception results. The SVC_I-VR model, which includes visual rotational velocity (VR) perception, was found to best predict the effects of different vision conditions on sickness development; however, perceptual predictions by the SVC_I-VR model do not match data for certain paradigms (e.g., somatogravic illusion, tilt perception in a centrifuge). All perceptual data are accurately matched by the

MSOM-VR+VV variant (visual rotational velocity (VR) and visual vertical/orientation perception (VV)), yet the MSOM fails to reproduce the well-known sickness-frequency sensitivity. Consequently, no single model captures both motion sickness and motion perception. The strong match between SVC$_I$-VR and motion sickness data supports conflict theory, implicating verticality (subjective vertical) conflict as the primary driver of sickness. The SVC$_I$-VR model, subsequently referred to as SVC-VR in the next chapters, was selected as the best compromise for sickness prediction and served as the basis for motion sickness modelling and mitigation in further chapters. These conclusions address Objective 2.

Chapter 4 presents a novel framework for predicting motion sickness (in terms of MISC) accumulation in time by combining a group-average 'conflict generation' model with an individualised 'conflict accumulation' model. Using acceleration and angular rotational data, the model parameters were tuned to each individual's motion sickness response. By fitting across various conditions and different datasets, the model estimates a single parameter set per participant, enabling a highly personalised understanding of their motion sickness dynamics. This framework achieves an average RMSE of 1.54 with just two estimated and personalised parameters – a gain (K_1) and a time constant (T_1). The combined conflict generation and personalised accumulation model yields 34% improvements over traditional group-averaged models (1.54 RMSE for AM2 vs 2.06 RMSE for AM0). Stochastic modelling of the parameter distribution is further found to enable effective sampling for untested scenarios, enhancing adaptability and reducing reliance on extensive human testing, thereby supporting personalised applications in driving simulators and real-world automated-vehicle contexts. These results address Objective 1 and 3.

Chapter 5 investigates human pitch motion perception under varying visual and mechanical motion conditions and evaluates the predictive performance of the Subjective Vertical Conflict (SVC) model. Participants consistently underestimated pitch rotation amplitude by around 20% and exhibited an average response delay of 0.75 seconds, with no significant effect of different vision conditions in the presence of full platform motion. Using published parameter values, the tested SVC models produced highly unrealistic pitch perception predictions. Especially the SVC-VR model, which omits visual verticality perception, predicted an incorrect motion direction in the Only Vision condition. Retuning the SVC-VR model significantly improved its fit to the human response data, and incorporating vestibular perception thresholds further enhanced accuracy. These findings reveal the complexity of sensory integration in motion perception and expose limitations of current models. These conclusions address Objective 2.

In chapter 6, a novel motion cueing algorithm is proposed that explicitly reduces motion sickness as predicted by the Subjective Vertical Conflict (SVC) model using a Model Predictive Control (MPC) algorithm. The cost function penalises both sensory conflict and specific-force errors to balance fidelity and comfort. Human-in-the-loop experiments compared four simulator motion settings: reference Adaptive Washout and No Motion cases, as well as two variations of the MPC-based algorithm, one emphasising pure specific force tracking and the other balancing specific-force tracking with sickness minimisation (i.e., 'compromise' solution). The experiments were performed on a hexapod driving simulator with participants exposed to passive driving. Experimental motion sickness results closely matched the sickness model predictions. As predicted by the model, the No Motion condi-

tion yielded the lowest sickness levels, but was rated lowest for fidelity. The compromise MPC-based solution reduced sickness by over 50% (average MISC level 3 to 1.5) compared to the Adaptive Washout and the MPC focusing purely on specific force tracking, without a significant reduction in fidelity rating. This model-based approach that takes into account both the simulator dynamics and time evolution of motion sickness offers a significant advancement in achieving an optimal control of motion sickness and specific force recreation in driving simulators, supporting broader simulator use. These conclusions address Objective 3.

Collectively, the findings address the three objectives. Objective 1 is addressed by collecting new experimental datasets and combining different available datasets that measure motion sickness using person-specific metrics, specifically through the MIsery SCale (MISC), to capture participants' unique response profile during driving simulator and automated vehicle exposure with varying vision and motion conditions tested on the same participants. This resulted in a total of four datasets obtained from real vehicle driving and four datasets obtained from tests on a simulator across varying vision and motion conditions. These datasets enabled the development and validation of person-specific prediction models for motion sickness. Objective 2 is addressed through systematic validation of vision effects in state-of-the-art motion perception and motion sickness models, revealing that no single model reproduces all experimental sickness and perception data. Models incorporating both visual rotational velocity and orientation perception align more closely with perceptual outcomes, while others (specifically the SVC with only a visual rotational velocity input) better capture sickness dynamics, underscoring the need for models that simultaneously and accurately capture perceptual outcomes and sickness dynamics. Objective 3 is achieved by the novel model framework that combines a group-average conflict generation model with an individualised accumulation model, providing strong predictive accuracy. By using it in a Model Predictive Control motion cueing algorithm, sickness can be reduced by over 50% relative to the baseline, without a significant loss in fidelity. Together, the work provides a coherent pathway to personalised prediction and mitigation of motion sickness, clarifies the limits of current perceptual models under visual-vestibular conditions, and yields practical modelling and control strategies for driving simulators and real-world automated-vehicle applications.

7.2 Conclusion

As the role of car occupants shifts from active drivers to passive passengers in automated vehicles and driving simulators, the relevance of motion sickness as a key challenge is growing. This dissertation systematically examined the mechanisms driving motion sickness, introduced advanced modelling frameworks for its accurate prediction, and applied them in motion cueing algorithms for motion sickness mitigation. Through a combination of experimental and modelling approaches, this work identifies the mechanisms underlying motion sickness, focusing on how these conflicts accumulate over time and how visual conditions alter both perception and sickness responses.

A central contribution is the development of a person-specific predictive model framework

that captures pronounced individual variability with a limited set of parameters. These frameworks enable accurate, person-specific predictions by estimating just a few individualised parameters, yielding clear improvements over traditional group-averaged approaches. Building on these insights, a model-predictive control (MPC) motion cueing algorithm was developed and shown to significantly reduce motion sickness in simulators without sacrificing realism, providing a highly valuable tool for both research and practical vehicle applications. Collectively, these advancements contribute towards new understanding and practical methods for predicting and controlling motion sickness, supporting automated vehicles and simulators that can adapt in real time to individual comfort requirements.

As automated mobility systems become more prevalent, the ability to predict and control motion sickness in a personalised manner will be essential for user acceptance and comfort. This thesis delivers a rigorous foundation for personalised prediction and mitigation, clarifying where current perceptual models succeed and where they need refinement under visual–vestibular conditions. It charts a path toward adaptive mobility systems that intelligently accommodate the unique profiles of passengers, thereby enhancing comfort and supporting the broader adoption of automated transport technologies.

7.3 Recommendations for Future Work

Based on the findings and limitations discussed above, several recommendations for future research and methodological improvement are warranted.

Firstly, the present work relied on data which used the MIsery SCale (MISC) by Bos et al. (2005) for quantifying motion sickness responses. This consistency in measurement was essential, as motion sickness scales are not interchangeable and no established conversions between them exist. Without a common scale, datasets cannot be pooled, parameters cannot be estimated robustly, and models cannot be compared or ruled out fairly. Using MISC across studies (or at least alongside other measures) will enable larger shared datasets, which we need to identify mechanisms, improve models, and move toward a single model that covers both perception and sickness.

Second, the experiments described in chapter 2 and chapter 5 were constrained in the range of vision and motion conditions explored, respectively. Expanding the amplitude range in motion perception paradigms and increasing the variety of vision manipulations in motion sickness studies would allow for a more comprehensive assessment of both model predictions and human variability. Such expanded testing would better inform the parameterisation and broader applicability of the proposed models. Steps towards this have already been taken by Bos et al. (2024), where the experimental protocols have been extended to incorporate wider motion profiles and ranges. However, these extensions do not yet systematically vary visual conditions. This is crucial as without controlled variation in visual cues, we cannot identify model parameters tied to vision, test visual–vestibular interactions, or validate models across the conditions they are meant to predict. Experimental designs that combine wider motion profiles with systematic visual manipulations are therefore needed.

In addition, vision modelling should be improved. Currently, the models implement vision in three ways: external, internal, or not at all. Visual inputs are limited to rotational cues—visual rotational velocity (VR) or visual vertical (VV). This leaves a major gap. Conflicts driven by linear visual motion are not represented. Yet in cars, stop–go, braking, and lateral translations are often the most nauseogenic. Future work should therefore capture and model translational optic flow. Additionally, enabling real-time extraction of both rotational and translational visual motion (similar to what was done by (Liu et al., 2024)) and integrating these with vestibular signals would let models respond to changing inputs and better predict visually driven conflicts.

A further recommendation is that individualisation can be further improved by also enabling a personalised conflict generation model. Evidence by Irmak et al. (2021) indicates substantial interpersonal variability in the conflict generation model as well. Future modelling should therefore also address individualisation of the conflict generation component, for example, by personalising feedback gains that capture individual differences in the weighting of visual signals (such as $K_{\omega vis}$ in the SVC-VR model by Wada et al. (2020)). This refinement would enable the modelling framework to perhaps better account for variations in sickness sensitivity under visually rich conditions, while leaving responses to purely vestibular stimuli unaffected, thereby improving the accuracy of personalised predictions.

It is also important to strengthen validation in real vehicles. Although several vehicle datasets were used in this dissertation alongside simulator studies, further on-road experiments are encouraged to corroborate simulator findings and assess contextual effects (e.g., natural head posture, task engagement, traffic environment). Studies such as Irmak et al. (2020); Talsma et al. (2023) provide relevant examples. While operationally and logistically demanding, such work is necessary to generalise conclusions to naturalistic settings.

The current MPC-based motion cueing implementations utilise only the (group-level) conflict generation aspect of the modelling framework, reserving the (individualised) accumulation model for retrospective assessment and analysis only. Incorporating both conflict generation and individualised accumulation models in real-time MPC operation is likely to yield further gains in motion sickness mitigation and also enable a ‘replication mode’, where the controller targets a desired sickness trajectory observed in real vehicles. This would make it easier to match simulator and on-road experiments, transfer and validate parameters across platforms, and address the key challenge of joint model–experiment benchmarking.

Moreover, while this dissertation focused on applications in motion cueing algorithms, the underlying frameworks have direct applications for motion planning (Jain et al., 2023a). Future work could leverage these models to develop motion planning algorithms that optimise not only time and efficiency, but also ride comfort along given routes. Such systems could offer user-selectable modes akin to ‘eco’, ‘sport’, or ‘comfort’, balancing travel objectives and motion sickness mitigation as suited to individual passenger preferences. Additionally, we can use the sickness model within active suspension control to work backwards and minimise predicted conflict. The controller shapes chassis motion by adjusting damping and roll or pitch to reduce perceived accelerations and dose, which improves ride comfort and lowers sickness along the route (Zheng et al., 2022).

Future research should extend the current modeling framework to address active control scenarios. Throughout this thesis, we applied the observer framework primarily to passive motion. In these cases, the internal model relies on sensory feedback to estimate the state. However, the complete observer theory by Oman (1982) also relies on an efference copy. This is a copy of the motor commands used to predict self-motion. This component was not used during the passive tests in chapters 3 and 4. Future applications of these models to active driving must include this mechanism. This is necessary to explain why active drivers are much less likely to get sick than passengers.

Collectively, these recommendations can enable broader generalizability, more precise personalisation, and enhanced applicability of motion sickness models and mitigation strategies, supporting further advances in both the scientific understanding and practical management of motion sickness in simulated and real-world transport environments.

Bibliography

Akaike, H. (1998). Information Theory and an Extension of the Maximum Likelihood Principle. *Biogeochemistry*, 1998:199–213.

Alexander, S. J., Cotzin, M., Klee, J. B., and Wendt, G. R. (1947). Studies of motion sickness: XVI. The effects upon sickness rates of waves of various frequencies but identical acceleration. *Journal of Experimental Psychology*, 37(5):440–448.

Allred, A. R. and Clark, T. K. (2024). A computational model of motion sickness dynamics during passive self-motion in the dark. *Experimental Brain Research 2024 242:5*, 242(5):1127–1148.

Allred, A. R., Gopinath, A. R., and Clark, T. K. (2025). Validating sensory conflict theory and mitigating motion sickness in humans with galvanic vestibular stimulation. *Communications Engineering 2025 4:1*, 4(1):78–.

Angelaki, D. E., Shaikh, A. G., Green, A. M., and Dickman, J. D. (2004). Neurons compute internal models of the physical laws of motion. *Nature*, 430(6999):560–564.

Ariel, D. and Sivan, R. (1984). False Cue Reduction in Moving Flight Simulators. *IEEE Transactions on Systems, Man and Cybernetics*, SMC-14(4):665–671.

Bae, I., Kim, J. H., Moon, J., and Kim, S. (2019). Lane Change Maneuver based on Bezier Curve providing Comfort Experience for Autonomous Vehicle Users. In *Intelligent Transportation Systems Conference*, pages 2272–2277.

Bäuerle, A., Anken, R. H., Hilbig, R., Baumhauer, N., and Rahmann, H. (2004). Size and cell number of the utricle in kinetotically swimming fish: A parabolic aircraft flight study. *Advances in Space Research*, 34(7 SPEC. ISS.):1598–1601.

Baumann, G., Jurisch, M., Holzapfel, C., Buck, C., and Reuss, H.-C. (2021). Driving simulator studies for kinetosis-reducing control of active chassis systems in autonomous vehicles. In *Driving Simulation Conference Proceedings*, pages 51–58, Munich, Germany. Driving Simulation Association.

Bellem, H., Klüver, M., Schrauf, M., Schöner, H.-P., Hecht, H., and Krems, J. F. (2017). Can we study autonomous driving comfort in moving-base driving simulators? A validation study. *Human factors*, 59(3):442–456.

Berger, D. R., Schulte-Pelkum, J., and Bülthoff, H. H. (2010). Simulating believable forward accelerations on a stewart motion platform. *ACM Transactions on Applied Perception (TAP)*, 7(1).

Berkouwer, W., Stroosma, O., van Paassen, R., Mulder, M., and Mulder, B. (2005). Measuring the Performance of the SIMONA Research Simulator's Motion System. In *AIAA Modeling and Simulation Technologies Conference and Exhibit*, Guidance, Navigation, and Control and Co-located Conferences. American Institute of Aeronautics and Astronautics.

Berthoz, A. and Droulez, J. (1982). Linear Self Motion Perception. *Tutorials on Motion Perception*, pages 157–199.

Bertolini, G. and Straumann, D. (2016). Moving in a moving world: A review on vestibular motion sickness. *Frontiers in Neurology*, 7(FEB):14.

Bock, O. L. and Oman, C. M. (1982). Dynamics of subjective discomfort in motion sickness as measured with a magnitude estimation method. *Aviation, space, and environmental medicine*, 53(8):773–777.

Bos, J., Kuiper, O. X., and Schmidt, E. A. (2020). Motion Predictability and Sickness. In *Driving Simulation Conference Proceedings*, pages 179–182, Antibes, France. Driving Simulation Association.

Bos, J. E. (2011). Nuancing the relationship between motion sickness and postural stability. *Displays*, 32(4):189–193.

Bos, J. E. and Bles, W. (1998). Modelling motion sickness and subjective vertical mismatch detailed for vertical motions. *Brain Research Bulletin*, 47(5):537–542.

Bos, J. E. and Bles, W. (2002). Theoretical considerations on canal–otolith interaction and an observer model. *Biological Cybernetics 2002 86:3*, 86(3):191–207.

Bos, J. E., Bles, W., and Groen, E. L. (2008). A theory on visually induced motion sickness. *Displays*, 29(2):47–57.

Bos, J. E., de Vries, S. C., van Emmerik, M. L., and Groen, E. L. (2010). The effect of internal and external fields of view on visually induced motion sickness. *Applied Ergonomics*, 41(4):516–521.

Bos, J. E., Mackinnon, S. N., and Patterson, A. (2005). Motion Sickness Symptoms in a Ship Motion Simulator: Effects of Inside, Outside, and No View. *Aviation, Space, and Environmental Medicine*, 76(12):1111–1118.

Bos, J. E., Nooij, S. A. E., and Souman, J. L. (2021). (Im)possibilities of studying carsickness in a driving simulator. pages 59–63. Driving Simulation Association.

Bos, J. E., Souman, J. L., Nooij, S., and Diels, C. (2024). *Advancing ISO 2631-1 by considering pre-emesis symptoms in carsickness - Driving Simulation Proceedings*. Driving Simulation Association, Strasbourg, France.

Brandt, T., Dichgans, J., and Koenig, E. (1973). Differential effects of central versus peripheral vision on egocentric and exocentric motion perception. *Experimental Brain Research*, 16(5):476–491.

Bruschetta, M., Cenedese, C., Beghi, A., and Maran, F. (2018). A motion cueing algorithm with look-Ahead and driver characterization: Application to vertical car dynamics. *IEEE Transactions on Human-Machine Systems*, 48(1):6–16.

Butler, C. A. and Griffin, M. J. (2006). Motion sickness during fore-and-aft oscillation: effect of the visual scene. *Aviation, space, and environmental medicine*, 77(12):1236–1243.

Cano Porras, D., Zeilig, G., Doniger, G. M., Bahat, Y., Inzelberg, R., and Plotnik, M. (2020). Seeing Gravity: Gait Adaptations to Visual and Physical Inclines – A Virtual Reality Study. *Frontiers in Neuroscience*, 13:1308.

Clark, T. K., Newman, M. C., Karmali, F., Oman, C. M., and Merfeld, D. M. (2019). Mathematical models for dynamic, multisensory spatial orientation perception. *Progress in Brain Research*, 248:65–90.

Cleij, D., Venrooij, J., Pretto, P., Pool, D. M., Mulder, M., and Bülthoff, H. H. (2017). Continuous subjective rating of perceived motion incongruence during driving simulation. *IEEE Transactions on Human-Machine Systems*, 48(1):17–29.

Correia Grácio, B. J., de Winkel, K. N., Groen, E. L., Wentink, M., and Bos, J. E. (2013). The time constant of the somatogravic illusion. *Experimental Brain Research*, 224(3):313–321.

De Graaf, B., Bos, J. E., Tielemans, W., Rameckers, F., Rupert, A. H., and Guedry, F. E. (1997). OTOLITH CONTRIBUTION TO OCULAR TORSION AND SPATIAL ORIENTATION DURING ACCELERATION. Technical report, Nava Aerospace Medical Research Laboratory.

De Winkel, K. N., Irmak, T., Kotian, V., Pool, D. M., and Happee, R. (2022). Relating individual motion sickness levels to subjective discomfort ratings. *Experimental Brain Research 2022*, 1:1–10.

de Winkel, K. N., Talsma, T. M. W., and Happee, R. (2022). A meta-analysis of simulator sickness as a function of simulator fidelity. *Experimental Brain Research*, 240(12):1–17.

Desai, R., Cvetković, M., Papaioannou, G., and Happee, R. (2023). Evaluation of Motion Comfort using Advanced Active Human Body Models and Efficient Simplified Models. *IEEE Conference on Intelligent Transportation Systems, Proceedings, ITSC*, pages 5351–5356.

Dichgans, J. and Brandt, T. (2009). Optokinetic Motion Sickness And Pseudo-Coriolis Effects Induced By Moving Visual Stimuli. *http://dx.doi.org/10.3109/00016487309121519*, 76(1-6):339–348.

Diels, C. and Bos, J. E. (2016). Self-driving carsickness. *Applied ergonomics*, 53:374–382.

Diels, C., Ye, Y., Bos, J. E., and Maeda, S. (2022). Motion Sickness in Automated Vehicles: Principal Research Questions and the Need for Common Protocols. *SAE International Journal of Connected and Automated Vehicles*, 5(2):121–134.

Domahidi, A. and Jerez, J. (2014). FORCES Professional. embotech GmbH (http://embotech.com/FORCES-Pro). *t uly (cit. on p. 30)*.

Donohew, B. and Griffin, M. (2004). Motion sickness: Effect of the frequency of lateral oscillation. *Aviation, space, and environmental medicine*, 75:649–656.

Drop, F. M., Pool, D. M., Van Paassen, M. M., Mulder, M., and Bülthoff, H. H. (2018). Objective Model Selection for Identifying the Human Feedforward Response in Manual Control. *IEEE transactions on cybernetics*, 48(1):2–15.

Ehrenstein, W. H. (2003). Basics of seeing motion. *Arquivos Brasileiros de Oftalmologia*, 66(5 SUPPL.):44–52.

Fabozzi, F. J., Focardi, S. M., Rachev, S. T., and Arshanapalli, B. G. (2014). Appendix E: Model Selection Criterion: AIC and BIC. *The Basics of Financial Econometrics*, pages 399–403.

Fang, Z. and Kemeny, A. (2012). Explicit MPC motion cueing algorithm for real-time driving simulator. In *7th International Power Electronics and Motion Control Conference*, volume 2, pages 874–878. IEEE.

Feng, F., Bao, S., Sayer, J. R., Flannagan, C., Manser, M., and Wunderlich, R. (2017). Can vehicle longitudinal jerk be used to identify aggressive drivers? An examination using naturalistic driving data. *Accident Analysis & Prevention*, 104:125–136.

Gianna, C., Heimbrand, S., and Gresty, M. (1996). Thresholds for detection of motion direction during passive lateral whole-body acceleration in normal subjects and patients with bilateral loss of labyrinthine function. *Brain Research Bulletin*, 40(5-6):443–447.

Golding, J. and Markey, H. M. (1996). Effect of frequency of horizontal linear oscillation on motion sickness and somatogravic illusion. *Aviation Space & Environmental Medicine*, 67(2):121–126.

Golding, J. F. (2006a). Motion sickness susceptibility. *Autonomic Neuroscience*, 129(1-2):67–76.

Golding, J. F. (2006b). Predicting individual differences in motion sickness susceptibility by questionnaire. *Personality and Individual Differences*, 41(2):237–248.

Golding, J. F. (2016). Motion sickness. *Handbook of Clinical Neurology*, 137:371–390.

Golding, J. F., Arun, S., Wortley, E., Wotton-Hamrioui, K., Cousins, S., and Gresty, M. A. (2009). Off-vertical axis rotation of the visual field and nauseogenicity. *Aviation, space, and environmental medicine*, 80(6):516–21.

Golding, J. F., Finch, M. I., and Stott, J. R. (1997). Frequency effect of 0.35-1.0 Hz horizontal translational oscillation on motion sickness and the somatogravic illusion. *Aviation, Space, and Environmental Medicine*, 68(5):396–402.

Gottsdanker, R. M. (1956). The ability of human operators to detect accerelation of target motion. *Psychological Bulletin*, 53(6):477–487.

Graybiel, A. (1969). Structural elements in the concept of motion sickness. *Aerospace medicine*, 40 4:351–367.

Griffin, M. and Mills, K. (2002a). Effect of magnitude and direction of horizontal oscillation on motion sickness. *Aviation, space, and environmental medicine*, 73:640–646.

Griffin, M. J. and Mills, K. L. (2002b). Effect of frequency and direction of horizontal oscillation on motion sickness. *Aviation, space, and environmental medicine*, 73(6):537–543.

Griffin, M. J. and Newman, M. M. (2004). Visual field effects on motion sickness in cars. *Aviation, space, and environmental medicine*, 75(9):739–748.

Groen, E. L. and Bles, W. (2004). How to use body tilt for the simulation of linear self motion. *Journal of Vestibular Research*, 14(5):375–385.

Groen, E. L., Clark, T. K., Houben, M. M. J., Bos, J. E., and Mumaw, R. J. (2022). Objective Evaluation of the Somatogravic Illusion from Flight Data of an Airplane Accident. *Safety 2022, Vol. 8, Page 85*, 8(4):85.

Happee, R., Kotian, V., and de Winkel, K. (2023). Neck stabilization through sensory integration of vestibular and visual motion cues. *Frontiers in Neurology*, 14:1266345.

Harmankaya, H., Brietzke, A., Xuan, R. P., Shyrokau, B., Happee, R., and Papaioannou, G. (2024). Efficient Motion Sickness Assessment : Recreation of On-Road Driving on a Compact Test Track. *Submitted*.

Heerspink, H. M., Berkouwer, W. R., Stroosma, O., Van Paassen, M. M., Mulder, M., and Mulder, J. A. (2005). Evaluation of vestibular thresholds for motion detection in the SIMONA Research Simulator. *Collection of Technical Papers - AIAA Modeling and Simulation Technologies Conference 2005*, 2:1212–1231.

Hickman, M. A., Cox, S. R., Mahabir, S., Miskell, C., Lin, J., Bunger, A., and McCall, R. B. (2008). Safety, pharmacokinetics and use of the novel NK-1 receptor antagonist maropitant (Cerenia™) for the prevention of emesis and motion sickness in cats. *Journal of Veterinary Pharmacology and Therapeutics*, 31(3):220–229.

Hogerbrug, M., Venrooij, J., Pool, D. M., and Mulder, M. (2020). Simulator Sickness Ratings Reduce with Simulator Motion when Driven Through Urban Environments. In *Driving Simulation Conference Proceedings*, pages 175–178, Antibes, France. Driving Simulation Association.

Houck, J. A., Telban, R. J., and Cardullo, F. M. (2005). Motion cueing algorithm development: Human-centered linear and nonlinear approaches. Technical report, Langley Research Center.

Howarth, H. V. C. and Griffin, M. J. (2003). Effect of roll oscillation frequency on motion sickness. *Aviation, space, and environmental medicine*, 74(4):326–331.

Huppert, D., Benson, J., and Brandt, T. (2017). A Historical View of Motion Sickness—A Plague at Sea and on Land, Also with Military Impact. *Frontiers in Neurology*, 8(APR):114.

Inoue, S., Dang, V. T., Liu, H., and Wada, T. (2025). Construction of a computational model of individual progression of motion sickness symptoms based on subjective vertical conflict theory. *Experimental Brain Research 2025 243:5*, 243(5):108–.

Inoue, S., Liu, H., and Wada, T. (2023). Revisiting Motion Sickness Models Based on SVC Theory Considering Motion Perception. *SAE Technical Papers*.

Inoue, S., Liu, H., and Wada, T. (2024). A Digital Human Model for Symptom Progression of Vestibular Motion Sickness based on Subjective Vertical Conflict Theory. In *AHFE international*, volume 159.

International Organization For Standardization (1997). ISO 2631-1:1997 - Mechanical vibration and shock - Evaluation of human exposure to whole-body vibration - Part 1: General requirements.

Irmak, T., de Winkel, K. N., and Happee, R. (2025). Visually induced motion sickness correlates with on-road car sickness while performing a visual task. *Experimental Brain Research*, 243(4):1–8.

Irmak, T., De Winkel, K. N., Pool, D. M., Bülthoff, H. H., and Happee, R. (2021). Individual motion perception parameters and motion sickness frequency sensitivity in fore-aft motion. *Experimental Brain Research*.

Irmak, T., Kotian, V., Happee, R., de Winkel, K. N., and Pool, D. M. (2022). Amplitude and Temporal Dynamics of Motion Sickness. *Frontiers in systems neuroscience*, 16.

Irmak, T., Pool, D., de Winkel, K., and Happee, R. (2023). Validating models of sensory conflict and perception for motion sickness prediction. *Biological Cybernetics*.

Irmak, T., Pool, D. M., and Happee, R. (2020). Objective and subjective responses to motion sickness: the group and the individual. *Experimental Brain Research*.

Jain, V., Kumar, S. S., Papaioannou, G., Happee, R., and Shyrokau, B. (2023a). Optimal Trajectory Planning for Mitigated Motion Sickness: Simulator Study Assessment. *IEEE Transactions on Intelligent Transportation Systems*.

Jain, V., Lazcano, A., Happee, R., and Shyrokau, B. (2023b). Motion Cueing Algorithm for Effective Motion Perception: A frequency-splitting MPC Approach. *arXiv preprint*.

Jalgaonkar, N., Sousa Schulman, D., Ojha, S., and Awtar, S. (2021). A Visual-Vestibular Model to Predict Motion Sickness Response in Passengers of Autonomous Vehicles. *SAE International Journal of Advances and Current Practices in Mobility*, 3(5):2421–2432.

Joseph, J. A. and Griffin, M. J. (2008). Motion Sickness: Effect of Changes in Magnitude of Combined Lateral and Roll Oscillation. *Aviation, space, and environmental medicine*, 79(11):1019–1027.

Kamiji, N., Kurata, Y., Wada, T., and Doi, S. (2007). Modeling and validation of carsickness mechanism. In *Proceedings of the SICE Annual Conference*, pages 1138–1143. IEEE, IEEE.

Keshavarz, B. and Hecht, H. (2011). Validating an efficient method to quantify motion sickness. *Human Factors*, 53(4):415–426.

Khalid, H., Turan, O., and Bos, J. E. (2011a). Theory of a subjective vertical-horizontal conflict physiological motion sickness model for contemporary ships. *Journal of Marine Science and Technology*, 16(2):214–225.

Khalid, H., Turan, O., Bos, J. E., and Incecik, A. (2011b). Application of the subjective vertical–horizontal-conflict physiological motion sickness model to the field trials of contemporary vessels. *Ocean Engineering*, 38(1):22–33.

Khusro, Y. R., Zheng, Y., Grottoli, M., and Shyrokau, B. (2020). MPC-based motion-cueing algorithm for a 6-DOF driving simulator with actuator constraints. *Vehicles*, 2(4):625–647.

Kolff, M., Himmels, C., Venrooij, J., Parduzi, A., Pool, D. M., Riener, A., and Mulder, M. (2025). Effect of motion mismatches on ratings of motion incongruence and simulator sickness in urban driving simulations. *Transportation Research Part F: Traffic Psychology and Behaviour*, 115:103370.

Kolff, M., Schwienbacher, M., Venrooij, J., Pool, D. M., and Mulder, M. (2022). Motion Cueing Quality Comparison of Driving Simulators using Oracle Motion Cueing. In *Driving Simulation Conference Proceedings*, Strasbourg.

Kotian, V., Irmak, T., Pool, D., and Happee, R. (2024). The role of vision in sensory integration models for predicting motion perception and sickness. *Experimental Brain Research*, 242(3):685–725.

Kotian, V., Pool, D. M., and Happee, R. (2023). Modelling individual motion sickness accumulation in vehicles and driving simulators. In *Proceedings of the Driving Simulation Conference*, Antibes, France.

Kotian, V., Pool, D. M., and Happee, R. (2025). Personalising Motion Sickness Models: Estimation and Statistical Modeling of Individual-Specific Parameters. *Frontiers in Systems Neuroscience*, 19:1531795.

Krapp, H. G. and Hengstenberg, R. (1996). Estimation of self-motion by optic flow processing in single visual interneurons. *Nature 1996 384:6608*, 384(6608):463–466.

Kufver, B. and Förstberg, J. (1999). *A net dose model for development of nausea*, volume 330. Statens vag-och transportforskningsinstitut., VTI sartryck 330.

Kuiper, O. X., Bos, J. E., and Diels, C. (2018). Looking forward: In-vehicle auxiliary display positioning affects carsickness. *Applied ergonomics*, 68:169–175.

Kuiper, O. X., Bos, J. E., Schmidt, E. A., Diels, C., and Wolter, S. (2020). Knowing What's Coming: Unpredictable Motion Causes More Motion Sickness. *Human Factors*, 62(8):1339–1348.

Lambert, E., Romano, R., and Watling, D. (2019). Optimal path planning with clothoid curves for passenger comfort. In *Int. Conf. on Vehicle Technology and Intelligent Transport Systems*, pages 609–615.

Lamprecht, A., Steffen, D., Nagel, K., Haecker, J., and Graichen, K. (2022). Online Model Predictive Motion Cueing With Real-Time Driver Prediction. *Trans. on Intelligent Transportation Systems*, 23(8):12414–12428.

Laurens, J., Meng, H., and Angelaki, D. E. (2013). Computation of linear acceleration through an internal model in the macaque cerebellum. *Nature Neuroscience*, 16(11):1701–1708.

Lawther, A. and Griffin, M. J. (1988). Motion sickness and motion characteristics of vessels at sea. *Ergonomics*, 31(10):1373–1394.

Lewkowicz, R. (2019). A centrifuge-based flight simulator: Optimization of a baseline acceleration profile based on the motion sickness incidence. *Acta Astronautica*, 164:23–33.

Li, D. and Chen, L. (2022). Mitigating motion sickness in automated vehicles with vibration cue system. *Ergonomics*, 65(10):1313–1325.

Li, D. and Hu, J. (2021). Mitigating motion sickness in automated vehicles with frequency-shaping approach to motion planning. *Robotics and Automation Letters*, 6(4):7714–7720.

Lim, K., Karmali, F., Nicoucar, K., Merfeld, D. M., Karmali, L. K., Merfeld, N. K., and Lim, K. (2017). Perceptual precision of passive body tilt is consistent with statistically optimal cue integration. *Journal of neurophysiology*, 117(5):2037–2052.

Liu, H., Inoue, S., and Wada, T. (2022). Motion Sickness Modeling with Visual Vertical Estimation and Its Application to Autonomous Personal Mobility Vehicles. In *2022 IEEE Intelligent Vehicles Symposium (IV)*, pages 1415–1422. IEEE.

Liu, H., Inoue, S., and Wada, T. (2024). Subjective Vertical Conflict Model With Visual Vertical: Predicting Motion Sickness on Autonomous Personal Mobility Vehicles. *IEEE Transactions on Intelligent Transportation Systems*, 25(8):9878–9894.

Mayne, R. (1974). *A Systems Concept of the Vestibular Organs*. Springer, Berlin, Heidelberg.

McCauley, M., Royal, J., Wylie, C., O'Hanlon, J., and Mackie, R. (1976). Motion Sickness Incidence: Exploratory Studies of Habituation, Pitch and Roll, and the Refinement of a Mathematical Model. Technical report, Canyon Research Group Inc Goleta Ca Human Factors Research Div.

Merfeld, D. M., Young, L. R., Oman, C. M., and Shelhamer, M. J. (1993). A Multidimensional Model of the Effect of Gravity on the Spatial Orientation of the Monkey. *Journal of Vestibular Research*, 3(2):141–161.

Merfeld, D. M., Zupan, L., and Peterka, R. J. (1999). Humans use internal models to estimate gravity and linear acceleration. *Nature*, 398(6728):615–618.

Merfeld, D. M., Zupan, L. H., and Gifford, C. A. (2001). Neural Processing of Gravito-Inertial Cues in Humans. II. Influence of the Semicircular Canals During Eccentric Rotation. *Journal of Neurophysiology*, 85(4):1648–1660.

Metzulat, M., Metz, B., Landau, A., Neukum, A., and Kunde, W. (2024). Does the visual input matter? Influence of non-driving related tasks on car sickness in an open road setting. *Transportation Research Part F: Traffic Psychology and Behaviour*, 104:234–248.

Miller, E. F. and Graybiel, A. (1969). *A STANDARDIZED LABORATORY MEANS OF DETERMINING SUSCEPTIBILITY TO CORIOLIS (MOTION) SICKNESS*. Naval Aerospace Medical Institute, Naval Aerospace Medical Center, 1058 edition.

Munir, S., Hovd, M., Fang, Z., Olaru, S., and Kemeny, A. (2017). Complexity reduction in motion cueing algorithm for the ULTIMATE driving simulator. *IFAC-PapersOnLine*, 50(1):10729–10734.

Newman, M. C. (2009). *A Multisensory Observer Model for Human Spatial Orientation Perception*. PhD thesis, Massachusetts Institute of Technology.

Nooij, S. A. E., Pretto, P., Oberfeld, D., Hecht, H., Bülthoff, H. H., and Bü Lthoff, H. H. (2017). Vection is the main contributor to motion sickness induced by visual yaw rotation: Implications for conflict and eye movement theories. *PLOS ONE*, 12(4):e0175305.

O'Hanlon, J. F. and McCauley, M. E. (1974). Motion sickness incidence as a function of the frequency and acceleration of vertical sinusoidal motion. *Aerospace medicine*, 45(4):366–369.

Oman, C. M. (1982). A Heuristic Mathematical Model for the Dynamics of Sensory Conflict and Motion Sickness Hearing in Classical Musicians. *Acta Oto-Laryngologica*, 94(sup392):4–44.

Oman, C. M. (1990). Motion sickness: a synthesis and evaluation of the sensory conflict theory. *Canadian Journal of Physiology and Pharmacology*, 68(2):294–303.

Oman, C. M. and Cullen, K. E. (2014). Brainstem processing of vestibular sensory exafference: Implications for motion sickness etiology. *Experimental Brain Research*, 232(8):2483–2492.

Parrish, R. V., Dieudonne, J. E., Bowles, R. L., and Martin, D. J. (1975). Coordinated Adaptive Washout for Motion Simulators. *Journal of Aircraft*, 12(1):44–50.

Qazani, M. R. C., Asadi, H., Khoo, S., and Nahavandi, S. (2019). A linear time-varying model predictive control-based motion cueing algorithm for hexapod simulation-based motion platform. *IEEE Transactions on Systems, Man, and Cybernetics: Systems*, 51(10):6096–6110.

Qian, J., Nadri, M., and Dufour, P. (2017). Optimal input design for parameter estimation of nonlinear systems: case study of an unstable delta wing. *International Journal of Control*, 90(4):873–887.

Reason, J. (1978a). Motion sickness: Some theoretical and practical considerations. *Applied Ergonomics*, 9(3):163–167.

Reason, J. T. (1978b). Motion sickness adaptation: a neural mismatch model. *Journal of the Royal Society of Medicine*, 71(11):819–829.

Reid, L. and Nahon, M. (1985). Flight simulation motion-base drive algorithms: part 1. Developing and testing equations. Technical Report 296, University of Toronto Institute for Aerospace Studies.

Rengifo, C., Chardonnet, J. R., Mohellebi, H., and Kemeny, A. (2021). Impact of human-centered vestibular system model for motion control in a driving simulator. *IEEE Transactions on Human-Machine Systems*, 51(5):411–420.

Reuten, A. J., Nooij, S. A., Bos, J. E., and Smeets, J. B. (2021). How feelings of unpleasantness develop during the progression of motion sickness symptoms. *Experimental Brain Research*, 239(12):3615–3624.

Reuten, A. J. C., Bos, J., and Smeets, J. B. J. (2020). The metrics for measuring motion sickness. In *Driving Simulation Conference Proceedings*, pages 183–186, Antibes, France. Driving Simulation Association.

Riccio, G. E. and Stoffregen, T. A. (1991). An ecological Theory of Motion Sickness and Postural Instability. *Ecological Psychology*, 3(3):195–240.

Rojas, C. R., Welsh, J. S., Goodwin, G. C., and Feuer, A. (2007). Robust optimal experiment design for system identification. *Automatica*, 43(6):993–1008.

Romano, R. A., Park, G. D., Paul, V., and Allen, R. W. (2016). Motion cueing evaluation of off-road heavy vehicle handling. Technical report, SAE Technical Paper.

Salter, S., Diels, C., Herriotts, P., Kanarachos, S., and Thake, D. (2019). Motion sickness in automated vehicles with forward and rearward facing seating orientations. *Applied ergonomics*, 78:54–61.

Schwarz, G. (1978). Estimating the Dimension of a Model. *https://doi.org/10.1214/aos/1176344136*, 6(2):461–464.

Seidman, S., Telford, L., and Paige, G. (1998). Tilt perception during dynamic linear acceleration. *Exp Brain Res*, 119:307–314.

Sousa Schulman, D., Jalgaonkar, N., Ojha, S., Rivero Valles, A., Jones, M. L., and Awtar, S. (2023). A Visual-Vestibular Model to Predict Motion Sickness for Linear and Angular Motion. *Human Factors*.

Stevens, S. S. (1946). On the theory of scales of measurement. *Science*, 103(2684):677–680.

Stroosma, O., van Paassen, M. M. R., and Mulder, M. (2003). Using the SIMONA Research Simulator for Human-machine Interaction Research. In *AIAA Modeling and Simulation Technologies Conference and Exhibit*, Guidance, Navigation, and Control and Co-located Conferences. American Institute of Aeronautics and Astronautics.

Talsma, T. M., Hassanain, O., Happee, R., and de Winkel, K. N. (2023). Validation of a moving base driving simulator for motion sickness research. *Applied Ergonomics*, 106:103897.

Telban, R. J. and Cardullo, F. M. (2001). An integrated model of human motion perception with visual-vestibular interaction. *AIAA Modeling and Simulation Technologies Conference and Exhibit*.

Thorpe, S., Fize, D., and Marlot, C. (1996). Speed of processing in the human visual system. *Nature*, 381(6582):520–522.

Tokumaru, O., Kaida, K., Ashida, H., Mizumoto, C., and Tatsuno, J. (1998). Visual influence on the magnitude of somatogravic illusion evoked on advanced spatial disorientation demonstrator. *Aviation, Space, and Environmental Medicine*, 69(2):111–116.

Valko, Y., Lewis, R. F., Priesol, A. J., and Merfeld, D. M. (2012). Vestibular labyrinth contributions to human whole-body motion discrimination. *The Journal of neuroscience : the official journal of the Society for Neuroscience*, 32(39):13537–13542.

van der Steen, F. (1998). *Self-motion perception*. PhD thesis, TU Delft.

Veltena, M. C. (2015). Movement Simulator. *U.S. Patent No. 8996179B2*.

Vingerhoets, R. A., Medendorp, W. P., and Van Gisbergen, J. A. (2006). Time course and magnitude of illusory translation perception during off-vertical axis rotation. *Journal of Neurophysiology*, 95(3):1571–1587.

Wada, T. (2021). Computational Model of Motion Sickness Describing the Effects of Learning Exogenous Motion Dynamics. *Frontiers in Systems Neuroscience*, 15:6.

Wada, T. and Bos, J. E. (2025). Theoretical considerations on models of vestibular self-motion perception as inherent in computational frameworks of motion sickness. *Biological Cybernetics 2025 119:4*, 119(4):1–19.

Wada, T., Kamij, N., and Doi, S. (2015). A Mathematical Model of Motion Sickness in 6DOF Motion and Its Application to Vehicle Passengers. *arXiv preprint*.

Wada, T., Kawano, J., Okafuji, Y., Takamatsu, A., and Makita, M. (2020). A Computational Model of Motion Sickness Considering Visual and Vestibular Information. In *2020 IEEE International Conference on Systems, Man, and Cybernetics (SMC)*, pages 1758–1763. IEEE, IEEE.

Wada, T. and Yoshida, K. (2016). Effect of passengers' active head tilt and opening/closure of eyes on motion sickness in lateral acceleration environment of cars. *Ergonomics*, 59(8):1050–1059.

Waespe, W. and Henn, V. (1977). Neuronal activity in the vestibular nuclei of the alert monkey during vestibular and optokinetic stimulation. *Experimental Brain Research 1977 27:5*, 27(5):523–538.

Wang, S. C. and Chinn, H. I. (1956). Experimental motion sickness in dogs; importance of labyrinth and vestibular cerebellum. *The American journal of physiology*, 185(3):617–623.

Wassersug, R. J., Izumi-kurotani, A., Yamashita, M., and Naitoh, T. (1993). Motion sickness in amphibians. *Behavioral and Neural Biology*, 60(1):42–51.

Werkhoven, P., Snippe, H. P., and Alexander, T. (1992). Visual processing of optic acceleration. *Vision Research*, 32(12):2313–2329.

Wijlens, R., van Paassen, M. M., Mulder, M., Takamatsu, A., Makita, M., and Wada, T. (2022). Reducing Motion Sickness by Manipulating an Autonomous Vehicle's Accelerations. *IFAC-PapersOnLine*, 55(29):132–137.

Wood, S. J. (2002). Human otolith–ocular reflexes during off-vertical axis rotation: effect of frequency on tilt–translation ambiguity and motion sickness. *Neuroscience Letters*, 323(1):41–44.

Wood, S. J., Reschke, M. F., Sarmiento, L. A., and Clément, G. (2007). Tilt and translation motion perception during off-vertical axis rotation. *Experimental Brain Research*, 182(3):365–377.

Yunus, I., Jerrelind, J., and Drugge, L. (2022). Evaluation of Motion Sickness Prediction Models for Autonomous Driving. In Orlova, A. and Cole, D., editors, *Lecture Notes in Mechanical Engineering*, pages 875–887, Cham. Springer International Publishing.

Zheng, Y., Shyrokau, B., and Keviczky, T. (2022). 3DOP: Comfort-oriented Motion Planning for Automated Vehicles with Active Suspensions. *IEEE Intelligent Vehicles Symposium, Proceedings*, 2022-June:390–395.

Zupan, L. H., Merfeld, D. M., and Darlot, C. (2002). Using sensory weighting to model the influence of canal, otolith and visual cues on spatial orientation and eye movements. *Biological Cybernetics*, 86(3):209–230.

A

Appendix for Chapter 2

A.1 Supplementary Figures

A.1.1 Individual Normalised MISC Rate

Figure A.1 shows the normalised MISC rate in the first motion exposure as a scatter plot with respect to the amplitude condition for all individuals that took part in the study. The MISC rate is normalised against the maximum MISC rate observed for a participant across all of their conditions. This gives a better representation of the amplitude sensitivity of the participants.

A.1.2 Model Fits to All Individual Responses

Figure S2 shows the fits of the three model variations for all participants and all conditions.

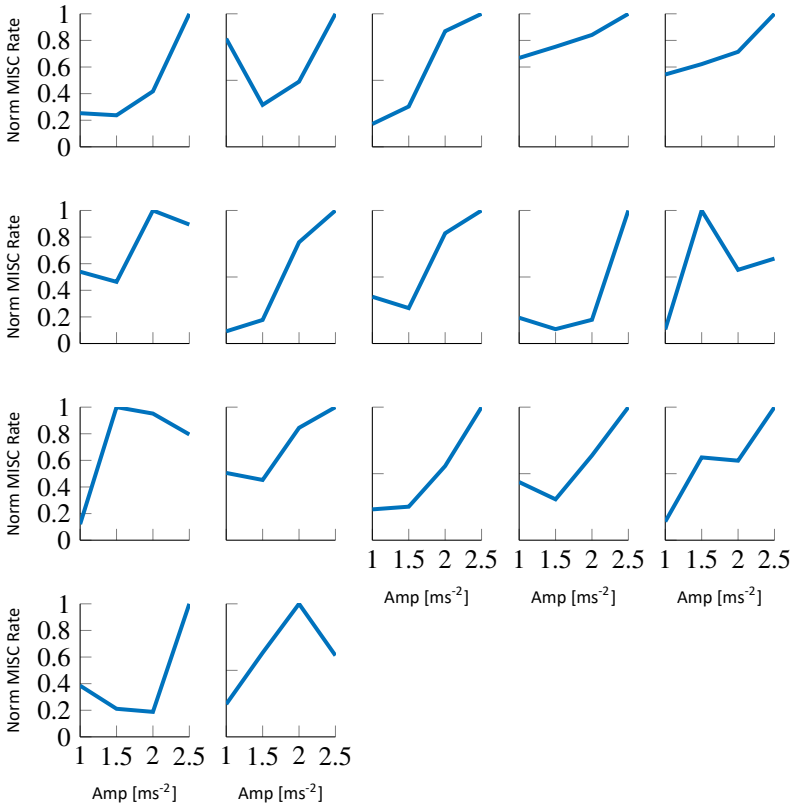

Figure A.1: Normalised MISC rate obtained from dividing the MISC at the end of the first motion exposure with the time to the end of the first motion exposure, shown for all individuals

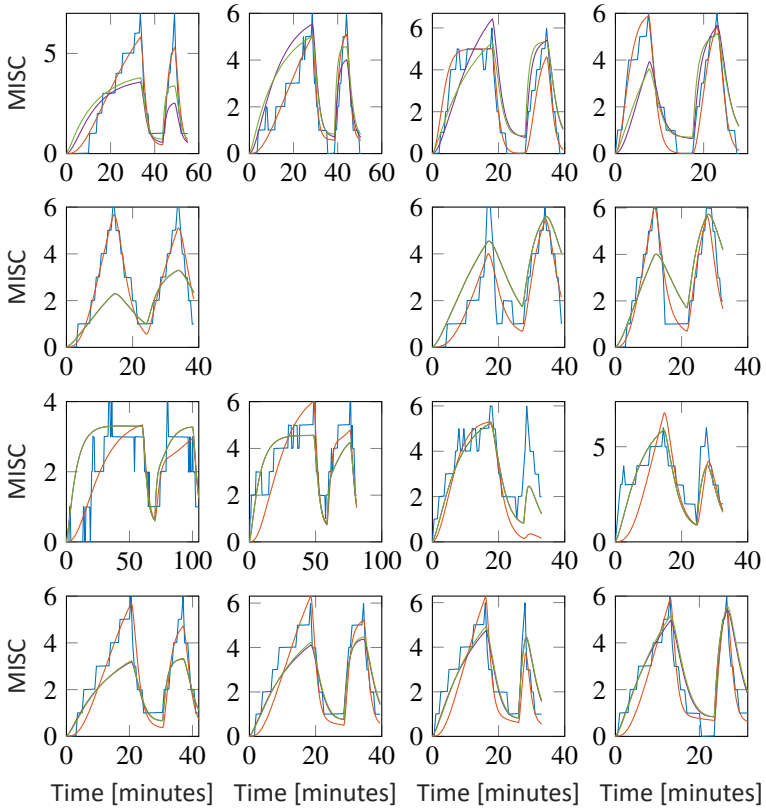
MISC
MISC
MISC
MISC
Time [minutes]
Time [minutes]
Time [minutes]
Time [minutes]
Observation
Session Fit
Individual-level Power
Group-level Power

(a)

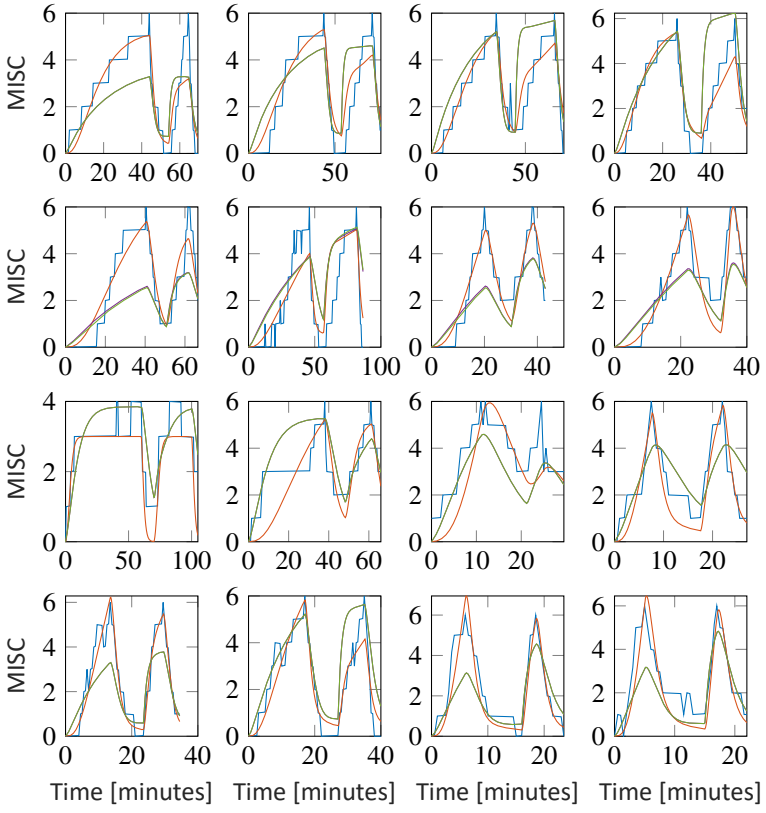
MISC
MISC
MISC
MISC
Time [minutes]
Time [minutes]
Time [minutes]
Time [minutes]

(b)

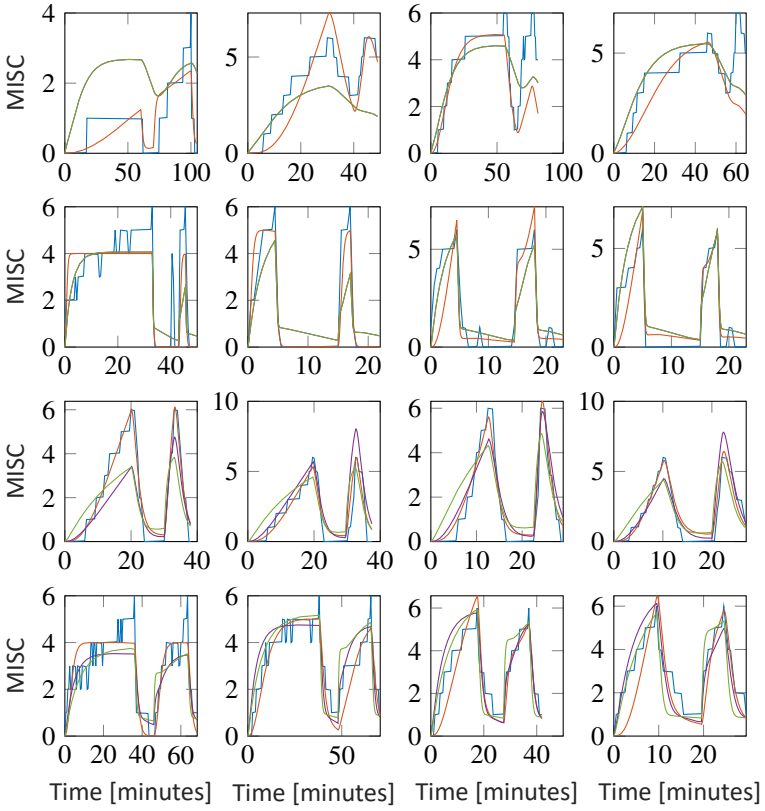
MISC
MISC
MISC
MISC
Time [minutes]
Time [minutes]
Time [minutes]
Time [minutes]

(c)

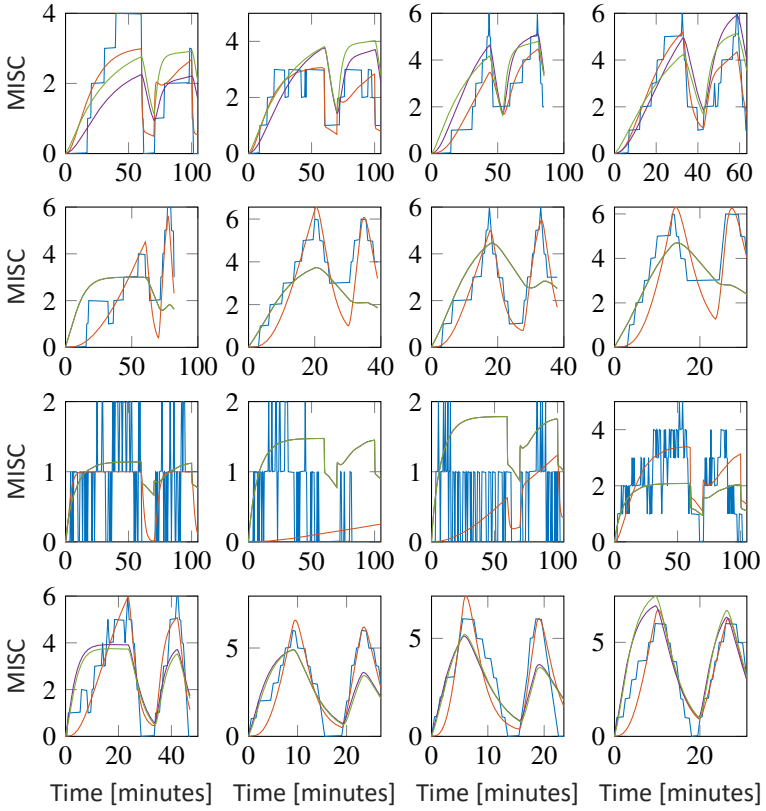

Figure S2: Three variations of the Oman model fitted to all sessions of all individuals. Each row is an individual participant, and each column is a motion condition, with increasing amplitude going from left to right

A.2 Sickness Forecasting

Figure S3 shows extrapolations from MISC 3 to the end of the first motion phase, for the Oman model (in orange) and real observation (in blue) for all participants.

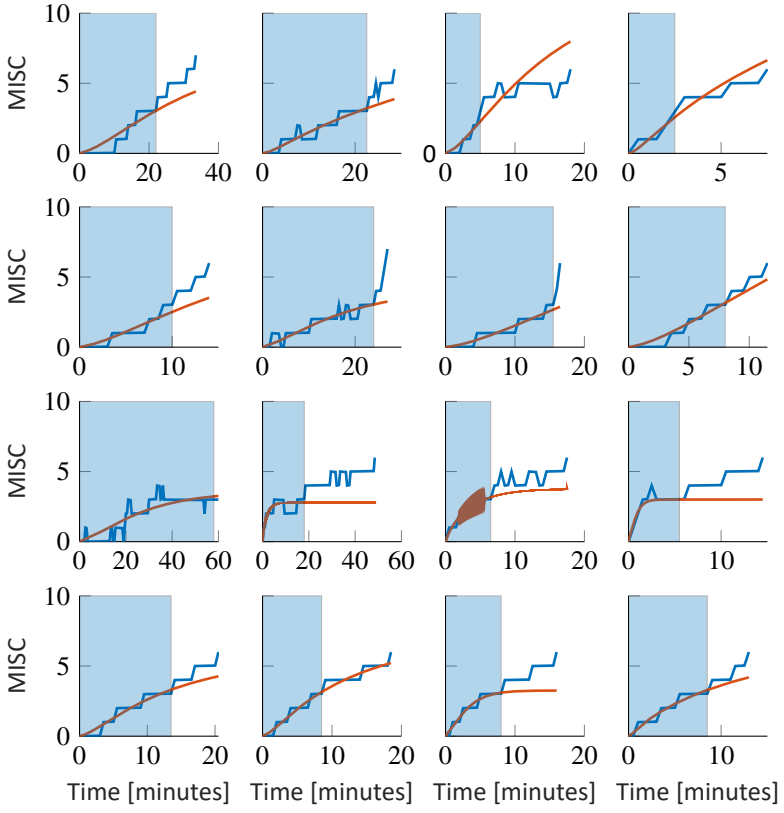

(a)

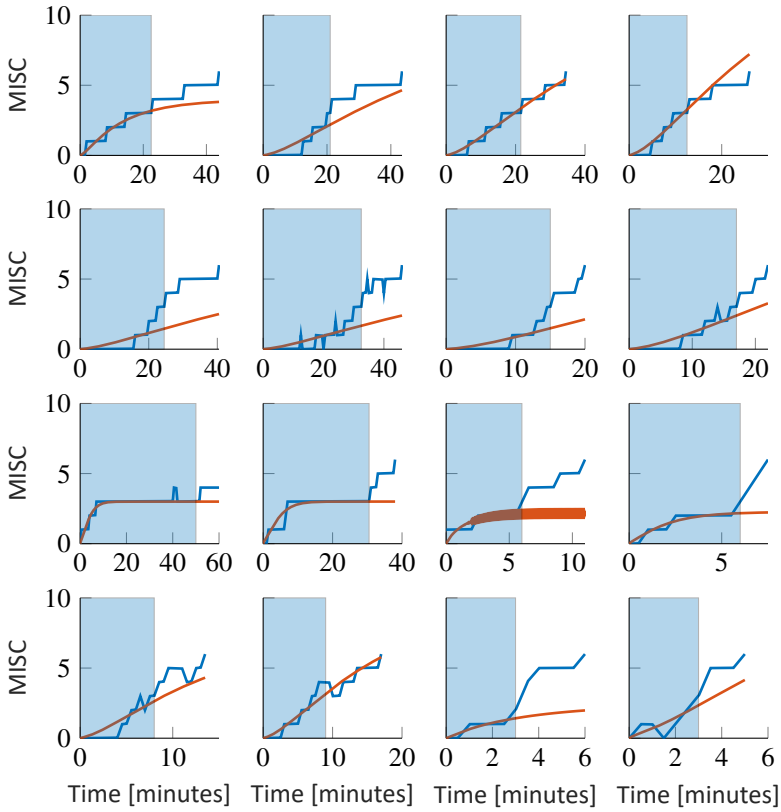
MISC
MISC
MISC
MISC
Time [minutes]
Time [minutes]
Time [minutes]
Time [minutes]

(b)

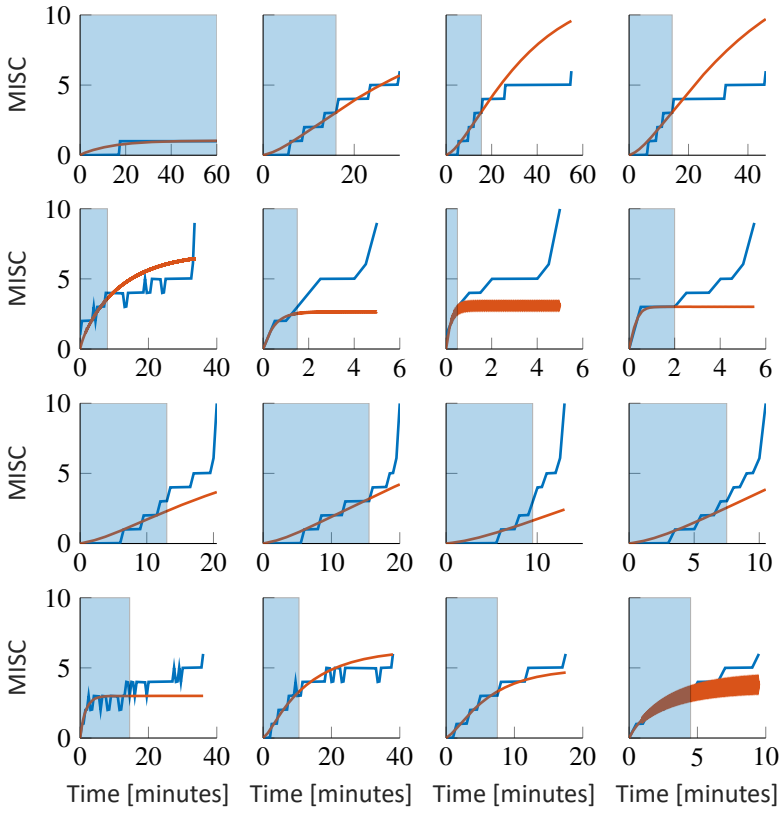
MISC
MISC
MISC
MISC
Time [minutes]
Time [minutes]
Time [minutes]
Time [minutes]

(c)

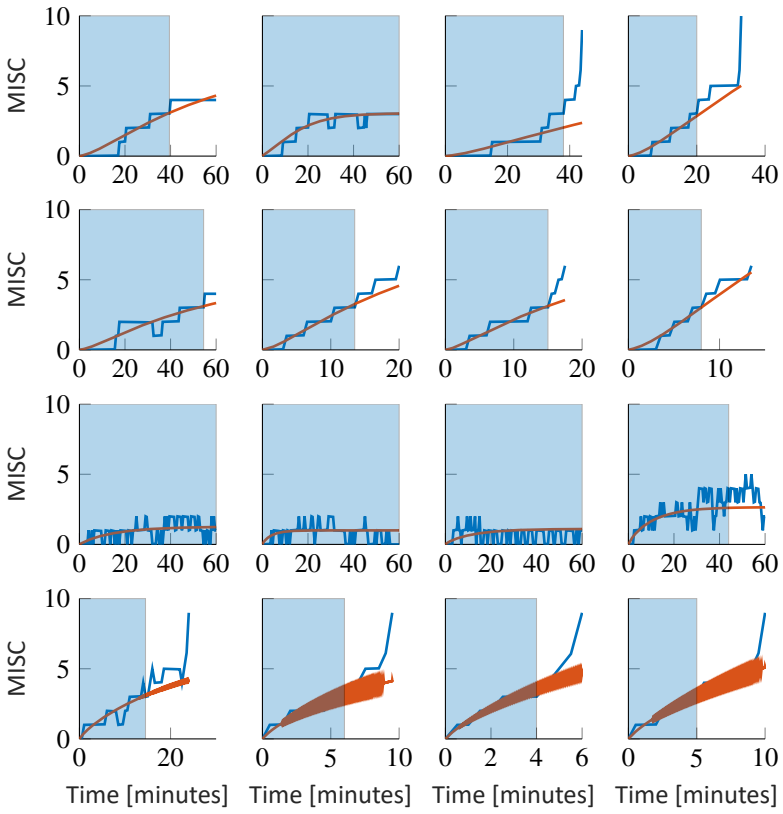

Figure S3: Extrapolations from MISC 3 to the end of the first motion phase, for the Oman model (in orange) and real observation (in blue) for all participants. The columns show responses for each amplitude condition, increasing in magnitude from left to right. The rows show results for each participant. The blue shaded area gives the observations the model has access to make forecasts

B

Appendix for Chapter 3

B.1 Vision Parameter sensitivity

Figures B.1 to B.3 show the vision loop gain parameter sensitivity for all three models, i.e., SVC_I, SVC_{NI}, and MSOM. The feedback gains for both the vision loops (*visual rotational velocity* and *visual vertical*) are varied from 0 to 20 and the frequency and amplitude sensitivity responses for sinusoidal pitch oscillations with 'external vision'.

In the SVC_I model, it is observed in figure B.1 that a higher gain for the *visual vertical* shifts the peak conflict frequency to a higher frequency. As K_{gvis} approaches 20, the peak conflict frequency approaches 0.5 Hz. On the other hand, a higher gain for *visual rotational velocity* (K_{wvis}) only reduces the conflict levels by providing correct estimates of pitching oscillations, which is the simulated input.

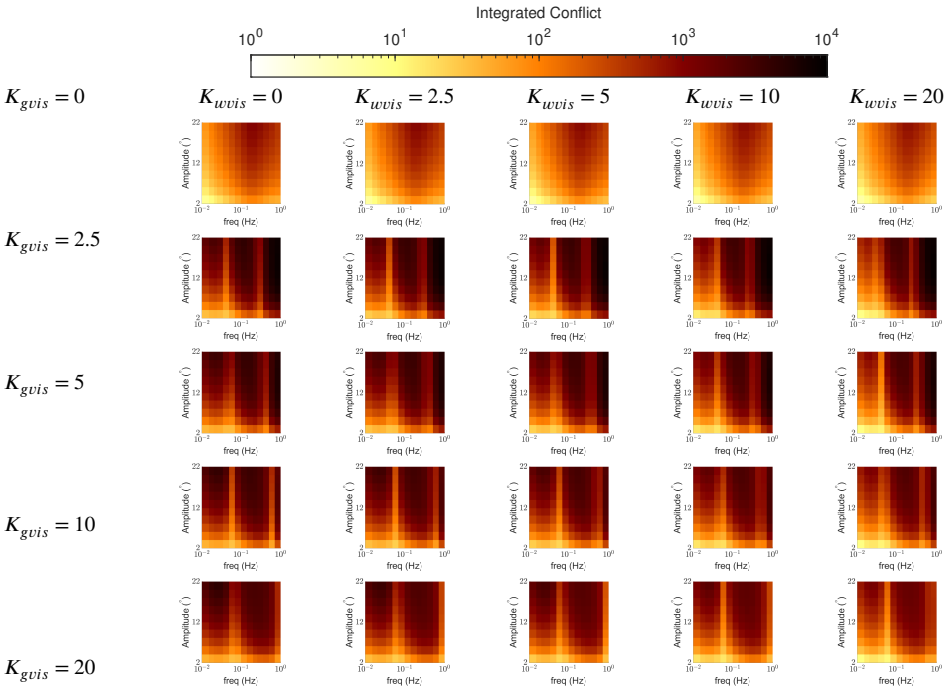

Figure B.1: Frequency sensitivity of integrated conflict with sinusoidal pitch oscillations for varying values of K_{wvis} and K_{gvis}, for the SVC_I model

Figure B.2 shows the effect of K_{wvis} and K_{gvis} on the SVC$_{NI}$ model. The effects are similar to effects in the SVC$_I$ model where, higher gains for the *visual vertical* move the peak conflict frequency to higher frequencies (around 0.5 Hz), while higher gains on the *visual rotational velocity* conflict reduce the conflict levels.

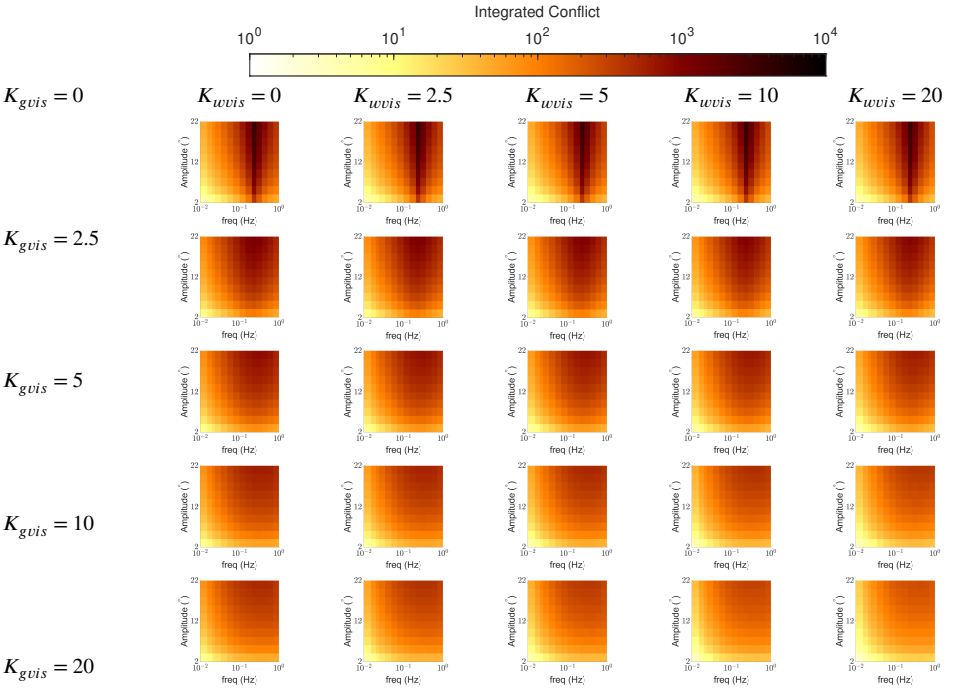

Figure B.2: Frequency sensitivity of integrated conflict with sinusoidal pitch oscillations for varying values of K_{wvis} and K_{gvis}, for the SVC$_{NI}$ model

In the MSOM, the use of *visual rotational velocity* reduces the magnitude of conflict, see figure B.3. The higher the gain on the *visual rotational velocity* (K_{wv}), the higher the reduction of conflict. The *visual vertical* feedback gain setting also has a similar effect on conflict. The higher the gain on the *visual vertical* (K_{wv}), the higher the reduction of conflict. Also, as seen in section 3.3.3, the *visual vertical* does help in motion perception tests.

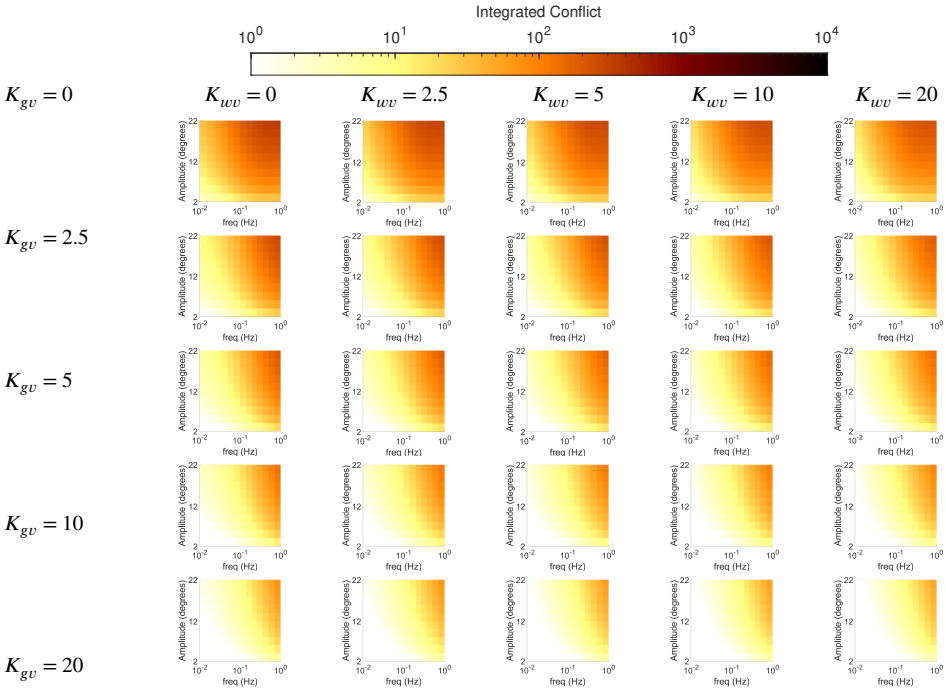

Figure B.3: Frequency sensitivity of integrated conflict with sinusoidal pitch oscillations for varying values of K_{wv} and K_{gv}, for the MSOM model

B.2 Pure Yaw simulations

As discussed in section 3.3.1, pure yaw rotations lead to no verticality conflict generation in any of the three models. This is due to the pure yaw motion not having any effect on the verticality vector. There are other conflict terms in the models that do get affected by pure yaw motion, however, these terms are not used for sickness predictions in our study. This absence of motion sickness holds true even with the presence of vision. Figure B.4 shows that different amplitudes of sinusoidal yaw at different frequencies show no motion sickness (zero conflict generation) and are thereby not visible in plots.

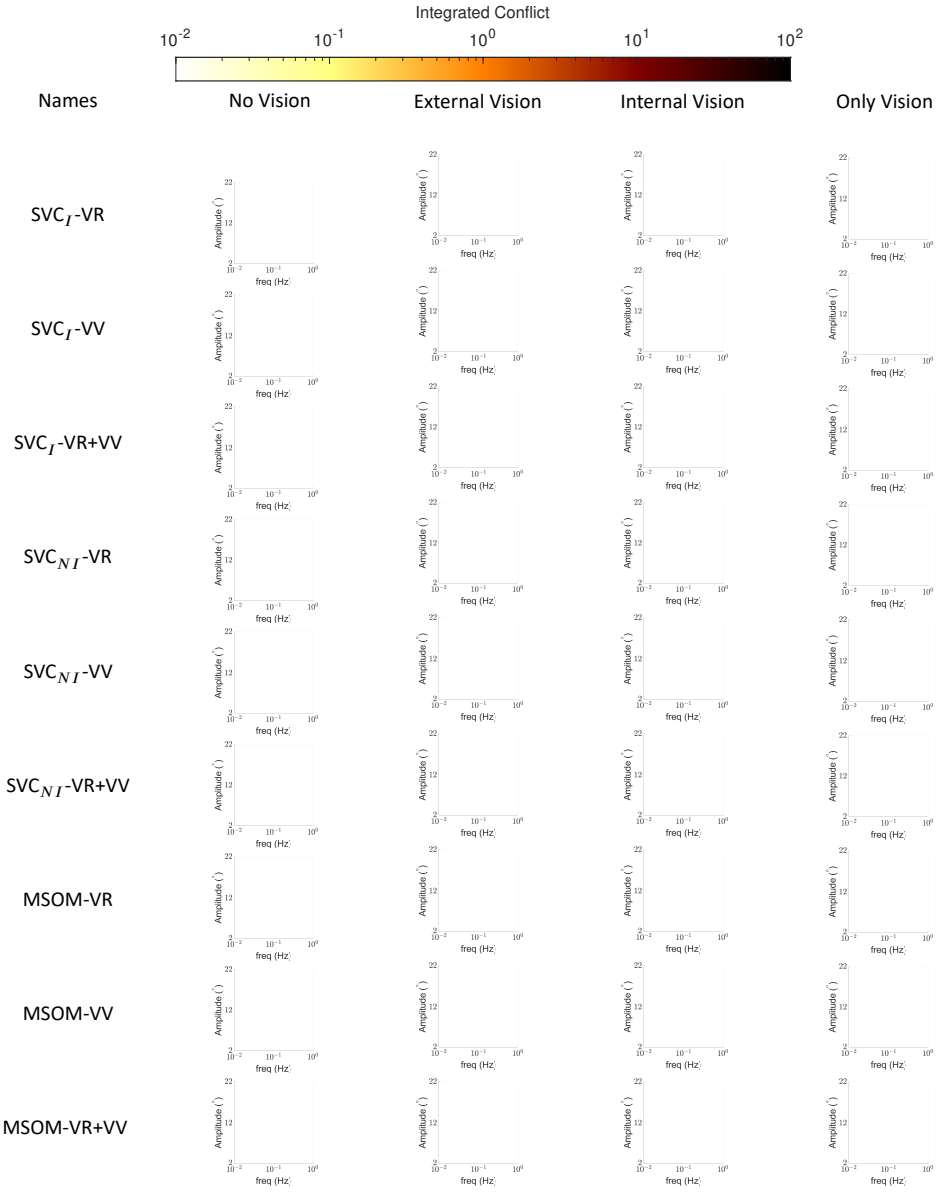

Figure B.4: Frequency sensitivity of integrated conflict with sinusoidal yaw oscillations for different vision conditions: 'no vision' (eyes closed), 'external vision' (eyes open and with outside view), 'internal vision' (eyes open and without outside view), 'only vision' (no motion) for the SVC$_I$, SVC$_{NI}$ and MSOM model

B.3 Slalom Drive

Here, the aim was to analyze the effect of the applied motion DOF on the magnitude of conflict which then in turn tells us about the sensitivity of motion sickness to each of these degrees of freedom. This will demonstrate the effect of the visual pathways for different motion degrees of freedom. The inputs, being real-world slalom drive data, are not identical for all degrees of freedom, it has high levels of lateral accelerations and yaw velocities. Hence it is expected that different degrees of freedom will result in different conflicts. Thus, on the removal of lateral accelerations or yaw velocities, it is expected that the conflict will greatly change. To make these comparisons, in the following sections, each degree of freedom will be turned off and compared with cases of all degrees of freedom turned off and on.

B.3.1 Effects of individual axis rotations

In this analysis, the rotational degrees of freedom are set to zero one by one. The translational degrees of freedom are left active. This is shown in figure B.5, where for each rotational degree of freedom all visual and vestibular signals are set to zero to quantify their contribution to the models' predictions. For reference, these effects are also compared with cases where all the rotation DOFs are removed and where all are active. The input data has strong yaw motion throughout the slalom drive. Pitch and roll are also present throughout the drive however, their magnitudes are much lower than the yaw. As yaw is the dominant rotation, it is expected that the removal of yaw will significantly influence conflict. The roll provides compensation of sensed vertical in the lateral direction and hence its removal will decrease conflict due to decreased error in the estimation of vertical in the Y-direction. The longitudinal accelerations are of a lower magnitude to induce any pitch and hence, removal of pitch is expected to have small effect on conflict.

For the SVC_I model, it is observed that the removal of the yaw indeed has the strongest effect (of increasing conflict) in all versions. Roll has a very low effect, however, it increases conflict. This increase in conflict in the absence of yaw and roll is due to an inaccurate estimate of vertical in the absence of yaw and roll.

For SVC_{NI} models, it is also observed that the removal of the yaw and roll has the effect of increasing conflict in all versions.

In both, SVC_I and SVC_{NI} models, the removal of pitch resulted in a reduction of conflict equivalent to that observed at no rotations. This is a consequence of the motion transforming into a basic 2D rotation in yaw due to the removal of pitch, as the roll is minimal. Consequently, the changes in verticality are reduced resulting in a better estimation of vertical, thus reducing conflict.

For the MSOM, it is also observed that the removal of any of the rotations has negligible effect in all versions. However, the magnitude of conflict is still less than in the SVC models, see figure B.5. This is because the conflict selected is the otolith conflict, which was proposed to correlate best with sickness (Irmak et al., 2023).

For all six models, yaw motion strongly affected conflict in complex 3D motion, highlighting the importance of using recorded or simulated head yaw in motion sickness predictions. this result is only found in the slalom drive whereas pure yaw did not elicit any conflict as described in appendix B.2.

From the results of all six models, it is evident that the MSOM is not suitable as a conflict generation model when strong rotations are present. The SVC_I models are able to perform as expected with the most dominant rotations in the slalom drive data having the most effect on conflict. Thus, SVC_I models are a better choice for simulations of human body rotations.

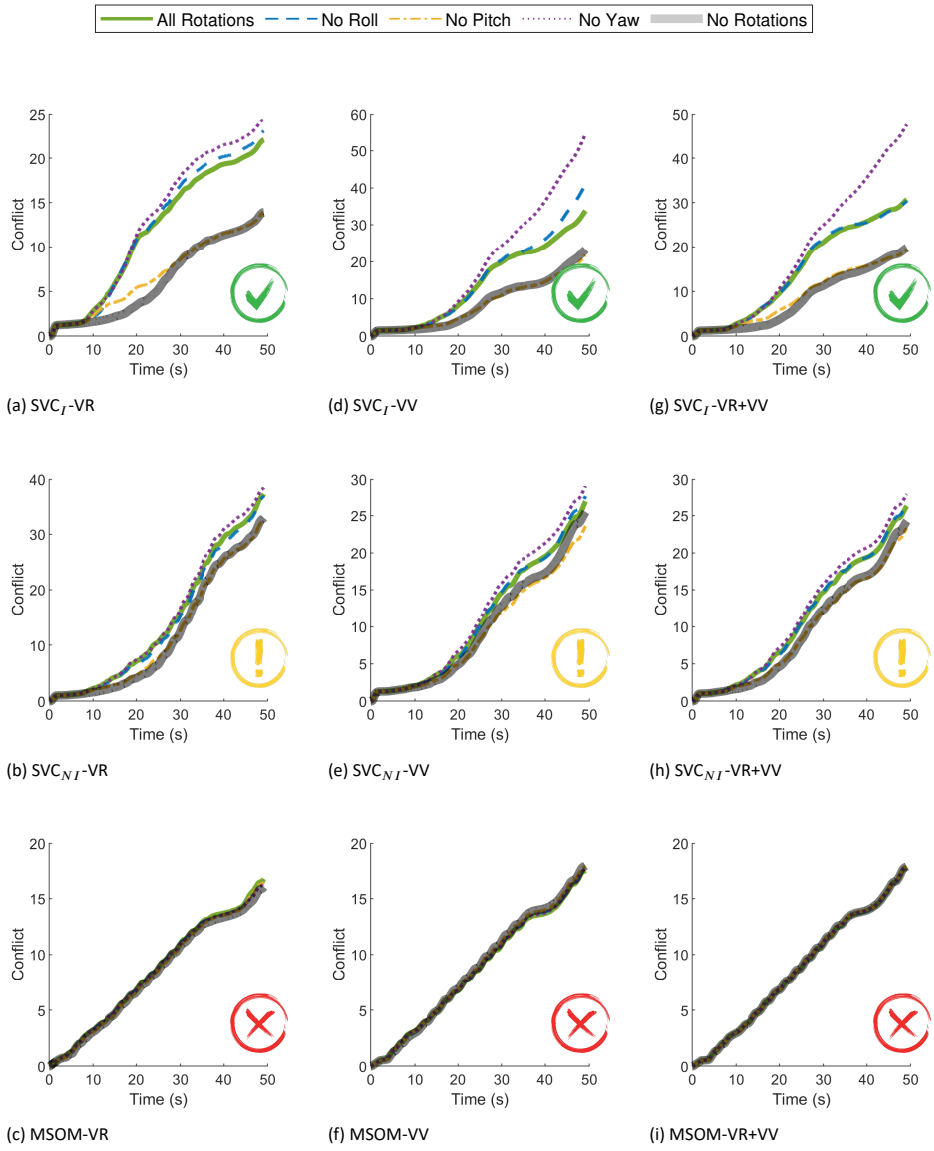

Figure B.5: Effect of rotational DOF on the conflict in the slalom drive

B.3.2 Effects of individual linear accelerations

In the previous section, the effects of each rotation on the models' sickness predictions for the slalom drive data were studied. Similarly, in this section, the effect of different linear DOFs will be studied while including all rotations. As in the previous section, each DOF is excluded and the data from the experiment is simulated. The results for the predicted conflict accumulation are shown in figure B.6.

The input data has large lateral accelerations (around 4 m/s^2) and that too for a larger duration than other linear accelerations. Longitudinal accelerations are mostly present at the start and end of the drive. Finally, the vertical accelerations are of very low magnitude (less than 1 m/s^2). Thus, it is expected that the removal of longitudinal or vertical accelerations will not result in appreciable changes in conflict. Only the absence of lateral accelerations will produce a decrease in conflict.

In the SVC$_I$ model, it is observed that the removal of lateral accelerations reduces conflict. Removal of longitudinal or vertical accelerations has very little effect on conflict accumulation due to their small magnitudes. These results imply that the linear degrees of freedom do have a large effect in models on SVC$_I$ model.

For the SVC$_{NI}$ model, the results are consistent across the three different versions: the removal of lateral accelerations has the most effect (of reducing conflict), followed by the removal of longitudinal accelerations. The omission of vertical accelerations only has no effect on the conflict. These results are as expected.

In the MSOM, it is observed that the variations in conflict accumulation due to switching off the accelerations are greater than due to switching off the rotations. When no linear accelerations and only rotations are applied, MSOM reports very low conflicts. This indicates that the conflict in MSOM is heavily dependent on linear accelerations and not on rotations. When the lateral accelerations are removed, there is a strong reduction in conflict. However, when the vertical acceleration input is disabled, no change in conflict compared to the 'all accelerations' case is observed. Longitudinal accelerations have an intermediate effect.

From these results, it is evident that the otolith conflict term in the MSOM very strongly depends on linear degrees of freedom, while conflict from SVC$_I$ and SVC$_{NI}$ models have a very low dependency on the linear degrees of freedom. Of all the models, only the SVC$_I$-VR and all of the SVC$_{NI}$ models are able to match the desired results.

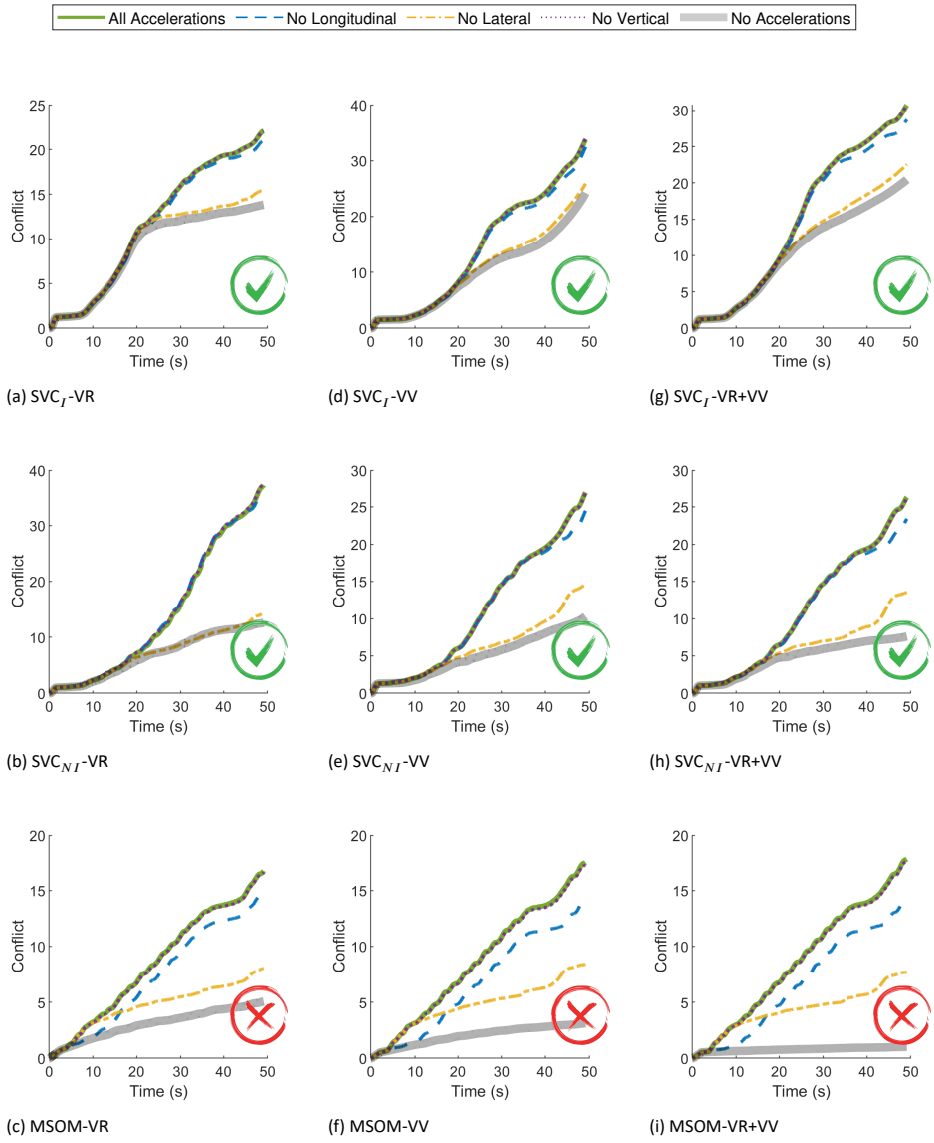

(a) SVC_I-VR (d) SVC_I-VV (g) SVC_I-VR+VV

(b) SVC_{NI}-VR (e) SVC_{NI}-VV (h) SVC_{NI}-VR+VV

(c) MSOM-VR (f) MSOM-VV (i) MSOM-VR+VV

Figure B.6: Effect of linear acceleration on conflict in the slalom drive

B.4 Visual-Vestibular Motion Sickness (VVMS) model

The Visual-Vestibular Motion Sickness (VVMS) model, a variation of the SVC model developed by Jalgaonkar et al. (2021); Sousa Schulman et al. (2023), incorporates visual inputs based on the non-linear visual-vestibular interaction model proposed by Telban and Cardullo (2001). It includes the 'visual rotational velocity' ('VR'), similar to SVC and MSOM models, and introduces 'visual inertia' ('VI'). However, at this moment the VVMS model lacks empirical validation and raises doubts about its physiological basis due to human limitations in visually perceiving acceleration (Gottsdanker, 1956; Werkhoven et al., 1992).

Testing the VVMS model alongside the other models in our comparison revealed its peculiar results in motion sickness and perception tests (appendices B.4.1 to B.4.3). We have used the parameters as published in Sousa Schulman et al. (2023). Appendix B.4 shows that sickness results are identical to the SVC_I-VR without vision, but adding vision marginally affects sickness results. Consequently, the VVMS model, in its current state, is not preferable for motion perception or sickness predictions. The conclusion of the paper remains unaffected by its inclusion in our comparison (late in the publication process), as the SVC-VR and MSOM-VR+VV models remain superior for predicting motion sickness and perception, respectively.

B.4.1 Motion Sickness

Sickness with Head Translation Figure B.7 shows that the responses for the VVMS model are identical to the SVC_I-VR model. This figure is an extension of figure 3.6. It can also be noted that the effect of vision is small on the integrated conflict for the cases with physical motion ('external', 'internal' and 'no' vision). The absence of motion sickness in 'only vision' case for the VVMS-VR is consistent with all other models.However, VVMS-VI and VVMS-VR+VI do show sickness at low frequencies. Despite the promise shown by VVMS models utilizing 'VI' in predicting sickness during pure translation, it is critical to acknowledge that humans do not possess the ability to perceive visual inertia.

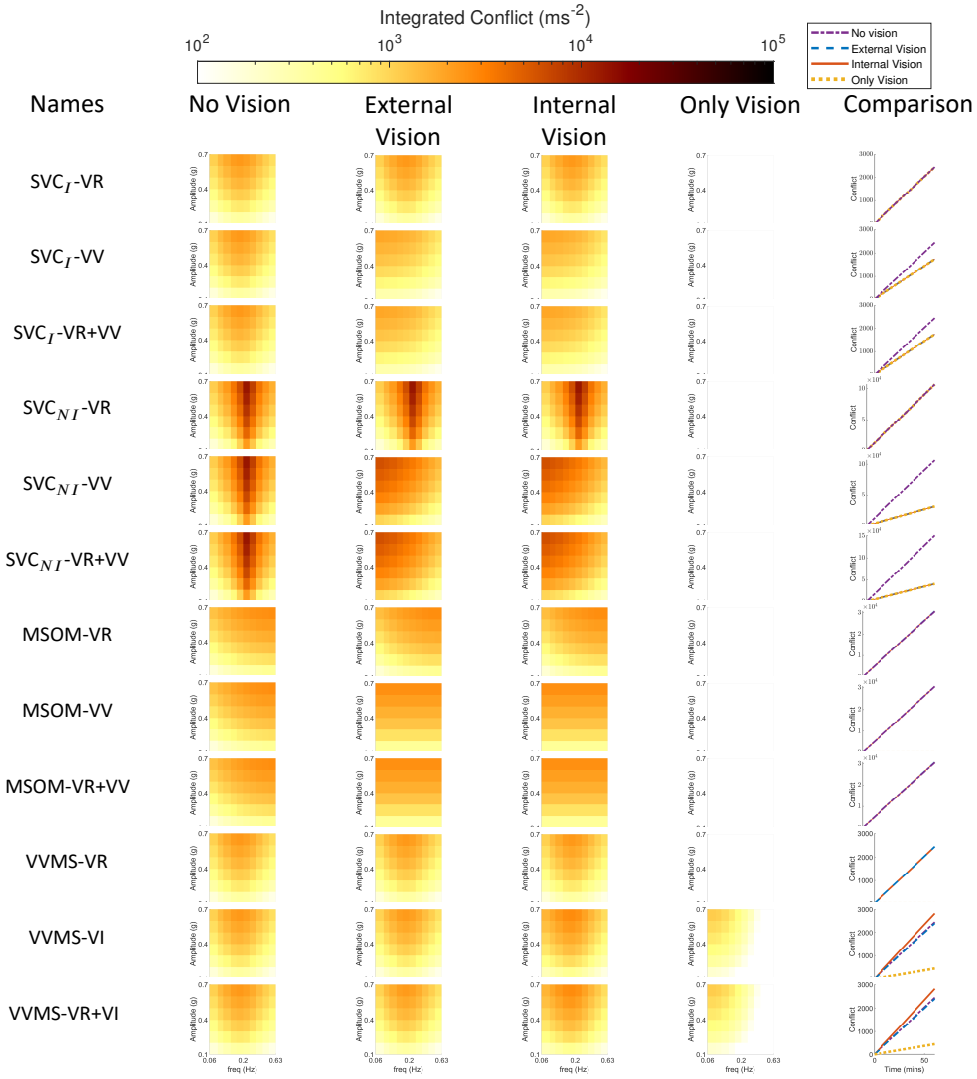

Figure B.7: Frequency sensitivity of integrated conflict (m/s) with sinusoidal fore-aft motion for different vision conditions: 'no vision' (eyes closed), 'external vision' (eyes open and with outside view), 'internal vision' (eyes open and without outside view), 'only vision' (no motion) and comparison of vision cases at 0.2 Hz and 0.7 g fore-aft motion for SVC_I, SVC_{NI} and MSOM (Plots for the 'no vision' case are the same as in figure 3.4)

Sickness with Head Rotation The conflict accumulation can be seen in figure B.8 for motion sickness with rotations. This figure is an extension of figure 3.7. The VVMS model gives a high-pass response with more motion sickness at higher frequencies. This behaviour remains the same for 'no' and 'external' vision conditions across all variations in the VVMS model (VR, VI, VR+VI). In the VVMS-VR model, the 'internal' and 'only' vision conditions too show the sane high pass dynamics but with 'only' vision having very low levels ofconflict and also a different peak frequency. For the VVMS models with 'VI', a very different frequency and amplitude dynamics is seen where the peak frequency decreases with increase in amplitude. this may be due to an occurrence of resonance at particular frequencies and amplitudes.

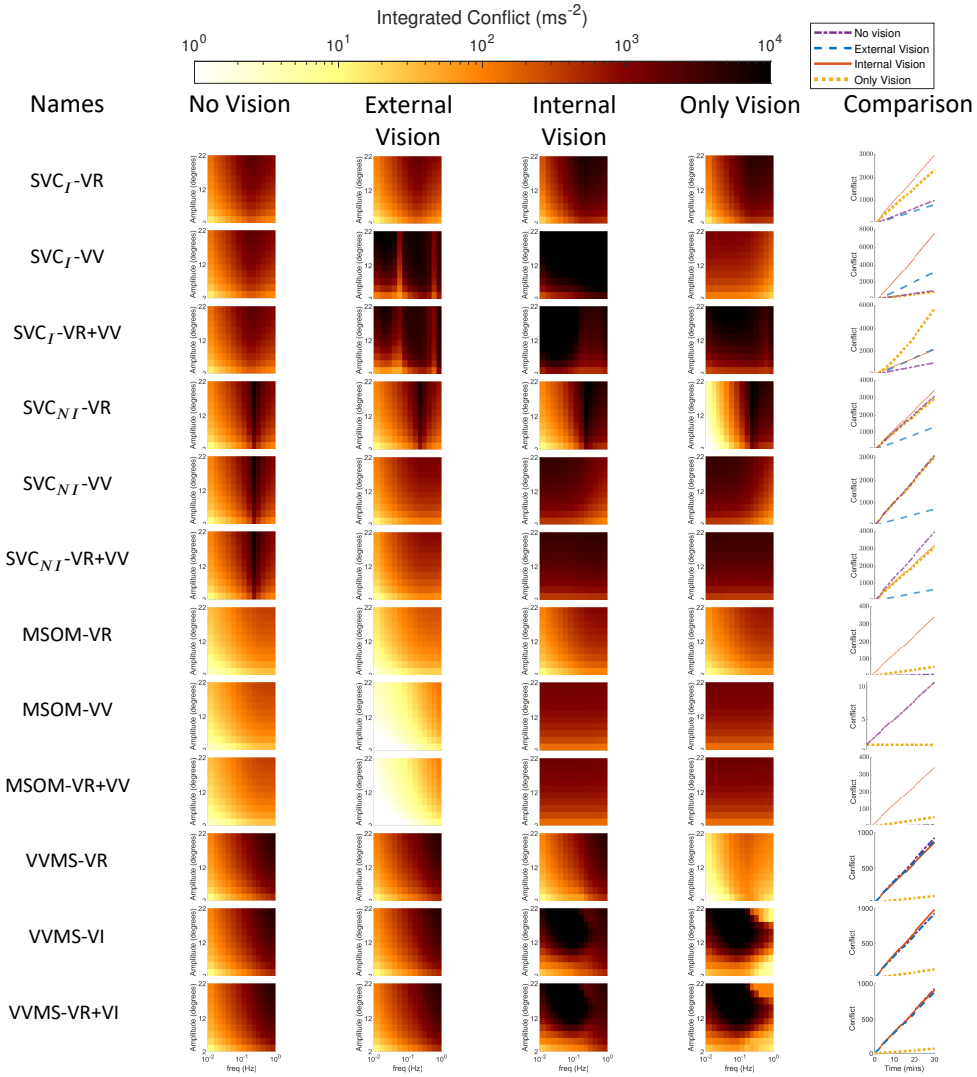

Figure B.8: Frequency sensitivity of integrated conflict (m/s) with sinusoidal pitch motion for different vision conditions: 'no vision' (eyes closed), 'external vision' (eyes open and with outside view), 'internal vision' (eyes open and without outside view), 'only vision' (no motion) and comparison of vision cases at 0.2 Hz and 20° pitch motion for SVC_I, SVC_{NI} and MSOM

B.4.2 Motion Perception Paradigm Tests

We have queried the same signals as the other SVC models in our comparison.

EVAR (Earth Vertical Axis Rotation) and OVAR (Off-Vertical Axis Rotation) Figure B.9 shows the yaw angular velocity perception to stimuli of EVAR at 60°/s. The VVMS model gives a perfect perception of yaw velocity in cases with physical motion ('external', 'internal' and 'no' vision cases). However, there is no perception of rotational velocity in 'only vision' case, where there is no physical motion. This is not what was expected and seen in Waespe and Henn (1977).

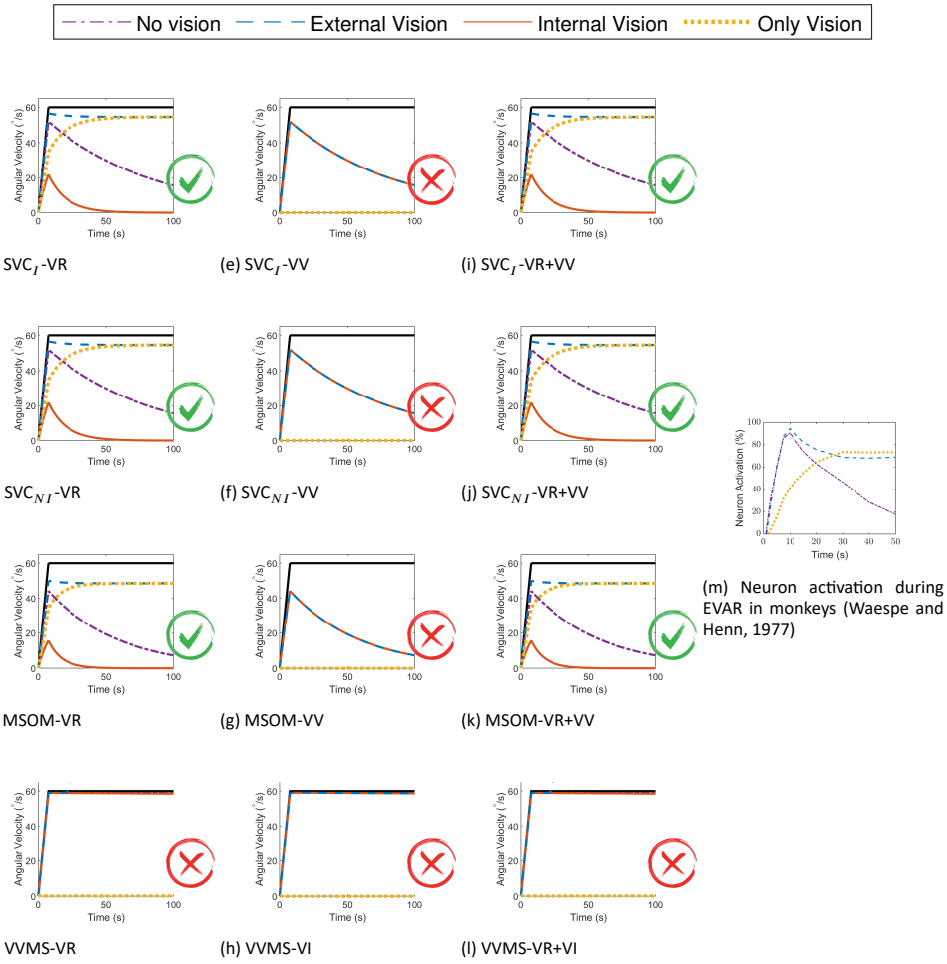

Figure B.9: Angular velocity perception during EVAR at 60°/s;
Red cross - Result in disagreement with literature, Green Tick - Result in agreement with literature.

Somatogravic Illusion The results for all the variations of the VVMS model (see figure B.10) are identical to the results of the SVC_I-VR model. This means there is no effect of these visual inputs on responses to somatogravic illusion.

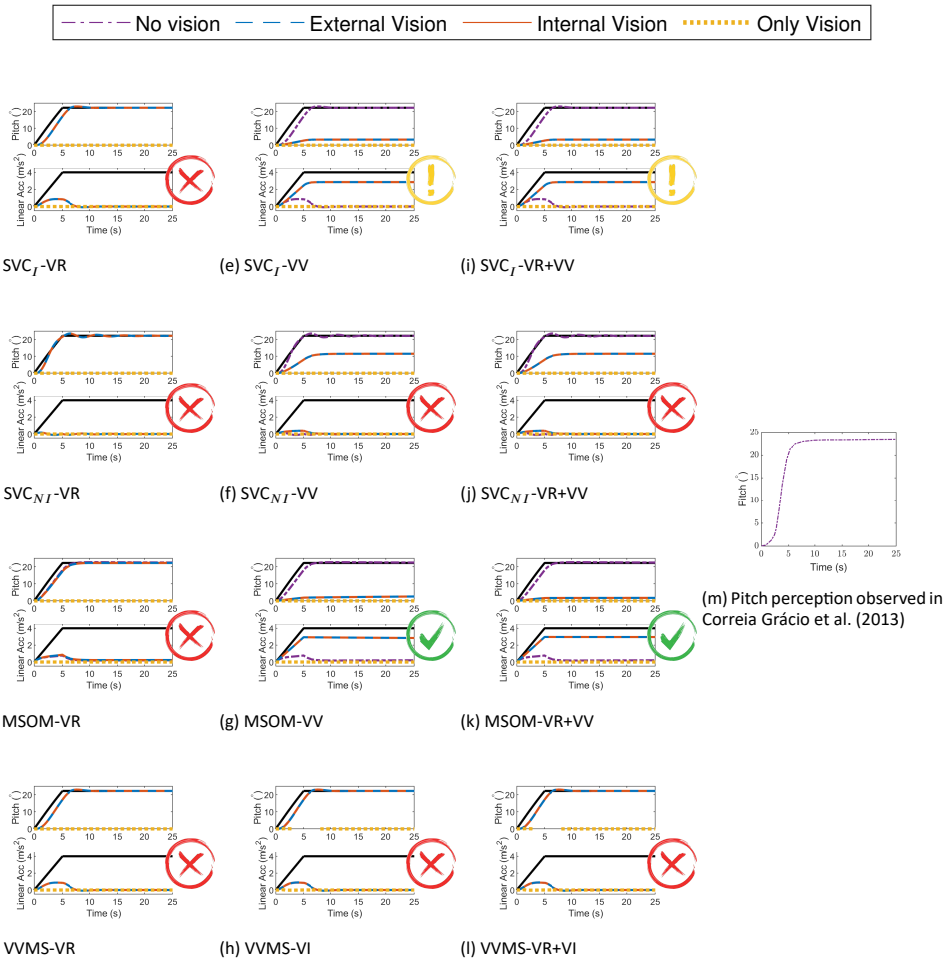

Figure B.10: Pitch perception during constant acceleration of 4 m/s^2 (somatogravic illusion); For each condition the upper graph shows the perceived pitch and the lower graph the perceived acceleration. Black lines describe the applied acceleration in the lower graph, and the equivalent rotation in the upper graph.
Red cross - Result in disagreement with literature, Green Tick - Result in agreement with literature, Yellow Exclamation - Some of the results are in agreement with literature.

Centrifugation The VVMS's response to inputs representative of centrifugation are shown in figure B.11. The response for the first 30 seconds is identical in all three variations of VVMS mode (VR, VI, VR+VI). However, the magnitude of the perceived roll-tilt is underestimated. Also, the VVMS model estimates that this illusion occurs in all conditions with physical motion, regardless of the vision condition. After around 40 seconds, the responses for the external vision case for the VVMS-VR and VVMS-VR+VI models become unstable. This is likely due to the lags and delays that are accounted for in the model for the visual cues Sousa Schulman et al. (2023).

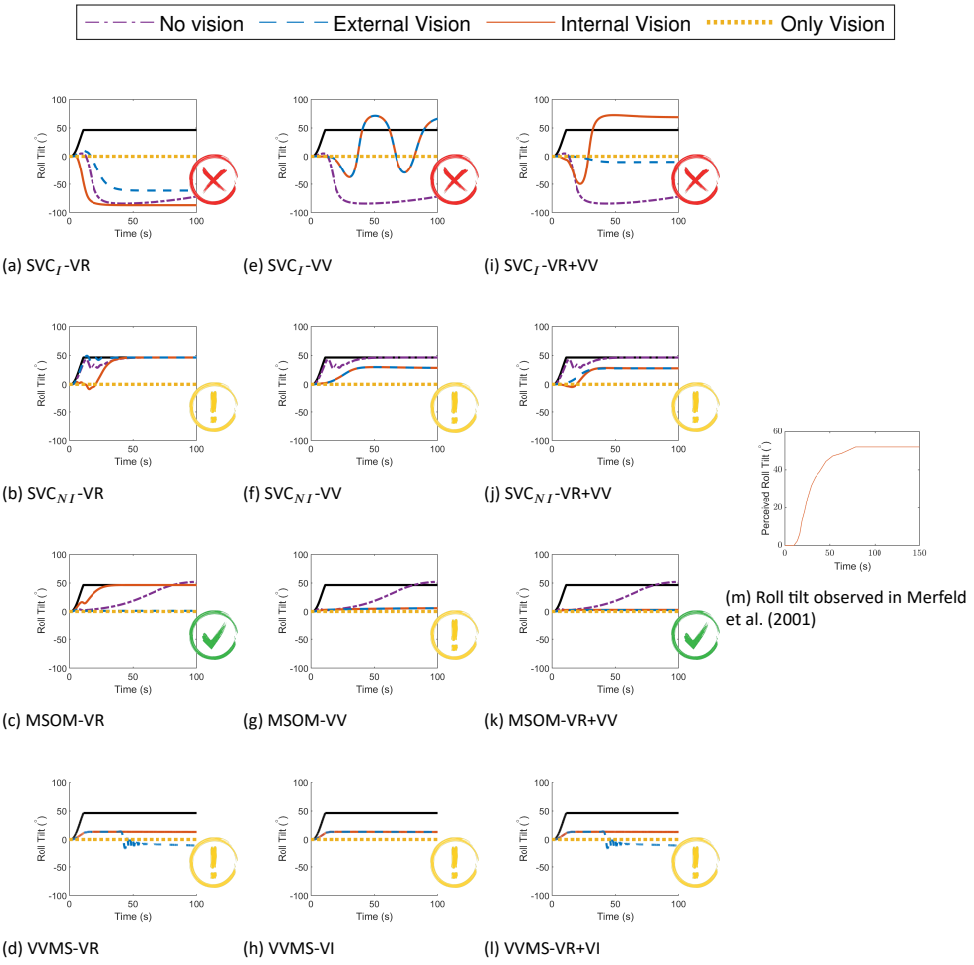

(a) SVC$_I$-VR (e) SVC$_I$-VV (i) SVC$_I$-VR+VV

(b) SVC$_{NI}$-VR (f) SVC$_{NI}$-VV (j) SVC$_{NI}$-VR+VV

(m) Roll tilt observed in Merfeld et al. (2001)

(c) MSOM-VR (g) MSOM-VV (k) MSOM-VR+VV

(d) VVMS-VR (h) VVMS-VI (l) VVMS-VR+VI

Figure B.11: Roll-tilt perception during centrifuge at 250˚/s; The black lines describe the applied motion translated to an equivalent tilt angle.
Red cross - Result in disagreement with literature, Green Tick - Result in agreement with literature, Yellow Exclamation - Some of the results are in agreement with literature.

B.4.3 Motion Sickness Predictions for Real-World Sickening Drive

Figure B.12 shows the integrated subjective vertical conflict generated due to Slalom manoeuvre Irmak et al. (2020), as introduced in section 3.2.2, by all the models for the considered vision cases. This figure is an extension of figure 3.11. Here, we present supplementary plots for the VVMS models. In the case of the VVMS model, it can be observed that the predicted conflict levels are generally low when 'only' vision is considered, particularly in the VR model. Conversely, the responses for the 'external' and 'no' vision conditions are essentially identical. In contrast, the 'internal' vision condition exhibits the highest sickness levels in models with 'VI'. However, the VVMS-VR model demonstrates low conflict levels during 'internal' vision.

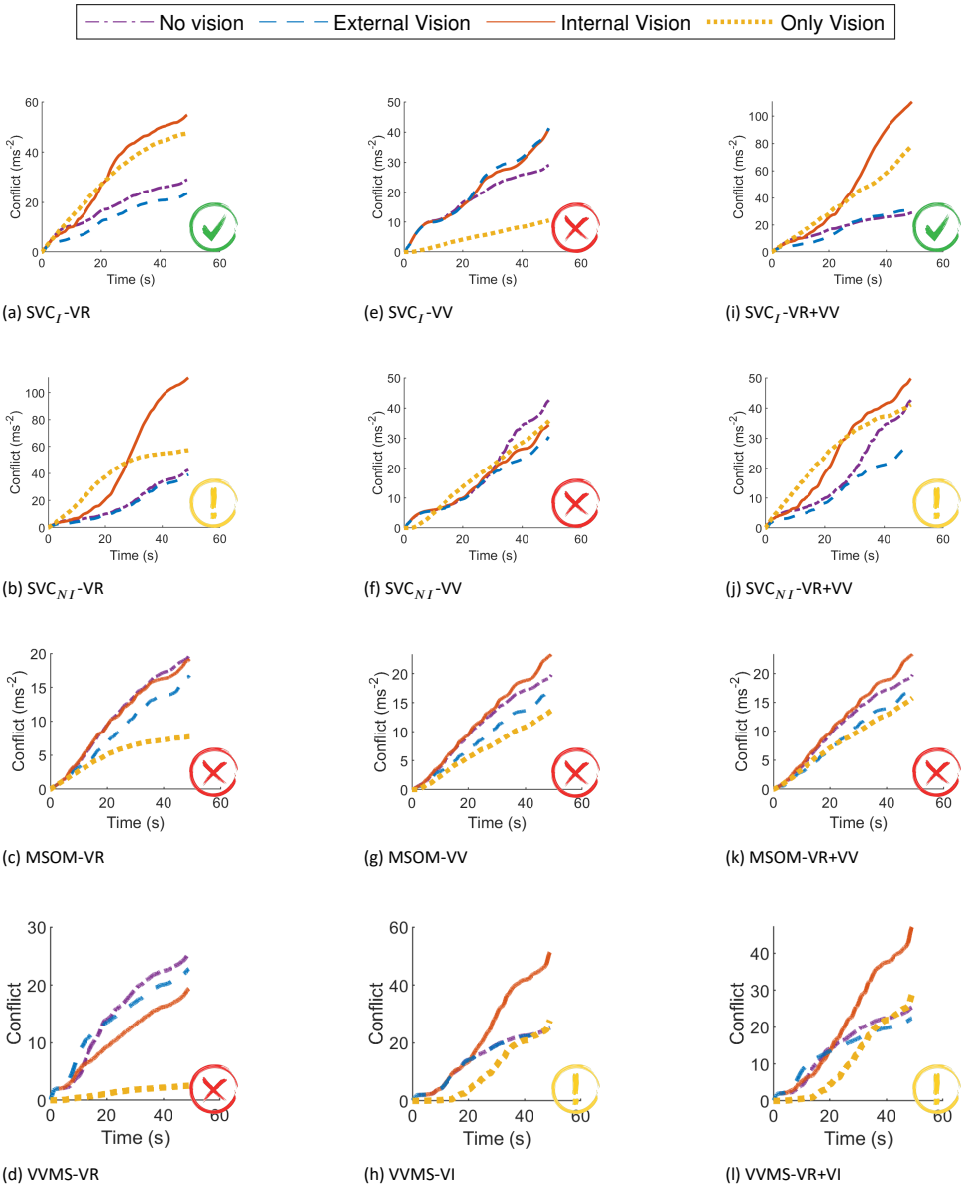

(a) SVC_I-VR (e) SVC_I-VV (i) SVC_I-VR+VV

(b) SVC_{NI}-VR (f) SVC_{NI}-VV (j) SVC_{NI}-VR+VV

(c) MSOM-VR (g) MSOM-VV (k) MSOM-VR+VV

(d) VVMS-VR (h) VVMS-VI (l) VVMS-VR+VI

Figure B.12: Effect of vision on the accumulated conflict (m/s^2) for SVC_I, SVC_{NI} and MSOM during slalom drive of 47 s for 'no', 'external', 'internal', and 'only' vision conditions;
Red cross - Incorrect, Yellow Exclamation - Uncertain, Green Tick - Correct order of responses for vision conditions

C

Appendix for Chapter 4

C.1 Motion stimuli in each of the datasets

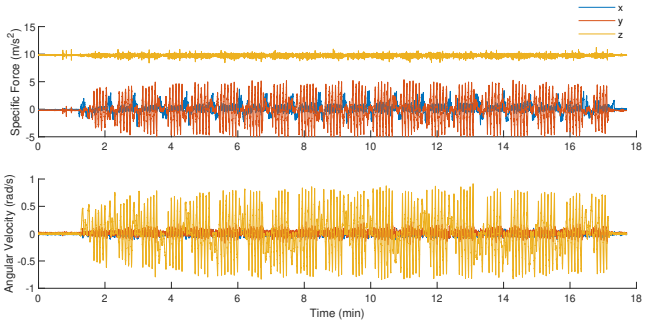

Figure C.1: Slalom Drive dataset (Irmak et al., 2020) head specific forces and angular velocities for one participant

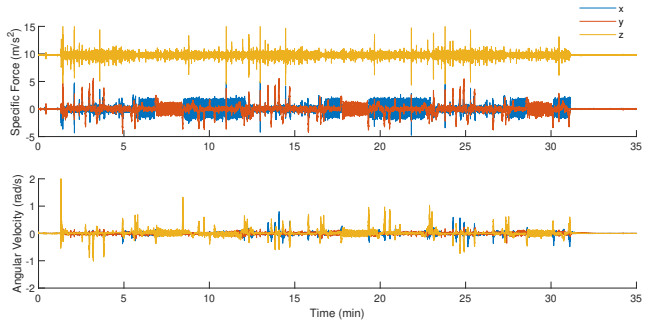

Figure C.2: Car and Simulator dataset (Talsma et al., 2023) vehicle specific forces and angular velocities for one participant

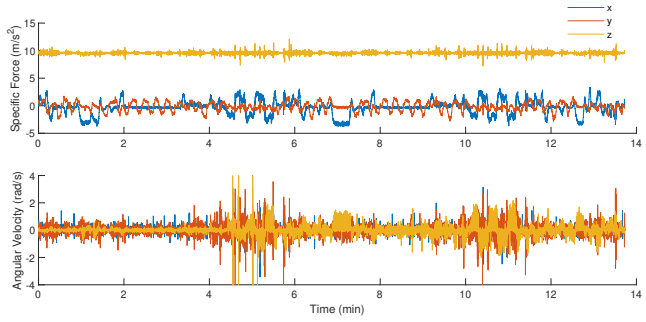

Figure C.3: NDRT Drive dataset (Metzulat et al., 2024) vehicle specific forces and angular velocities for one participant

C.2 Fitting results for all data

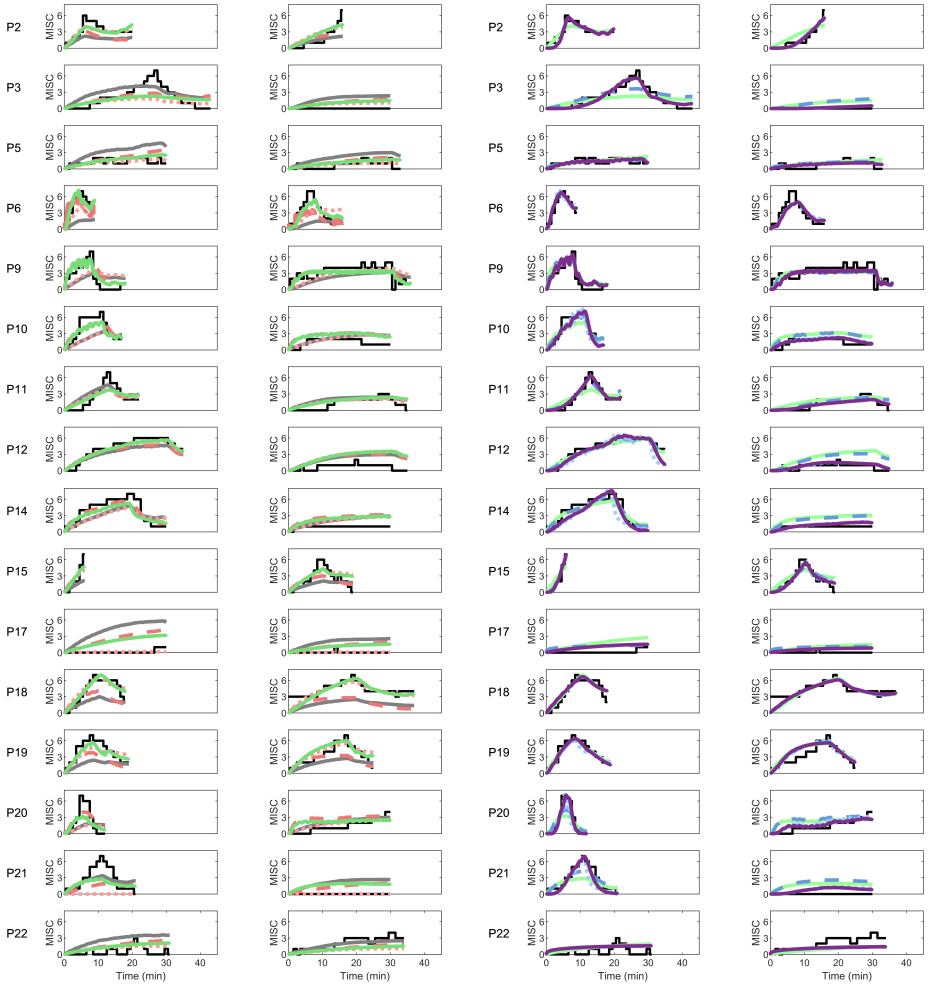

(a) AM0, AM1a, Am1b, AM2

(b) AM3, AM4a, Am4b, AM5

Figure C.4: Motion sickness responses (MISC) in Slalom Drive by Irmak et al. (2020); experiment in black, fitted AM0 in grey, AM1a in dashed red, AM1b in dotted light red, and AM2 in green, AM3 in light green, AM4a in dashed blue, AM4b in dotted light blue, and AM5 in violet for all participants (participant label shown on the left) for the conditions of internal (left column) and external (right column) vision.

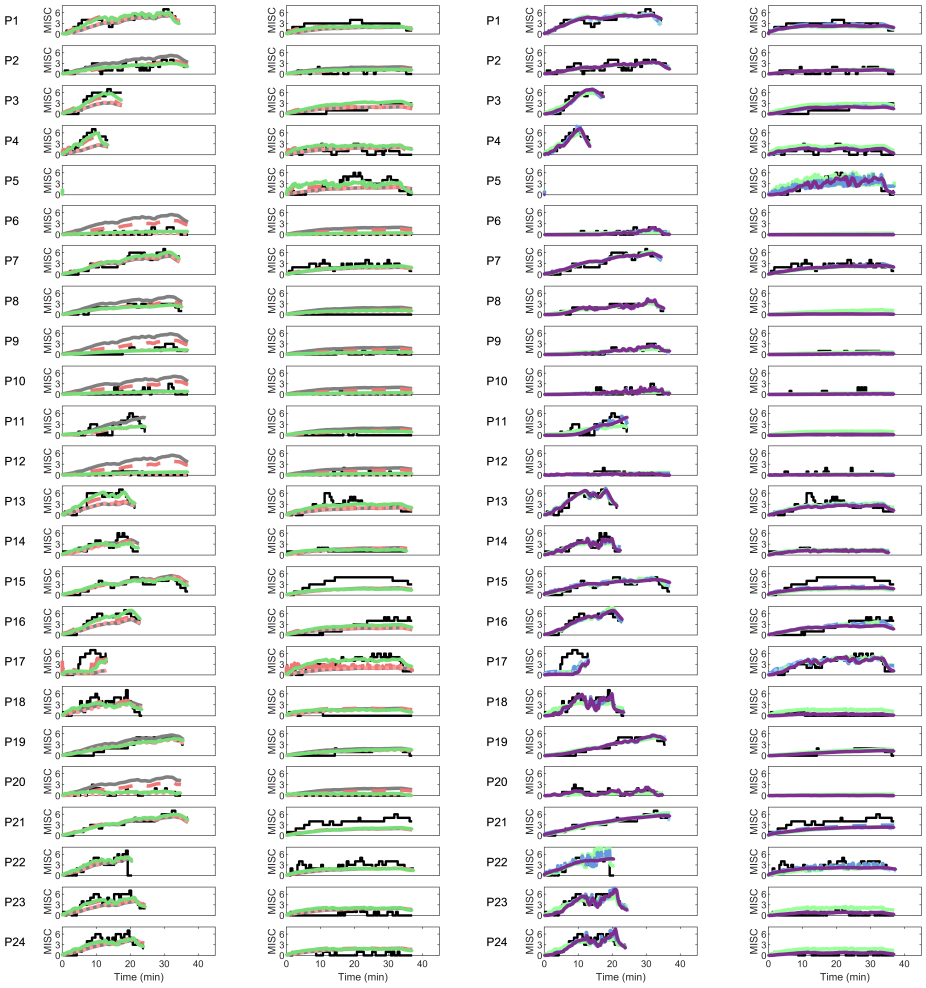

(a) AM0, AM1a, Am1b, AM2

(b) AM3, AM4a, Am4b, AM5

Figure C.5: Motion sickness responses (MISC) in Car and Simulator by Talsma et al. (2023); experiment in black, fitted AM0 in grey, AM1a in dashed red, AM1b in dotted light red, and AM2 in green, AM3 in light green, AM4a in dashed blue, AM4b in dotted light blue, and AM5 in violet for all participants (participant label shown on the left) for the conditions of internal (left column) and external (right column) vision.

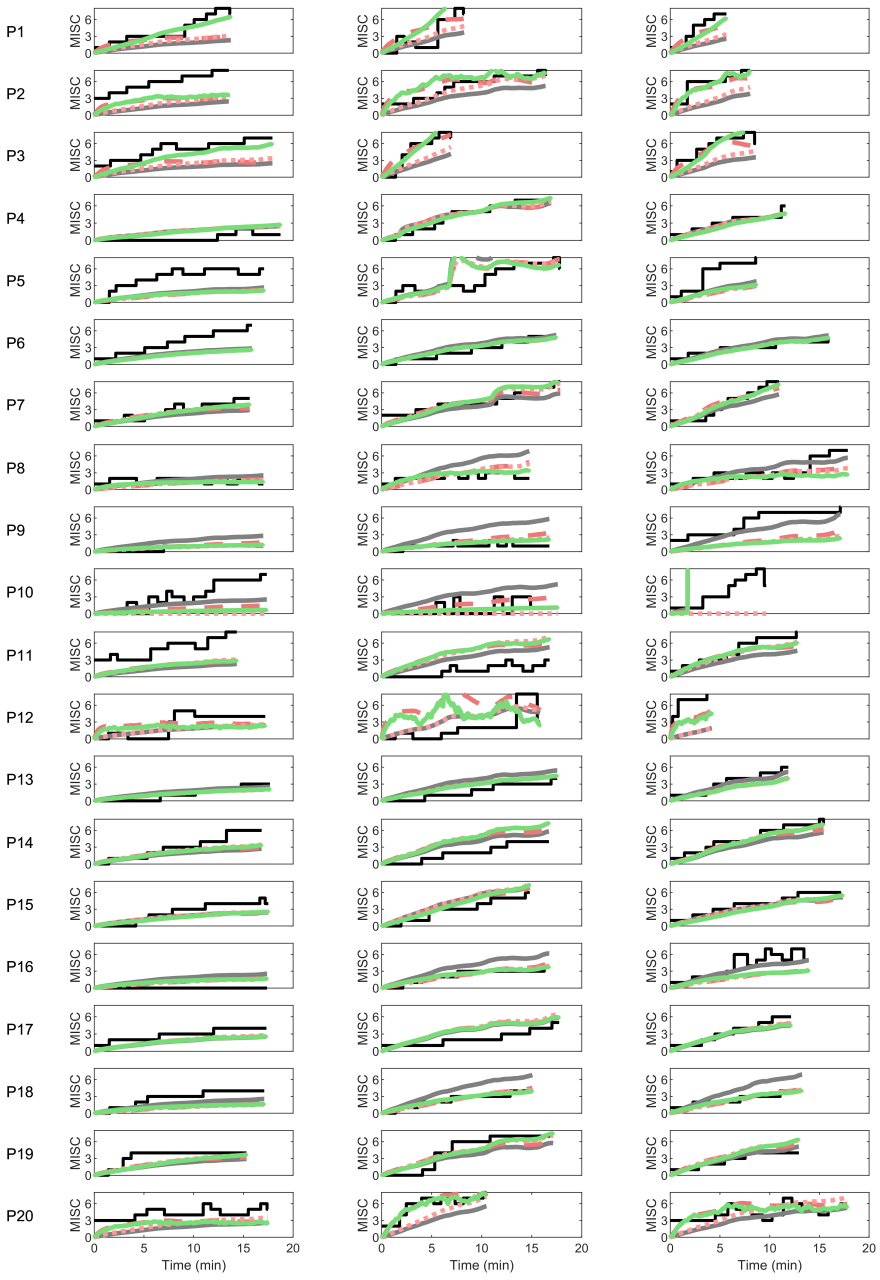

(a) AM0, AM1a, Am1b, AM2

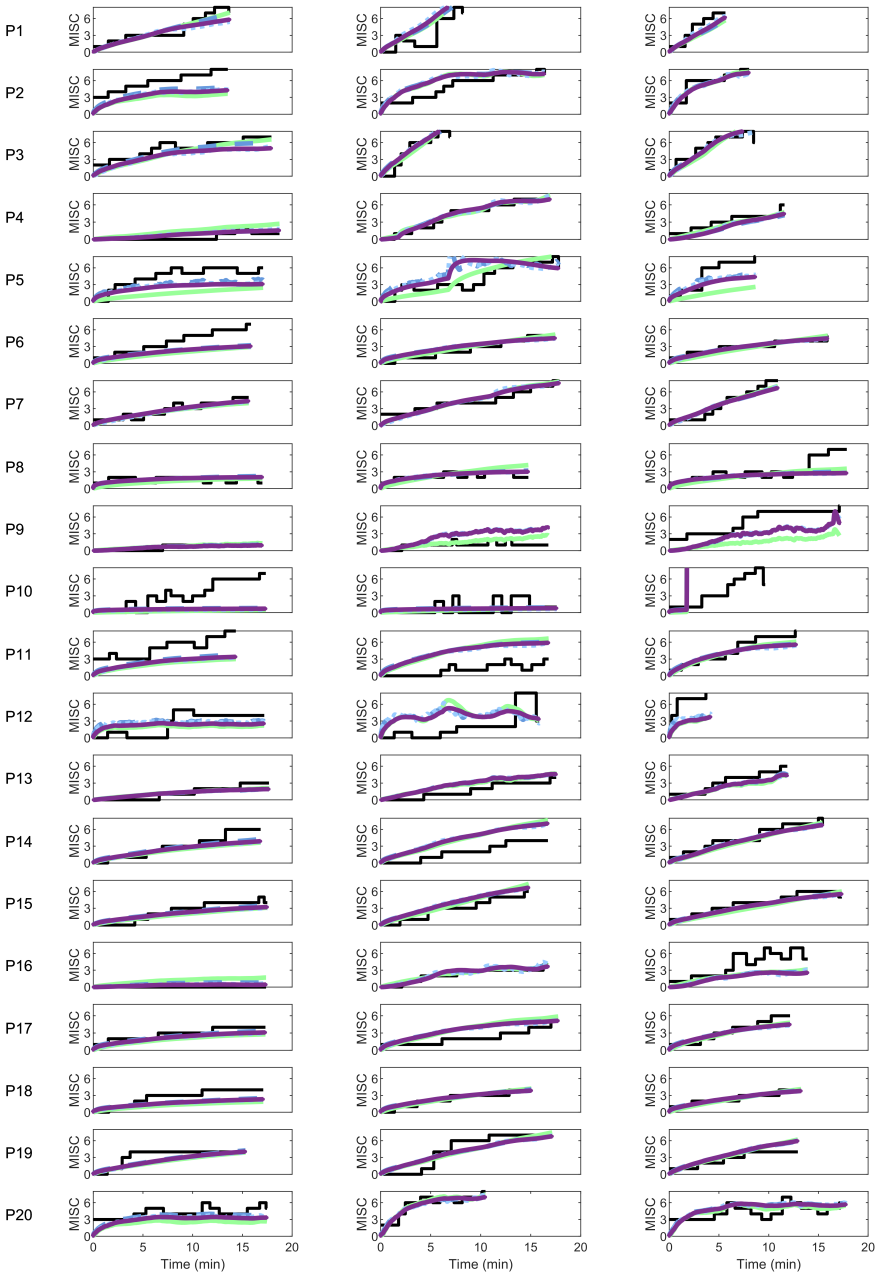

(b) AM3, AM4a, Am4b, AM5

Figure C.6: Motion sickness responses (MISC) in NDRT Drive by Metzulat et al. (2024); experiment in black, fitted AM0 in grey, AM1a in dashed red, AM1b in dotted light red, and AM2 in green, AM3 in light green, AM4a in dashed blue, AM4b in dotted light blue, and AM5 in violet for all participants (participant label shown on the left) for the conditions of internal (left column) and external (right column) vision.

C.3 Parameter Distribution Model

A 3-component Gaussian Mixture Model (GMM), as used in section 4.3.2, in 2 dimensions can be expressed mathematically as a weighted sum of three Gaussian distributions. The model is given by:

$$p(\mathbf{x}) = \sum_{j=1}^{3} \pi_j \mathcal{N}(\mathbf{x}|\boldsymbol{\mu}_j, \Sigma_j)$$

Where:

- $p(\mathbf{x})$ is the probability density function of the GMM. - π_j is the weight of the j-th Gaussian component, satisfying $\sum_{j=1}^{3} \pi_j = 1$. - $\mathcal{N}(\mathbf{x}|\boldsymbol{\mu}_j, \Sigma_j)$ is the Gaussian density function, defined as:

$$\mathcal{N}(\mathbf{x}|\boldsymbol{\mu}_j, \Sigma_j) = \frac{1}{2\pi|\Sigma_j|^{1/2}} \exp\left(-\frac{1}{2}(\mathbf{x}-\boldsymbol{\mu}_j)^\top \Sigma_j^{-1}(\mathbf{x}-\boldsymbol{\mu}_j)\right)$$

In this expression, $\boldsymbol{\mu}_j$ is the mean vector of the j-th Gaussian component, and Σ_j is the 2x2 covariance matrix.

C.4 Discretised Predictions

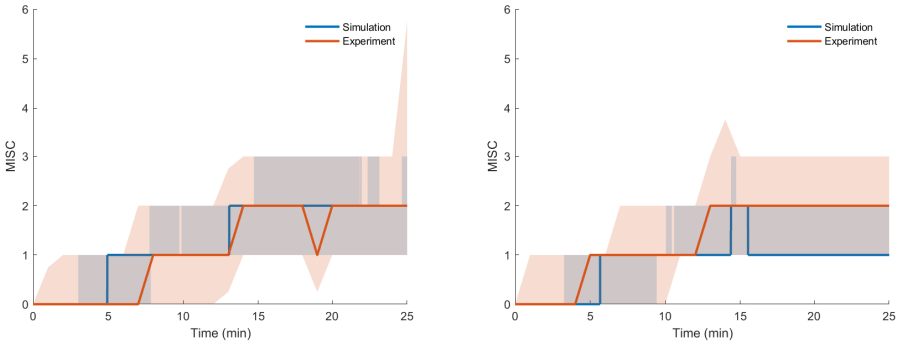

(a) On Road

(b) On Track

Figure C.7: Experimentally reported MISC and discretised Predictions of MISC on the 'Sickness recreation' dataset (Harmankaya et al., 2024) from sampled parameter sets from the probability density function of the parameter distribution (estimated gain (K_1) and time constant (T_1)) for the AM2 model.

C.5 Parameter Distribution

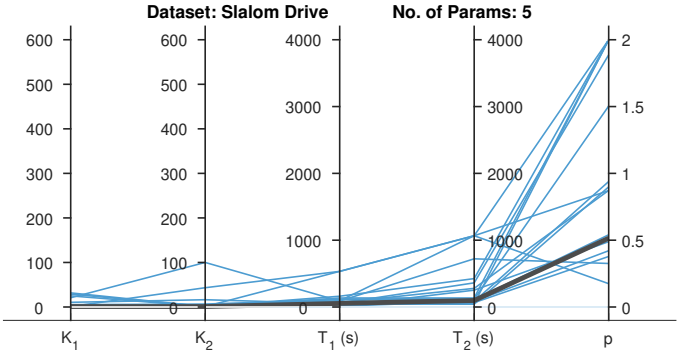

(a) Slalom drive dataset

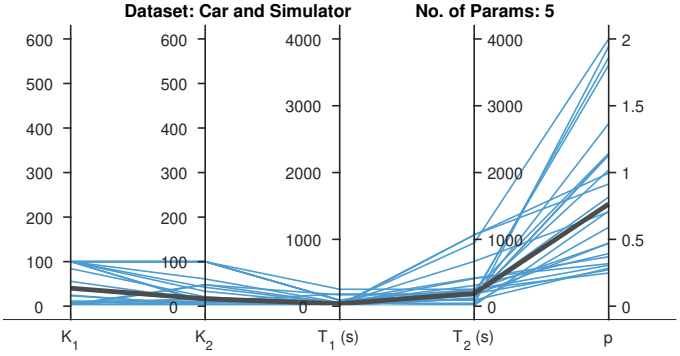

(b) Car and Simulator dataset

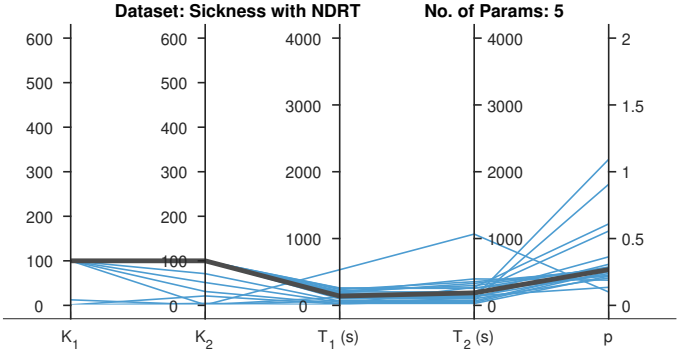

(c) NDRT Drive dataset

Figure C.8: Parameter distribution (estimated gain (K_1) and time constant (T_1)) for the AM5 model (blue) with median values (black) for the three datasets

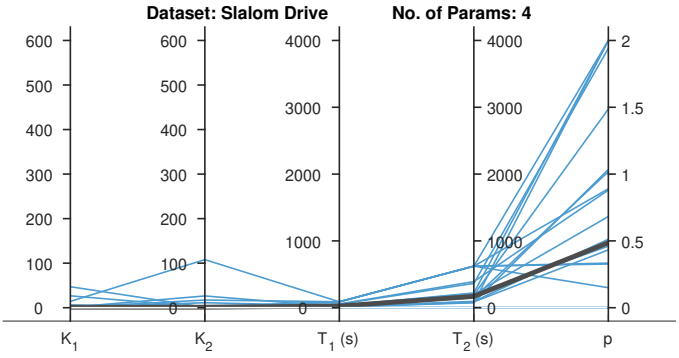

(a) Slalom drive dataset

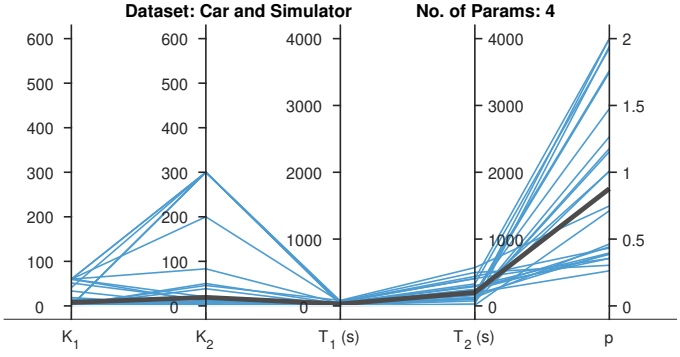

(b) Car and Simulator dataset

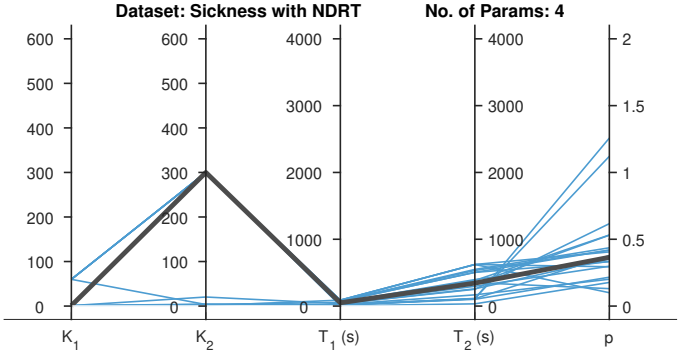

(c) NDRT Drive dataset

Figure C.9: Parameter distribution (estimated gain (K_1) and time constant (T_1)) for the AM4b model (blue) with median values (black) for the three datasets

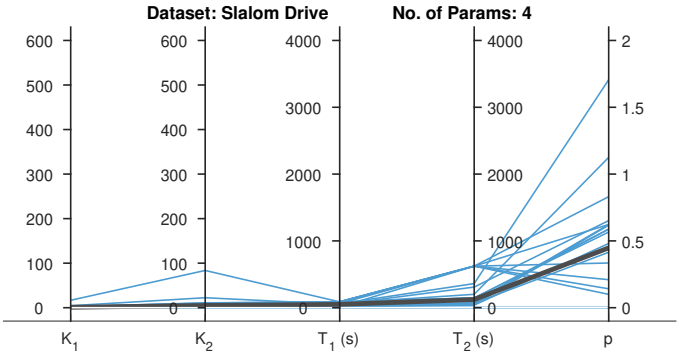

(a) Slalom drive dataset

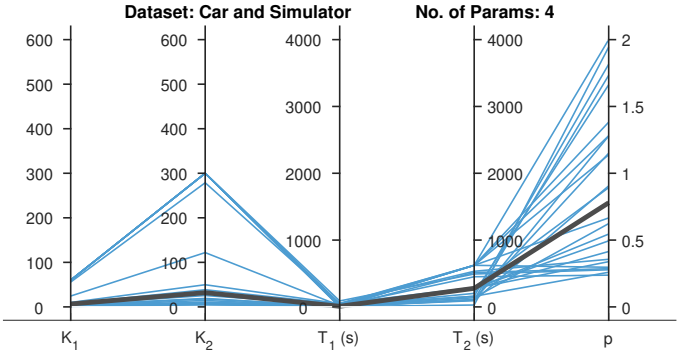

(b) Car and Simulator dataset

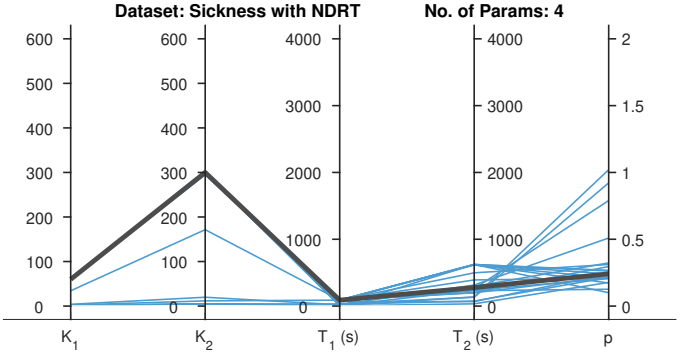

(c) NDRT Drive dataset

Figure C.10: Parameter distribution (estimated gain (K_1) and time constant (T_1)) for the AM4a model (blue) with median values (black) for the three datasets

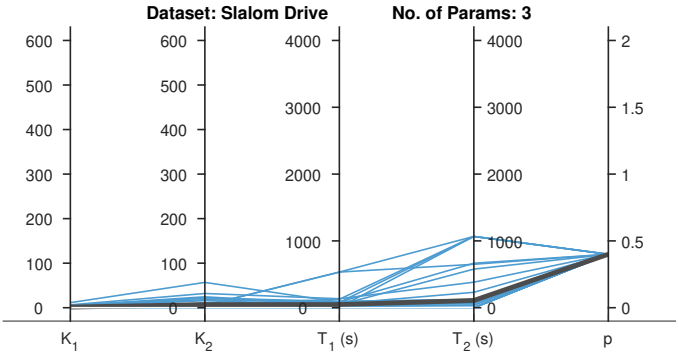

(a) Slalom drive dataset

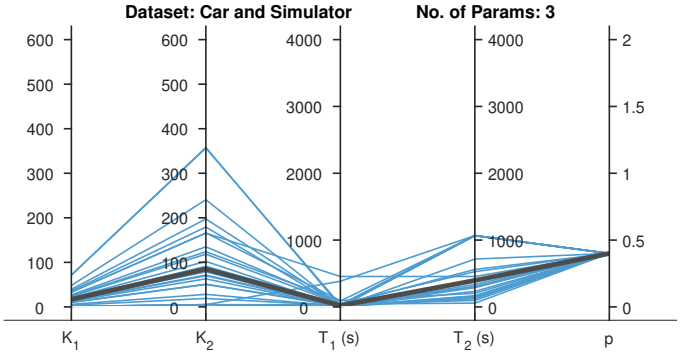

(b) Car and Simulator dataset

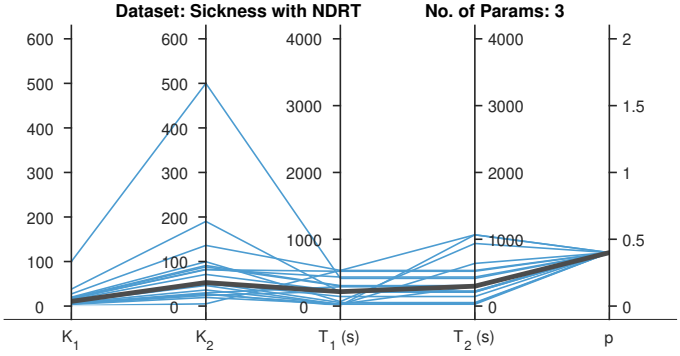

(c) NDRT Drive dataset

Figure C.11: Parameter distribution (estimated gain (K_1) and time constant (T_1)) for the AM3 model (blue) with median values (black) for the three datasets

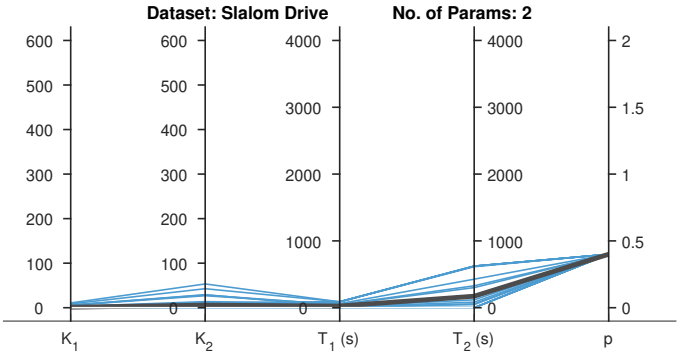

(a) Slalom drive dataset

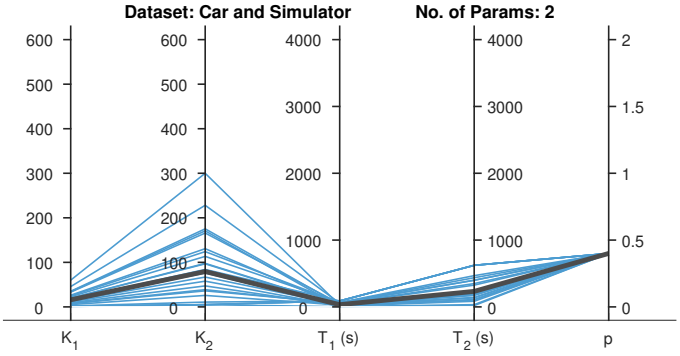

(b) Car and Simulator dataset

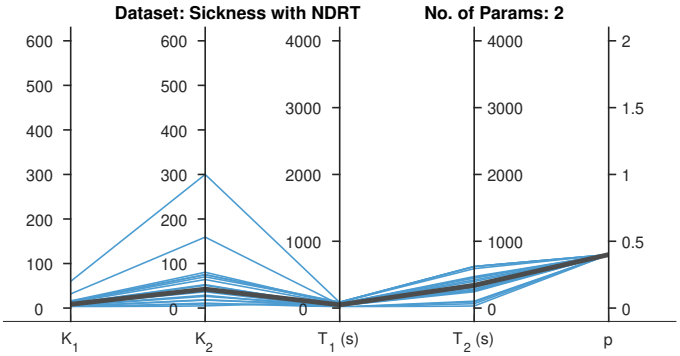

(c) NDRT Drive dataset

Figure C.12: Parameter distribution (estimated gain (K_1) and time constant (T_1)) for the AM2 model (blue) with median values (black) for the three datasets

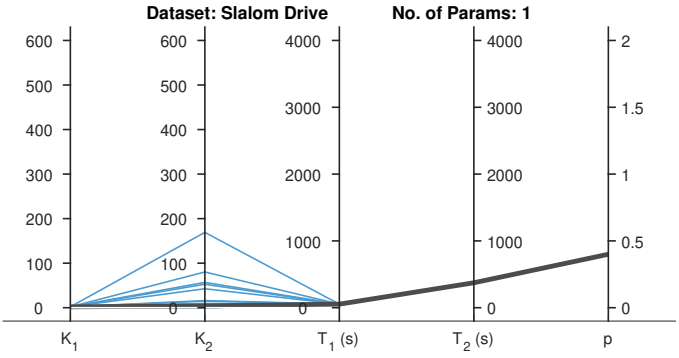

(a) Slalom drive dataset

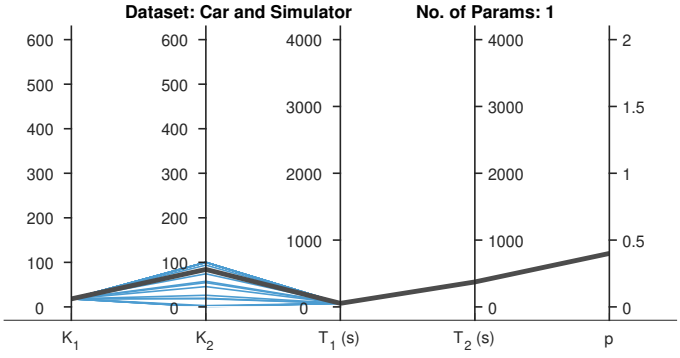

(b) Car and Simulator dataset

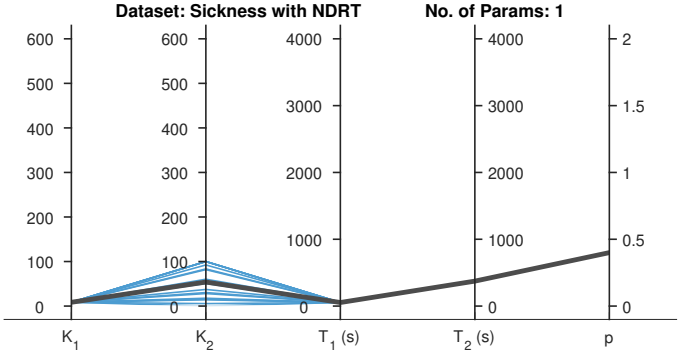

(c) NDRT Drive dataset

Figure C.13: Parameter distribution (estimated gain (K_1) and time constant (T_1)) for the AM1b model (blue) with median values (black) for the three datasets

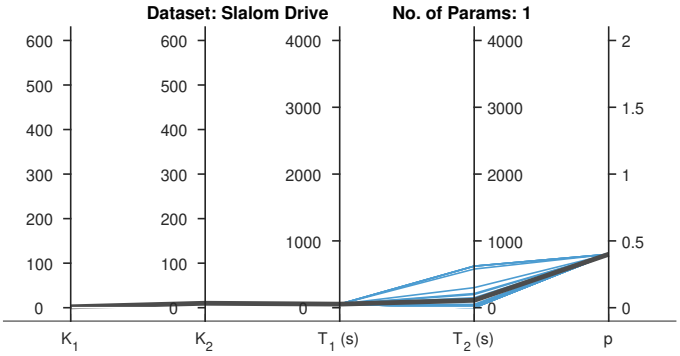

(a) Slalom drive dataset

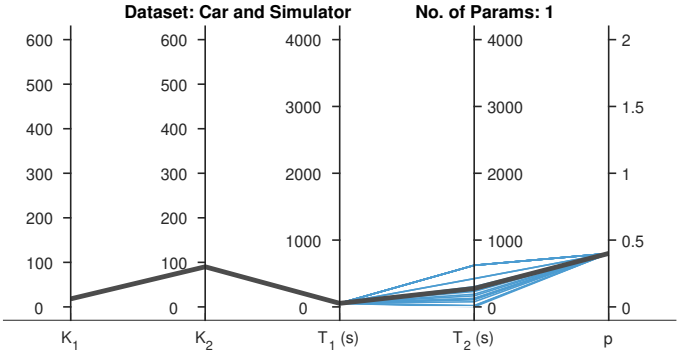

(b) Car and Simulator dataset

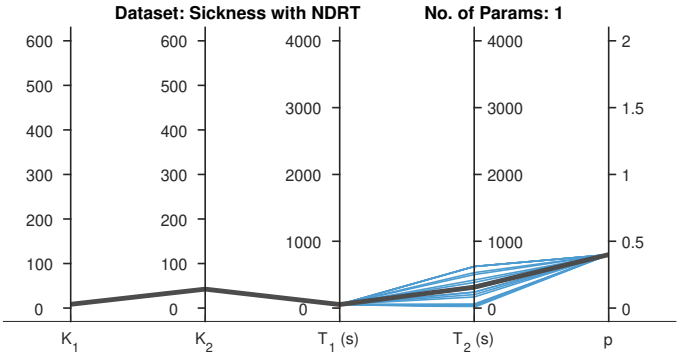

(c) NDRT Drive dataset

Figure C.14: Parameter distribution (estimated gain (K_1) and time constant (T_1)) for the AM1a model (blue) with median values (black) for the three datasets

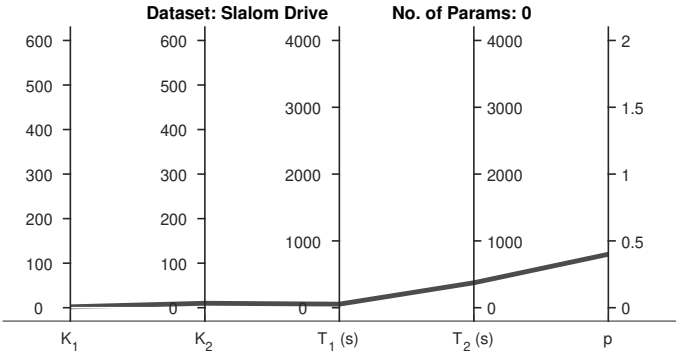

(a) Slalom drive dataset

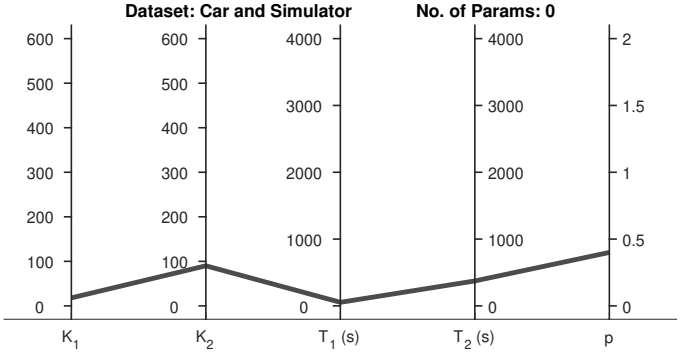

(b) Car and Simulator dataset

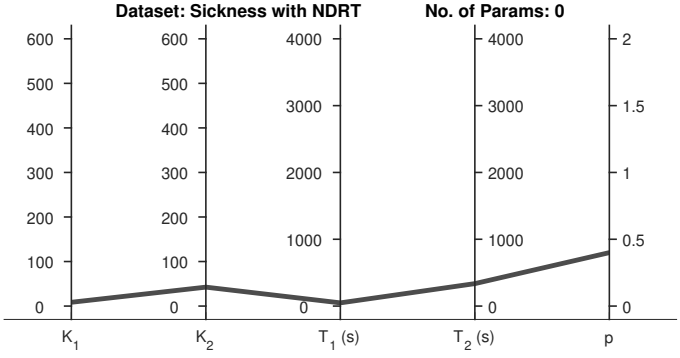

(c) NDRT Drive dataset

Figure C.15: Parameter distribution (estimated gain (K_1) and time constant (T_1)) for the AM0 model (blue) with median values (black) for the three datasets

C.6 MIsery SCale (MISC)

The MIsery SCale (MISC) for motion sickness is an established subjective measure from 0 to 10 used to quantify the severity of discomfort experienced during motion sickness based on symptoms such as nausea, dizziness and general feeling of unwell (Bos et al., 2005). It has now been rebranded as the Motion Illness Symptoms Classification (MISC) scale (Reuten et al., 2021).

Table C.1: MIsery SCale (MISC) as described in Bos et al. (2005); Reuten et al. (2021)

Symptoms		Score
No Probliems		0
Slight discomfort but no specific symptoms		1
Dizziness, warm, headache, stomach awareness, sweating, etc.	vage	2
	some	3
	medium	4
	severe	5
Nausea	some	6
	medium	7
	severe	8
	retching	9
Vomiting		10

D

Appendix for Chapter 5

D.1 Human response variance for all conditions

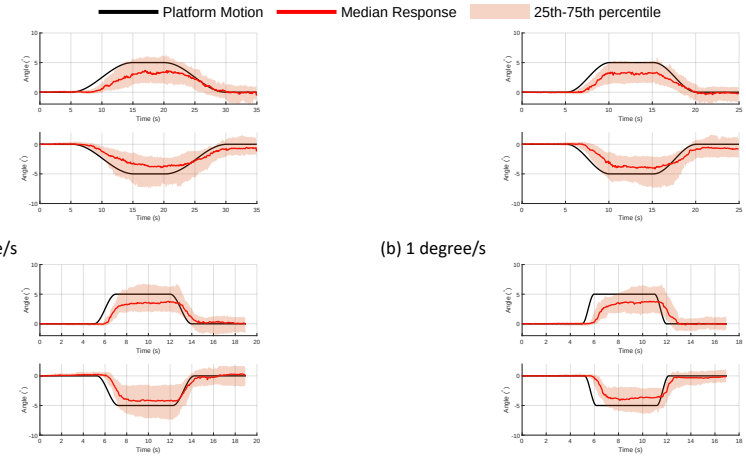

(a) 0.5 degree/s

(b) 1 degree/s

(c) 2.5 degree/s

(d) 5 degree/s

Figure D.1: Mean response across various rotational rates for 'External Vision' with the 25th and 75th percentile responses as the shaded region.

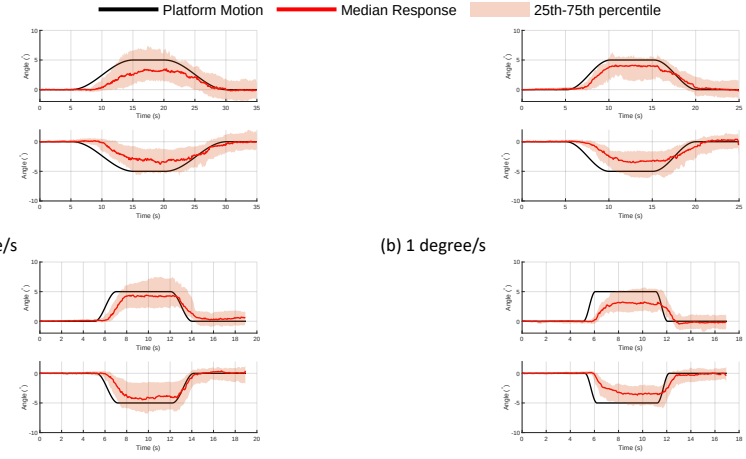

(a) 0.5 degree/s

(b) 1 degree/s

(c) 2.5 degree/s

(d) 5 degree/s

Figure D.2: Mean response across various rotational rates for 'Internal Vision' with the 25th and 75th percentile responses as the shaded region.

(a) 0.5 degree/s

(b) 1 degree/s

(c) 2.5 degree/s

(d) 5 degree/s

Figure D.3: Mean response across various rotational rates for 'No Vision' with the 25th and 75th percentile responses as the shaded region.

(a) 0.5 degree/s

(b) 1 degree/s

(c) 2.5 degree/s

(d) 5 degree/s

Figure D.4: Mean response across various rotational rates for 'Only Vision' with the 25th and 75th percentile responses as the shaded region.

D.2 Box-plots for metrics for human responses

We calculated settling times, rise times, lag times and steady-state amplitude as metrics for analysing the participants' responses. Figure 5.6 shows how these metrics are calculated. Analysis of variance (ANOVA) was conducted to determine whether direction, vision, or rotational rate had a significant effect on the measured outcomes. The results are discussed in section 5.3.1.

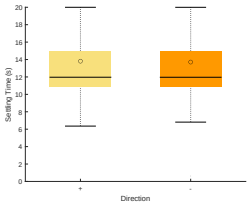

(a) Settling Times

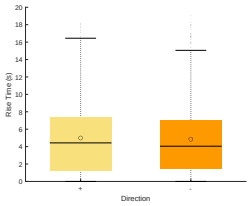

(b) Rise Times

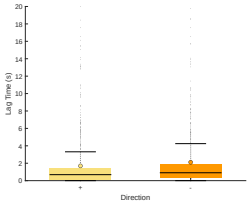

(c) Lag Times

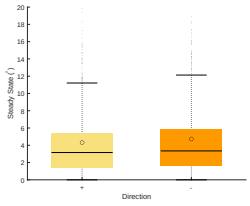

(d) Steady State Amplitude

Figure D.5: Box-plots comparing the two directions of motion stimuli (+ indicates forward and - indicates rearward pitch) averaged over vision conditions.

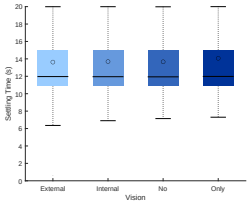

(a) Settling Times

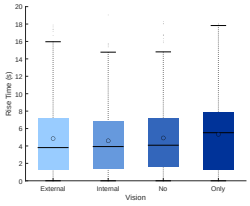

(b) Rise Times

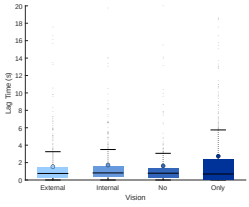

(c) Lag Times

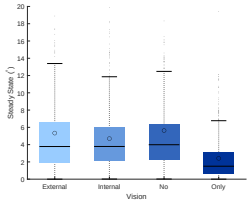

(d) Steady State Amplitude

Figure D.6: Box-plots comparing the four vision conditions.

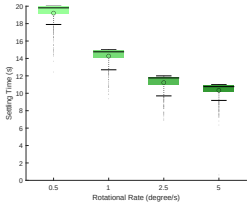

(a) Settling Times

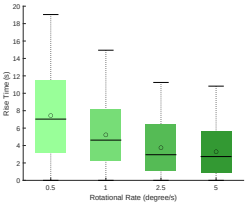

(b) Rise Times

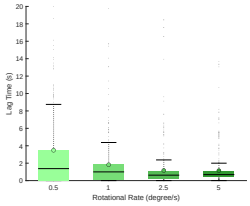

(c) Lag Times

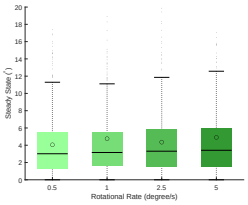

(d) Steady State Amplitude

Figure D.7: Box-plots comparing the four rotational rates of the motion stimuli.

D.3 MSOM MODEL PARAMETERS

Table D.1: MSOM model parameters adopted from Kotian et al. (2024) and the original sources

	Parameter Symbol	Value	Explanation
Vestibular Feedback Gains	K_a	-4	as in Newman (2009)
	K_f	4	
	$K_{f\omega}$	8	
	K_ω	8	
	K_1	$K_\omega/(K_\omega+1)$	
Visual Feedback Gains	K_{x_v}	0.1	as in Newman (2009)
	$K_{\dot{x}_v}$	0.75	
	K_{g_v}	10	
	K_{ω_v}	10	
Perception Time Constant	$\tau_{scc}(s)$	5.7	as in Merfeld et al. (1993)

D.4 COMPARISON WITH SVC MODEL

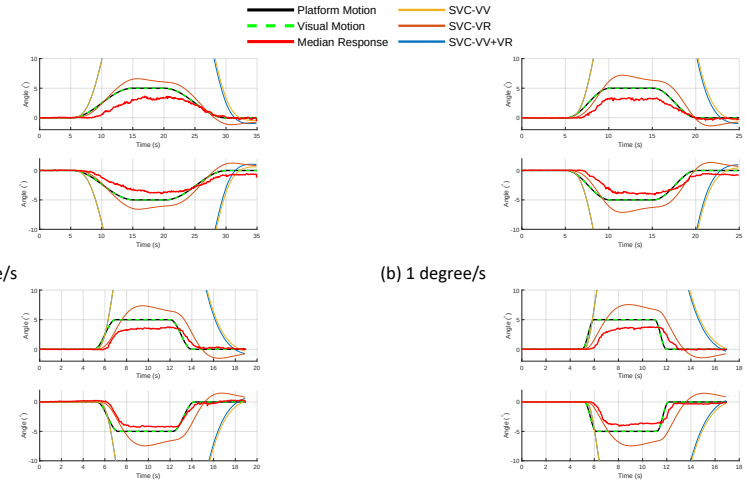

(a) 0.5 degree/s

(b) 1 degree/s

(c) 2.5 degree/s

(d) 5 degree/s

Figure D.8: Median response across various rotational rates and various vision conditions compared with responses from the SVC model for the 'External Vision' condition

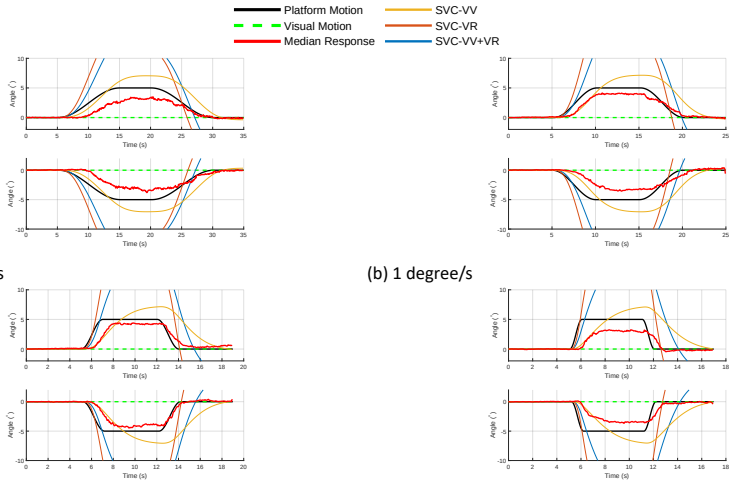

(a) 0.5 degree/s

(b) 1 degree/s

(c) 2.5 degree/s

(d) 5 degree/s

Figure D.9: Median response across various rotational rates and various vision conditions compared with responses from the SVC model for the 'Internal Vision' condition

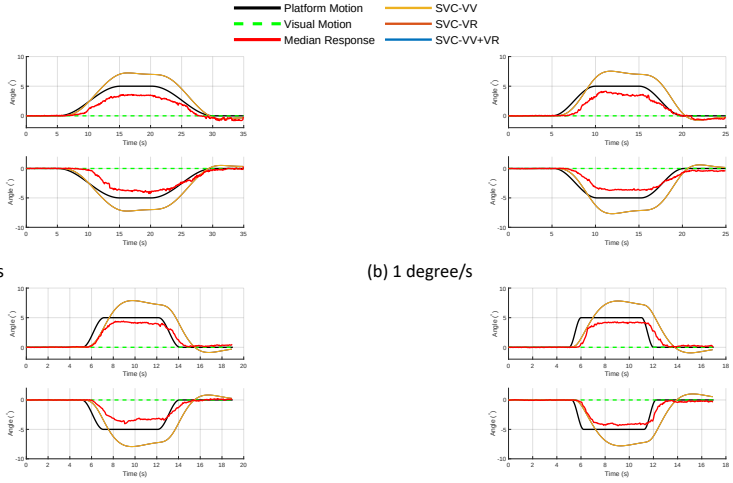

(a) 0.5 degree/s

(b) 1 degree/s

(c) 2.5 degree/s

(d) 5 degree/s

Figure D.10: Median response across various rotational rates and various vision conditions compared with responses from the SVC model for the 'No Vision' condition

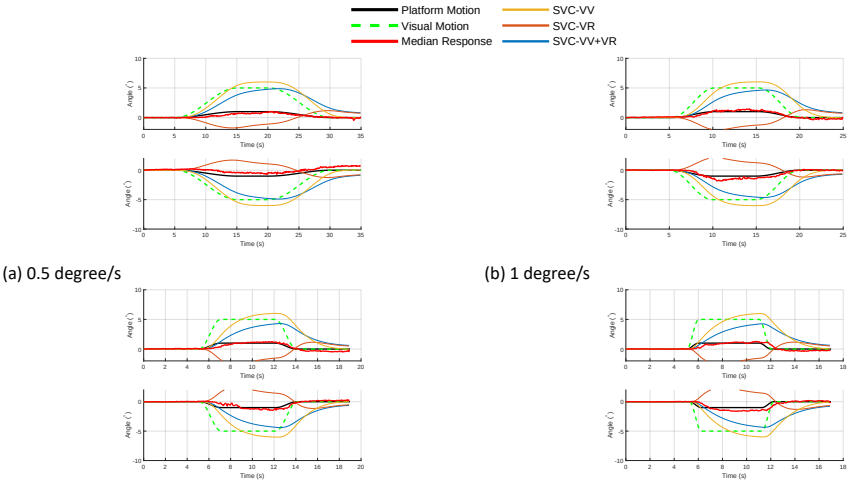

(a) 0.5 degree/s

(b) 1 degree/s

(c) 2.5 degree/s

(d) 5 degree/s

Figure D.11: Median response across various rotational rates and various vision conditions compared with responses from the SVC model for the 'Only Vision' condition

D.5 Comparison with MSOM model

The figures below compare the MSOM model with its published parameters to our experimental data. Lines MSOM-VV+VR represent the complete MSOM model using both visual verticality (VV) and visual rotation velocity (VR) inputs. The other MSOM lines (MSOM-VR) and MSOM-VV) just illustrate effects of the separate loops and do not suggest that these incomplete models should match human responses.

The results below show that with the published parameters MSOM predicts overall reasonable results with notable effects of the vision loops. However with internal vision the complete MSOM model (VV+VR) highly underestimates the perceived motion indicating dominance of visual perception. The opposite happens in Only Vision where MSOM-VV+VR predicts negligible motion perception.

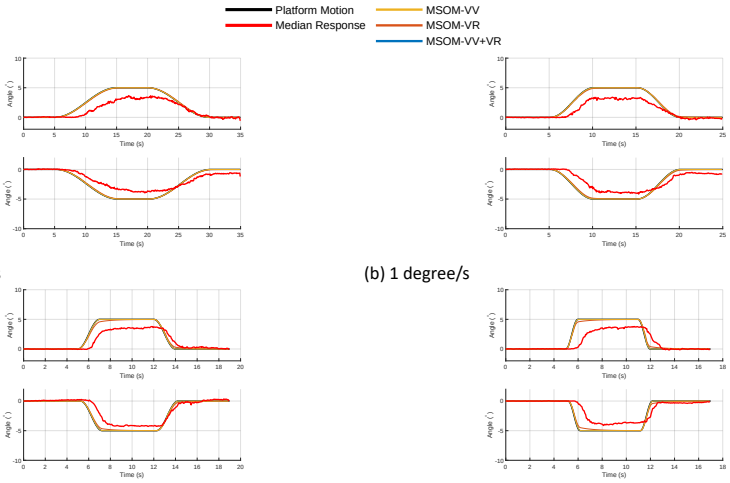

(a) 0.5 degree/s

(b) 1 degree/s

(c) 2.5 degree/s

(d) 5 degree/s

Figure D.12: Mean response across various rotational rates compared with responses from the MSOM model for the 'External Vision' condition

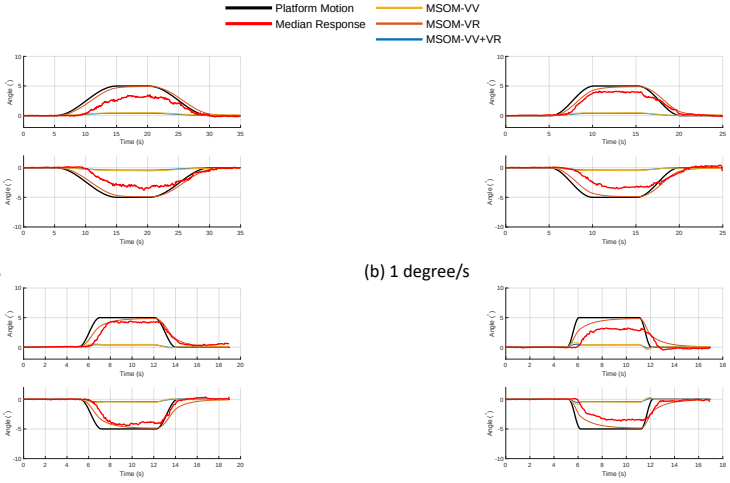

(a) 0.5 degree/s

(b) 1 degree/s

(c) 2.5 degree/s

(d) 5 degree/s

Figure D.13: Mean response across various rotational rates compared with responses from the MSOM model for the 'Internal Vision' condition

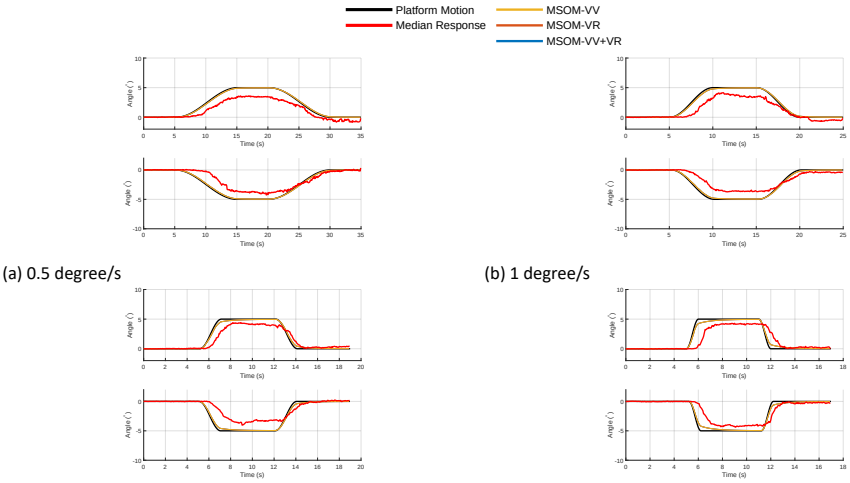

(a) 0.5 degree/s

(b) 1 degree/s

(c) 2.5 degree/s

(d) 5 degree/s

Figure D.14: Mean response across various rotational rates compared with responses from the MSOM model for the 'No Vision' condition

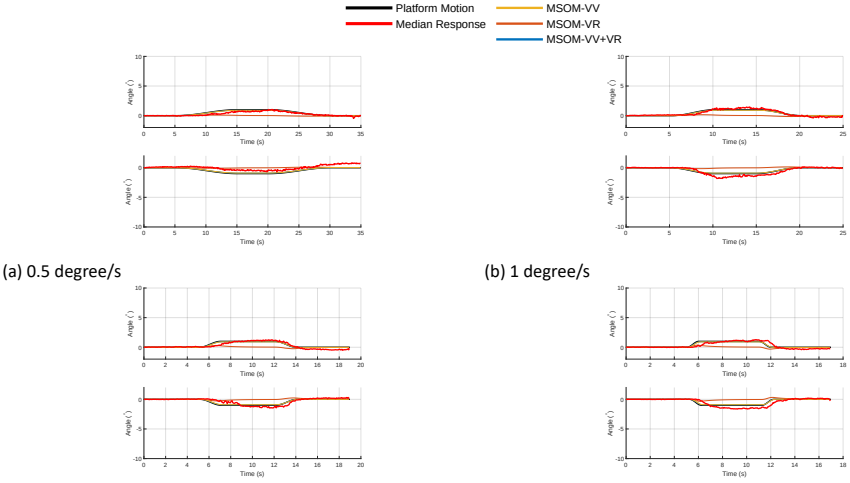

(a) 0.5 degree/s

(b) 1 degree/s

(c) 2.5 degree/s

(d) 5 degree/s

Figure D.15: Mean response across various rotational rates compared with responses from the MSOM model for the 'Only Vision' condition

D.6 SVC-VR Tuning Results

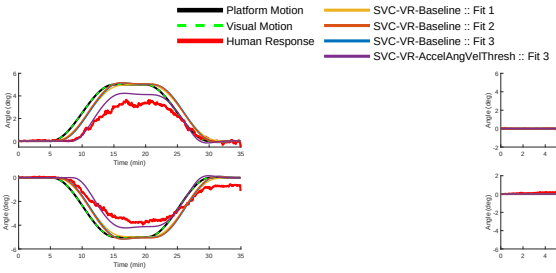

(a) 0.5 degree/s

(b) 1 degree/s

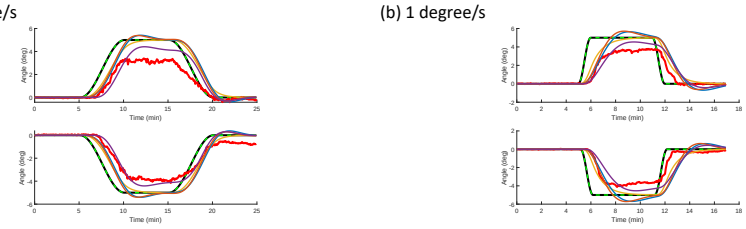

(c) 2.5 degree/s

(d) 5 degree/s

Figure D.16: Mean response across various rotational rates and various vision conditions compared with responses from the re-tuned (Fit 1, 2 and 3) SVC-VR-Baseline model and (Fit 3) SVC-VR-AccelAngVelThresh for the 'External Vision' condition

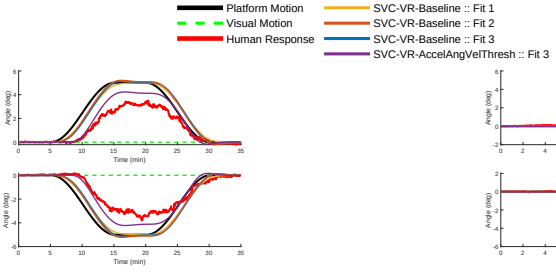

(a) 0.5 degree/s

(b) 1 degree/s

(c) 2.5 degree/s

(d) 5 degree/s

Figure D.17: Mean response across various rotational rates and various vision conditions compared with responses from the re-tuned (Fit 1, 2 and 3) SVC-VR-Baseline model and (Fit 3) SVC-VR-AccelAngVelThresh for the 'Internal Vision' condition

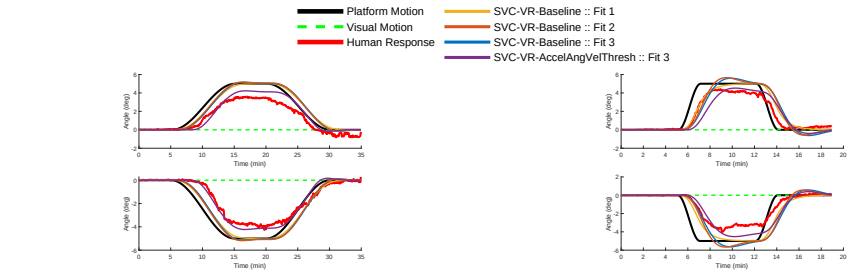

(a) 0.5 degree/s

(b) 1 degree/s

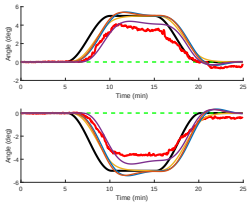

(c) 2.5 degree/s

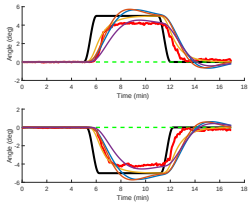

(d) 5 degree/s

Figure D.18: Mean response across various rotational rates and various vision conditions compared with responses from the re-tuned (Fit 1, 2 and 3) SVC-VR-Baseline model and (Fit 3) SVC-VR-AccelAngVelThresh for the 'No Vision' condition

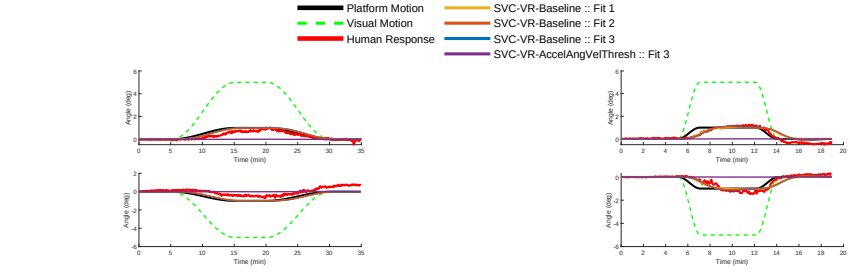

(a) 0.5 degree/s

(b) 1 degree/s

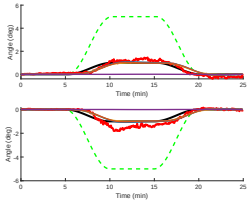

(c) 2.5 degree/s

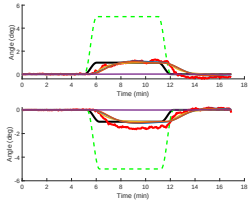

(d) 5 degree/s

Figure D.19: Mean response across various rotational rates and various vision conditions compared with responses from the re-tuned (Fit 1, 2 and 3) SVC-VR-Baseline model and (Fit 3) SVC-VR-AccelAngVelThresh for the 'Only Vision' condition

D.7 Derivation of $K_{vc} = \tau$

Tuning the SVC parameters will affect perception and motion sickness results and may disrupt the validation, as shown in Kotian et al. (2024) for the original SVC parameters. Here, we address the effect on frequency sensitivity for motion sickness.

Irmak et al. (2023) has shown that under purely translation motion without vision, the conflict generated by the SVC model can be given by

$$H(s) = \frac{C_v(s)}{f_s(s)} = \frac{s}{\tau s^2 + (1 + K_{ac}\tau)s + K_{vc}},$$

where f_s is the specific force input, τ, K_{ac}, and K_{vc} are system parameters.

Substituting $s = j\omega$, we get

$$H(j\omega) = \frac{j\omega}{-\tau\omega^2 + j\omega(1 + K_{ac}\tau) + K_{vc}}.$$

The magnitude of the transfer function at frequency ω is

$$|H(j\omega)| = \frac{\omega}{\sqrt{\left(K_{vc} - \tau\omega^2\right)^2 + \omega^2(1 + K_{ac}\tau)^2}}.$$

we want to find the frequency ω at which the magnitude peaks by solving

$$\frac{d}{d\omega}|H(j\omega)| = 0.$$

Let's say,

$$D(\omega) = (K_{vc} - \tau\omega^2)^2 + \omega^2(1 + K_{ac}\tau)^2,$$

so that

$$|H(j\omega)|^2 = \frac{\omega^2}{D(\omega)}.$$

Taking the derivative,

$$\frac{d}{d\omega}|H(j\omega)|^2 = \frac{2\omega D(\omega) - \omega^2 D'(\omega)}{D(\omega)^2} = 0,$$

which implies

$$2\omega D(\omega) - \omega^2 D'(\omega) = 0.$$

For $\omega \neq 0$, divide both sides by ω:

$$2D(\omega) - \omega D'(\omega) = 0.$$

We compute $D'(\omega)$ as

$$\begin{aligned} D'(\omega) &= \frac{d}{d\omega}\left[(K_{vc} - \tau\omega^2)^2 + \omega^2(1 + K_{ac}\tau)^2\right] \\ &= 2(K_{vc} - \tau\omega^2)(-2\tau\omega) + 2\omega(1 + K_{ac}\tau)^2 \\ &= -4\tau\omega(K_{vc} - \tau\omega^2) + 2\omega(1 + K_{ac}\tau)^2. \end{aligned}$$

Substituting back into the equation yields

$$2\left[(K_{vc} - \tau\omega^2)^2 + \omega^2(1 + K_{ac}\tau)^2\right] - \omega\left[-4\tau\omega(K_{vc} - \tau\omega^2) + 2\omega(1 + K_{ac}\tau)^2\right] = 0.$$

Expanding and simplifying,

$$2(K_{vc} - \tau\omega^2)^2 + 2\omega^2(1 + K_{ac}\tau)^2 + 4\tau\omega^2(K_{vc} - \tau\omega^2) - 2\omega^2(1 + K_{ac}\tau)^2 = 0,$$

which reduces to

$$2(K_{vc} - \tau\omega^2)^2 + 4\tau\omega^2(K_{vc} - \tau\omega^2) = 0.$$

Dividing both sides by 2,

$$(K_{vc} - \tau\omega^2)^2 + 2\tau\omega^2(K_{vc} - \tau\omega^2) = 0,$$

or equivalently,

$$\begin{aligned} (K_{vc} - \tau\omega^2)\left[(K_{vc} - \tau\omega^2) + 2\tau\omega^2\right] &= 0. \\ (K_{vc} - \tau\omega^2)(K_{vc} + \tau\omega^2) &= 0. \end{aligned}$$

This gives two cases:

$$K_{vc} - \tau\omega^2 = 0 \quad or \quad K_{vc} + \tau\omega^2 = 0$$

The second case yields no real solution for ω. From the first case, we find the peak frequency as

$$\boxed{\omega = \sqrt{\frac{K_{vc}}{\tau}}.}$$

This is the frequency at which the magnitude $|H(j\omega)|$ achieves its maximum.

Angular frequency ω (in radians per second) can be converted to frequency f (in hertz) by,

$$f = \frac{\omega}{2\pi}.$$

and therefore,

$$f = \frac{1}{2\pi}\sqrt{\frac{K_{vc}}{\tau}}.$$

When $K_{vc} = \tau$, this becomes

$$f = \frac{1}{2\pi} \approx 0.159 \text{ Hz}.$$

The above derivation holds for conditions without vision. However, the frequency sensitivity experiments by McCauley et al. (1976) were performed with internal vision. Figure D.20 shows that with Fit 3 (enforcing $K_{vc} = \tau$), the desired peak frequency is also obtained for the SVC-VR model but not for the SVC-VR+VV model.

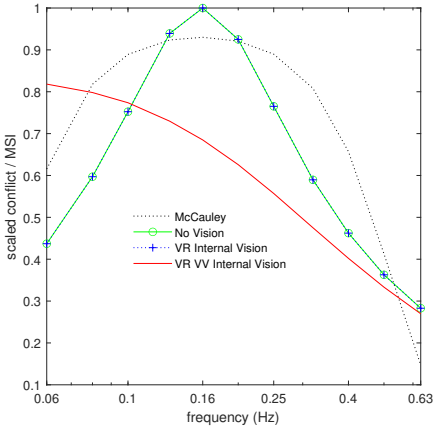

Figure D.20: Motion sickness frequency sensitivity in vertical loading at 0.7 m/s^2 with experimental data by McCauley et al. (1976) compared to three SVC model parameter sets. The vertical axis represents motion sickness incidence (MSI) from McCauley et al. (1976) and model lines represent conflict magnitude. The model lines are scaled equally towards their collective maximum. Since MSI relates to conflict in a complex manner an exact match is not to be expected. The line "No Vision" uses Fit 3 in tables 5.2 and 5.4 with all vision gains set to zero. The line VR Internal Vision ads a visual rotational velocity gain $K_\omega = 10$, and the line VR VV Internal Vision also ads a visual verticality gain $K_{gvis} = 5$. These high visual gains were based on the published models and not on the current data. These results show that frequency sensitivity is not affected by the VR loop but is strongly affected by the VV loop. These results were obtained for internal vision in vertical loading. Results for external vision are identical since there is no rotation. Results for horizontal loading are also identical due to the inherent symmetry of the SVC model.

D.8 Tuning SVC-VR+VV

Table D.2 shows fitted responses with the complete SVC model with both visual rotation velocity (VR) and visual verticality (VV). The SVC-VR+VV model shows a better fit as compared to the SVC-VR model for several variants, but RMSEs are almost identical for the best fitting model AccelAngVelThresh. Interestingly, the additional parameter K_{gvis} of SVC-VR+VV is estimated between 0.21 and 0.62 and is much below the original value of 5. This suggests a modest role of verticality perception in the current experiment. Even though a horizon was not displayed, participants may have reconstructed a verticality percept from the displayed dot pattern.

Table D.2: Parameter values and the average RMSEs for all variations of the SVC-VR+VV model compared with the original parameters from Kamiji et al. (2007); Kotian et al. (2024); Liu et al. (2022); Wada et al. (2020). Visual vertical is assumed to be the true vertical.

Model	Variation	Fit type	$K_{\omega vis}$	K_{gvis}	$K_{\omega c}$	K_{ac}	K_{vc}	τ	τ_{SCC}	Average RMSE	RMSE per vision condition			
											External	Internal	No	Only
SVC-VR+VV	Baseline	Original	10.00	5.00	10.00	1.00	5.00	5.00	7.00	1.75	2.15	1.89	2.15	0.80
		Fit 1	14.57	0.26	5.40	0.54	1.04	0.10	1.11	0.49	0.41	0.41	0.80	0.34
		Fit 2	0.43	0.34	8.10	1.31	2.27	1.14	5.94	0.67	0.54	0.43	1.25	0.43
		Fit 3	3.86	0.32	11.82	0.15	1.00	1.00	5.00	0.66	0.66	0.52	1.01	0.44
	AccelThresh	Original	10.00	5.00	10.00	1.00	5.00	5.00	7.00	1.62	2.17	1.90	1.59	0.81
		Fit 1	0.14	0.20	5.14	0.28	1.24	0.38	10.73	0.48	0.48	0.42	0.39	0.63
		Fit 2	0.72	0.28	6.71	0.51	1.68	1.30	7.17	0.64	0.68	0.52	0.64	0.70
		Fit 3	0.84	0.30	5.03	0.13	1.15	1.15	7.99	0.66	0.77	0.63	0.57	0.66
	AngVelThresh	Original	10.00	5.00	10.00	1.00	5.00	5.00	7.00	1.49	2.20	1.95	1.00	0.81
		Fit 1	14.55	0.46	5.00	0.73	1.72	0.32	1.10	0.55	0.51	0.48	0.83	0.38
		Fit 2	0.09	0.30	7.48	2.02	3.09	1.00	5.55	0.52	0.47	0.42	0.83	0.37
		Fit 3	0.39	0.31	5.03	0.20	1.00	1.00	5.02	0.66	0.66	0.57	1.00	0.39
	AccelAngVelThresh	Original	10.00	5.00	10.00	1.00	5.00	5.00	7.00	1.40	2.22	1.96	0.59	0.83
		Fit 1	7.19	0.20	10.64	1.00	2.27	0.38	1.15	0.47	0.40	0.40	0.38	0.71
		Fit 2	0.00	0.21	9.93	3.00	9.06	2.09	5.62	0.47	0.47	0.42	0.36	0.62
		Fit 3	0.00	0.26	8.36	0.81	5.99	5.99	7.61	0.63	0.69	0.60	0.60	0.63

D.9 Stimuli with prolonged duration

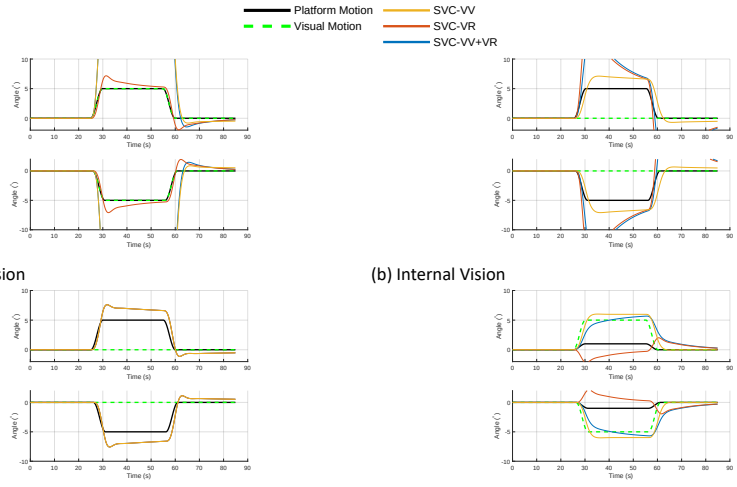

(a) External Vision

(b) Internal Vision

(c) No Vision (the models coincide)

(d) Only Vision

Figure D.21: Predictions from the three SVC model variants with original parameters for stimuli with prolonged duration with mean rotational rates of 1 degree/s.

E

Appendix for Chapter 6

E.1 MPC Algorithm Weight Settings

For the simulations presented in this chapter, model predictive control (MPC) is implemented using `ForcesPro` Domahidi and Jerez (2014), using the Primal dual interior point (PDIP) algorithm. The maximum iterations are chosen to be 200, to ensure convergence and avoid sub-optimal solutions. The optimisation has been performed on Intel(R) Xeon(R) W-2223 CPU @3.60GHz with 32GB RAM.

In this work, we consider two major contribution terms that define the primary objective of the algorithm, along with several minor terms that help guide the MPC toward the desired performance. The two primary objective terms should have the highest contribution in the cost function.

Since the cost terms have different units, their relative contributions cannot be directly determined by the weights alone. To address this, we normalise the cost terms. This normalisation facilitates the assignment of weights, enabling each term to be tuned based on its priority. Specifically, a preliminary simulation is used to estimate the maximum expected value of each cost term. Each term in the cost function is then divided by its corresponding maximum, ensuring that the normalised errors lie within comparable ranges.

This approach allowed us to explore the full trade-off spectrum, or Pareto front, between competing objectives such as motion perception (via specific force tracking) and motion sickness mitigation (via RMS sensory conflict). While the normalisation does not provide a universal or mathematically exact scaling, the estimated maxima—derived from representative scenarios—offer a robust basis for comparative analysis.

Should future scenarios diverge significantly from those used during this normalisation phase, the scaling bounds can be re-evaluated and updated accordingly.

The final selected weights are tabulated in table E.1.

Table E.1: Penalization weights for the objective function terms

penalisation weight	used Value
w_θ (angular orientation)	1e-4
w_ω (angular velocity)	1e-1
w_s (displacement)	1e-2
w_j (translational jerk)	1e-4
$w_{ang,j}$ (angular jerk)	1e-4
w_δ (slack variable)	1e-4

The w_s and w_θ correspond to the parameters k1 and k3, respectively, in appendix E.5, that affect the shape of the non-linear weight function. w_ω, w_j, $w_{ang,j}$ and w_δ are the penalisation weights for angular velocity, translational jerk, angular jerk and the slack variable. Note that all weights are represented as 2×2 diagonal matrices to apply separate penalties in the longitudinal and lateral directions, except for the slack variable weight w_δ, which

remains scalar since it does not relate to spatial dimensions.

For the initial analysis, a penalisation weight of unity is set for specific force tracking. Additionally, the penalisation weights on the angular orientation and the platform displacement is a dynamical non-linear weight which changes based on the platform state (see appendix E.5 under workspace management) the penalisation weight chosen for this quantity just scales the overall non-linear shape of the weight based on the platform state.

E.1.1 Penalisation Weight for Angular Orientation

The weight on angular orientation was varied between 1e-4 and 1e-1. The weight of 1e-1 provides deteriorated specific force tracking performance, while the weights 1e-2, 1e-3 and 1e-4 provide almost identical responses. Hence, the weight of 1e-4 is chosen as it provides desirable performance, while keeping a lower contribution in the cost term.

E.1.2 Penalisation Weight for Angular Velocity

The weight on angular velocity was also varied between 1e-4 and 1e-1. While all the weights provided a very similar response in the specific force generation, the weights had very different responses for the angular velocities. The weight of 1e-1 provides almost no excessive motion, whereas all other weights show excess oscillations in angular velocity. Thus the authors choose the weight of 1e-1 for the penalisation on angular velocity.

E.1.3 Penalisation Weight for Displacement

The weight on translational displacement was varied between 1e-4 and 1e-1 as well. While a weight of 1e-4 tracks the specific force desirably for the majority of the simulation, at various instances, it performs a jerky motion when it reaches the limits of the workspace. With the weight 1e-3 we obtain desirable specific force tracking performance, however oscillations are observed in the angular velocity with this setting. The weight 1e-1 and 1e-2 provide a very similar response with no excess oscillation in the angular velocity. Thus due to its lower contribution towards the overall objective function, 1e-2 is chosen as the preferred weight for the simulations.

E.1.4 Penalisation Weight for Translational Jerk

The weight on translational jerk was varied between 1e-4 and 1e-1 as well. All the explored weights provided near identical responses. Thus the weight of 1e-4 is used to have the lowest possible contribution to the objective function, while providing a desirable performance.

E.1.5 Penalisation Weight for Angular Jerk

The weight on angular jerk was varied between 1e-5 and 1e-2 as well. The weight of 1e-2 renders a profile that does not follow the reference specific force properly. While the weight of 1e-3 traces the specific force, it exhibits oscillations in the tilt rate. The weights 1e-5 and 1e-4 provide a desirable specific force tracking, with the weight of 1e-4 also attaining slightly lower tilt rate values. Thus the weight of 1e-4 is selected for the simulations in this work.

E.2 Questionnaire

Participants rated realism on a 5-point Likert scale with the following questions:

- How closely did the ride's motion correspond to the video?
  [0 = Not at all, 5 = Completely coherent]
- How close did the cornering feel compared to a real car?
  [0 = Not at all, 5 = Exactly like a real car]
- How realistic did the acceleration and deceleration feel compared to a real car?
  [0 = Not at all, 5 = Exactly like a real car]
- Were there any unnatural motions that did not match real driving?
  [0 = Not at all, 5 = A lot of them]

E.3 Motion Sickness Model

The MPC-based algorithm needs a motion sickness prediction model to calculate a motion sickness metric (J_{MS}) for the cost function (J_c). For this, we use the Subjective Vertical Conflict with Visual Rotational velocity (SVC-VR) as described by Kotian et al. (2023). The model was first introduced by Wada et al. (2020) and later validated and found to be favourable for motion sickness predictions in vehicles for a population by Kotian et al. (2024). This model (Wada et al. (2020)) predicts the motion sickness incidence (MSI), which is a group-averaged metric representing the percentage of people who will develop motion sickness. This is not suitable as we need a scale based on the severity of motion sickness in an individual. This way we will have better control on how much the severity of sickness varies with different algorithms. For this, we used the model by Kotian et al. (2023), which adapted the model by Wada et al. (2020) to predict motion sickness for an individual in MIsery SCale (MISC). This model accepts specific forces, angular rotations and visual flow (visual angular rotation) as inputs and gives motion sickness in MISC as output.

It is important to mention that the platform's motion is different from the visual cues. In this study we simulate conditions with out of the window view. Thus, the vehicle angu-

lar velocities are given for the vision angular velocity input to the SVC model, while the vestibular system is provided with the platform motion.

The motion sickness score output from the accumulation model has a large time constant due to the slow dynamics of the accumulation model. The high time constant of the accumulation model implies that a long prediction horizon would be required for it to function effectively. However, as demonstrated in Jain et al. (2023a), optimising for motion sickness over a short horizon can still lead to effective reduction of accumulated sickness over longer durations—provided that an appropriate short-term proxy, such as instantaneous sensory conflict, is used. As we optimise the motion at each time instant, we want to calculate the instantaneous response to the motion stimuli which drives motion sickness. This is the sensory conflict that can be obtained by the first half part of the model, often termed the 'sensory conflict generation' model shown in figure 6.1.

We converted a Simulink implementation of the SVC-VR model into ordinary differential equations, which our MPC solver can use. The ordinary differential equations for the SVC-VR model are given below:

$$\dot{v}_s = \frac{f_{spec} - v_s}{\tau} - \omega_s \times v_s \tag{E.1}$$

$$\dot{\omega}_s = \dot{\omega} - \frac{\omega_s}{\tau_d} \tag{E.2}$$

$$\dot{\hat{v}}_s = \frac{\hat{f}_s - \hat{v}_s}{\tau} - \hat{\omega}_s \times \hat{v}_s \tag{E.3}$$

$$\dot{\hat{\omega}}_s = \frac{(K_{\omega,c} + K_\omega)\dot{\omega} + K_{\omega,vis}\dot{\omega}_{vis} - \frac{K_{\omega,c}}{\tau_d}(\omega_s - \hat{\omega}_s)}{1 + K_{\omega,vis} + K_{\omega,c}} - \frac{\hat{\omega}_s}{\tau_d} \tag{E.4}$$

$$\dot{\tilde{v}} = K_{vc}(v_s - \hat{v}_s) + K_{g,vis}(v_{vis} - \tilde{v}) \tag{E.5}$$

$$\dot{\hat{f}}_s = K_{vc}(v_s - \hat{v}_s) + K_{g,vis}(v_{vis} - \tilde{v}) + K_{ac}(f_s - v_s - \hat{f}_s + \hat{v}_s) + K_a\dot{a} \tag{E.6}$$

where $\hat{f}_s$ represents the estimated specific force vector, v_s and $\hat{v}_s$ are the sensed subjective vertical and estimated subjective vertical, respectively. ω_s and $\hat{\omega}_s$ are the sensed angular velocity and estimated angular velocity respectively. $\tau = 5\ s$, $\tau_d = 7\ s$, $K_{\omega,c} = 10$, $K_{a,c} = 1$, $K_{v,c} = 5$, $K_a = 0$, $K_\omega = 0$, $K_{\omega,vis} = 10$, $K_{g,vis} = 0$ are the parameters used for the SVC model taken from Kotian et al. (2025). Here, τ and τ_d are the time constants corresponding to the otoliths and the semicircular canals respectively. $K_{\omega,c}$, $K_{a,c}$, and $K_{v,c}$ are the vestibular feedback gains, K_a and K_ω are the anticipatory gains, $K_{\omega,\text{vis}}$ and $K_{g,\text{vis}}$ are the visual feedback gains.

The sensory conflict is derived by calculating the Euclidean norm or 2-norm of the differ-

ence between the sensed subjective vertical and estimated subjective vertical:

$$c_v = \left\| v_s - \hat{v}_s \right\|_2 = \left(\sum_{i=1}^{3} (v_{s_i} - \hat{v}_{s_i})^2 \right)^{1/2} \tag{E.7}$$

$$J_{MS} = w_{con} \quad {c_v}^2 \tag{E.8}$$

where, w_{con} is the weight on the conflict, c_v, to create the sensory conflict term quantifying motion sickness (J_{MS}) used in the objective function.

The sensory conflict is one-dimensional. The accumulation of this sensory conflict drives the overall motion sickness scores. Minimising this sensory conflict over the MPC time horizon will result in a reduction of motion sickness.

To demonstrate the effectiveness of the motion cueing algorithm, we also predict MISC over the entire experiment duration. Here we use the entire model framework by Kotian et al. (2023), including the 'conflict accumulation' model as shown in the bottom right in figure 6.1. To predict the variance in MISC across a population, we simulate the MISC for 1000 individuals with varying motion susceptibilities. These parameters are sampled from the parameter distribution described in Kotian et al. (2025). In that work, a 3-component probability distribution of parameter sets was generated for the model by Kotian et al. (2023), which can be sampled according to the desired motion sickness susceptibility. These parameter sets have been shown to generalise well for MISC predictions in new driving scenarios Kotian et al. (2025). This makes it ideal to use for testing and selecting algorithms.

E.4 Hexapod/Driving Simulator Dynamics

The motion of the hexapod platform is defined in a state-space form to facilitate implementation in the MPC. The base states include hexapod position (s_{hex}) and angular orientation (θ_{hex}). These base states are added to the state-space model with the relation

$$\dot{x}_{hex} = A_{hex} x_{hex} + B_{hex} u_{hex} \tag{E.9}$$

where the state vector, x_{hex}, comprises of the position, s_{hex}, translational velocity, v_{hex}, angular orientation, θ_{hex}, and angular velocity, ω_{hex}, of the hexapod and the input vector, u_{hex}, comprises of translational acceleration, a_{hex} and angular acceleration of each euler angle, α_{hex}. The matrices A_{hex} and B_{hex} represent the double integrator system of the inputs, adapted from Qazani et al. (2019).

As the algorithm is designed for both longitudinal and lateral degrees of freedom, each state comprises of components in x and y directions (roll and pitch for orientation). In this study, positive values correspond to forward, left, and upward orientations along the x, y, and z axes, with counterclockwise rotations indicated as positive.

To achieve realistic motion perception (one of the primary objectives of the algorithm), vehicular accelerations are tracked using specific forces generated by the driving simulator. The specific force consists of two components that arise through translational accelerations and gravity. This specific force encapsulates the combined effects of accelerations and gravity as perceived by the human via the otoliths (part of the vestibular system). Therefore, the specific force is calculated at the estimated head coordinate system, thereby incorporating the effects of platform rotation.

The translational component is the acceleration of the platform. The gravitational force vector at the estimated head location, G_{loc}, is defined by the relation:

$$G_{loc} = R^T [0\ 0\ g]' \tag{E.10}$$

Here R is the transformation matrix that resolves gravitational force to the vectors corresponding to longitudinal, lateral and vertical body reference frame directions and g is the acceleration due to gravity, acting in the inertial vertical direction.

The total specific force is defined as:

$$f_{spec} = a_{hex} - G_{loc} \tag{E.11}$$

where a is the translational acceleration of the platform. The tilt component, G_{loc}, provides an additional pseudo acceleration to the occupant of the simulator. The specific force is the quantity to be tracked to achieve realistic motion perception.

This shapes our cost function term for the MCA defining the motion perception term (J_{MP}), which is given by:

$$J_{MP} = (f_{spec} - f_{ref})\, w_{spec}\, (f_{spec} - f_{ref})^T \tag{E.12}$$

To reduce motion sickness stimuli (the secondary objective of the algorithm), sensory conflict (appendix E.3) needs to be minimised. Thus, the MPC includes the hexapod dynamics and the 6-DOF SVC model to predict the development of motion sickness over the prediction horizon.

Thus the complete analytical description of the dynamics of motion sickness development, through the platform motion, includes the following states:

$$x = [\theta_{hex}, \omega_{hex}, s_{hex}, v_{hex}, f_{tilt}, f_{all}, \hat{f}_{all}, \hat{v}_s, \omega_s, \hat{\omega}_s, v_s] \tag{E.13}$$

Here, f_{all} denotes the vector of specific forces in all three directions (x, y, z); $\hat{f}_{all}$ represents the estimated specific forces in those directions; and f_{tilt} corresponds to the tilt-generated specific force, which is equal to the local gravitational vector G_{loc}.

E.5 Workspace Management

The MPC considers these constraints over the prediction horizon to optimally use the workspace and generate realistic motion. Two additional strategies are employed here for effective workspace management: washout and dynamic constraints.

Washout: The simulator platform has the maximum potential of recreating the specific forces at its neutral position. To ensure the platform remains near its neutral position, we penalise its states in the cost function. In this work, we use non-linear weights (based on the platform orientation and position) for the washout instead of constant weights. This allows a single non-linear setting for all scenarios rather than tuning the washout weights for each scenario.
The non-linear weights are defined as

$$w_s = \frac{k_1}{k_2(|s_{hex}| - s_{lim})^2 + \Delta} \tag{E.14}$$

$$w_\theta = \frac{k_3}{k_2(|\theta_{hex}| - \theta_{lim})^2 + \Delta} \tag{E.15}$$

where k_1, k_2 and k_3 define the shape of the weight function, s_{lim} and θ_{lim} are the defined limits for the platform for displacement and tilt angle. Δ (here 0.01) is a small value added to the denominator to avoid singularity. The selected values are $k_1 = 1$, $k_2 = 50$ and $k_3 = 0.1$, these values were manually tuned to ensure that the penalisation is low near the neutral position, while high, close to the platform limits.

Dynamic constraints: In this study, we incorporate dynamic bounds on the platform position and orientation via the constraints proposed in Fang and Kemeny (2012), as 'braking constraints'.

The formulation of the constraints is

$$s_{hex,min} \leq s_{dyn} \leq s_{hex,max} \tag{E.16}$$

$$\theta_{hex,min} \leq \theta_{dyn} \leq \theta_{hex,max} \tag{E.17}$$

$$s_{dyn} = s_{hex} + c_v v_{hex} T_{dyn,s} + 0.5 c_u a_{hex,tran} T_{dyn,s}^2 \tag{E.18}$$

$$\theta_{dyn} = \theta_{hex} + c_w \omega_{hex} T_{dyn,\theta} + 0.5 c_u a_{hex,rot} T_{dyn,\theta}^2 \tag{E.19}$$

where, $c_v = 1, c_w = 1, c_u = 0.45, T_{dyn,\theta} = 0.5$, $T_{dyn,p} = 2.5$ and s_p, θ_p limits are 0.3 m and 20 deg respectively. The selected values were adopted from Munir et al. (2017). When the platform approaches its limits, the platform's acceleration and velocity reduce, to stay within the workspace envelope.

E.6 Yaw Channel

The fifth DoF (yaw) is controlled separately using a parallel washout channel, ensuring reduced computational complexity. For the simulator used in this work (DAVSi), the control commands we require to provide are yaw position velocity and acceleration. This is done by passing the acceleration through a high-pass filter to obtain the desired platform yaw acceleration. To ensure that the yaw angle returns back to it's neutral position at the end of the simulation, we use a second order high pass filter instead of a first order filter. The second-order high-pass filter used for this purpose is given as

$$HP(s) = \frac{s^2}{s^2 + 2\nu_{yaw}s + \nu_{yaw}^2} \tag{E.20}$$

Here, ν_{yaw} denotes the cut-off frequency of the high-pass filter. A value of 0.0159 Hz is used, consistent with the configuration used for our previous studies. Additionally, for simplicity, the damping ratio is kept to be 1 (critically damped).

As yaw motion also affects motion sickness, the yaw prediction for the future should also be communicated to the MPC. As the yaw washout is highly computationally efficient, it can calculate the solution to the reference yaw for the prediction horizon almost instantly. In our implementation, we include yaw information as online data for communication with the MPC.

E.7 Constraints

Constraints in the MPC are added to ensure that the hexapod's motions remain physically feasible and safe. These include workspace limits on position and orientation to prevent the platform from exceeding mechanical boundaries, as well as limits on velocities and accelerations, to avoid abrupt or excessive movements that could cause discomfort or destabilise the system.

For defining such constraints, the workspace limits of Delft Advanced Vehicle Simulator (DAVSi) are used (table E.2).

Table E.2: Workspace limits of the DAVSi

Quantity	Limit
θ_{hex}	$\pm 30 deg$
v_{hex}	$\pm 7.2 m/s$
a_{hex}	$\pm 9.81 m/s^2$
s_{hex}	$\pm 0.5 m$
a_{cmd}	$\pm 5 m/s^2$

Additionally, to minimise the perception of platform motion and avoid introducing false cues, it is essential to limit platform rotation rates below the human perception threshold. This threshold is typically considered to lie between 2–4°/s Houck et al. (2005); Khusro et al. (2020); Lamprecht et al. (2022). In this work, a value of 3°/s was selected based on subjective feedback from participants during a pilot study.

Rather than enforcing this as a hard constraint, we model it as a soft constraint to allow occasional violations when necessary to improve specific force tracking performance. This approach enables flexibility in generating higher specific forces without introducing excessive perceived motion. The tilt-rate constraint is therefore defined as:

$$-\omega_{thd} \leq \omega_{hex} + \delta\, \omega_{hex} - \delta \leq \omega_{thd} \tag{E.21}$$

Here, ω_{thd} is the selected perception threshold (3°/s for both pitch and roll rate), and δ is a positive slack variable included in the cost function. While violations of the threshold are permitted, they are penalized to encourage minimal deviation, balancing perceptual fidelity with motion cueing performance.

E.8 Comparison of MCAs

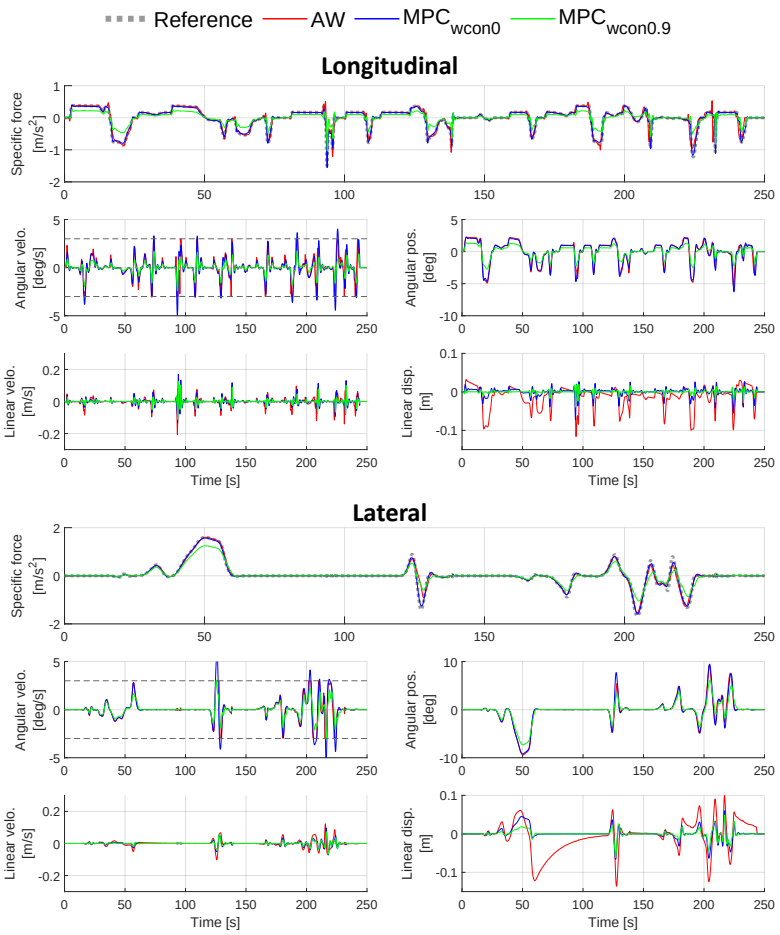

Figure E.1: Specific force, angular velocity, angular position, linear velocity and linear displacement data shown for different algorithm configurations. Longitudinal components in the upper graphs and Lateral components in the lower graphs.

About the Author

Varun Kotian was born in Mumbai, India. He began his PhD in 2021 at Delft University of Technology at the Department of Cognitive Robotics within the Faculty of Mechanical Engineering. His research is funded by Toyota Motor Europe and focuses on developing models for predicting motion sickness in automated driving and driving simulators.

Prior to his PhD research, Varun earned his master's in Vehicle Engineering from Delft University of Technology. His master's thesis, titled 'Amplitude Dynamics of Motion Sickness', laid the foundation for his PhD research. His background through his bachelor's degree in Mechanical Engineering from K. J. Somaiya College of Engineering has helped throughout his research.

Varun Kotian is not only a curious researcher, but also an avid traveller who enjoys hiking and snowboarding.

List of Publications

14. **Kotian, V.***, Jain, V.*, Lazcano A. M. R., Pool, D. M., Happee, R., & Shyrokau, B. (2025). Reducing Discomfort in Driving Simulators: Motion Cueing for Motion Sickness Mitigation. *TechRxiv preprint*. (Chapter 6)
13. **Kotian, V.**, Pool, D. M., Happee, R., Li, S. & Wada, T. (2025). Impact of Physical and Visual Motion on Subjective Perception of Vertical Orientation. *Research Square preprint*. (Chapter 5)
12. van Elburg, A., Gkentsidis, K., Sarrazin, M., Barendswaard, S., **Kotian, V.**, & Happee, R. (2025). Facial emotion recognition does not detect feeling unsafe in automated driving. *arXiv preprint*.
11. Schippers, E., Schrank, A., **Kotian, V.**, Messiou, C., Oehl, M., & Papaioannou, G. (2025). A motion for no motion: The redundancy of motion feedback in low-velocity remote driving of a real vehicle. *SSRN preprint*.
10. **Kotian, V.**, Jain, V., Pool, D. M., Happee, R., & Shyrokau, B. (2025). Predicting and Controlling Motion Sickness through Sensory Conflict Minimisation. *2nd Congress on Motion Sickness*, Akureyri, Iceland.
9. Happee, R., **Kotian, V.** & Pool, D. M. (2025). Modelling Motion Sickness at an Individual and Population Level. *VDI-Berichte*, Nr. 2450, 2025.
8. de Groot, O., Bertipaglia, A., Boekema, H., Jain, V., Kegl, M., **Kotian, V.**, Lentsch, T., Lin, Y., Messiou, C., Schippers, E., Tajdari, F., Wang, S., Xia, Z., Zaffar, M., Ensing, R., Garzon, M., Alonso-Mora, J., Caesar, H., Ferranti, L., Happee, R., Kooij, J. F. P., Papaioannou, G., Shyrokau, B., & Gavrila, D. M. (2025). A vehicle system for navigating among vulnerable road users including remote operation. *Proceedings of the IEEE Intelligent Vehicles Symposium (IV)*, Cluj-Napoca, Romania.
7. **Kotian, V.**, Pool, D. M., & Happee, R. (2025). Personalising Motion Sickness Models: Estimation and Statistical Modeling of Individual-Specific Parameters. *Frontiers in Systems Neuroscience*, 19, 1531795. (Chapter 4)
6. **Kotian, V.**, Irmak, T., Pool, D., & Happee, R. (2024). The role of vision in sensory integration models for predicting motion perception and sickness. *Experimental Brain Research*, 242(3), 685–725. (Chapter 3)
5. **Kotian, V.**, Pool, D. M., & Happee, R. (2023). Modelling individual motion sickness accumulation in vehicles and driving simulators. *Proceedings of the Driving Simulation Conference*, Antibes, France. (preliminary version of Chapter 4)
4. Papaioannou, G., Cvetkovic, M., Messiou, C., **Kotian, V.**, Shyrokau, B., & Happee, R. (2023). A novel experiment to unravel fundamental questions about postural stability and motion comfort in automated vehicles. *Proceedings of the 4th International Comfort Congress*, 123–126.
3. Happee, R., **Kotian, V.**, & de Winkel, K. (2023). Neck stabilization through sensory integration of vestibular and visual motion cues. *Frontiers in Neurology*, 14, 1266345.
2. De Winkel, K. N., Irmak, T., **Kotian, V.**, Pool, D. M., & Happee, R. (2022). Relating individual motion sickness levels to subjective discomfort ratings. *Experimental Brain Research*, 2022, 1, 1–10.
1. Irmak, T.*, **Kotian, V.***, Happee, R., de Winkel, K. N., & Pool, D. M. (2022). Amplitude and Temporal Dynamics of Motion Sickness. *Frontiers in Systems Neuroscience*, 16. (Chapter 2)

Included in this thesis.

* Contributed equally

Patents

1. Motion Cueing Algorithm for Motion Sickness Mitigation in Driving Simulators (2025).
2. Personalized motion sickness modelling and predictive mitigation in automated driving and simulation environments (2025).

Acknowledgments

Of all parts of a thesis, the acknowledgements are often read most closely. I am grateful for this chance to thank everyone who made these four years possible and meaningful.

First and foremost, I thank my promotor, Riender Happee. Your experience, clear guidance, and steady support shaped this PhD from start to finish. You gave me room to explore and pushed me to be bolder in my ideas and presentations. I learned a lot from your high standards and practical advice. I feel lucky to have worked with you.

I thank my co-promotor, Daan Pool. You were there when I was stuck, and your feedback was clear, fast, and hands-on, often outside normal hours. You helped me turn rough ideas into solid methods and text. Your direct comments and encouragement made many turning points possible in this thesis.

I also thank Barys Shyrokau. You brought me onto this project and mentored me closely. You taught me how to build a clear presentation and trusted me with real responsibility. You opened doors, supported me through setbacks, and helped me grow as a researcher. Thank you for the opportunities and collaboration.

I thank Xabier Akuten Carrera and Andrea Michelle Rios Lazcano from Toyota Motor Europe for funding my project through the TIPP project and for their steady support throughout, with special thanks to Andrea for career guidance. I am also grateful to the colleagues I worked with at Toyota for your time in meetings, technical reviews, and test days.

Finally, thanks to Barys for enabling my participation in the EU Horizon 2020 Framework Program under the Marie Sklodowska-Curie actions within the OWHEEL project, which made a three-month research visit to Japan possible.

I am grateful to Takahiro Wada for hosting me at Nara Institute of Science and Technology and for our collaboration. I enjoyed our outings around Kansai and your stories of ancient Japan. You made the visit memorable beyond the research.

I also thank Jelte Bos from TNO for many helpful discussions. Your perspective, so different from the engineers around me, broadened my thinking and challenged my assumptions.

At TU Delft, my thanks start with the secretaries of Cognitive Robotics, especially Hanneke Hustinx and Loulou Zorgui-Martens, for helping me through endless bureaucracy and visa issues.

Thank you to Mario Garzon Oviedo and Ronald Ensing for your essential help setting up the Toyota Prius for experiments and demos; your practical expertise made many things possible that would otherwise have stalled.

It's been a long time at TU Delft, and I still remember the people who left a mark on me,

even if they have moved on. First, thank you to Tugrul Irmak, my guide in the early phase of this research. You helped me not only academically but also pushed me beyond what I thought possible like the impromptu trip to Refuge des Conscrits. Ksander de Winkel, it was a pleasure working with you. I learned a lot, especially statistics, and enjoyed our lunch conversations. Jork Stapel, your advice when I was deciding on a PhD shaped both my choice and my approach. Marko Cvetkovic, I will remember our cold-night photo walks and the drive to Brussels. I value our long talks about research and life, and I hope there are many more conversations to come. Raj Desai, though brief, I enjoyed our office talks and hearing your perspectives. Farzam Tajdari, thank you for your company and for always being ready for a chat. Zimin Xia, the most focused person I know, thank you for the many dinners from Ares Foodie. Yanggu Zheng, I enjoyed your company every week on "Yanggu Day", that was always a good day. Andras Palfy, thanks for the great advice at the start of the PhD, especially to befriend the secretaries. Wilbert Tabone, it was always fun talking with you. Your absence is still felt in the office. Guopeng Li, though our time was short, I appreciated your motivating words. Yancong Lin, I will remember staying in the office with you until closing time. Xiaoyu Liu, it was always great talking to you in the office, and I look forward to your Linyi Chaoji.

Now to the people still at TU Delft: Shiming Wang, you opened the door to so many wonderful Chinese friends, I will always be grateful. I have enjoyed our dinners, even if we don't do them often enough now. Chrysovalanto Messiou, thank you for being the "yiayia" of our group. Your warmth made us better; and thanks for the de-stressing week in the Alps where we were a bit too close to danger a few times (maybe I should thank Daniel instead!). Soyeon Kim, I kept you here because you still return from time to time—thank you for always being kind and helpful. Xiaolin He, I really enjoyed spending time with you, you taught me how to eat and drink properly. Charlotte Croucher, I really got to know you during the Iceland trip where i think we both will forever cherish the nature, the drive, and the people. Vishrut, thank you for tolerating me, there was never a dull moment with you. Alberto, you were probably my longest-time office mate. I remember the COVID days when you came to setup your PC "setups" for the nth time. Mubariz, our conversations were always interesting, thanks for laughing with me through the hard times. Ted, the bold way you tackled your PhD truly inspired me.

Abel and Emma, my master students, thank you for your hard work and trust throughout our projects. It was a pleasure to collaborate with you, and I'm proud of what we achieved together.

To the friends who made a small Mumbai in Delft, Parshva, Tanay, Sahil, and Pranav, thank you for being ready to meet any weekend. Those moments felt like home and kept me grounded. A special thank you to Rucha for your constant support, kindness, and help with emails and decisions. Without you, this PhD would have been much harder.

To my family, thank you for your endless support. I know my choices were not what you expected, and I could not always be there while your challenges grew, yet you never complained and stood by me fully. Your patience, love, and faith kept me going. I hope to make you proud and to give back even a small part of what you have given me.

To all the participants in my studies, thank you for your time, effort, and patience. Many

of you returned several times, worked around busy schedules, and showed up even with setbacks like a flat tyre. Some of you even continued after vomiting, which I will never forget. I was moved by your commitment to science. Meeting you was one of the best parts of this work, and your help made this research possible.

If I have missed anyone who helped me along the way, please forgive me. Thank you all for your support.

Finally, I thank myself for not giving up. A line that kept me going, which I share with anyone who made it to the end of these acknowledgements:

There is a curse that follows the good.
The more you give, the more they take.
The more you love, the more they betray.
You stand in silence holding your pain,
because you think that's what strength is.
But deep down you wonder, why me? Why always me?
You sacrifice yourself for people who don't even care for you.
You forgive those who cut you the deepest,
and in return, the world rewards you with scars.
But hear me now, your kindness is not weakness.
The world doesn't break the weak, it breaks the strong.
It fears those who can endure, so let them hurt you. So let them doubt you.
Every scar you have is proof that you chose to rise and stay kind.
When the world begged you to be cruel, your pain is proof of your power.
Stay good even when it hurts.

Itachi Uchiha

Varun Kotian
Delft, October 2025

Propositions

accompanying the dissertation

Motion Perception and Sickness Modelling and Prediction for Automated Driving and Simulators

by

Varun Kotian

1. Individual variability in motion sickness development can be captured with only a personalised accumulation model.
   This proposition pertains to Chapter 2.
2. No single current model can simultaneously predict the effects of vision on both motion sickness and motion perception.
   This proposition pertains to Chapters 3 and 5.
3. Stochastic modelling of personalised parameters enables robust sickness predictions for untested driving scenarios.
   This proposition pertains to Chapters 4 and 6.
4. Fitting different parameters for different vision cases trades accuracy for overfitting; a practical model requires a single parameterisation that jointly explains all vision cases.
   This proposition pertains to Chapters 3, 4 and 5.
5. People who do not get motion sick should not conduct motion sickness research.
6. To study motion sickness in driving scenarios, experiments shorter than ten minutes are insufficient and should be avoided.
7. For both fun and comfort reasons, people will always want to have the option to manually drive a fully autonomous vehicle.
8. The more you know about connected systems, the more appealing simple, non-networked, analog options become.
9. GenAI replaces mundane work while amplifying the need for human experts.
10. The selfish intent of wanting peace initiates wars.

These propositions are regarded as opposable and defendable, and have been approved as such by the promotor Prof. Dr. Ir. R. Happee, and co-promotor, Dr. Ir. D. M. Pool.

Can we prevent motion sickness in the age of automated driving?

As automated vehicles position drivers as passive passengers and simulators become increasingly immersive, motion sickness has emerged as a critical barrier to user acceptance. Traditional models rely on group averages and focus on extreme outcomes, failing to capture the subtle, individual discomforts like nausea and dizziness that ruin the passenger experience.

This book presents a framework for predicting and mitigating motion sickness at the individual level by moving beyond a one-size-fits-all approach. The research introduces a personalized modeling method that adapts to specific user sensitivities using two key parameters and proposes critical updates to sensory conflict models to better align visual perception with reality. These culminate in a novel control algorithm for simulators that reduces motion sickness by over 50% without sacrificing realism. This work aims to bridge the gap between biological variability and mechanical design to create a more comfortable experience.

TU Delft